A CFD DESIGN STUDY OF AN AIR REACTOR CAVITY COOLING SYSTEM USING TRADITIONAL THERMAL ANALYSIS TECHNIQUES AND ENTROPY GENERATION ANALYSIS

A Dissertation

Presented in Partial Fulfillment of the Requirements for the

Degree of Doctor of Philosophy

with a

Major in Nuclear Engineering

in the

College of Graduate Studies

University of Idaho

by

Kurt D. Hamman

October 2015

Major Professor: Akira Tokuhiro, Ph.D.

Committee Members: Richard C. Martineau, Ph.D.
Vincent Mousseau, Ph.D.; Richard N. Christensen, Ph.D.

Department Administrator: Lee Ostrom, Ph.D.

Authorization to Submit Dissertation

This dissertation of Kurt David Hamman, submitted for the degree of Doctor of Philosophy with a major in Nuclear Engineering and titled "A CFD design study of an Air Reactor Cavity Cooling System using Traditional Thermal Analysis Techniques and Entropy Generation Analysis," has been reviewed in final form. Permission, as indicated by the signatures and dates given below, is now granted to submit final copies to the College of Graduate Studies for approval.

Major Professor _____ Date: _____
Akira Tokuhiro, Ph.D.

Committee Members _____ Date: _____
Richard C. Martineau, Ph.D.

_____ Date: _____
Vincent Mousseau, Ph.D.

_____ Date: _____
Richard N. Christensen, Ph.D.

Department Administrator _____ Date: _____
Lee Ostrom, Ph.D.

Abstract

Current research in advanced reactor designs has focused on passive safety systems, where in the event of a loss of cooling to the reactor core, excess heat will be removed by a passive safety heat removal system. A safety system is classified as 'passive' because it does not require a pump to circulate the fluid (i.e., forced circulation) or operator action to maintain cooling. The system relies on the natural circulation of a fluid (i.e., fluid density differences and gravity) to transfer the heat. Passive safety system designs include features that enhance natural circulation, such as using smooth pipes, minimizing flow obstructions, and maximizing density differences, which increase fluid velocity and hence the removal of more heat.

This research consisted of a CFD study of wall-bounded transitional flows and a passive reactor cavity cooling system. Yet in an effort to better understand fundamental phenomena, relative to the limits of natural circulation turbulence modeling, only forced circulation CFD analyses were performed. The initial phase of this research consisted of two types of CFD studies: 2D entropy generation rate boundary layer analyses of an isothermal transitional fluid flow over a flat plate, and 3D thermal performance analyses of a $\frac{1}{4}$–scale experimental air reactor cavity cooling system. The 2D flat plate boundary layer studies were important in that they provided insight into flow features, such as boundary layer development and entropy generation rate, in the 3D RCCS ducts as the air transitions from laminar to turbulent flow.

Using the results of the initial study as a baseline, this work analyzed the viscous and thermal boundary layer development, including estimating the entropy generation rate, in the heated duct section of the RCCS, which is characterized by nonuniform flow and heat transfer. A new engineering design process was developed, which incorporates not only traditional heat transfer and fluid flow (HTFF) analysis techniques but entropy generation minimization (EGM) concepts as well. This analysis process was successfully applied to the existing $\frac{1}{4}$–scale experimental air RCCS, resulting in the identification of the primary entropy dissipation mechanism and an improved design.

Vita

Education

- MBA, Idaho State University, 2006.
- MS Mechanical Engineering, University of Idaho, 1995.
  - *Thesis:* "The Efficient Addition of Void Fraction Effects in a Two–Phase Flow, Dilute Particle Volume Code"
  - *Committee:* Ray A. Berry, E. Clark Lemmon, Calvin E. Slater
- ME Nuclear Engineering, University of Idaho, 1995.
  - *Adviser:* Alan G. Stephens
- Naval Nuclear Power Training (Officer/S1W Prototype), 1988.
  (graduate-level coursework and nuclear power plant operations)
- BS Mechanical Engineering, *Cum Laude*, University of Idaho, 1986.
  (completed degree in 36 months)
- Naval Nuclear Power Training (Enlisted/S5G Prototype), 1981.
  (undergraduate-level coursework and nuclear power plant operations)

Relevant Experience

- University of Idaho (Idaho Falls); Nuclear Engineering Graduate Program, Graduate Research Assistant, September 2013 – September 2014.
- Idaho National Laboratory; Thermal Science and Safety Analysis Department, Computational Nuclear Engineer, April 2007 – August 2013.
- Idaho State University; College of Engineering, Adjunct Faculty and Laboratory Director, August 2000 – December 2001.
- Puget Sound Naval Shipyard; Engineering Duty Officer (maintenance and repair of nuclear powered vessels), February 1997 – July 2000.
- Naval Reactors Facility (A1W Prototype); Instructor, Operations Engineer, and Training Manager, January 1992 – January 1994.
- USS William H. Bates (SSN–680); Reactor Plant Chemistry/Radiological Controls Division Manager and Nuclear Reactor Plant Refueling Supervisor, September 1988 – December 1991.
- Naval Reactors Facility (S5G Prototype); Instructor and Mechanical Operator, March 1982 – July 1983.

Journal Articles, Conference Papers, and Reports (partial list)

- Hamman, K. D. and Berry, R. A. (2010). A CFD simulation process for fast reactor fuel assemblies. *Nuclear Engineering and Design* 240, 2304–2312.
- Martineau, R. C., Berry, R. A., Esteve, A., Hamman, K. D., et al., (2010). Comparison of natural convection flows under VHTR type conditions modeled by both the conservative and incompressible forms of the Navier–Stokes equations. *Nuclear Engineering and Design* 240, 1371–1385.
- Hamman, K. D., Tokuhiro, A. T., Muci, M. A., and Corradini, M. L. (2015). CFD Analysis of the $\frac{1}{4}$–Scale Air Reactor Cavity Cooling System Inlet Plenum. 23rd International Conference on Nuclear Engineering (ICONE23), Chiba, Japan.
- McCreery, G., McIlroy, H., Hamman, K., and Zhang, H. (2008). Wire–Wrapped Rod Bundle Matched Index–of–Refraction Experiments. 16th International Conference on Nuclear Engineering (ICONE16), Orlando, FL.
- Hamman, K. D., et al., (2012). Bounding Thermal Analysis in the ATR Small B–Positions. Idaho National Laboratory report (ECAR-1687).
- Hamman, K. D., et al., (2010). AGR–2 Pre–Test Prediction Analyses using the PARFUME Code for U.S. Fuel Particles. Idaho National Laboratory report (ECAR-1020 Rev. 2).

Scholarships & Awards

- U.S. Navy Advanced Education Program, 1994 – 1995.
  (Program Sponsor: Naval Postgraduate School)
- U.S. Navy Nuclear Enlisted Commissioning Program, 1983 – 1986.
  (Program Sponsor: DOE Office of Naval Reactors)

Invited Seminar Presentations

- 2013: 'WATER HAS NO CRACKS . . .' (History of the Naval Nuclear Propulsion Program and its presence in Idaho), INL. [`http://tinyurl.com/mt3k6cu`]
- 2012: 'Reality and Nature . . . The Challenger Disaster Revisited,' INL Nuclear Science and Technology Seminar Series. [`http://tinyurl.com/ltz29ev`]
- 2010: 'U.S. Naval Nuclear Powered Ship Inactivation, Disposal, and Recycling,' Eastern Idaho Project Management Institute. [`http://tinyurl.com/k4wxzpb`]

Licenses and Qualifications

- Professional Engineer, State of Idaho, Mechanical Engineering (#8116), 1996.
- Qualified Engineer by the DOE Office of Naval Reactors (S5W Reactor), 1990.

Acknowledgments

I would like to thank my Major Professor Akira Tokuhiro for his advice, patience, and leeway in completing this research. Additionally, I would like to express my gratitude to Richard C. Martineau, Vincent Mousseau, and Richard N. Christensen for offering their time and support as committee members. And yes, I should acknowledge the professors and teachers along the way that inspired me to explore not only the technical stuff, but the nontechnical aspects of engineering as well.

Yet, I would be remiss in not thanking the unsung heroes, working behind the scenes keeping the 'reactor critical.' To the university staff who are tasked with the challenge of managing the 'deliverables' and enforcing the 'rules' – thank you. To all the computer support personnel who maintain those boxes that assemble 'ones' and 'zeros' – thank you. And to all librarians, guardians of the works of some of the 'greatest minds' and 'best teachers' – a special thank you. This research would not have been possible without your support.

Finally, to my wife Cory and sons Curtis and Kyle, thanks for your words of encouragement, patience, and advice – both technical and philosophical.

Never Stop Learning ...

Dedication

To those involved with practical reactors . . .

"Those involved with practical reactors,
humbled by their experience, speak less and worry more."

$\sim$ Hyman G. Rickover (1900 – 1986), Father of the Nuclear Navy

Table of Contents

Authorization to Submit Dissertation . . . . . **ii**

Abstract . . . . . **iii**

Vita . . . . . **iv**

Acknowledgments . . . . . **vi**

Dedication . . . . . **vii**

Table of Contents . . . . . **viii**

List of Figures . . . . . **xi**

List of Tables . . . . . **xv**

Nomenclature . . . . . **xvi**

Chapter 1: Introduction **1**

1.1 Reactor Cavity Cooling System Designs 1

1.1.1 Air RCCS 2

1.1.2 Water RCCS 5

1.2 Traditional Thermal Analysis 7

1.2.1 Thermal Analysis Example 7

1.3 Boundary Layer Transition 8

1.3.1 Natural and Bypass Transition 9

1.3.2 DNS and RANS Capabilities 12

1.4 Entropy 13

1.4.1 An Enigmatic Concept 14

1.4.2 Theoretical Formulation 15

1.4.3 Expanded Terms 21

1.4.4 Closure 22

Chapter 2: Literature Review **24**

2.1 Air Reactor Cavity Cooling System 24

2.2 Boundary Layer Transition 26

2.3 Entropy Generation Minimization and Models 28

2.3.1 Global and Local Models 31

2.3.2 EVM and DSM Closure Modeling 32

2.4 Verification and Validation 33

2.5 Related Research Limitations 35

Chapter 3: Entropy Generation Modeling **37**

3.1 Lumped Parameter Model 37

3.2 Direct Method Model 38

3.3 Modeled RAET Equation 42

3.4 Other Models 42

Chapter 4: Methods **43**

4.1 General Design and Analysis Process 43

4.2 Software 46

4.3 Hardware 47

4.4 Modeling and Simulation 50

4.4.1 Boundary Layer Transition 50

4.4.2 Inlet-Plenum Designs 53

4.4.3 Inlet-Plenum 58

4.4.4 Duct 4 65

Chapter 5: Results **74**

5.1 Traditional HTFF Analysis 74

5.2 Entropy Generation Analysis 87

5.2.1 Duct 4 87

5.2.2 Inlet-Plenum 92

5.3 Analysis Summary 93

5.4 Verification and Validation 93
5.4.1 Boundary Conditions 94
5.4.2 Calibration 97
5.4.3 Other Elements of V&V 99
5.4.4 Solution Uncertainty 102

Chapter 6: Conclusions and Contributions 108
6.1 Summary 108
6.2 Conclusions and Recommendations 110
6.3 Discipline Contributions 111

References 113

Appendices 122
Appendix A: EPSCoR Project Report 122
Appendix B: RCCS Project Report 173
Appendix C: Wall-bounded Flows 201

List of Figures

1.1 RCCS basic heat transfer process 4

1.2 GA-MHTGR RCCS panel (Bechtel National, 1992) 4

1.3 Air RCCS geometry (rotated view) 6

1.4 Water RCCS schematic (Lommers, 2010) 6

1.5 Traditional thermal analysis (Kock, 2003) 8

1.6 Stages of turbulence onset (Kachanov, 1994) 10

1.7 Natural boundary layer transition (White, 1991) 11

1.8 Predicting transition using shear stress (Mayle and Schulz, 1997) . . . 11

1.9 Non-calibrated and calibrated γ-Re_θ RANS turbulence model 13

2.1 Entropy production rate versus D/L (Herwig and Kock, 2007) 31

4.1 General design process 44

4.2 Duct 4 analysis process 45

4.3 Modeling and simulation process 46

4.4 Speedup curve (Icestorm) 49

4.5 Speedup curve (Aries) 49

4.6 Speedup curve (Big-STEM) 50

4.7 3D ZPG mesh 51

4.8 Streamwise mesh refinement (C_f *vs.* x) 52

4.9 Streamwise mesh refinement–enlarged (C_f *vs.* x) 52

4.10 Design A 54

4.11 Design B 54

4.12 Design C 55

4.13 Design E 55

4.14 Design A4 inlet-plenum 56

4.15 Design E6 inlet-plenum 56

4.16 Thermal design HTA 57

4.17 Thermal design HTB 57

4.18 Thermal design HTC 58
4.19 Inlet-plenum Duct 4 vertical plane (Mesh 4X) 60
4.20 Inlet-plenum outlet to Duct 4 (Mesh 4X) 60
4.21 Duct 4 isovelocity 2.5 m/s plot (Mesh 4X) 61
4.22 Duct 4 vertical plane vector-velocity plot (Mesh 4X) 61
4.23 Inlet-plenum residuals vs. iterations (Mesh 4X) 63
4.24 Inlet-plenum residuals vs. Tdr (Mesh 4X) 63
4.25 Inlet-plenum (University of Wisconsin) 64
4.26 Duct 4 vertical plane contour plot (Mesh 4X) 64
4.27 Mean velocity profiles (wide plane, 1.9 m) 66
4.28 Mean velocity profiles (center plane, 1.9 m) 66
4.29 Unstructured mesh 66
4.30 Duct 4 structured mesh 67
4.31 Inlet-plenum data plane (pink outline) 68
4.32 Duct 4 velocity contours 68
4.33 Duct 4 analysis planes (T, C, B) 70
4.34 Duct 4 analysis plane (W) 70
4.35 Analysis planes 71
4.36 Boundary layer development (Simon, 2015) 72
4.37 Freestream gradient map (Technique 1) 73
4.38 Freestream gradient map (Technique 2) 73
4.39 Freestream gradient map (Technique 3) 73

5.1 Wall shear stress vs. freestream direction - A4(HTA) 75
5.2 Wall shear stress vs. freestream direction - E6(HTA) 75
5.3 Wall shear stress vs. freestream direction - E6(HTB) 75
5.4 Wall shear stress vs. freestream direction - E6(HTC) 76
5.5 Heat transfer coefficient vs. freestream direction - A4(HTA) 76
5.6 Heat transfer coefficient vs. freestream direction - E6(HTA) 76
5.7 Heat transfer coefficient vs. freestream direction - E6(HTB) 77

5.8 Heat transfer coefficient vs. freestream direction - E6(HTC) 77
5.9 Velocity contour plots (40"–80") - A4/E6 (HTA) 81
5.10 Temperature contour plots (40"–80") - A4/E6 (HTA) 81
5.11 Velocity horizontal profile plots - A4/E6 (HTA) 82
5.12 Temperature horizontal profile plots - A4/E6 (HTA) 82
5.13 Boundary layer velocity profiles (wide plane, L = 2.4 m) 82
5.14 99% boundary layer (A4) - left(LHS)/right(RHS) 85
5.15 Momentum boundary layer (A4) - left(LHS)/right(RHS) 85
5.16 99% Boundary layer (E6) - left(LHS)/right(RHS) 85
5.17 Momentum boundary layer (E6) - left(LHS)/right(RHS) 86
5.18 Thermal boundary layer (A4) - left(LHS)/right(RHS) 86
5.19 Enthalpy boundary layer (A4) - left(LHS)/right(RHS) 86
5.20 Thermal boundary layer (E6) - left(LHS)/right(RHS) 87
5.21 Enthalpy boundary layer (E6) - left(LHS)/right(RHS) 87
5.22 Design comparison 88
5.23 Relative viscous entropy contribution (E6-HTA) 89
5.24 Relative design comparison 89
5.25 Global entropy dissipation coefficient (A4-HTA) 90
5.26 Global viscous entropy dissipation coefficient (A4-HTA) 91
5.27 Global entropy dissipation coefficient (E6-HTA) 91
5.28 Global viscous entropy dissipation coefficient (E6-HTA) 92
5.29 Wall shear stress vs. freestream direction (A4/E6 HTA) 94
5.30 Heat transfer coefficient vs. freestream direction (A4/E6 HTA) 94
5.31 Skin friction (C_f), DNS ZPG (solid) (Nolan and Zaki, 2013) 96
5.32 Skin friction (C_f), ZPG (MATLAB-Nolan and Zaki DNS data) 96
5.33 Graph "A" (Appendix A) Graph "B" (Ghasemi et al., 2013) 97
5.34 BC influence on RANS turbulence models 98
5.35 RANS transition model (C_f vs. x) - example calibration 99
5.36 Duct 4 residuals vs. iterations (example) 100

5.37 Inlet-plenum residuals vs. iterations (Design E6) 101
5.38 Net mas flow vs. iterations (Design A4 HTA) 101
5.39 Net heat transfer vs. iterations (Design A4 HTA) 101
5.40 Entropy dissipation coefficient uncertainty (2 vs. 1) 106
5.41 Entropy dissipation coefficient uncertainty (3 vs. 1) 106
5.42 Data plane interpolation (A4) 107
5.43 Data plane interpolation (E6) 107

List of Tables

4.1 Inlet-Plenum spatial convergence results (Design A4) 60

5.1 Flow parameters (0”–40”) 74

5.2 Flow parameters (40”–80”) 74

5.3 Duct 4 entropy results (0”–40”) 92

Nomenclature

Acronyms

$2D$	Two dimensional
$3D$	Three dimensional
$A4$	Inlet-plenum baseline design
ANL	Argonne National Laboratory
ATR	Advanced Test Reactor
BC	Boundary condition
BL	Boundary layer
CFD	Computational fluid dynamics
CHF	Critical heat flux
DNS	Direct numerical simulation
DOE	Department of Energy
DSM	Differential second–moment (closure model)
EGA	Entropy generation analysis
EGM	Entropy generation minimization
EGR	Entropy generation rate
$EPSCoR$	Experimental Program to Stimulate Competitive Research
$E6$	Inlet-plenum improved design
EVM	Eddy viscosity (closure) model
GA	General Atomics
GE	General Electric
HPC	High Performance Computing
HTA	Heat Transfer 'A' (design)
HTB	Heat Transfer 'B' (design)
HTC	Heat Transfer 'C' (design)
$HTFF$	Heat transfer and fluid flow
LHS	Left-hand side
$MHTGR$	Modular high temperature gas reactor
$M\&S$	Modeling ans simulation

$NSTF$	Natural Convection Shutdown Heat Removal Test Facility
$RAET$	Reynolds Averaged Entropy Transport (Equation)
$RANS$	Reynolds-averaged Navier-Stokes
$RCCS$	Reactor cavity cooling system
RHS	Right-hand side
SNL	Sandia National Laboratory
$STEM$	Science, Technology, Engineering, and Math
$TAMU$	Texas A&M University
Tdr	Turbulent dissipation rate (ϵ)
Tke	Turbulent kinetic energy (k)
$T-S$	Tollmien-Schlichting (waves)
UW	University of Wisconsin
$VHTR$	Very high temperature reactor
$V\&V$	Verification and Validation
ZPG	Zero pressure gradient

Greek Symbols

Ω	Number of microstates corresponding to a given macrostate
δ	Boundary layer thickness (m)
α	Thermal diffusivity ($\frac{W}{m^2 \cdot K}$)
α_t	Turbulent thermal diffusivity ($\frac{W}{m^2 \cdot K}$)
∞	Freestream value
κ_h	Von Karman constant (thermal), $\kappa \approx 0.44$
κ	Von Karman constant (viscous), $\kappa \approx 0.41$
λ	Second viscosity coefficient ($Pa \cdot s$)
λ	Boltzmann constant ($\frac{J}{K}$)
μ	Dynamic viscosity ($Pa \cdot s$)
θ	Momentum Thickness (m)
θ_h	Enthalpy Thickness (m)
ν	Kinematic viscosity ($\frac{m^2}{s}$)

Φ	Dissipation of mechanical energy ($\frac{W}{m^3}$)
Φ_Θ	Loss of mechanical energy ($\frac{W \cdot K}{m^3}$)
ρ	Density ($\frac{kg}{m^3}$)
ϵ	Turbulent dissipation ($\frac{J}{kg \cdot s}$)
μ_t	Turbulent viscosity ($Pa \cdot s$)
τ_w	Wall shear stress ($\frac{N}{m^2}$)

Roman Symbols

C_f	Skin friction coefficient, $C_f = \frac{\tau_w}{\frac{1}{2}\rho U_\infty^2}$
c_p	Specific heat capacity at constant pressure ($\frac{J}{kg \cdot K}$)
c_v	Specific heat capacity at constant volume ($\frac{J}{kg \cdot K}$)
D	Hydraulic diameter (m)
E	Energy (J)
e	Specific internal energy ($\frac{J}{kg}$)
f	friction factor
h	Convective heat transfer coefficient ($\frac{W}{m^2 K}$)
h	Specific enthalpy ($\frac{J}{kg}$)
k	Thermal conductivity ($\frac{W}{m \cdot K}$)
k	Turbulent kinetic energy ($\frac{J}{kg}$)
k_t	Turbulent conductivity ($\frac{W}{m \cdot K}$)
L_e	Entrance Length (m)
$\frac{D\rho}{Dt}$	Density Material Derivative, $\frac{D\rho}{Dt} = \frac{\partial \rho}{\partial t} + \vec{v} \cdot \nabla \rho$
$\dot{m}$	Mass flowrate ($\frac{kg}{s}$)
Nu	Nusselt number, $Nu = \frac{hD}{k}$
P	Pressure (Pa)
p	Pressure (Pa)
Pr	Prandtl number
Pr_t	Turbulent Prandtl number
Q	Heat (J)
q	Heat flux ($\frac{W}{m^2}$)

r	Specific energy generation rate ($\frac{J}{kg \cdot s}$)
Re_D	Reynolds number, $Re_D = \frac{\rho U D}{\mu}$
Re_x	Reynolds number, $Re_x = \frac{\rho U x}{\mu}$
$\dot{S}$	Entropy generation rate ($\frac{J}{K \cdot s}$)
S	Entropy ($\frac{J}{K}$)
s	Specific entropy ($\frac{J}{kg \cdot K}$)
s'	Fluctuating specific entropy ($\frac{J}{kg \cdot K}$)
$\dot{S}'$	Entropy generation rate per unit length ($\frac{J}{s \cdot K \cdot m}$)
$\dot{S}''$	Entropy generation rate per unit area ($\frac{J}{s \cdot K \cdot m^2}$)
$\dot{S}'''$	Entropy generation rate per unit volume ($\frac{J}{s \cdot K \cdot m^3}$)
$S_{PRO,\overline{D}}$	mean flow contribution to viscous dissipation ($\frac{J}{K \cdot s \cdot m^3}$)
$S_{PRO,D'}$	turbulent contribution to viscous dissipation ($\frac{J}{K \cdot s \cdot m^3}$)
$S_{PRO,\overline{C}}$	mean flow contribution to thermal dissipation ($\frac{J}{K \cdot s \cdot m^3}$)
$S_{PRO,C'}$	turbulent contribution to thermal dissipation ($\frac{J}{K \cdot s \cdot m^3}$)
T	Temperature (K)
T'	Fluctuating temperature (K)
$\overline{T}$	Mean temperature (K)
U	Mean velocity ($\frac{m}{s}$)
u	x-velocity ($\frac{m}{s}$)
u'	Fluctuating x-velocity ($\frac{m}{s}$)
$\overline{u}$	Average x-velocity ($\frac{m}{s}$)
u^+	$u^+ = \frac{u}{u_\tau}$
u_τ	Friction velocity [$u_\tau = \sqrt{\frac{\tau_w}{\rho}}$] ($\frac{m}{s}$)
v	y-velocity ($\frac{m}{s}$)
$\vec{v}$	Vector velocity ($\frac{m}{s}$)
v'	Fluctuating y-velocity ($\frac{m}{s}$)
$\overline{v}$	Average y-velocity ($\frac{m}{s}$)
W	Work (J)
w	Wall value

w	z-velocity ($\frac{m}{s}$)
w'	Fluctuating z-velocity ($\frac{m}{s}$)
$\overline{w}$	Average z-velocity ($\frac{m}{s}$)
x	Streamwise coordinate (m)
y	Wall normal coordinate (m)
y^+	$y^+ = \frac{yu_\tau}{\nu}$

Chapter 1: Introduction

The objective of the research presented in this dissertation was to develop and apply a design process, using computational fluid dynamics (CFD) applied to an existing experimental design – characterized by nonuniform flow, heat transfer, and entrance effects – of a cross-cutting decay heat removal system for a nuclear reactor. The limitations of CFD when used with turbulence models were first established. Following a design process that employs both traditional heat transfer and fluid flow (HTFF) analysis techniques, and entropy generation analysis (EGA), thermodynamic irreversibilities, both viscous and thermal, were identified. The premise for this research was that traditional HTFF techniques are the primary design tool of choice for CFD engineers. Yet knowledge of the entropy generation rate (EGR), within the context of CFD limitations (e.g., turbulence models), would provide valuable information that could influence component and system designs – ultimately improving the safety of nuclear power plants.

1.1. Reactor Cavity Cooling System Designs

Current research in advanced reactor designs has focused on passive safety systems, where in the event of a loss of cooling to the reactor core, excess heat will be removed by a passive safety heat removal system. A safety system is classified as 'passive' because it does not require a pump to circulate the fluid (i.e., forced circulation) or operator action to maintain cooling. The system relies on the natural circulation of a fluid (i.e., fluid density differences and gravity) to transfer the heat. Passive safety system designs include features that enhance natural circulation, such as using smooth pipes, minimizing flow obstructions, and maximizing density differences, which increase fluid velocity and hence the removal of more heat.

Two passive reactor cavity cooling system (RCCS) designs are being evaluated for further development in support of the next generation of nuclear plants, specifically the very high temperature gas reactor. The first design, which uses water as the working fluid, is referred to as the water RCCS; the second design, which uses air as the working fluid, is referred to as the air RCCS.

The basic and applied research conducted as part of this dissertation, was applied to the air RCCS design; but a significant portion of this research, including methods, is applicable to the water RCCS design as well.

1.1.1. Air RCCS

The air reactor cavity cooling system (RCCS) is a safety-related passive decay heat removal system undergoing further development in support of the next generation of nuclear plants, specifically the very high temperature gas reactor. In particular, the RCCS was designed (in the late 1990s) by General Atomics (GA) for the Modular High Temperature Gas Reactor (MHTGR).

The General Atomics RCCS design functions as a heat removal medium during normal operating conditions and in the event that the MHTGR forced cooling systems (i.e., Heat Transport System and Shutdown Cooling System) are not available. The heat transfer process is straightforward (cf. Figure 1.1). Residual and decay heat is transferred passively from the uninsulated reactor vessel via radiation and convection to the RCCS cooling panel and ducting, which is located within the reactor cavity adjacent to the concrete cavity walls surrounding the reactor vessel. This heat is transferred to the air, flowing inside the RCCS via natural convection, eventually being exhausted to the atmosphere. Consequently, air flow through the RCCS is a function of the reactor vessel temperature and the outside air temperature (Bechtel National, 1992).

Figure 1.2 shows a plan view of the GA-MHTGR RCCS panel, including the relative position of the riser tubes (i.e., ducts). The panel, constructed of carbon steel, surrounds the reactor vessel over its full circumference and length. The riser panel consists of 227 vertical steel tubes each having an external dimension of 5 cm x 25 cm (2 in. x 10 in.) with 4.76 mm (0.1875 in.) wall thickness. The tubes are arranged with a 5 cm (2 in.) gap between the adjacent tubes. The physical arrangement and tube design are intended to enhance heat transfer as follows: “The total number, cross-sectional shape, and configuration of the tubes provide the optimal surface area for radiative and convective heat transfer and optimal cross-sectional area for air flow.

In addition, the gap between the tubes allow a fraction of the thermal radiation from the reactor vessel to reach the reflective surface on the cold downcomer. The reflected radiation then heats up the back side of the tubes, permitting utilization of the entire tube surface area and enhancing the heat transfer." (Bechtel National, 1992). Of the total heat transferred to the riser tubes, approximately 90% comes from radiation and 10% comes from convection.

The University of Wisconsin (UW) designed and built an air RCCS experimental facility, which was constructed in collaboration with Argonne National Laboratory (ANL) as part of an overall effort to provide experimental data for computer code development (e.g., validation). The UW facility is a $\frac{1}{4}$-scale air RCCS design, and the ANL design, located at the ANL Natural Convection Shutdown Heat Removal Test Facility (NSTF), is a $\frac{1}{2}$-scale air cooled RCCS. Both designs are based on the GA RCCS design concept (Lomperski et al., 2011; Muci, 2014b).

The UW $\frac{1}{4}$–scale RCCS stands over 13 meters in height with 6 vertical riser ducts that represent a 9.5 degree sector slice of the full-scale GA air RCCS concept. The UW RCCS consists of three major components: inlet-plenum, heated cavity with six rectangular riser ducts, and an outlet-plenum with two cylindrical exhaust ducts (cf. Figure 1.3). The UW RCCS is capable of operating in either forced or natural circulation.

The basic flow path is straightforward. Air flows from the inlet piping into the inlet-plenum where mixing of the air occurs prior to entering the six riser ducts. Thirty-two electrical resistance heaters inside the heated cavity can generate 40 kW to simulate radiating heat from the reactor pressure vessel to the six riser ducts. The heaters cover approximately 80% of the height of the riser ducts. The outlet plenum allows for proper mixing before the heated air returns to the outside environment via two cylindrical exhaust ducts (Muci, 2014b). The air RCCS geometry, including nominal dimensions, is shown in Figure 1.3; the nominal dimensions of the riser duct cross-sections are 4.44 cm x 24.66 cm (1.75 in. x 9.71 in.).

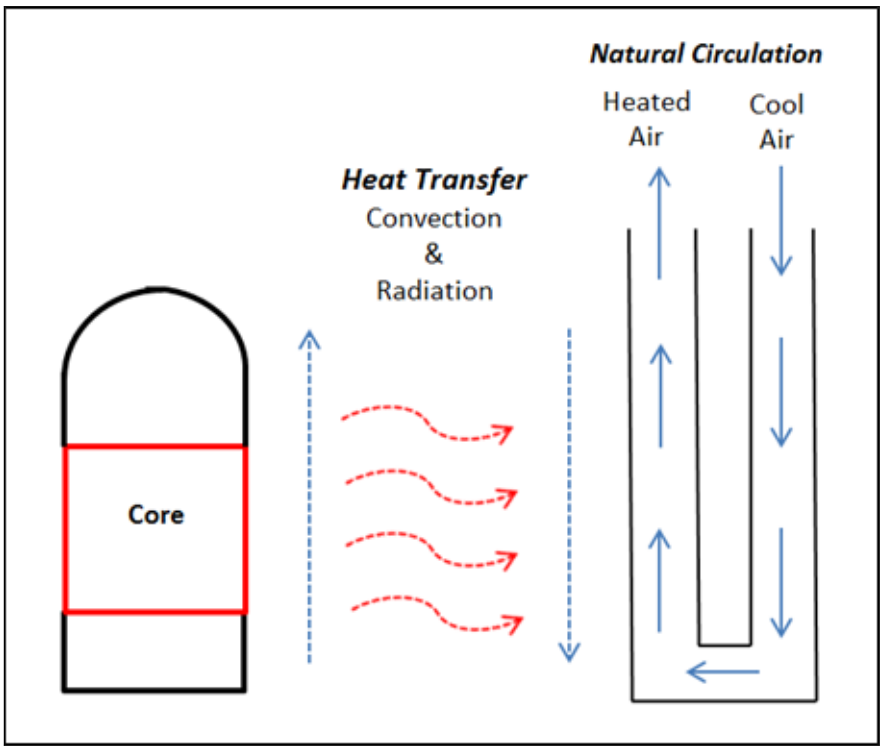

Figure 1.1: RCCS basic heat transfer process

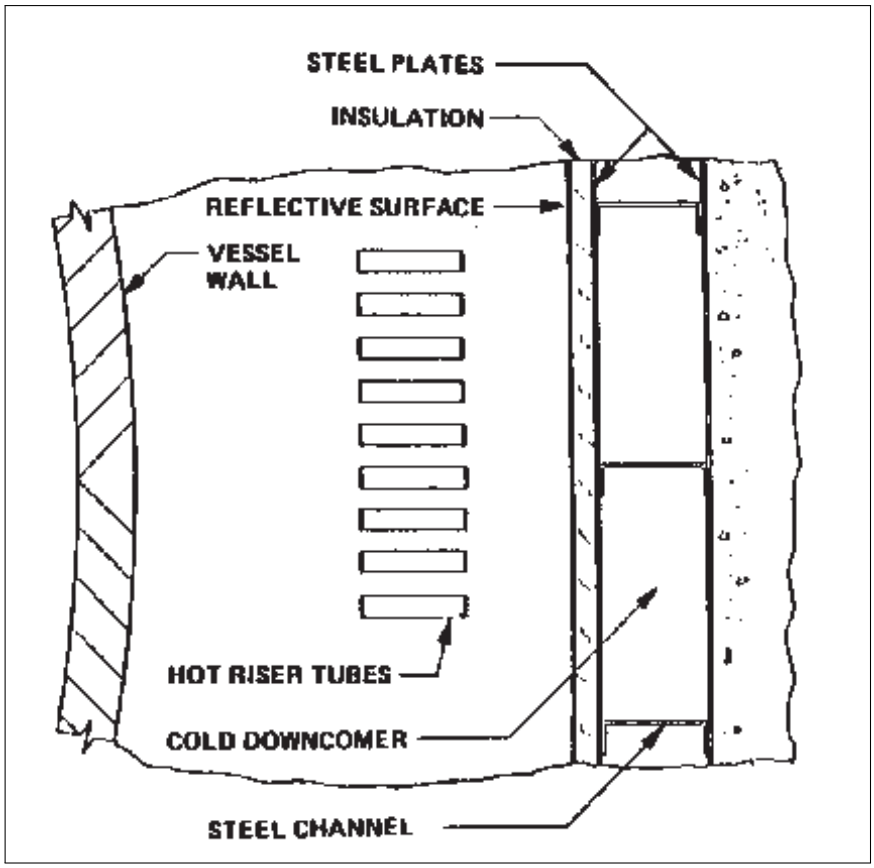

Figure 1.2: GA-MHTGR RCCS panel (Bechtel National, 1992)

Numerous forced circulation and natural circulation experiments were conducted at the UW $\frac{1}{4}$–scale air RCCS experimental facility. A significant amount of experimental data was collected. Noteworthy is that during some experiments, flow instabilities were observed, resulting in flow reversals in the system. The exact cause of the flow reversals was not determined; although some possibilities, including environmental wind speed and direction, are discussed by Muci (2014b).

1.1.2. Water RCCS

The water reactor cavity cooling system (RCCS) is a safety-related passive decay heat removal system undergoing further development in support of the next generation of nuclear plants (Corradini, 2012). Similar to the air RCCS, the system operates continuously during normal operation, but in conjunction with an active secondary cooling system (cf. Figure 1.4). During accident conditions, which assumes active cooling is not available (e.g., loss of electrical power), the secondary cooling system is no longer available. Therefore, heat is removed under natural circulation in a manner similar to the air RCCS. In fact, the phenomenological process is the same.

A significant amount of applied research, both experimental and CFD modeling, was performed on the water RCCS design by the same investigators of the air RCCS. The details of this research are outside the scope of this work. Additional information about the water RCCS research can be found in the literature [e.g., Frisani (2010); Omotowa (2014)].

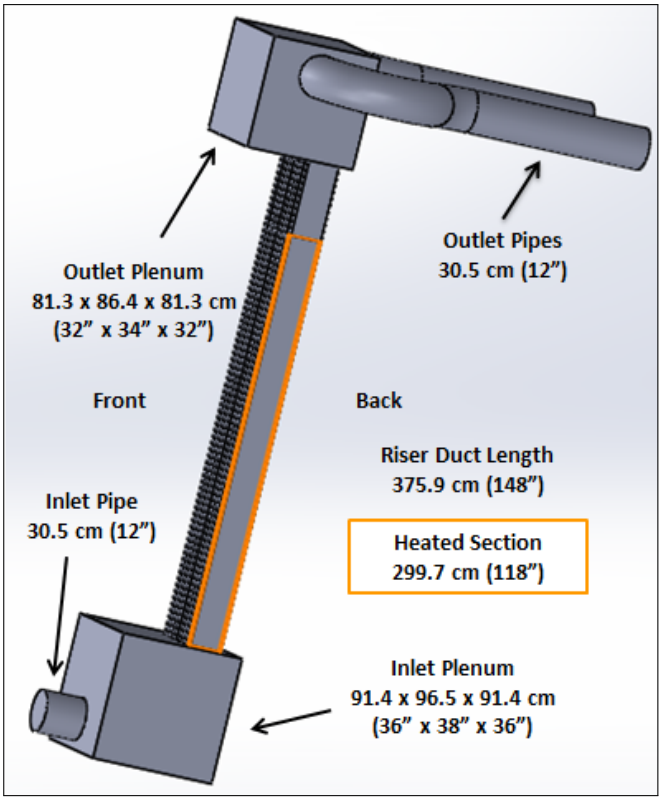

Figure 1.3: Air RCCS geometry (rotated view)

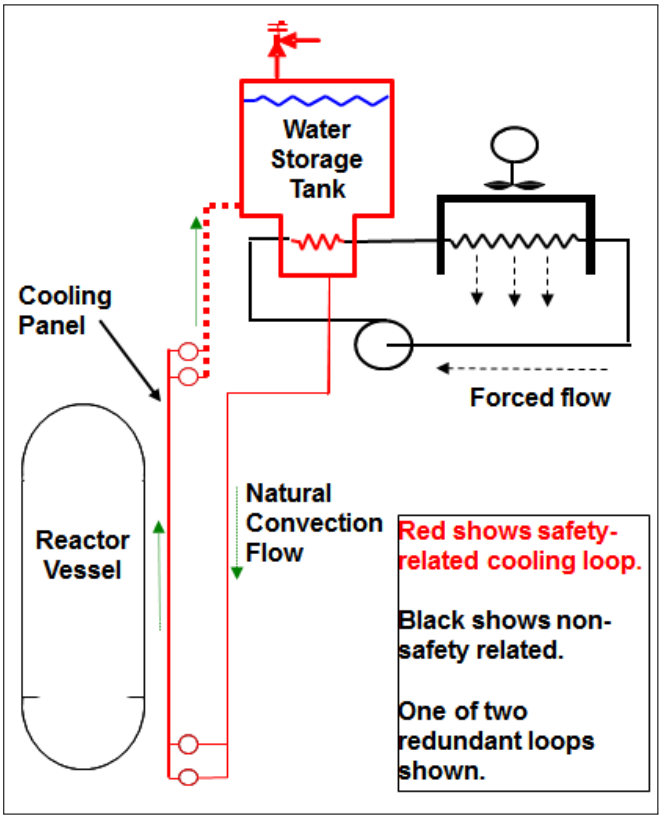

Figure 1.4: Water RCCS schematic (Lommers, 2010)

1.2. Traditional Thermal Analysis

Traditional heat transfer and fluid flow (HTFF) analysis, commonly referred to as thermal analysis, has been used successfully for years in the design, operation, and maintenance of complex engineering systems and components including spacecraft, nuclear power plants, irradiation experiments in nuclear reactors, and spray nozzles.

The thermal analysis and design process requires fundamental principles from heat transfer (e.g., heat transfer coefficient), fluid mechanics (e.g., wall shear stress, head loss), thermodynamics (e.g., fluid properties), and engineering economics (e.g., project cost). These principles in conjunction with the governing equations of fluid flow (e.g., Navier-Stokes and energy equation) along with empirical correlations are used to predict the system and component operating conditions such as pressure, mass flowrate, and temperature in order to ensure adequate cooling is provided in order to prevent exceeding specified thermal limits (e.g., CHF, melting temperature).

It has been the author's experience that empirically derived correlations for heat transfer and fluid flow are used in conjunction with average velocity and temperature results obtained from CFD codes (i.e., traditional HTFF analysis) in the thermal design of engineering components in order to develop a workable, but not necessarily the best, design (Hamman et al., 2012). Although traditional HTFF analysis has been used successfully, situations occur where it is difficult to establish the optimal design. The following example demonstrates that design situations can occur where traditional HTFF analysis techniques lead to inconclusive results.

1.2.1. Thermal Analysis Example

In his dissertation, loosely translated as 'Determination of local entropy production in turbulent flows and their use for the evaluation of convective transport processes,' Fabian Kock presents a typical example of the trade-off that engineers make in the thermal analysis of system components (Kock, 2003). The component under study is a pipe, with an internal turbulence promoter (i.e., spiraling tape), heated at the midsection. Using traditional HTFF techniques, Nusselt number and skin friction coefficient for several diameter to length (D/L) ratios, which essentially rep-

resents the number of twists in the spiraling tape, are computed. Figure 1.5 presents the working design 'wanted' and 'unwanted' results. Specifically, the Nusselt number (Nu) increases, indicating a wanted result of improved heat transfer; but the skin friction coefficient (C_f) increases as well, indicating an unwanted increase in differential pressure. Although several working designs are determined, the traditional HTFF thermal analysis approach is not capable of determining the optimal design.

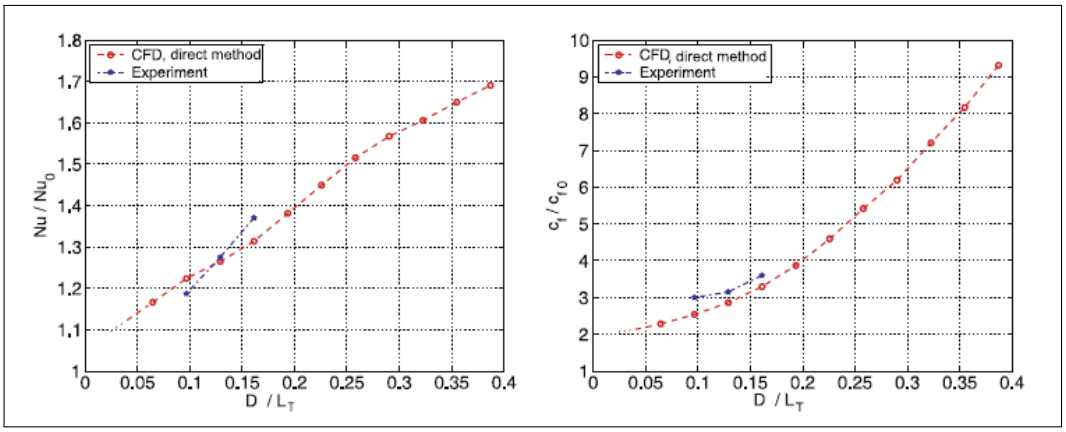

Figure 1.5: Traditional thermal analysis (Kock, 2003)

1.3. Boundary Layer Transition

Studying boundary layer transition from both a basic and applied research perspective was an integral part of this dissertation research. Yet, given the complexities of turbulence and the vast amount of research conducted on this topic over the last century, it was not practical to delve into all the aspects of boundary layer development such as stability theory, transition mechanisms (e.g., natural, bypass, and separated-flow), or experimental studies. In short, this study focuses primarily on the fundamentals of boundary layer transition in sufficient depth necessary to understand and apply boundary layer phenomena to improve the design of a RCCS.

It is well known that the design and performance of a cooling system depends on whether or not the boundary layer is laminar, transitional, or turbulent. Laminar flows consist of small fluid particles flowing in parallel layers, with no mixing between layers; hence, they are characterized as having poor heat transfer characteristics. Turbulent flows have good heat transfer properties including reliable friction and heat transfer correlations; yet modeling turbulent flows is complex. Likewise, the

unpredictability and complexities associated with transitional flows make it difficult to develop robust empirical friction and heat transfer correlations. In fact, Meyer and Olivier (2011) state "It is normally advised when designing heat exchangers to remain outside the transitional flow regime due to the uncertainty and flow instability in this region."

1.3.1. Natural and Bypass Transition

The transition mechanisms related to this study include natural and bypass transition. Both mechanisms have been observed experimentally and numerically using direct numerical simulation (DNS). Whether a fluid undergoes transition via natural or bypass transition depends on several factors related to boundary layer and freestream disturbances, such as surface roughness, pressure effects, and freestream turbulence intensity.[1]

Figure 1.6 depicts the three stages of boundary layer formation, over a smooth surface, leading up to the onset of fully turbulent flow. The first stage, referred to as receptivity, characterizes the process by which external disturbances (e.g., vortices, acoustic fluctuations, surface roughness) become internalized within the boundary layer, resulting in the generation of Tollmien-Schlichting (T-S) waves (Saric et al., 2002). The second stage of transition is characterized by small amplitude waves traveling down the boundary layer, where they can be either attenuated or further amplified; this stage is described by linear stability theory as long as the amplitude of the waves remain small (Reed and Saric, 1996). Finally, if the waves continue to be amplified to approximately 1% to 2% of the freestream velocity, nonlinear breakdown of the unstable waves occurs and the transition to fully turbulent flow occurs (Kachanov, 1994).

The natural transition process is characterized by the three stages of turbulence onset (cf. Figure 1.6). Figure 1.7 provides a description of this process: the flow enters the domain with as stable laminar flow with a freestream velocity U_∞ with a turbulence intensity level typically less than 1%. As a result of this disturbance, Tollmien-

[1] A more extensive discussion of boundary layer transition, including CFD modeling, can be found in Appendix A; Kachanov (1994); Mayle (1991); White (1991).

Schlichting (T-S) waves develop at a freestream Reynolds number Re_{crit}/Re_c of approximately 91,000. The T-S waves are amplified, eventually evolving into hairpin vortices (3D vortex breakdown), followed by turbulent spot formation. Eventually the turbulent spots coalesce, resulting in the transition to fully turbulent flow at a Reynolds number (Re_{tr}/Re_t) of approximately $1x10^6$ (Versteeg and Malalasekera, 1995; White, 1991).

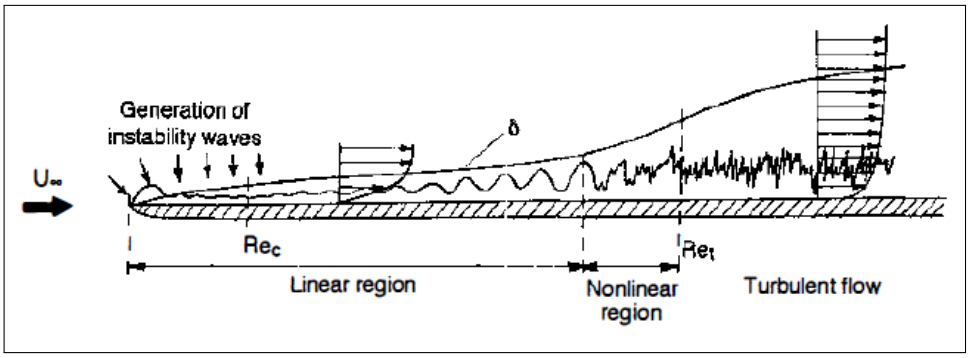

Figure 1.6: Stages of turbulence onset (Kachanov, 1994)

Bypass transition occurs when flow enters the domain as stable laminar flow with a freestream velocity U_∞ and a turbulence intensity level typically greater than 1%. As a consequence of this relatively high disturbance level, the flow may rapidly transition into turbulent spot formation without ever passing through the linear stage of turbulence onset. This transition process is classified as bypass transition since some or all of the 'natural' transition phases (e.g., T-S waves, 3D vortex breakdown) are not observed; they are 'bypassed.' Bypass transition is a complex process that is very sensitive to inlet freestream turbulence conditions (e.g., turbulence intensity) and environmental effects, such as pressure gradients (cf. Appendix A).[2]

Predicting transition as the flow passes through the stages of turbulence onset is complicated; in fact, the mechanisms are not completely understood. Yet, from a practical perspective, transition is generally considered to begin when skin friction coefficient begins to deviate from its value computed using the Blasius equation. And, transition is considered complete when wall shear stress reaches a turbulent value

[2]Recent research, including a fluid motion video, related to DNS prediction of boundary layer transition physics provides a much better visual perspective of the 3D structures that form during the transition process (Sayadi et al., 2011, 2013).

computed using, for example, empirical correlations. Figure 1.8 illustrates a plot of skin friction coefficient (C_f) versus Reynolds number (Re_x); these two parameters are typically used to depict and evaluate the transition process. A plot of local convective heat transfer coefficient (h) and a freestream parameter such as Reynolds number (Re_x) are used to depict and evaluate the transition process as well.

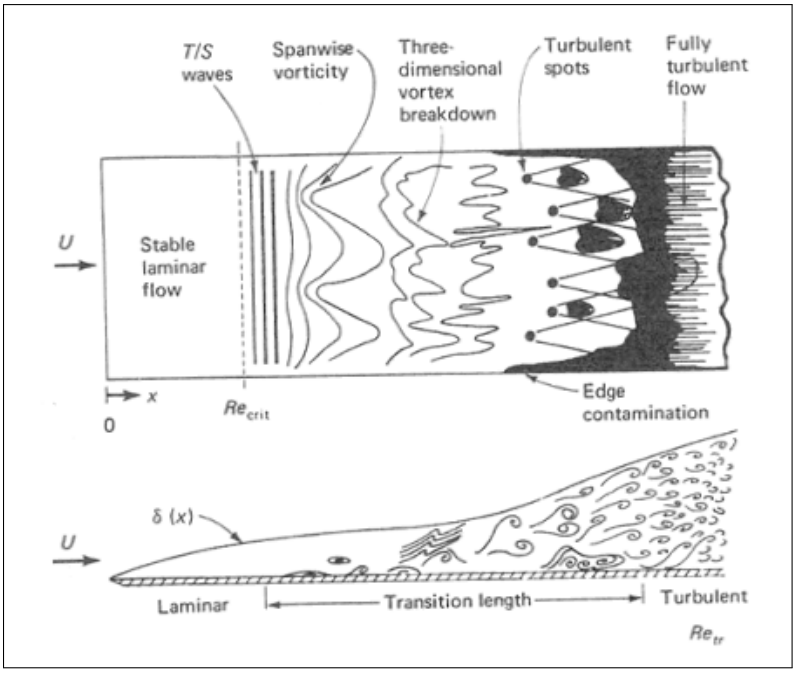

Figure 1.7: Natural boundary layer transition (White, 1991)

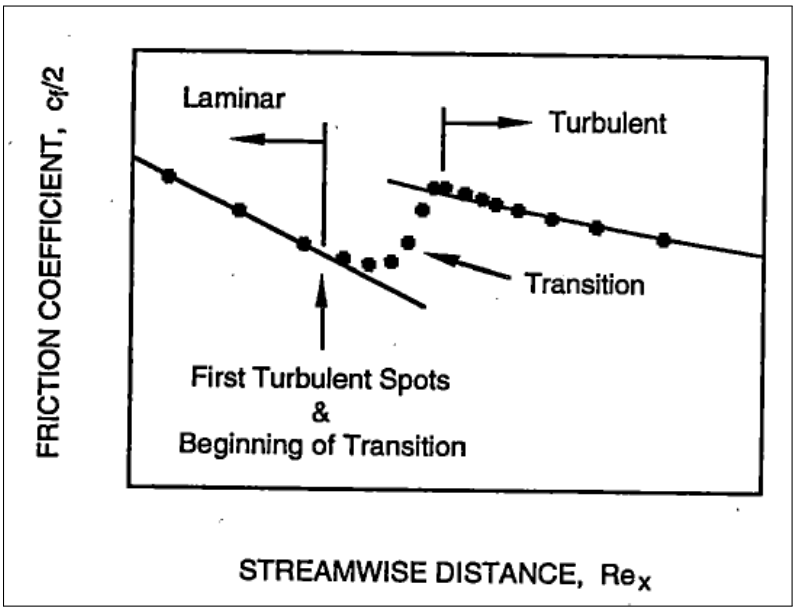

Figure 1.8: Predicting transition using shear stress (Mayle and Schulz, 1997)

1.3.2. DNS and RANS Capabilities

For decades, turbulence modeling research has been performed in an effort to predict turbulence phenomena including the transition from laminar to turbulent flow. Consequently two CFD simulation techniques, Reynolds-averaged Navier-Stokes (RANS) turbulence modeling and direct numerical simulation (DNS), have evolved.[3] The research documented in this dissertation is primarily associated with the RANS CFD simulation technique applied to wall-bounded flows.

Although the details of the RANS and DNS CFD simulation techniques are outside the scope of this dissertation, several points regarding the capabilities and limitations of each technique should be made:

1. The DNS approach to simulating turbulent flow is capable of predicting the onset and transition to turbulence. Unfortunately this technique is too costly (in terms as computational overhead and thus resources) for engineering applications; therefore, it is used mainly as a research tool. [4]

2. In general, DNS results are considered equivalent to experimental data and thus served as the phenomenological reference for the 2D flat plate boundary layer studies (AGARD, 1998; Ferziger and Perić, 2002; Moin and Mahesh, 1998).

3. RANS turbulence modeling is not capable of adequately predicting transition since RANS averaging eliminates the effects of linear disturbance growth. Additionally, RANS based turbulence models, specifically designed to predict transition, are not 'predictive' models in that they require calibration to either DNS or experimental data. Furthermore, the calibration process is complex and time consuming. Figure 1.9 compares two graphs showing a non-calibrated plot and a calibrated plot. The solid black plot was developed from the DNS data

[3] DNS and RANS are numerical techniques to approximate turbulence phenomena. DNS solves the Navier-Stokes equations without the need for any turbulence modeling. RANS computes the mean flow, and the turbulent velocity fluctuations are modeled (AGARD, 1998; Pope, 2001).

[4] In the CFD discipline, computational overhead refers to anything that results in an increase of computation time. For example, for a given number of processors on a given computer, larger meshes (i.e., more computational elements) will result in an increase in computation time.

of Nolan and Zaki (2012). The solid red plot represents the SST $k-\omega$ γRe_θ RANS data. Calibration of the RANS data results in the γRe_θ plot approximating the DNS plot as shown in the second graph of Figure 1.9. This was an initial contribution of this dissertation research.

4. RANS turbulence models continue to be the computational tool of choice for industrial CFD applications; their popularity is primarily due to their lower computational resource requirements, robustness, and reliability. When available, experimental data should be used in conjunction with RANS results. Although, it is not uncommon for RANS results to be used, when experimental data is not available, as long as limitations are acknowledged, and appropriate safety factors can be applied (Hamman et al., 2012; Shigley and Mitchell, 1983; Ullman, 2003).

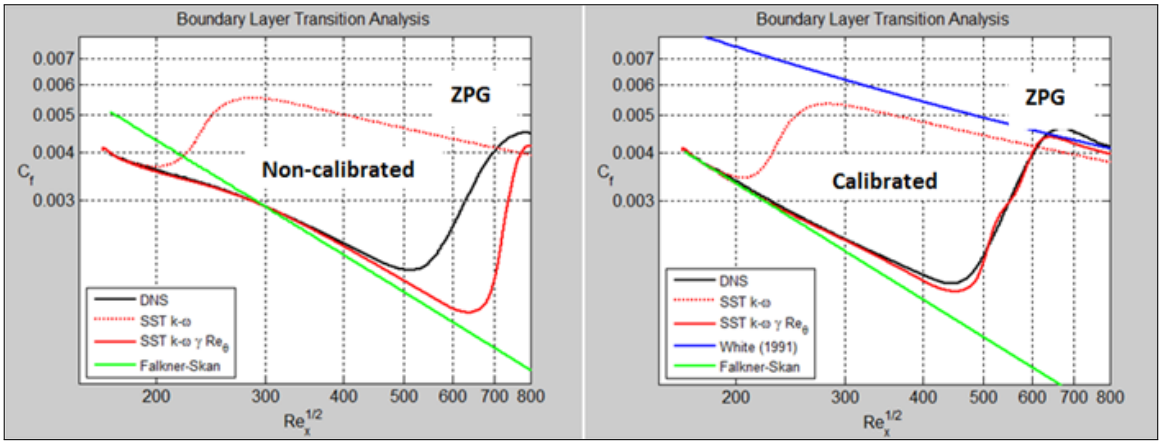

Figure 1.9: Non-calibrated and calibrated γ-Re_θ RANS turbulence model

1.4. Entropy

"I hesitate to use the terms 'first law' and 'second law', because there are almost as many 'first and second laws' as there are thermodynamicists, and I have been told by these people for so many years that I disobey their laws that now I prefer to exult in my criminal status and give non-condemning names to the concrete mathematical axioms I wish to use in my outlaw studies of heat and temperature. The term 'entropy'

seems superfluous, also, since it suggests nothing to ordinary persons and only intense headaches to those who have studied thermodynamics but have not given in and joined the professionals."

– Clifford Truesdell (1919-2000), in "Rational Thermodynamics (1969)" [5]

1.4.1. An Enigmatic Concept

Ever since the introduction of the Second Law of Thermodynamics in 1865 by Rudolph Clausius, efforts to incorporate this thermodynamic concept in the engineering design process have faltered. Contributing to its unpopularity among practicing engineers and students, is the enigmatic concept of entropy and its assorted mathematical expressions. Let me provide some examples:

In the preface to his 2008 book titled "Entropy Demystified: The Second Law Reduced to Plain Common Sense," Arieh Ben-Naim, describes his first encounter with entropy and the Second Law of Thermodynamics as a student in a lecture hall (Ben-Naim, 2012). "... I was fascinated with its mysterious nature." He continues with his recollection by sharing the lecturers perspective on this topic: "If you do not understand the Second Law, do not be discouraged. You are in good company. You will not be able to understand it at this stage, but you will understand it when you study statistical thermodynamics."

Having taken statistical thermodynamics as part of my coursework and revisited the subject of thermodynamics (and its many tacit assumptions) as part of my dissertation research, entropy and the Second Law of Thermodynamics continues to invoke headaches, albeit at much less frequency and severity. Nevertheless as a computational engineer, my intent is not to fuel the never-ending debate over the merits of entropy, classical versus statistical thermodynamics (e.g., two views of matter), or the Second Law. My goal is to apply the principles of the first and second law in conjunction with heat transfer, thermodynamics, and fluid mechanics principals in an effort to solve engineering problems, including advancing the safety of nuclear

[5] Clifford Truesdell was an American mathematician, natural philosopher, and historian of science. He along with Richard Toupin formulated the general form of the Clausius-Duhem inequality (Ball and James, 2002).

power plants and contributing to the research in this field.

Despite its unpopularity and the different perspectives regarding the structure of matter, the second law continues to be applied to solve some of the most challenging problems. For example, the Second Law has been applied to thermodynamic cycles (Equation 1.1), changes in thermodynamic states (Equation 1.2), continuum mechanics via the Clausius-Duhem inequality (Equation 1.3), and statistical mechanics via Ludwig Boltzmann's molecular interpretation (Equation 1.4).[6,7] Unfortunately, application of the second law of thermodynamics in the design process is overshadowed by the unambiguous first law of thermodynamics (e.g., $dE = \delta W + \delta Q$) [Hamman and Berry (2010); Hamman et al. (2012); Hamman and Skerjanc (2012)].

$$\oint \frac{\delta Q}{T} \leq 0 \tag{1.1}$$

$$S_E - S_B \geq \int_B^E \frac{\delta Q}{T} \tag{1.2}$$

$$\frac{ds}{dt} \geq \frac{r}{T} - \frac{1}{\rho}\nabla \cdot \left(\frac{\vec{q}}{T}\right) \tag{1.3}$$

$$S = \lambda \cdot log(\Omega) \tag{1.4}$$

1.4.2. Theoretical Formulation

Although the concept of entropy is surrounded in controversy, the second law provides the theoretical foundation for tackling some of the most challenging engineering problems, particularly by those who do not shy away from mathematics. Therefore recognizing the importance of understanding entropy from a mathematical

[6]The Clausius-Duhem inequality is one of several mathematical expressions of the second law, which limits energy transfer to occur in certain directions. Furthermore, similar to thermodynamic state relations, this (in)equality is only valid near thermal equilibrium.

[7]"$S = k \cdot ln(\Omega)$ is easily the second most important formula of physics, next to $E = mc^2$ – or at a par with it."(Müller, 2007)

perspective, this section revisits the development of the differential form of the turbulent entropy transport equation. In addition to the math, the underlying assumptions and constraints associated with the entropy transport equation are highlighted. Noteworthy is that the entropy transport equation is based on the second law of thermodynamics; yet it is coupled to the first law of thermodynamics through the viscous dissipation function.

Beginning with a thermodynamic state relationship for entropy, a differential relationship, in terms of material derivatives of internal energy and entropy, is formed. This equation is combined with the thermal energy equation resulting in an equation describing the rate of change of entropy. As a consequence of the thermal energy equation, the viscous dissipation function (Φ) appears in the rate of change of entropy equation; therefore, a brief discussion of this term is included in this section as well. Finally, the Reynolds rules of time averaging are implemented resulting in the differential form of the turbulent entropy transport equation, where the entropy source terms are collected on the right-hand-side of the equation. What follows are the details of the derivation in which only isotropic Newtonian fluids are considered.

Malvern (1969) in his classic continuum mechanics text states "The second law of thermodynamics postulates the existence of entropy as a state function." Therefore, beginning with the thermodynamic state relationship for internal energy (e), as a function of entropy (s) and density (ρ) and reproducing the mathematical derivation of Whitaker (1992) using his notation, Equation 1.11 results.[8]

$$e = e(s, \rho) \tag{1.5}$$

Taking the material derivate of internal energy, simplifying, and introducing the material derivative form of the continuity equation,

$$\frac{De}{Dt} = \left(\frac{\partial e}{\partial s}\right)_{\rho} \frac{Ds}{Dt} + \left(\frac{\partial e}{\partial \rho}\right)_{s} \frac{D\rho}{Dt} = T\frac{Ds}{Dt} + \frac{p}{\rho^2}\frac{D\rho}{Dt} \tag{1.6}$$

[8]See Whitaker (1992) for additional details related to Equation 1.8.

$$\rho\frac{De}{Dt} = T\rho\frac{Ds}{Dt} + \frac{p}{\rho}\frac{D\rho}{Dt} \tag{1.7}$$

$$\frac{D\rho}{Dt} + \rho\nabla\cdot\vec{v} = 0 \tag{1.8}$$

$$\rho\frac{De}{Dt} = T\rho\frac{Ds}{Dt} - p\nabla\cdot\vec{v} \tag{1.9}$$

Introducing the general form of the thermal energy equation for compressible flows, a consequence of the first law of thermodynamics,

$$\rho\frac{De}{Dt} = -\nabla\cdot\vec{q} - p\nabla\cdot\vec{v} + \Phi \tag{1.10}$$

where Φ represents the viscous dissipation function (Whitaker, 1992; White, 1991). The viscous dissipation function is presented in Equation 1.12 where μ represents the dynamic viscosity and λ represents the second viscosity coefficient, both properties constrained to describing the behavior of Newtonian fluids. Finally, combining Equation 1.9 and Equation 1.10 produces an equation describing the rate of change of entropy.

$$\rho\frac{Ds}{Dt} = \frac{1}{T}\Big(-\nabla\cdot\vec{q} + \Phi\Big) \tag{1.11}$$

Given the importance of the viscous dissipation function to the rate of entropy generation, it is prudent to digress in order to briefly discuss its relationship to the thermal energy equation and the controversy surrounding the second viscosity coefficient. First of all, the viscous dissipation function Φ is a consequence of the first law of thermodynamics. Specifically, the thermal energy equation, containing Φ and primarily used in heat transfer studies, is obtained by subtracting the the mechanical energy equation from the total energy equation (Whitaker, 1992). Moreover, it should be noted that there is some controversy surrounding the final term in Equation 1.12,

which contains the second coefficient of viscosity parameter λ. This controversy is related to Stokes's hypothesis where $\lambda + \frac{2}{3}\mu = 0$.[9] However, for incompressible flows, where the divergence of the velocity field is zero ($\nabla \cdot \vec{v} = 0$), Equation 1.12 reduces to Equation 1.13.

$$\Phi = \mu\Big[2\Big\{\Big(\frac{\partial u}{\partial x}\Big)^2 + \Big(\frac{\partial v}{\partial y}\Big)^2 + \Big(\frac{\partial w}{\partial z}\Big)^2\Big\} + \Big(\frac{\partial u}{\partial y} + \frac{\partial v}{\partial x}\Big)^2 + \Big(\frac{\partial u}{\partial z} + \frac{\partial w}{\partial x}\Big)^2 + \Big(\frac{\partial v}{\partial z} + \frac{\partial w}{\partial y}\Big)^2\Big] + \lambda\Big(\frac{\partial u}{\partial x} + \frac{\partial v}{\partial y} + \frac{\partial w}{\partial z}\Big)^2 \tag{1.12}$$

$$\Phi = \mu\Big[2\Big\{\Big(\frac{\partial u}{\partial x}\Big)^2 + \Big(\frac{\partial v}{\partial y}\Big)^2 + \Big(\frac{\partial w}{\partial z}\Big)^2\Big\} + \Big(\frac{\partial u}{\partial y} + \frac{\partial v}{\partial x}\Big)^2 + \Big(\frac{\partial u}{\partial z} + \frac{\partial w}{\partial x}\Big)^2 + \Big(\frac{\partial v}{\partial z} + \frac{\partial w}{\partial y}\Big)^2\Big] \tag{1.13}$$

Continuing on with the turbulent entropy transport equation derivation, and using the relationship

$$\frac{1}{T}\nabla \cdot \vec{q} = \nabla \cdot \Big(\frac{\vec{q}}{T}\Big) + \frac{\vec{q} \cdot \nabla T}{T^2} \tag{1.14}$$

Equation 1.15, which is applicable to laminar flows, results after substituting 1.14 into Equation 1.11 and rearranging.

$$\rho\frac{Ds}{Dt} = -\nabla \cdot \Big(\frac{\vec{q}}{T}\Big) - \frac{\vec{q} \cdot \nabla T}{T^2} + \frac{\Phi}{T} \tag{1.15}$$

The last two terms on the right-hand-side of Equation 1.15 represent the volumetric entropy generation rate (EGR). And, as a consequence of the second law of thermodynamics (Reynolds and Perkins, 1977), the EGR must be greater than or equal to zero.

Focusing on the material derivative on the left-hand side Equation 1.15, evaluation

[9] See Schlichting (1968) and White (1991) for additional information on this topic.

of the material derivate results in the following terms

$$\rho\Big(\frac{\partial s}{\partial t} + u\frac{\partial s}{\partial x} + v\frac{\partial s}{\partial y} + w\frac{\partial s}{\partial z}\Big) \tag{1.16}$$

Assuming incompressible flow[10], expressing the dependent variables in terms of a time average and a fluctuating component ($s = \overline{s} + s', u = \overline{u} + u', v = \overline{v} + v', w = \overline{w} + w'$), and following Reynolds rules of time averaging described by White (1991) where

$$\rho\Big(\overline{u'\frac{\partial s'}{\partial x}} + \overline{v'\frac{\partial s'}{\partial y}} + \overline{w'\frac{\partial s'}{\partial z}}\Big) = \rho\Big(\frac{\partial \overline{u's'}}{\partial x} + \frac{\partial \overline{v's'}}{\partial y} + \frac{\partial \overline{w's'}}{\partial z}\Big) - \rho\Big(\overline{s'\frac{\partial u'}{\partial x}} + \overline{s'\frac{\partial v'}{\partial y}} + \overline{s'\frac{\partial w'}{\partial z}}\Big) \tag{1.17}$$

$$\rho\Big(\overline{u'\frac{\partial s'}{\partial x}} + \overline{v'\frac{\partial s'}{\partial y}} + \overline{w'\frac{\partial s'}{\partial z}}\Big) = \rho\Big(\frac{\partial \overline{u's'}}{\partial x} + \frac{\partial \overline{v's'}}{\partial y} + \frac{\partial \overline{w's'}}{\partial z}\Big) \tag{1.18}$$

results in the turbulent description of the material derivative term on the left-hand side of Equation 1.15,

$$\rho\Big(\frac{\partial \overline{s}}{\partial t} + \overline{u}\frac{\partial \overline{s}}{\partial x} + \overline{v}\frac{\partial \overline{s}}{\partial y} + \overline{w}\frac{\partial \overline{s}}{\partial z}\Big) + \rho\Big(\frac{\partial \overline{u's'}}{\partial x} + \frac{\partial \overline{v's'}}{\partial y} + \frac{\partial \overline{w's'}}{\partial z}\Big) \tag{1.19}$$

Since the averaging of the three terms on the right-hand-side of Equation 1.15 involves some complexities, primarily due to the dependent variable temperature in the denominator of each term and the fact that

$$\frac{1}{\overline{T}} \neq \overline{\Big(\frac{1}{T}\Big)}$$

[10]Favre (1992) discusses the general case where density is variable.

the terms are represented with an averaging operator as shown in Equation 1.20.[11]

$$\rho\Big(\frac{\partial \overline{s}}{\partial t}+\overline{u}\frac{\partial \overline{s}}{\partial x}+\overline{v}\frac{\partial \overline{s}}{\partial y}+\overline{w}\frac{\partial \overline{s}}{\partial z}\Big)+\rho\Big(\frac{\partial \overline{u's'}}{\partial x}+\frac{\partial \overline{v's'}}{\partial y}+\frac{\partial \overline{w's'}}{\partial z}\Big)+\overline{\nabla\cdot\Big(\frac{\vec{q}}{T}\Big)} = \overline{\Big(\frac{\Phi}{T}\Big)}+\overline{\Big(-\frac{\vec{q}\cdot\nabla T}{T^2}\Big)} \tag{1.20}$$

On the left-hand side of Equation 1.20, the first through third terms represent convection, turbulent flux, and molecular flux respectively. The two terms on the right-had side represent the viscous and thermal contributions to entropy generation rate.

Defining the second term on the right-hand-side of Equation 1.20 as follows,

$$\overline{\Big(-\frac{\vec{q}\cdot\nabla T}{T^2}\Big)}=\overline{\Big(\frac{\Phi_\Theta}{T^2}\Big)} \tag{1.21}$$

results in the time-averaged entropy transport equation in Kock and Herwig (2004):

$$\rho\Big(\frac{\partial \overline{s}}{\partial t}+\overline{u}\frac{\partial \overline{s}}{\partial x}+\overline{v}\frac{\partial \overline{s}}{\partial y}+\overline{w}\frac{\partial \overline{s}}{\partial z}\Big)+\rho\Big(\frac{\partial \overline{u's'}}{\partial x}+\frac{\partial \overline{v's'}}{\partial y}+\frac{\partial \overline{w's'}}{\partial z}\Big)+\overline{\nabla\cdot\Big(\frac{\vec{q}}{T}\Big)} = \overline{\Big(\frac{\Phi}{T}\Big)}+\overline{\Big(\frac{\Phi_\Theta}{T^2}\Big)} \tag{1.22}$$

Assuming isotropic thermal properties and transforming Equation 1.22 from expanded notation to indicial notation and applying Fourier's law of thermal conduction $\vec{q}=-k\frac{dT}{dx_i}$, results in the equation presented by Naterer and Camberos (2008):

$$\frac{\partial(\rho\overline{s})}{\partial t}+\frac{\partial}{\partial x_i}\Big[\rho u_i\overline{s}+\rho\overline{u_i's'}-\overline{\frac{k}{T}\frac{\partial T}{\partial x_i}}\Big]=\overline{\frac{\tau_{ij}}{T}\frac{\partial u_i}{\partial x_j}}+\overline{\frac{k}{T^2}\Big(\frac{\partial T}{\partial x_i}\Big)^2} \tag{1.23}$$

So far, only Equation 1.10, the thermal energy equation, and the thermodynamic state relation $e=e(s,\rho)$, have been used in the derivation of Equation 1.22 and Equation 1.23. Of note is that both the first law of thermodynamics and the second law of thermodynamics have been utilized in the above derivation. Yet, the inequality

[11] Note that Equation (2) of Herwig and Kock (2007), which was reproduced as Equation (1) in Appendix A, has a typo. Specifically, the first term on the right-hand side of Equation (1) of Appendix A should have a negative sign. A thorough derivation of the entropy transport equation can be found in (Kock, 2003).

associated with the second law of thermodynamics has not been addressed? However, comparing the Reynolds-averaged Clausius-Duhem (in)equality, presented by Jansen (1993) and reproduced in Equation 1.24 below (excluding the internal heat generation term), with the entropy transport equations, it can be concluded that the inequality associated with the second law of thermodynamics is implicitly assumed in the above derivation. Yet regardless of the theoretical subtleties, what is important to recognize is that for real thermodynamic processes, the two terms on the right-hand side of Equation 1.22 and Equation 1.23 must be greater than zero.[12]

$$\left(\overline{\rho}\widetilde{s}\right)_{,t} + \left(\overline{\rho}\widetilde{s}\widetilde{u}_i\right)_{,i} + \left(\overline{\left[\frac{-\kappa T_{,i}}{T}\right]} + \overline{\rho}\widetilde{u_i''s''}\right)_{,i} = \overline{\left[\frac{\Upsilon(\mathbf{u},\mathbf{u})}{T}\right]} + \overline{\left[\kappa\frac{T_{,i}T_{,i}}{T^2}\right]} \tag{1.24}$$

Note: Υ represents the viscous dissipation function, a comma indicates partial differentiation, and the summation convention is to be applied on repeated indices. Additional details about the mathematical notation can be found in Jansen (1993).

1.4.3. Expanded Terms

The two averged EGR terms on the right-hand-side of Equation 1.23 can be expanded further using Reynolds averaging rules. Consistent with the notation and results presented by Kramer-Bevan (1992), the following equations result:

$$\overline{\frac{1}{T}\tau_{ij}\partial_j u_j} = \mu\overline{\left(\frac{1}{2}\left(\frac{1}{T}\partial_j u_i^2 + 2\frac{1}{T}\partial_i u_j\partial_j u_i + \frac{1}{T}\partial_i u_j^2\right) - \frac{2}{3}\frac{1}{T}\partial_i u_i\partial_k u_k\right)} \tag{1.25}$$

$$\begin{aligned}\overline{\frac{1}{T}\tau_{ij}\partial_j u_j} = \mu\Big[&\overline{\left(\frac{1}{T}\right)}\partial_j\overline{u}_i\partial_j\overline{u}_i + \overline{\left(\frac{1}{T}\right)}\overline{\partial_j u_i'\partial_j u_i'} + 2\partial_j\overline{u}_i\overline{\left(\frac{1}{T}\right)'\partial_j u_i'} \\ &+\overline{\left(\frac{1}{T}\right)'\partial_j u_i'\partial_j u_i'} + \overline{\left(\frac{1}{T}\right)}\partial_j\overline{u}_i\partial_i\overline{u}_j + \overline{\left(\frac{1}{T}\right)}\overline{\partial_j u_i'\partial_i u_j'} \\ &+\partial_j\overline{u}_i\overline{\left(\frac{1}{T}\right)'\partial_i u_j'} + \partial_i\overline{u}_j\overline{\left(\frac{1}{T}\right)'\partial_j u_i'} + \overline{\left(\frac{1}{T}\right)'\partial_j u_i'\partial_i u_j'} \\ &-\frac{2}{3}\Big(\overline{\left(\frac{1}{T}\right)}\partial_i\overline{u}_i\partial_k\overline{u}_k + \overline{\left(\frac{1}{T}\right)}\overline{\partial_i u_i'\partial_k u_k'} + 2\partial_i\overline{u}_i\overline{\left(\frac{1}{T}\right)'\partial_k u_k'} + \overline{\left(\frac{1}{T}\right)'\partial_i u_i'\partial_k u_k'}\Big)\Big]\end{aligned} \tag{1.26}$$

[12] Upon comparing the terms of Equations 1.23 and 1.24, the equivalent terms can be identified.

Returning to Equation 1.21 and writing this equation in indicial notation,

$$\overline{\Big(-\frac{\vec{q}\cdot\nabla T}{T^2}\Big)} = \overline{\Big(-\frac{q_i\partial_i T}{T^2}\Big)} \tag{1.27}$$

the following equation results:

$$\begin{aligned}\overline{\Big(-\frac{q_i\partial_i T}{T^2}\Big)} = &-\overline{q_i}\partial_i\overline{T}\Big(\overline{\frac{1}{T}}\Big)\Big(\overline{\frac{1}{T}}\Big) - \overline{q_i}\partial_i\overline{T}\overline{\Big(\frac{1}{T}\Big)'\Big(\frac{1}{T}\Big)'} - 2\overline{q_i}\Big(\overline{\frac{1}{T}}\Big)\overline{\partial_i T'\Big(\frac{1}{T}\Big)'}\\ &-\overline{q_i}\partial_i T'\overline{\Big(\frac{1}{T}\Big)'\Big(\frac{1}{T}\Big)'} - 2\partial_i\overline{T}\Big(\overline{\frac{1}{T}}\Big)\overline{q_i'\Big(\frac{1}{T}\Big)'} - \partial_i\overline{T}\overline{q_i'\Big(\frac{1}{T}\Big)'\Big(\frac{1}{T}\Big)'}\\ &-\Big(\overline{\frac{1}{T}}\Big)\Big(\overline{\frac{1}{T}}\Big)\overline{q_i'\partial_i T'} - 2\Big(\overline{\frac{1}{T}}\Big)\overline{q_i'\partial_i T'\Big(\frac{1}{T}\Big)'} - \overline{q_i'\partial_i T'\Big(\frac{1}{T}\Big)'\Big(\frac{1}{T}\Big)'}\end{aligned} \tag{1.28}$$

Recognizing the challenges associated with modeling the terms on the right-hand side of Equation 1.28, Kramer-Bevan (1992) simplified this expression by substituting $k\partial_i T$ for $-q_i$ and $\partial_i lnT$ for $\frac{\partial_i T}{T}$ (before time averaging) resulting in the following expression:

$$\overline{\Big(-\frac{q_i\partial_i T}{T^2}\Big)} = \overline{k\partial_i lnT\partial_i lnT} = k\partial_i\overline{lnT}\partial_i\overline{lnT} + k\overline{\partial_i\Big(lnT\Big)'\partial_i\Big(lnT\Big)'} \tag{1.29}$$

1.4.4. Closure

The averaging of the expanded terms was introduced in Section 1.4.3. Yet, as with any mathematical expression developed to describe the transport of fluid flow parameters, sufficient information in the form of models or analytical expressions must be available to solve the transport equation. [13]

Extended Averaging and Closure

Kramer-Bevan (1992) searched the literature for closure models for the terms generated as a result of the extended averaging process. The results of his search concluded that "A search of the literature uncovered no models for many of the correlations ... " and "A search of the literature uncovered no models for correlations

[13] In general, closure is the process in which the terms that develop upon performing RANS averaging are approximated using physical models or analytical expressions.

involving the term $\left(\frac{1}{T}\right)'$."

RAET Equation and Closure

First introduced by Adeyinka and Naterer (2004), the 'Reynolds Averaged Entropy Transport (RAET)' equation, a name coined by Orhan (2014), is a mathematical expression for the rate of entropy generation, specifically the right-hand side EGR terms. The RAET equation assumes that the fluctuating component of temperature T', where $T = \overline{T} + T'$, is small compared to the mean temperature $\overline{T}$.[14] The RAET equation is provided below.[15]

$$\begin{aligned}\overline{T}\overline{\dot{S}_{gen}} &= \overline{T}\Big[\frac{\partial(\rho\overline{s})}{\partial t} + \frac{\partial}{\partial x_i}\Big(\rho\overline{u}_i\overline{s} + \rho\overline{u_i's'} - \overline{\frac{k}{T}\frac{\partial T}{\partial x_i}}\Big)\Big] \\ &= k\frac{\partial}{\partial x_i}\overline{(lnT)}\frac{\partial\overline{T}}{\partial x_i} + k\overline{\frac{\partial}{\partial x_i}(lnT)'\frac{\partial T'}{\partial x_i}} + \overline{\tau_{ij}}\frac{\partial\overline{u}_i}{\partial x_j} + \overline{\tau'_{ij}\frac{\partial u'_j}{\partial x_j}} \\ &\quad -\Big(\rho\overline{T'u'_i}\frac{\partial\overline{s}}{\partial x_i} + \rho\overline{u_i}\overline{T'\frac{\partial s'}{\partial x_i}} + \overline{T'\frac{\partial(\rho u'_i s')}{\partial x_i}} + k\overline{T'\frac{\partial}{\partial x_i}(lnT)}\Big) \qquad (1.30)\end{aligned}$$

Orhan and Uzol (2012) referring to the (RAET) equation, stated that the equation "... requires heavy modelling effort and these models are mostly nonexistent in the open literature." In this dissertation research, the modeling approach used by Adeyinka and Naterer (2004) is beyond the scope of this research; therefore, the entropy generation rate terms for this study were developed using the traditional EGR modeling approach (cf. Section 3.2).

[14] Kramer-Bevan (1992) refers to this assumption as the 'Small Thermal Turbulence Assumption (STTAss).'

[15] For a detailed derivation, including the physical meaning of each term, readers are encouraged to consult Adeyinka and Naterer (2004).

Chapter 2: Literature Review

2.1. Air Reactor Cavity Cooling System

CFD analyses of the $\frac{1}{2}$–scale ANL NSTF and the UW $\frac{1}{4}$–scale air RCCS have been reported in the literature. In 2005, ANL published a report characterizing the applicability of the NSTF for the simulation of the VHTR RCCS; the commercial CFD software STAR–CD was used for the analyses (CD-adapco, 2015b). Two CFD simulations were developed to demonstrate that the NSTF could produce thermal-hydraulic flows that are representative of those in full-scale GA RCCS (Tzanos, 2005).

In 2010, ANL published a second report which focused on the analysis of the GA air RCCS design in support of scaling studies and instrumentation support. The report includes CFD studies of the full-scale GA RCCS and the NSTF 'experiment-scale' simplified RCCS geometries; the commercial CFD software STAR–CCM+ was used for the analyses (CD-adapco, 2015a). This study concluded that converged steady-state natural convection solutions can be obtained that identify key flow features for both geometries (Lomperski et al., 2010).

A third ANL report was published, which was a continuation of the 2010 ANL report. This study included scaling relationships and CFD analyses. The CFD work provided some insight into the appropriate STAR-CCM+ simulation settings. For example, a comparison between the realizable K-Epsilon ($k-\epsilon$) and the Menter SST K-Omega ($k-\omega$) turbulence models concluded that in the absence of experimental data to validate the turbulence model, the realizable K-Epsilon turbulence model should be used. Although not explicitly stated in the report, it appears, based on a review of the figures, that wall functions were used to model the viscous boundary layer (cf. Appendix C). Mesh refinement studies were performed, and more than 15 million computational elements with local refinement in the riser ducts were used. The study concluded that "... the scaling evaluation updated the basis that the air-cooled RCCS can be simulated at the ANL NSTF facility at a prototypic-scale in the lateral direction and about half-scale in the vertical direction." (Lomperski et al., 2011).

A conference paper was published summarizing the simulation results of the ANL NSTF natural circulation operation; the commercial CFD software STAR-CCM+ was used. Mesh refinement and convergence studies were performed using the K-Epsilon turbulence model. In addition, studies were performed evaluating the effects of convection within the reactor cavity (Dave et al., 2012). A subsequent publication identified difficulties in obtaining good convergence (Hu and Pointer, 2013). Improved convergence was obtained by shifting from the segregated solver, which is a SIMPLE-type algorithm, to the coupled solver. In addition, the mesh was refined resulting in greater than 20 million elements. Based on a review of the figures presented in the paper, it appears that wall functions were used to model the viscous boundary layer (cf. Appendix C).

A conference paper was published in 2013 summarizing the results of simulating the 'experiment-$\frac{1}{4}$ scale' RCCS using the commercial CFD software FLUENT (ANSYS, 2015; Lisowski et al., 2013). The CFD simulation was used to assist in determining the placement of six riser ducts in addition to providing confidence that adequate mixing will take place in the outlet plenum. Due to facility space limitations at UW, a six riser duct heated assembly was constructed instead of a 12 riser duct assembly, which would have been consistent with the ANL 'experiment-$\frac{1}{2}$ scale' RCCS. The symmetry model consisted of 2.2 million tetrahedral computational elements. The following simulation settings were used: SIMPLE pressure-velocity coupling scheme, "SST $k-\epsilon$ turbulence model" [sic], body force weighted pressure method, and 2nd order spatial discretization.

Recently a conference paper was published summarizing the results of simulating the ANL NSTF, using air as the working fluid, and a scaled model of the ANL NSTF RCCS, using water as the working fluid. The scaled model of the RCCS is being designed and built at University of Michigan (UM). Both CFD simulations used the commercial software STAR–CCM+. The 3-D simulations were generated on a polyhedral mesh with prism layers on the plenum and riser walls. The realizable K-Epsilon two layer model with two-layer wall treatment was used. Additional details

on the CFD simulation settings can be found in the conference paper (Nguyen et al., 2014).

To the best of the author's knowledge, the CFD simulations discussed above did not resolve the viscous and thermal boundary layers; most if not all simulations employed wall functions (cf. Appendix C).[16]

2.2. Boundary Layer Transition

Although the majority of engineering flows can be categorized as turbulent, a significant amount of boundary layer transitional flow research, primarily simulation based, has been reported in the literature. One motivation for transitional flow research is that laminar and turbulent heat transfer and fluid flow parameters differ significantly; for example, significant increases in friction and heat transfer properties are observed during the transition process (Meyer and Olivier, 2011; Wang et al., 2013). Additionally, the onset of boundary layer transition can change depending on the system design. For example, studies have shown that adverse and favorable pressure gradients, surface roughness, and system inlet conditions such as freestream turbulence intensity and oscillatory velocity behavior influence boundary layer transition.

Environmental effects on transition, such as the pressure gradient influence on boundary layer streak intensity, were studied by Zaki and Durbin (2006), using direct numerical simulation (DNS) predictions. Their effort was directed at understanding the behavior of boundary layer streaks and characterizing the relationship between streak intensity and transition location. One of the conclusions from this study was that "... the boundary-layer streaks are highly unstable, and adverse pressure gradient has little contribution; transition takes place swiftly independent of the mean gradient in pressure." Moreover, a recent numerical study by Nolan and Zaki (2013) provides insight into the relationship between boundary layer streaks and transition onset, including the relationship between turbulent spot growth rates and pressure gradient.

[16] For the majority of simulations, insufficient information was reported to determine whether or not the boundary layers were resolved.

From an experimental perspective, Abu-Ghannam et al. (1999) studied, using a wind tunnel, the effects of curvature on boundary layers under ZPG and FPG conditions at turbulence intensity levels ranging from 0.8% to 6.4%. They concluded that transition was delayed on a surface with convex curvature at low levels of turbulence intensity; yet, at high turbulence levels and ZPG, transition along convex surfaces behaved similarly to flat surfaces. More recently, Jonas et al. (2011) performed wind tunnel studies, which investigated boundary layer development on an aerodynamically smooth surface and on surfaces covered with sandpaper. One of several conclusions reached by Jonas et al. was that "Turbulent spot production starts sooner and with higher intensity in the rough wall boundary layer than in the smooth one at otherwise equal conditions and the increase of the free stream turbulence intensity amplifies this process."

Within the last 10 years, efforts, both computational and experimental, have been directed at predicting the transition regime (cf. Figure 1.8). Recognizing a gap in the current knowledge of turbulent duct flow, Lien et al. (2004) conducted a study on measuring the entrance length for fully developed smooth channel flow. As part of their study, a detailed literature review was performed. Based on this review, Lien et al. (2004) argued that "Efforts to compile information from existing literature have revealed data that is scattered and unreliable. Present-day experimentalists are still without a definitive guide to the necessary length for an intended experimental facility." Additionally, they conducted an experimental study focused on measuring the entrance length for fully developed smooth channel flow. Based on a literature review by Wang et al. (2013), it was concluded "... that there is an incomplete understanding of may details of the transition process." Of interest was that their study indicated existing correlations could not predict friction factor and heat transfer freestream transition characteristics. From a computational perspective, DNS is capable of predicting transition (Wu and Moin, 2010). But, classic RANS turbulence models are not capable of predicting transition. Recognizing the shortcomings of RANS turbulence models in predicting transition, efforts to develop RANS transition

models for general-purpose CFD codes began in early 2000 (Langtry, 2006; Menter et al., 2002). The STAR-CCM+ $\gamma - Re_\theta$ is just one example of a transition model that has been incorporated into general-purpose CFD codes.

The general conclusion that can be drawn from these research studies is that predicting the thermal and viscous characteristics of transition flow is important, yet difficult, since the underlying physical phenomena that occur when laminar flow transitions to turbulent flow, under the influence of pressure gradients and different geometries, is complex.

2.3. Entropy Generation Minimization and Models

Over the last three decades, there has been some interest in studying entropy from both a basic and applied research perspective. Yet, the popularity of this engineering discipline should not be considered burgeoning. In spite of its unpopularity, progress continues to be made in entropy-related research, including incorporating entropy into the engineering design process.

In 1982, Bejan (1982), introduced a concept that integrated fluid mechanics, heat transfer, and thermodynamics. Referred to as 'Entropy Generation Minimization' (EGM), this new discipline included the inherent thermodynamic reversibility of a system in the engineering design and analysis process. This discipline involves conducting an entropy generation analysis (EGA) to determine the smallest value of entropy generation rate (EGR) for a given design. It is beneficial in that it provides the engineer with EGR information at a local level, revealing the location of viscous and thermal irreversibilities, including the impact of design changes on these irreversibilities. Additionally, it allows the engineer to evaluate the relative performance, from both a viscous and thermal perspective, of different designs. [17]

As a result of the growth of the EGM field (1980s and 1990s), Bejan wrote a new book related to optimization of engineering systems and components. The book expanded on topics similar to those found in his 1982 book, but presented the subject

[17] EGM is an engineering discipline governed by the entropy transport equation, which provides the theoretical basis for computing EGR. It should not be construed as a formal mathematical 'minimization' process. Readers are encouraged to consult (Bejan, 1996) for additional information on EGM.

matter in more of a chronological format. For example, entropy-related thermodynamic, fluid mechanics, and heat transfer concepts were presented first, followed by component then system applications (Bejan, 1996).

In 1996, Bejan et al. (1996), published a book on thermal design and optimization. The book was written from a contemporary perspective, and it is intended for engineering students at the graduate level, practicing engineers, and technical managers working in the energy field. The book departs from traditional thermal system design texts by addressing "material drawn from the best of contemporary thinking about design and design methodology" and including "current developments in engineering thermodynamics, heat transfer, and engineering economics relevant to design." Additionally, the book discusses the importance of minimizing entropy generation rate (EGR). In short, reducing EGR reduces irreversibilities; therefore, the engineering design approaches the 'ideal' isentropic condition. Finally, from a practical engineering design perspective, the authors make a very important observation: "Engineers should be able to recognize irreversibilities, evaluate their influence, and develop cost-effective means for reducing them. However, the need to achieve profitable rates of production, high heat transfer rates, rapid accelerations, and so on invariably dictates the presence of significant irreversibilities. Furthermore, irreversibilities are tolerated to some degree in every type of system because the changes in design and operation required to reduce them would be too costly."

In 2006, Alabi et al. (2006) presented entropy generation analysis results associated with the flow over a Boeing 747-200 commercial aircraft. Their study used the entropy generation rate (EGR) model proposed by Moore and Moore (1983). They reported both inviscid and viscous contributions to EGR, which showed that the inviscid results underestimated the total entropy production by a factor of about 1000.

In 2007, Herwig and Kock (2007) published a study demonstrating the advantages of the EGM as an engineering tool. The results of a CFD analysis, computed using wall functions (cf., Appendix C), were used to calculate entropy generation

rate for several working designs until an optimal design was determined based on the minimization of entropy generation rate. For example, they demonstrated that the minimum entropy generation rate for air passing through a pipe heated at the midsection occurs at a turbulence promoter diameter to length (D/L) ratio of approximately 0.18. Figure 2.1 presents the working design results.

In 2008, Naterer and Camberos (2008) introduced a design methodology, based on the concept of entropy, referred to as 'Entropy-based Design' (EBD). In addition to including analytical expressions in the design and analysis process, the theoretical foundation of their EBD book extended to experimental and numerical techniques such as particle image velocimetry (PIV) and CFD. This same year, Iandoli et al. (2008) provided several examples of how entropy generation rate is applied to turbomachinery designs. And in 2009, Sciubba (2009) provided some insight into the order of magnitude of various terms in his EGR equation for an air-cooled gas turbine stator and a radial air compressor. Furthermore he includes a discussion on the influence of turbulence models, using the $k-\epsilon$ model as an example, on the entropy generation rate.

From more of a fundamental research perspective, Walsh and McEligot have published several articles related to the entropy generation, specifically in boundary layers (McEligot et al., 2008a,b; Walsh et al., 2011). Their efforts were directed at developing new knowledge of the entropy generation process. As a start, their primary focus was the study of entropy generation due to friction in viscous boundary layers for isothermal flows experiencing varying streamwise pressure gradients on flat-plate geometry. Their research utilized DNS results to quantify the entropy generation rate during the transition from laminar to turbulent flow for several pressure gradients, including zero pressure gradient (ZPG), favorable pressure gradient (FPG), and adverse pressure gradients (APG). In their 2011 publication, they suggested evaluating boundary layer entropy-related phenomena using RANS codes: "Provided Reynolds-averaged Navier-Stokes codes can predict the transition process adequately including sensitivity to inflow turbulence length scale - which is problematical - some may be

useful in predicting entropy generation rates S''' or S''."

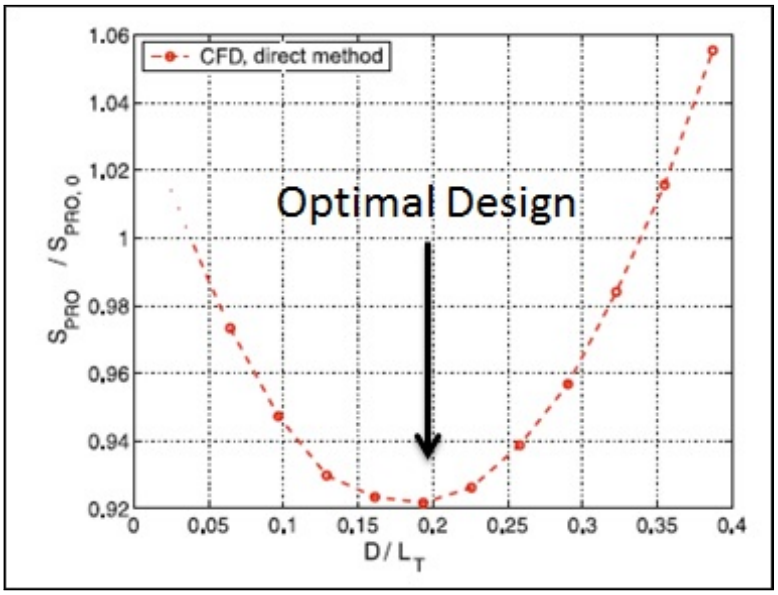

Figure 2.1: Entropy production rate versus D/L (Herwig and Kock, 2007)

2.3.1. Global and Local Models

Entropy Generation Rate (EGR) models can be classified into several categories, including global models and local models. Global models, in general, are relatively simple models, which require heat transfer and fluid flow boundary conditions such as velocity, pressure, temperature, and heat flux. Using these boundary conditions, global models will provide an average value for heat transfer and fluid flow contributions to EGR. The Lumped Parameter Model (cf. Section 3.1) is an example of a global model.

Local models provide a complete quantitative description of heat transfer and fluid flow contributions to EGR; their input is typically velocity and temperature fields obtained from a CFD simulation. Depending on how model closure is obtained, local models can be further classified as being based on either eddy viscosity modeling (EVM) or differential second moment (DSM) based modeling. The 'Direct Method Model,' presented in Section 3.2 is an example of a local model developed using EVM closure; and The 'RAET Model,' presented in Section 3.3 is an example of a local model developed using DSM closure.

2.3.2. EVM and DSM Closure Modeling

In 2004, Adeyinka and Naterer (2004), outlined the process of modeling the turbulence correlations associated with the RAET equation using linear eddy viscosity model (EVM) closure and differential second-moment (DSM) closure. Noteworthy is that differential second-moment closure models are not as popular as EVMs.

Eddy viscosity closure models are based on the assumption that the quantity eddy viscosity (μ_t) exists. Yet unlike molecular viscosity (μ), which is a material parameter (e.g., specific heat capacity or thermal conductivity), eddy viscosity is a variable that depends on other flow variables. Eddy viscosity is also referred to as turbulent viscosity in the literature, and it is primarily associated with the turbulent-viscosity hypothesis (Equation 2.1), introduced by Boussinesq in 1877 (Pope, 2001).[18]

$$\rho\overline{v_i'v_j'} = -\mu_t\Big(\frac{\partial\overline{v_i}}{\partial x_j} + \frac{\partial\overline{v_j}}{\partial x_i}\Big) + \frac{2}{3}\rho k\delta_{ij} \tag{2.1}$$

In the context of eddy viscosity models of mean entropy production, Adeyinka and Naterer (2004) shared their perspective on the shortcomings of EVMs. "The linear eddy viscosity model assumes a Boussineq relationship between the turbulent stresses (or second-moments) and the mean strain rate tensor through an isotropic eddy viscosity. Although these models attempt to minimize complexity, it is difficult to ascertain if the essence of relevant irreversibilities has been captured with sufficient accuracy, due to lack of experimental data. It should be noted that no relevant experimental data regarding these turbulence correlations of entropy production has been measured and reported in the literature (to our knowledge)."

Differential second-moment closure models are obtained by solving transport equations for unknown secondary-moments such as turbulent stress ($\overline{u_iu_j}$) and turbulent fluxes ($\overline{Tu_j}$). According to Hanjalić and Jakirlić (2002): "DSMs have long been expected to replace the currently popular two-equation $k-\epsilon$ and other eddy viscosity

[18]The turbulent-viscosity hypothesis is used to close the Reynolds averaged Navier-Stokes (RANS) equations. And, the basis of the $k-\epsilon$ turbulence model is the assumption of the validity of the turbulent-viscosity hypothesis, Equation 2.1, (Schäfer, 2006).

models as the industrial standard for Computational Fluid Dynamics (CFD). However, despite more than three decades of development and significant progress, these models are still viewed by some as a development target rather than as a proven and mature technique for solving complex flow phenomena. Admittedly, DSMs do not always show superiority over two-equation EVM models. One reason for this is that more terms need to be modelled. While this offers an opportunity to capture the physics of various turbulence interactions better, the advantage may be lost if some of the terms are modelled wrongly. ... These advances, together with the growing awareness among industrial CFD users of the limitations of two-equation eddy viscosity models and the need to model complex flows with higher accuracy, will lead in future to a much wider use of DSMs in CFD." Additional details associated with DSMs can be found in Hanjalić and Jakirlić (2002).

2.4. Verification and Validation

Advances in computer technology over the last 30 years has resulted in a great deal of emphasis on the use of computers to simulate physical processes; consequently, a new computational engineering field, loosely referred to as Verification and Validation (V&V), has emerged. In 1998, Patrick Roache authored the popular book 'Verification and Validation in Computational Science and Engineering,' which provides a good discussion on V&V concepts, applications, and lessons learned; furthermore, he provides a practical discussion on code quality assurance and certification, an often overlooked aspect of the modeling and simulation process.

In 2003, Knupp and Salari published their book 'Verification of Computer Codes in Computational Science and Engineering,' which addresses the concept of verification from more of a mathematical perspective, specifically verifying the code order of accuracy (Knupp and Salari, 2003). William Oberkampf and Christopher Roy (2010) coauthored a recent book titled 'Verification and Validation in Scientific Computing,' which encompasses a lot of information from a mathematical, computer science, engineering, risk, and management and planning perspective (Oberkampf and Roy, 2010). Collectively these books provide a solid foundation for managers, technical leads, and

computational engineers and analysts to understand and apply V&V techniques in the engineering design process.

The V&V process establishes that the mathematical equations, used to describe the physical phenomena of interest, were solved correctly and that the correct mathematical equations were used to describe the physical phenomena. For example and with respect to 'correct mathematical equations,' it would be inappropriate to use the Bernoulli Equation to describe viscous dissipation in a boundary layer. And, with respect to solving the 'mathematical equations correctly,' it is paramount that the code syntax is free of errors (i.e., bugs). In general, the use of the term V&V implicitly assumes, but not necessarily, that uncertainty quantification (UQ) and code quality assurance (QA) principles are included as well.

Code verification, establishing that the code is mathematically correct (e.g., free of coding errors), is the first step in the V&V process. Some code verification activities include: simple tests such as verifying the code conserves mass, order of accuracy and mesh refinement studies, and evaluation of discretization error (assuming an exact solution is available) (Oberkampf and Roy, 2010). The responsibility for software verification primarily resides with the commercial code vendors and independent code developer. But, ultimately the responsibility for ensuring a code is verified, rests with the users and their technical managers.

Validation, determining that the results of the simulation are an accurate representation of the real world, primarily resides with the CFD practitioner (AIAA, 1998; ASME, 2008). As part of the validation process, CFD practitioners rely on experimental data and/or DNS results to assess their numerical results. Noteworthy, is the underlying assumption that the experimental data and/or DNS results are accurate. In fact, a statement by Roache (1998) that "Experimental data is not as sacrosanct as many computational practitioners believe," highlights the importance of CFD practitioners understanding the capabilities and limitations of not only experimental data, but DNS results as well. Likewise, it is important that experimentalists understand the capabilities and limitations of computational fluid dynamics.

Verification and validation of computational engineering software, especially for nuclear safety-related systems, is a significant undertaking, which must be approached with an understanding of the V&V process and consideration for project schedules and costs. Noteworthy is that different organizations establish different methodologies, which incorporate V&V&UQ and QA principles. For example, the nuclear industry follows ASME-NQA-1 quality assurance requirements for software associated with nuclear safety systems (ASME, 2008); while academia relies on the peer review process to evaluate the quality of computational research (Shuttleworth, 2015). Additionally, several professional societies and investigators have published V&V literature, but to date only V&V guidelines have been agreed upon [AIAA (1998); ASME (2009)].

Noteworthy is that incorporating V&V principles in the design process is mandatory for safety-related calculations (i.e., nuclear reactor safety); yet, it is important that non-safety-related calculations (e.g., fundamental research) should have some degree of rigor established - on par with the risk associated with the use of incorrect results.

Finally, the principles of V&V are the primary means to determine the credibility (e.g., accuracy and reliability) of computational simulations in high-consequence fields such as nuclear engineering and reactor safety. Therefore consistent with the spirit of Oberkampf and Trucano (2008) that " . . . we need to move from the culture of glossy marketing and arrogance to a culture that forthrightly addresses the limitations, weaknesses, and uncertainty of our simulations.", a significant amount of effort was made to identify the limitations, weaknesses, and qualitative uncertainty of the simulations conducted for this research.

2.5. Related Research Limitations

From an applied research perspective, the limitations of related research and practical applications in this area are threefold: (1) in general, design engineers, practicing engineers, and academic institutions place little emphasis on the usefulness of EGA in the design process; contributing to this shortcoming is the confusing nature of the

concept of entropy. For example, it has been the author's experience that design processes, including those that utilize CFD methods, published in the literature or those utilized by engineering firms, only employ traditional HTFF analysis techniques. If used in the design process, EGA is primarily employed as a stand-alone analysis technique; but again, use of EGA in the design process is not common. In short, the author is neither aware of nor has he experienced the use of EGA coupled with HTFF in a practical engineering setting, (2) recent efforts, by other research institutions, to conduct modeling and simulation of the air RCCS have been limited to the use of wall functions, resulting in an increase in the uncertainty of the CFD results. Contributing to this research limitation is the increase in computational overhead as the result of resolving the boundary layer and the lack of sufficient computational resources, and (3) a thorough analysis of the limitations, weaknesses, and uncertainty associated with nuclear engineering CFD simulations of the air RCCS, published in the literature, is lacking. The author reviewed several dissertations and numerous journal articles which employed computational techniques and/or codes. These documents neither addressed verification and validation nor mentioned contributions to solution uncertainty in their research results.

From a basic research perspective, the limitations of related research in this area are numerous. First of all, the author was not able to locate literature associated with duct or plate flows characterized by all of the following: nonuniform flow, nonuniform heat transfer, and entrance effects. Secondly, the author was not able to locate any literature that address the process of computing freestream parameters under nonuniform flow conditions. Additionally, to the best of the author's knowledge, no other research has identified heat transfer as the primary dissipation mechanism for the UW experimental air RCCS.

Chapter 3: Entropy Generation Modeling

3.1. Lumped Parameter Model

Early entropy studies used 'Lumped Parameter' models to determine entropy generation rates (Sciacovelli et al., 2015). These models incorporate experimental heat transfer and fluid friction data, which are typically based on the underlying assumption of homogeneous internal working fluid properties and uniform fluid flow parameters (e.g., velocity and temperature). They are typically used in situations where the pointwise velocity and temperature fields are not known.

Bejan (1996) developed a Lumped Parameter model (Equation 3.1) to calculate the entropy generation rate for ducts of arbitrary geometry with heat transfer at the walls. The first term on the right side of Equation 3.1 represents the viscous dissipation contribution and the second term represents the thermal dissipation contribution.

$$\dot{S}' = \frac{32\dot{m}^3 f}{\pi^2 \rho^2 T D^5} + \frac{q'^2}{\pi k T^2 N u} \tag{3.1}$$

Equation 3.1 can be written in terms of heat flux and entropy generation rate:

$$\dot{S} = \frac{32\dot{m}^3 f L}{\pi^2 \rho^2 T D^5} + \frac{q''^2 D^2 \pi L}{k T^2 N u} \tag{3.2}$$

For fully developed turbulent flow, the Nusselt number is given by the Dittus-Boelter correlation (Equation 3.3) and the friction factor for smooth pipes is given by the Fanning friction factor (Equation 3.4) for smooth pipes,

$$Nu = 0.023 Re_D^{0.8} Pr^n \tag{3.3}$$

where $n = 0.4$ is used for this study.[19,20] The Dittus-Boelter equation property

[19] Readers are urged to consult Winterton (1998) for a historical perspective on the Dittus-Boelter equation.

[20] The Dittus-Boelter correlation is based on fully developed flow. The flows analyzed in this study are impacted by entrance effects, resulting in non-fully developed flows. Therefore, the Dittus-Boelter correlation would under-predict the convective heat transfer (cf. Section 5.1).

constraints include: $0.7 \leq Pr \leq 120$ and $2500 \leq Re_D \leq 1.24x10^5$ (Bejan, 2013).

$$f = 0.046 Re_D^{-0.2} \tag{3.4}$$

3.2. Direct Method Model

The 'Direct Method' model, a model we attribute to Kock and Herwig (2004), is based on the underlying assumptions (e.g., isotropic, Newtonian incompressible flow) presented in Section 1.4.2 and the supposition that the EGR terms consist of both a mean and a fluctuating term. Beginning with Equation 1.22, which is repeated below, the derivation of the Direct Method model is as follows:

$$\rho\Big(\frac{\partial \overline{s}}{\partial t} + \overline{u}\frac{\partial \overline{s}}{\partial x} + \overline{v}\frac{\partial \overline{s}}{\partial y} + \overline{w}\frac{\partial \overline{s}}{\partial z}\Big) + \rho\Big(\frac{\partial \overline{u's'}}{\partial x} + \frac{\partial \overline{v's'}}{\partial y} + \frac{\partial \overline{w's'}}{\partial z}\Big) + \overline{\nabla \cdot \Big(\frac{\vec{q}}{T}\Big)} = \overline{\Big(\frac{\Phi}{T}\Big)} + \overline{\Big(\frac{\Phi_\Theta}{T^2}\Big)} \tag{3.5}$$

Time averaging of the two EGR terms results in two terms (Equations 3.8 and 3.9), and a mean and a fluctuating component for each term. Expanding the reciprocal of temperature (Equations 3.6 and 3.7) and assuming that the fluctuating component of temperature T' in the denominator is small compared to the mean temperature $\overline{T}$, results in the following equations:[21,22]

$$\frac{1}{\overline{T} + T'} = \frac{1}{\overline{T}}\frac{1}{(1 + \frac{T'}{\overline{T}})} = \frac{1}{\overline{T}}\Big[1 - \frac{T'}{\overline{T}} + \Big(\frac{T'}{\overline{T}}\Big)^2 \mp ...\Big] \tag{3.6}$$

$$\frac{1}{(\overline{T} + T')^2} = \frac{1}{\overline{T^2}}\frac{1}{(1 + \frac{T'}{\overline{T}})^2} = \frac{1}{\overline{T^2}}\Big[1 - 2\frac{T'}{\overline{T}} + 3\Big(\frac{T'}{\overline{T}}\Big)^2 \mp ...\Big] \tag{3.7}$$

[21]The assumption that T' is small compared to the mean temperature ($\overline{T}$) is referred to as the Small Thermal Turbulence Assumption (STTAss) by Kramer-Bevan (1992).

[22]A detailed derivation of the equations associated with the Direct Method Model can be found in (Kock, 2003).

$$\frac{\overline{\Phi}}{\overline{T}} = S_{PRO,\overline{D}} + S_{PRO,D'} \tag{3.8}$$

$$\frac{\overline{\Phi_\Theta}}{\overline{T}^2} = S_{PRO,\overline{C}} + S_{PRO,C'} \tag{3.9}$$

$$S_{PRO,\overline{D}} = \frac{\mu}{\overline{T}}\Big[2\Big\{\Big(\frac{\partial \overline{u}}{\partial x}\Big)^2 + \Big(\frac{\partial \overline{v}}{\partial y}\Big)^2 + \Big(\frac{\partial \overline{w}}{\partial z}\Big)^2\Big\} + \Big(\frac{\partial \overline{u}}{\partial y} + \frac{\partial \overline{v}}{\partial x}\Big)^2 + \Big(\frac{\partial \overline{u}}{\partial z} + \frac{\partial \overline{w}}{\partial x}\Big)^2 + \Big(\frac{\partial \overline{v}}{\partial z} + \frac{\partial \overline{w}}{\partial y}\Big)^2\Big] \tag{3.10}$$

$$S_{PRO,D'} = \frac{\mu}{\overline{T}}\Big[2\Big\{\overline{\Big(\frac{\partial u'}{\partial x}\Big)^2} + \overline{\Big(\frac{\partial v'}{\partial y}\Big)^2} + \overline{\Big(\frac{\partial w'}{\partial z}\Big)^2}\Big\} + \overline{\Big(\frac{\partial u'}{\partial y} + \frac{\partial v'}{\partial x}\Big)^2} + \overline{\Big(\frac{\partial u'}{\partial z} + \frac{\partial w'}{\partial x}\Big)^2} + \overline{\Big(\frac{\partial v'}{\partial z} + \frac{\partial w'}{\partial y}\Big)^2}\Big] \tag{3.11}$$

$$S_{PRO,\overline{C}} = \frac{k}{\overline{T}^2}\Big[\Big(\frac{\partial \overline{T}}{\partial x}\Big)^2 + \Big(\frac{\partial \overline{T}}{\partial y}\Big)^2 + \Big(\frac{\partial \overline{T}}{\partial z}\Big)^2\Big] \tag{3.12}$$

$$S_{PRO,C'} = \frac{k}{\overline{T}^2}\Big[\overline{\Big(\frac{\partial T'}{\partial x}\Big)^2} + \overline{\Big(\frac{\partial T'}{\partial y}\Big)^2} + \overline{\Big(\frac{\partial T'}{\partial z}\Big)^2}\Big] \tag{3.13}$$

where $S_{PRO,\overline{D}}$ represents the mean flow contribution to viscous dissipation, $S_{PRO,D'}$ represents the turbulent contribution to viscous dissipation, $S_{PRO,\overline{C}}$ represents the mean temperature contribution to thermal dissipation, and $S_{PRO,C'}$ represents the turbulent contribution to thermal dissipation.

With respect to CFD RANS analyses, sufficient velocity and temperature fields are available during the post-processing phase to compute $S_{PRO,\overline{D}}$ and $S_{PRO,\overline{C}}$. But, insufficient information is available to compute the corresponding fluctuating contributions; so $S_{PRO,D'}$ and $S_{PRO,C'}$ must be modeled.

Herwig and Kock (2007) propose the following models:

$$S_{PRO,D'} \approx \frac{\rho \epsilon_{cfd}}{\overline{T}} \tag{3.14}$$

$$S_{PRO,C'} \approx \frac{\alpha_t}{\alpha} S_{PRO,\overline{C}} = \frac{k_t}{k} S_{PRO,\overline{C}} \tag{3.15}$$

$$k_t = \frac{c_p \mu_t}{\mathrm{Pr}_t} \tag{3.16}$$

where ϵ_{cfd} represents the turbulent dissipation and μ_t represents turbulent viscosity, both computed as part of a CFD RANS turbulent model (e.g., $k-\epsilon$), α represents thermal diffusivity, k represents thermal conductivity, and Pr_t represents turbulent Prandtl number, which is the ratio of eddy diffusivity for momentum to eddy diffusivity for heat.[23]

Using the models proposed by Herwig and Kock (2007), the Direct Method Model (e.g., EGR terms) is summarized as follows:

$$\frac{\overline{\Phi}}{\overline{T}} \approx S_{PRO,\overline{D}} + \frac{\rho \epsilon_{cfd}}{\overline{T}} \tag{3.17}$$

$$\overline{\frac{\Phi_\Theta}{T^2}} \approx \left(1 + \frac{k_t}{k}\right) S_{PRO,\overline{C}} \tag{3.18}$$

An important point to address is that mathematically ϵ_{cfd}, associated with popular RANS turbulence models, differs from the classical (i.e., true) definition of the turbulent dissipation function (Wilcox, 2000). Specifically, ϵ_{cfd} is defined as shown in Equations 3.19 through 3.21:

$$\epsilon_{cfd} = \frac{\mu}{\rho} \overline{\frac{\partial u_i'}{\partial x_k} \frac{\partial u_i'}{\partial x_k}} \tag{3.19}$$

$$\epsilon_{true} = \frac{1}{2} \frac{\mu}{\rho} \overline{\left(\frac{\partial u_i'}{\partial x_k} + \frac{\partial u_k'}{\partial x_i}\right)^2} \tag{3.20}$$

[23] "There are many who would argue, and quite convincingly, that recent advances in turbulent flow modeling make the concept of eddy diffusivity obsolete, and without an eddy diffusivity Turbulent Prandtl Number has no meaning." (Kays, 1994)

$$\epsilon_{cfd} = \epsilon_{true} - \frac{\partial}{\partial x_k}\Big(\frac{\mu}{\rho}\overline{u_i'\frac{\partial u_k'}{\partial x_i}}\Big) \tag{3.21}$$

From an engineering perspective, using (ϵ_{cfd}) is convenient; but it does result in additional uncertainty. Wilcox (2000) shares his perspective on the significance of this difference: "In practice, the difference between ϵ (ϵ_{cfd}) and ϵ_{true} is small and should be expected to be significant only in regions of strong gradients, e.g., shock waves or the viscous wall region. In the latter case (viscous wall region), Bradshaw and Perot (1993) have shown that the maximum difference is just 2%, and can thus be ignored."

A two-dimensional representation of the 'Direct Method Model,' where the x-direction represents the freestream direction and the y-direction represents the wall normal direction can be formed by eliminating the derivatives of the EGR terms related to the z-direction as follows:

Beginning with Equation 3.17 and Equation 3.18,

$$\frac{\overline{\Phi}}{\overline{T}} \approx S_{PRO,\overline{D}} + \frac{\rho\epsilon_{cfd}}{\overline{T}} \tag{3.22}$$

$$\overline{\frac{\Phi_\Theta}{T^2}} \approx \Big(1 + \frac{k_t}{k}\Big)S_{PRO,\overline{C}} \tag{3.23}$$

and substituting the equation for $S_{PRO,\overline{D}}$ and $S_{PRO,\overline{C}}$ results in the following 2-D EGR equations,

$$\frac{\overline{\Phi}}{\overline{T}} \approx \frac{\mu}{\overline{T}}\Big[2\Big\{\Big(\frac{\partial\overline{u}}{\partial x}\Big)^2 + \Big(\frac{\partial\overline{v}}{\partial y}\Big)^2\Big\} + \Big(\frac{\partial\overline{u}}{\partial y} + \frac{\partial\overline{v}}{\partial x}\Big)^2\Big] + \frac{\rho\epsilon_{cfd}}{\overline{T}} \tag{3.24}$$

$$\overline{\frac{\Phi_\Theta}{T^2}} \approx \Big(\frac{k + k_t}{\overline{T}^2}\Big)\Big[\Big(\frac{\partial\overline{T}}{\partial x}\Big)^2 + \Big(\frac{\partial\overline{T}}{\partial y}\Big)^2\Big] \tag{3.25}$$

3.3. Modeled RAET Equation

The work of Adeyinka and Naterer (2004) motivated Orhan (2014) to extend the entropy generation production by developing closure models for the terms on the right-hand-side of Equation 1.30. Specifically, he developed models for the following terms: $\overline{u_i's'}$, $\overline{\frac{\partial}{\partial x_i}(lnT)'\frac{\partial T'}{\partial x_i}}$, $\overline{T'\frac{\partial s'}{\partial x_i}}$, and $\overline{T'\frac{\partial(\rho u_i's')}{\partial x_i}}$. The resulting equation (Equation 3.26) is presented below.

$$\frac{\partial(\rho\overline{s})}{\partial t}+\frac{\partial}{\partial x_i}\Big[\rho\overline{u_i s}-(\frac{k+k_t}{c_v})\frac{\partial\overline{s}}{\partial x_i}\Big]=\frac{k}{\overline{T}^2}\Big(\frac{\partial\overline{T}}{\partial x_i}\Big)^2+\frac{k}{\overline{T}^2}\overline{\Big(\frac{\partial T'}{\partial x_i}\Big)^2}+$$
$$\frac{k}{2}\frac{\partial}{\partial x_i}\Big(\frac{1}{\overline{\overline{T}}}\Big)\frac{\partial\overline{T'^2}}{\partial x_i}+\frac{\overline{\tau_{ij}}}{\overline{T}}\frac{\partial\overline{u_i}}{\partial x_j}+\frac{\overline{\epsilon}}{\overline{T}}-\Big(\frac{\rho}{\overline{T}}\overline{u_i'T'}\frac{\partial\overline{s}}{\partial x_i}\Big)-\frac{\rho C_v}{\overline{T}}\overline{u_i}\overline{\Big(T'\Big)^2}\frac{\partial}{\partial x_i}\Big(\frac{1}{\overline{\overline{T}}}\Big)-$$
$$\frac{\rho C_v}{2\overline{T}^2}\Big(\frac{\partial\overline{(T'^2)}}{\partial x_i}\Big)-\frac{\rho C_v}{\overline{T}}\overline{u_i'\Big(T'\Big)^2}\frac{\partial}{\partial x_i}\Big(\frac{1}{\overline{\overline{T}}}\Big)-\frac{\rho C_v}{2\overline{T}^2}\overline{\frac{\partial(u_i'T'^2)}{\partial x_i}} \tag{3.26}$$

In order to solve Equation 3.26, Orhan (2014), applied the DSM closure strategies of Hanjalić and Jakirlić (2002), developing transport equations for the following terms: $\overline{u_i'T'^2}$, $\overline{u_i'T'}$, and $\overline{T'^2}$. Finally, the constant coefficients associated with each transport equation were modified (i.e., calibrated) using using DNS results. Due to the complexity of the mathematical process, readers are encouraged to consult Orhan (2014) and Hanjalić and Jakirlić (2002) for the details of his modeling process.

3.4. Other Models

In addition to the modeling techniques discussed in this section, numerous modeling approaches, simplified and complex, have been published in the literature, for example Moore and Moore (1983) and Drost and White (1991). Sciacovelli et al. (2015) and Adeyinka and Naterer (2004) provide an overview of the modeling approaches associated with entropy generation analysis.

Chapter 4: Methods

Entropy generation minimization (EGM) is a discipline, which combines classical principles of the heat transfer, fluid flow, and thermodynamic disciplines. As a consequence of its interdisciplinary character, EGM is considered distinct from these classical disciplines (Bejan, 1996).

This research employs the EGM process by conducting an entropy generation analysis (EGA) of six air RCCS designs, which are based on the UW $\frac{1}{4}$-scale air RCCS design. The primary focus of the design process was Duct 4 in which two boundary conditions (duct inlet and wall heat transfer) are altered (cf. Figures 4.16 through 4.18 and Figure 4.32). The design with the smallest entropy generation rate is considered the preferred design, which could be considered for further optimization (cf. Figure 5.22 through Figure 5.24). For example, optimization of the heated duct could be performed by changing the duct hydraulic diameter to length ratio, similar to the example presented in Figure 2.1.

Noteworthy is that the governing equation of EGM is the entropy transport equation discussed in Section 1.4.2 and Section 3.2. The entropy production terms, associated with the entropy transport equation, require velocity and temperature fields in order to calculate the entropy generation rate (EGR); therefore, the velocity and temperature fields were computed using computational fluid dynamics as described in this chapter.

4.1. General Design and Analysis Process

The general design process followed in this research (cf. Figure 4.1), consisted of four phases, which are described below in summary:

1. Basic research in modeling and simulation of boundary layer transition, which included evaluating capabilities and limitations of classic turbulence and the associated transition models, and investigating boundary layer entropy generation (cf. Appendix A). This phase is necessary in order to provide insight into fundamental flow features with minimal geometric complexity, such as

boundary layer development and entropy generation rate on a 2D flat plate.

2. Applied research in modeling and simulation of the UW $\frac{1}{4}$–scale air RCCS to evaluate and identify modeling and simulation issues such as problem size (e.g., mesh size), simulation settings, computing needs, turbulence models, and availability of experimental data (cf. Appendix B).

3. Detailed CFD analyses of two inlet-plenum designs (i.e., A4 and E6). This phase of the design process produces velocity and temperature fields necessary for the EGR calculations. Specifically, inlet boundary conditions for the Duct 4 CFD analyses were obtained from the inlet–plenum simulations [cf. Section 4.4.3 and (Hamman et al., 2015)].

4. Detailed HTFF and EGR analyses of Duct 4 designs (A4–HTA, A4–HTB, A4–HTC, E6–HTA, E6–HTB, E6–HTC). Specifically, two 40 inch sections (e.g., 0"–40" and 40"–80") were analyzed for each duct design, resulting in a total of 12 analyses (cf. Figures 4.2 and 4.3).

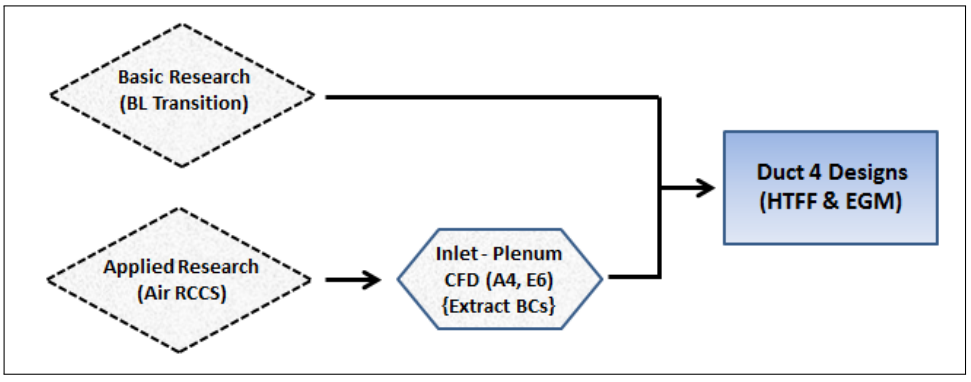

Figure 4.1: General design process

The detailed Duct 4 HTFF and EGR analysis process developed as part of this study consisted of applying classical heat transfer and fluid flow (HTFF) techniques and entropy generation analysis (EGA) techniques (cf. Figure 4.2). (It has been the author's experience that nuclear engineering design processes only employ traditional HTFF analysis, which does not include EGA.) The basic research conducted on boundary layer development over a smooth plate is included in the design process

because it played an important role in establishing capabilities and limitations of classic two-equation turbulence models (e.g., $k-\epsilon$, $k-\omega$) and the transitional turbulence models (e.g., $\gamma - Re_\theta$).[24] Furthermore, the 2D flat plate boundary layer studies were important in that they provided insight into flow features, such as boundary layer development and entropy generation rate.

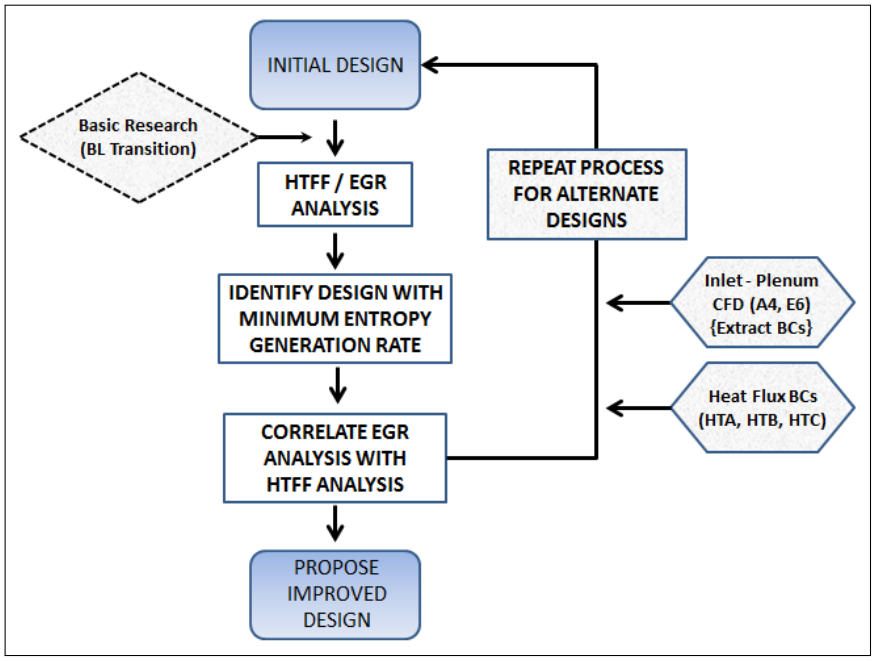

Figure 4.2: Duct 4 analysis process

The modeling and simulation process used in this study consisted of several steps, including: creating a computer aided design (CAD) solid-model; generating a computational mesh; establishing boundary conditions and simulation settings; running the simulation on high performance computers (HPCs); calculating HTFF and entropy parameters; and conducting preliminary V&V studies. The analysis process is illustrated in Figure 4.3. The primary purpose of the CFD analyses was to produce temperature and velocity field results, which were needed to compute entropy-related parameters (e.g., entropy generation rate). For example, the velocity and tempera-

[24]Given the diverse and complex turbulence model options available to users of general-purpose CFD codes, experienced computational analysts understand the importance of rigor in, for example, establishing boundary conditions, testing and calibrating transition models, conducting mesh refinement studies, and understanding the fundamental theory associated with the simulation settings.

ture fields obtained from the CFD analyses were imported into a MATLAB boundary analysis code where entropy generation rate parameters were calculated.

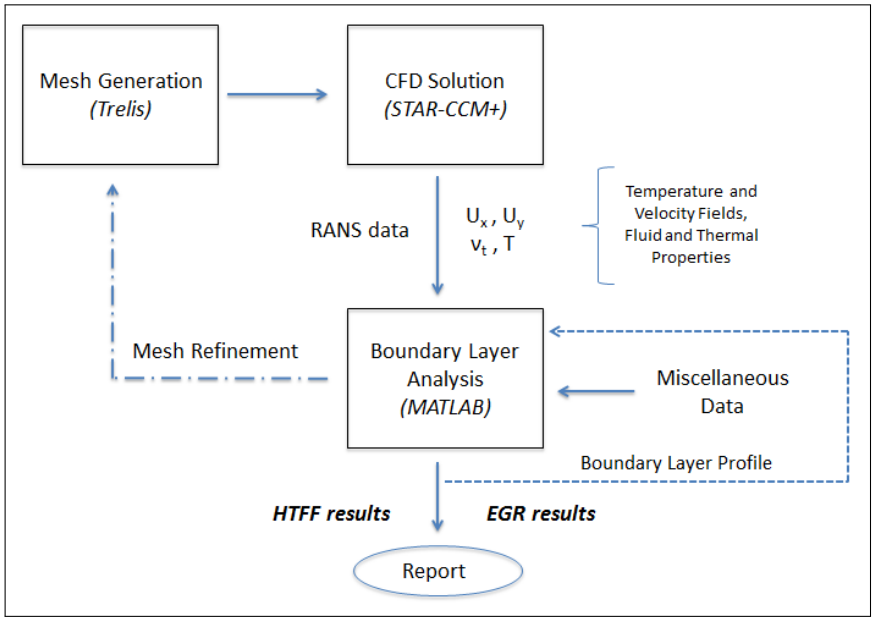

Figure 4.3: Modeling and simulation process

4.2. Software

Trelis Pro 14.0.4, the commercial version of Sandia National Laboratories (SNL) CUBIT meshing software, was used to generate the meshes for the Duct 4 analyses and the boundary layer transition analyses. This software was chosen, in lieu of the STAR-CCM+ trimmed cell mesher, due to its robustness and user options in generating a structured mesh with elements clustered in the plate wall normal direction (csimsoft, 2015). All other CFD simulations used the unstructured mesh generators available in STAR–CCM+.[25]

The commercial CFD code STAR–CCM+ (Version 8.04.010) was used to generate 3D velocity, turbulent viscosity, and temperature fields. STAR-CCM+ uses a cell-centered finite volume discretization technique to solve the governing equations of fluid flow including the transport equations associated with the turbulence models. Two numerical solvers, segregated and coupled, are available and several turbulence

[25]In general, a structured mesh consists of hex elements that follow a uniform pattern; an unstructured mesh does not follow a uniform pattern.

models are provided including variants of the K-Epsilon ($k-\epsilon$) and K-Omega ($k-\omega$) models.

STAR-CCM+ provides users with two options for a numerical solver: segregated and coupled. The segregated solver solves the governing equations in an uncoupled fashion. For example, using a SIMPLE-type algorithm, each equation is solved independently; although, the linking of the momentum and mass conservation equations is accomplished using a predictor-corrector approach. The coupled solver solves the mass and momentum equations in a coupled fashion. Each solver has advantages and disadvantages. For example, the coupled solver requires more memory; but it produces more accurate results for compressible flows and high Rayleigh number natural convection flows (CD-adapco, 2015a).

One of the widely used CFD turbulence models used for the analysis of a wide variety of industrial problems is the K-Epsilon ($k-\epsilon$) turbulence model. The turbulence model consists of two transport equations: turbulent kinetic energy (k) and turbulent dissipation rate (ϵ). Therefore, a 3-D simulation requires that a total of seven equations (mass, momentum, energy, and turbulence) are solved by the CFD software. A complete description of the solvers, governing equations, and turbulence models can be found in the STAR-CCM+ User Guide or the literature (Pope, 2001; Wilcox, 2000).

The velocity, turbulent viscosity, and temperature fields computed from the CFD analyses were imported into a boundary analysis code developed using MATLAB 2013a (8.1.0.604), which is a numerical computing environment and programming language (MathWorks, 2015). The code was written to calculate boundary layer parameters (e.g., wall shear stress, convective heat transfer coefficient) and entropy generation rate parameters using boundary layer equations [cf. (White, 1991)] and the entropy generation rate equations described in Section 3.2.

4.3. Hardware

A ZaReason 'Fortis Extreme 2' workstation with an AMD FX-8350 8-core processor and Linux Ubuntu 12.04 LTS operating system (Linux) was used to build

the CFD models. This workstation is referred to as Aries in this document. Small models were developed and run on this Linux box, but larger CFD models were run on the University of Idaho Big-STEM (HP DL 980G7) high performance computer. Big-STEM is comprised of 80 cores of the Intel Zeon EZ-4870 2.40 Ghz processors and 4 Tb of RAM with a Red-Hat 6.5 operating system (Linux); 64 processors were allocated by Big-STEM administrators for this work.

When running large-scale computational simulations, high performance computing (HPC) productivity should be assessed; but such an assessment can be complex. In an article, Kepner (2004) shares his perspective on this topic: "The measurement of productivity for a particular user on a particular system with a particular application is a difficult question that must encompass a variety of concepts."

One productivity metric which characterizes the integral hardware/software efficiency is a speedup. Typically, speedup is presented on a plot of speedup verses the number of processors. In general, speedup curves should be developed when it is expected that numerous large-scale production simulations will be run. From a computational engineering perspective, speedup metrics provide CFD practitioners with a realistic estimate of simulation times and the optimal number of processors.

An example of a speedup curve is shown in Figure 4.4. Two plots are shown in this figure: a linear plot, which represents the theoretical maximum achievable speedup, and the actual speedup. The linear curve represents the theoretical maximum achievable speedup for a given number of processors, and the nonlinear curve, which depends on several factors including hardware, software, and physics models, is the actual performance curve (Chhabra and Singh, 2007; El-Nashar, 2011; Yang et al., 2011). Noteworthy is that accessing more than 512 processors does not reduce simulation time; in fact, simulation time is increased. Additionally, in situations where several users are sharing the same computational resource, accessing more than 512 processors reduces the amount of processors available for other users. In short, it is not practical for analysts to access more than 512 processors, on a multiuser machine, unless additional memory is required.

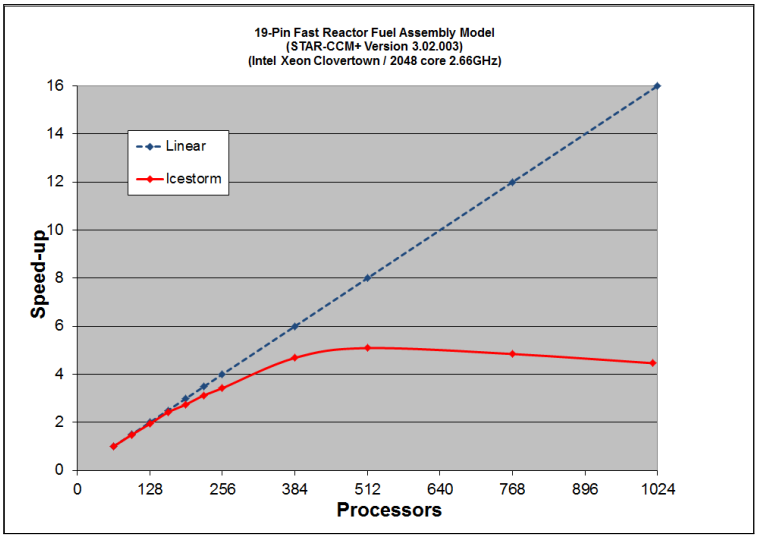

Figure 4.4: Speedup curve (Icestorm)

Recognizing the computational overhead requirements to simulate the RCCS, two speedup curves were developed using STAR-CCM+ Version 8.04.010. The first speedup curve developed was for the 8-core workstation Aries (Figure 4.5), and the second speedup curve was for Big-STEM (Figure 4.6). Note that for Big-STEM, linear behavior is observed for up to approximately 16 processors; and computational efficiency is reduced as this number is exceeded. Given that the maximum speedup for the workstation Aries is approximately four, it is not practical to run large simulations on this machine. But, Aries performs well for building STAR-CCM+ models and post-processing CFD results.

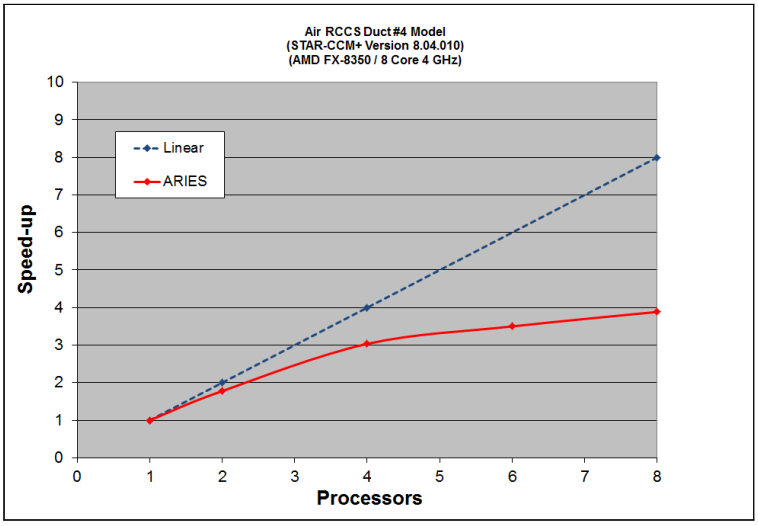

Figure 4.5: Speedup curve (Aries)

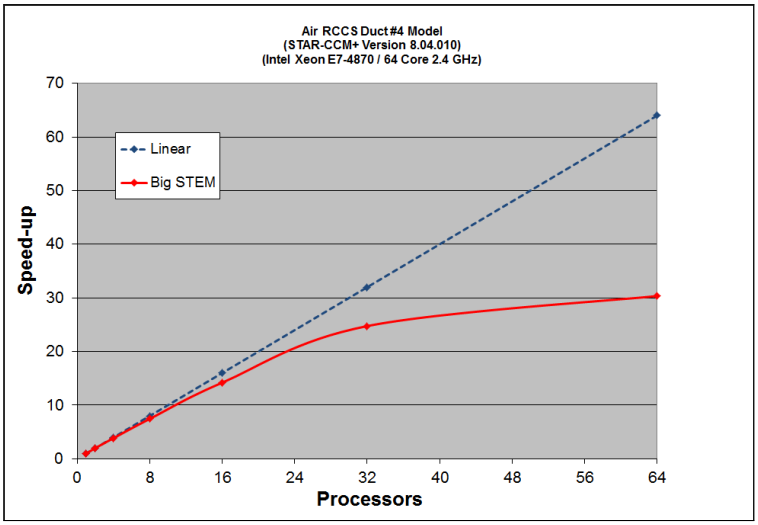

Figure 4.6: Speedup curve (Big-STEM)

4.4. Modeling and Simulation

As part of this research, a significant amount of modeling and simulation (M&S) was required. In fact, over 10 CFD models were constructed and over 20 CFD simulations were performed. The following is a summary of the M&S methods.

4.4.1. Boundary Layer Transition

The initial phase of this research consisted of a study, of an isothermal fluid flowing over a flat plate, to compare and contrast the transition characteristics of Reynolds-averaged Navier-Stokes turbulence and transition models to DNS results, under the influence of pressure gradients. The classical skin friction coefficient and local entropy generation rate were used as metrics to evaluate transition. Only a summary of the methods used for the boundary layer transition study will be presented in the main body of this dissertation; additional details are located in Appendix A.

A 2D computational mesh, similar to - but coarser than - the DNS meshes used by Nolan and Zaki (2013) was generated for each of the four RANS simulations. Trelis, the commercial version of Sandia National Laboratories (SNL) CUBIT meshing software, was used to generate the RANS meshes (csimsoft, 2015). This software was chosen due to its robustness and user options in generating a structured mesh with elements clustered in the plate wall normal direction; a bias scheme factor (i.e., wall normal expansion ratio) of 1.057 was chosen in order to obtain wall y^+ values

less than one. The mesh was imported into STAR-CCM+ commercial CFD software where simulations were performed in order to develop velocity, turbulence intensity, and turbulent viscosity fields. A 3D representation of the 2D mesh used in the boundary layer analyses, showing elements clustered near the plate wall (cf. bright yellow area), is shown in Figure 4.7.

The following STAR-CCM+ simulation settings were used to generate the RANS velocity fields: constant density, second order upwind discretization, SST-Mentor $k-\omega$ turbulence model, and the segregated solver. In an effort to evaluate the STAR-CCM+ transition model, one zero pressure gradient (ZPG) simulation using the $\gamma - Re_\theta$ model was performed. Boundary conditions for the CFD simulation were chosen in order to approximate those used by Nolan and Zaki (2013). Specifically, the inlet velocity profile was extracted from the DNS data of Nolan and Zaki; and the turbulence intensity profile was calculated from the DNS Reynolds stress values provided by Nolan and Zaki (2012).

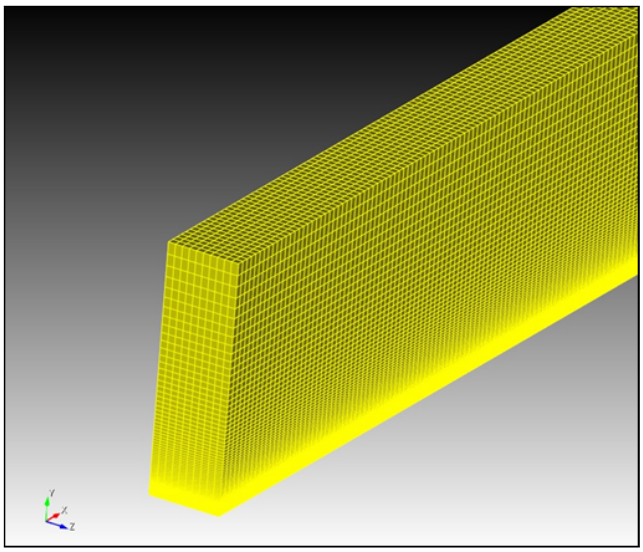

Figure 4.7: 3D ZPG mesh

A mesh refinement study was performed by reducing the element size until minimal change was observed in the skin friction coefficient. The final mesh size for the ZPG simulation was approximately 295,000 elements. The results of the mesh refinement study are shown in Figures 4.8 and 4.9.[26] The blue arrow on the graph in

[26]Three meshes were evaluated as part of the mesh refinement study in the freestream direction:

Figure 4.9 represents the direction of plot shift as the mesh is refined. A similar mesh refinement study was performed in the wall normal direction. The mesh chosen for the study consisted of 3,072 freestream elements and 96 wall normal elements, which resulted in a maximum wall y^+ value of 0.2. Simulation time for this mesh was 1.6 hours using 4 processors on Aries. Finally, the results were exported to a boundary layer analysis code developed using MATLAB, where the CFD results were used to calculate boundary layer and entropy generation parameters.

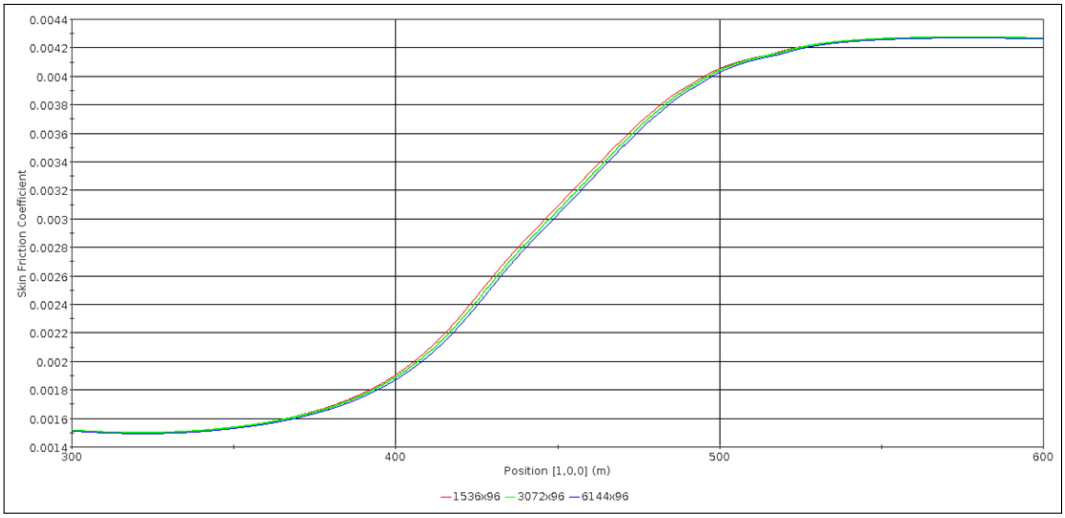

Figure 4.8: Streamwise mesh refinement (C_f *vs.* x)

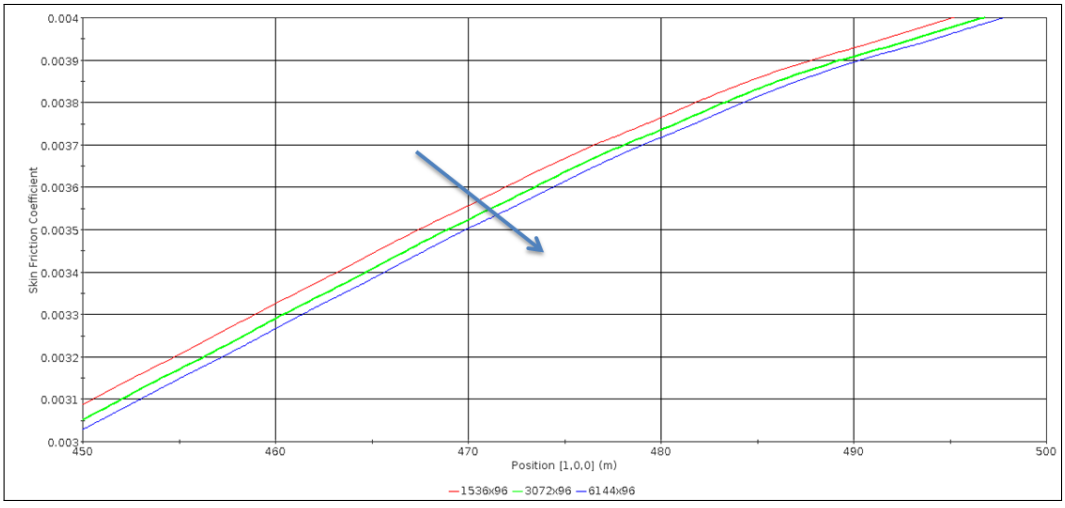

Figure 4.9: Streamwise mesh refinement–enlarged (C_f *vs.* x)

1536x96 (red plot), 3072x96 (green plot), and 6144x96 (blue plot).

4.4.2. Inlet-Plenum Designs

Using the commercial computer aided design (CAD) software package SOLIDWORKS, several geometric modifications to the original RCCS design (i.e., Design A4) were considered (cf. Figures 4.10 through 4.13). The primary differences between the designs is the relative location and shape of the inlet to the inlet-plenum and the location of the heated ducts relative to the top of the inlet-plenum. Of the four designs considered (i.e., B, C, D, and E), Design E was chosen to compare with the UW $\frac{1}{4}$–scale RCCS design. The decision to evaluate only Design E was primarily based on the significant amount of computational overhead and resources required for a CFD analysis of Designs B, C, and D; additionally, Design E appeared to have the most potential for developing a more uniform flow at the riser duct inlets, as compared to other designs. The designs considered are presented below.[27]

The A4 and E6 inlet plenum designs differ significantly. For example, the primary inlet flow enters at the bottom of the plenum for Design E6 as opposed to the front-side (Design A4). Additionally, the E6 riser ducts are centered on top of the inlet plenum, and are flush with the top. In contrast, the A4 riser ducts are offset from the plenum top, and they penetrate into the inlet-plenum approximately 4 inches. Using as-built dimensions provided by Muci (2014b), a computer aided design (CAD) solid model was created using SOLIDWORKS and imported into STAR-CCM+ (Systemes, 2015). Design A4 inlet-plenum is shown in Figure 4.14 and Design E6 inlet-plenum is shown in Figure 4.15.

As mentioned in Section 1, heat transfer from the reactor to the riser-ducts is primarily responsible for generating sufficient natural circulation air flow through the cooling system (cf. Figure 1.1). Therefore, in addition to the geometric design changes, three thermal designs, referred to as HTA, HTB, and HTC, were evaluated. The following description refers to Figures 4.16, 4.17, and 4.18.

Thermal design HTA represents the experimental configuration at UW where a bank of heaters simulates the heat produced by the reactor. The values for the heat

[27]Design D is not shown since the only difference between it and Design E is that the Design D riser-ducts penetrate approximately 4 inches into the inlet-plenum.

flux are based on the power required to approximate the experimentally obtained centerline temperature profile for Duct 4. The details on how the heat flux values were obtained are documented in pages 192 and 193 of the RCCS project report, which can be found in Appendix B. Thermal design HTB represents the rotation of Duct 4 clockwise by 90 degrees, while keeping the power reaching the duct the same. Thermal design HTC represents a situation where Duct 4 is exposed to a constant heat flux on all sides, while keeping the power reaching the duct the same.

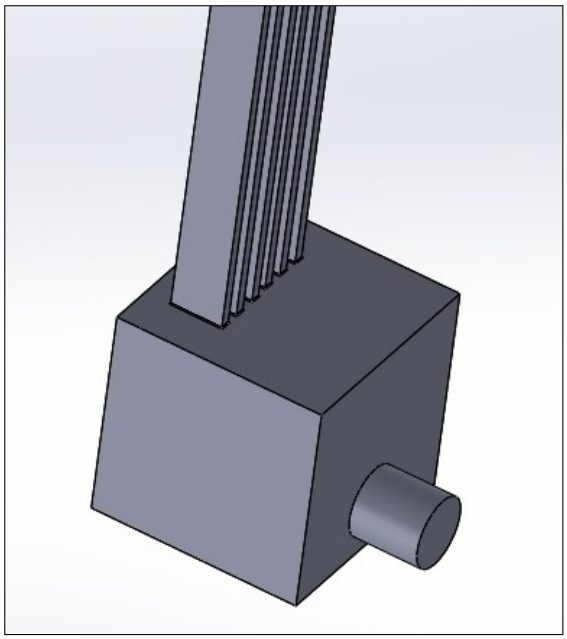

Figure 4.10: Design A

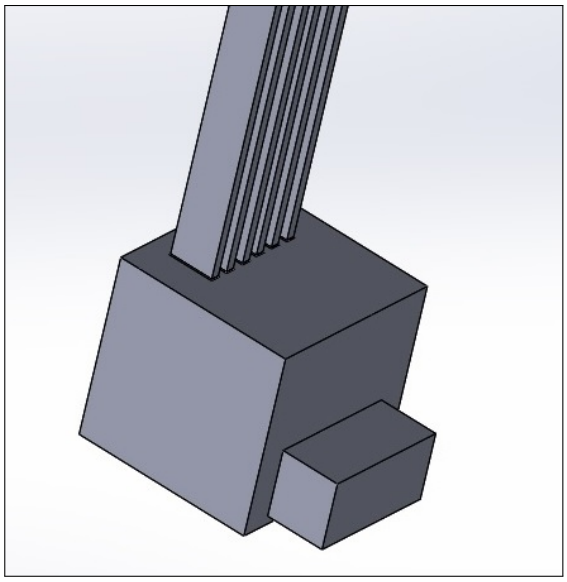

Figure 4.11: Design B

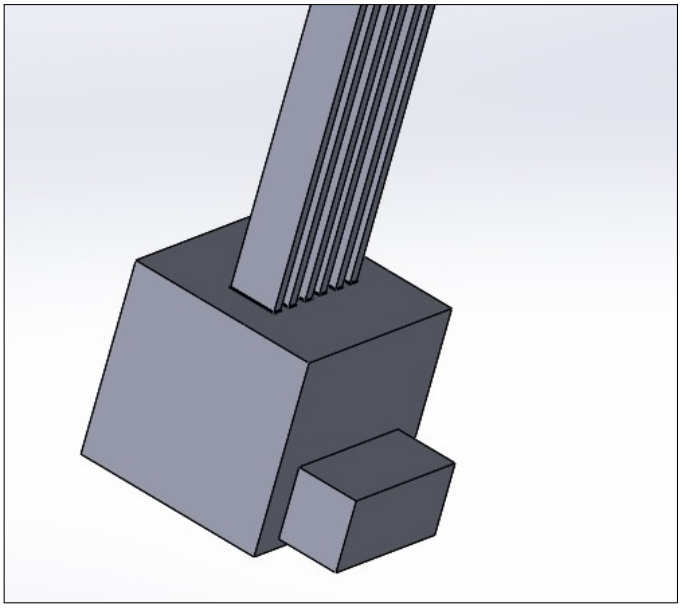

Figure 4.12: Design C

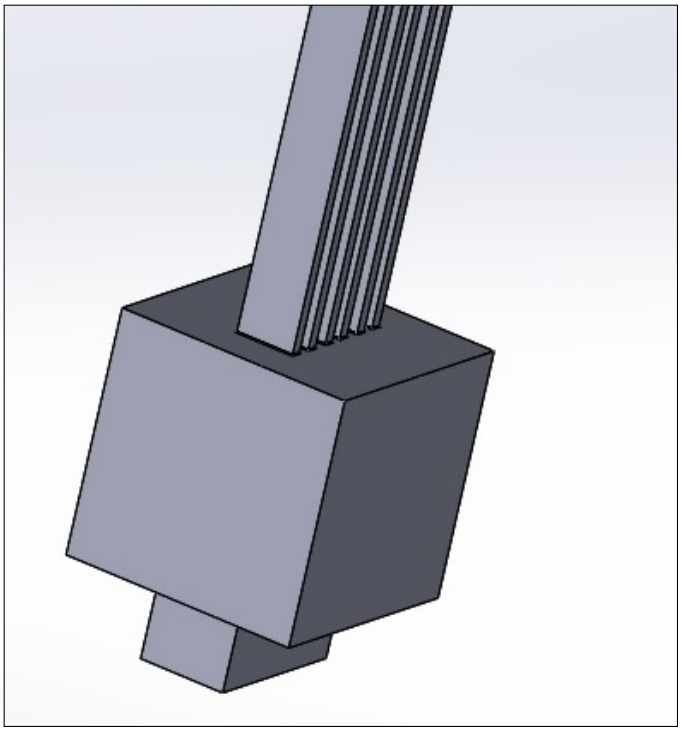

Figure 4.13: Design E

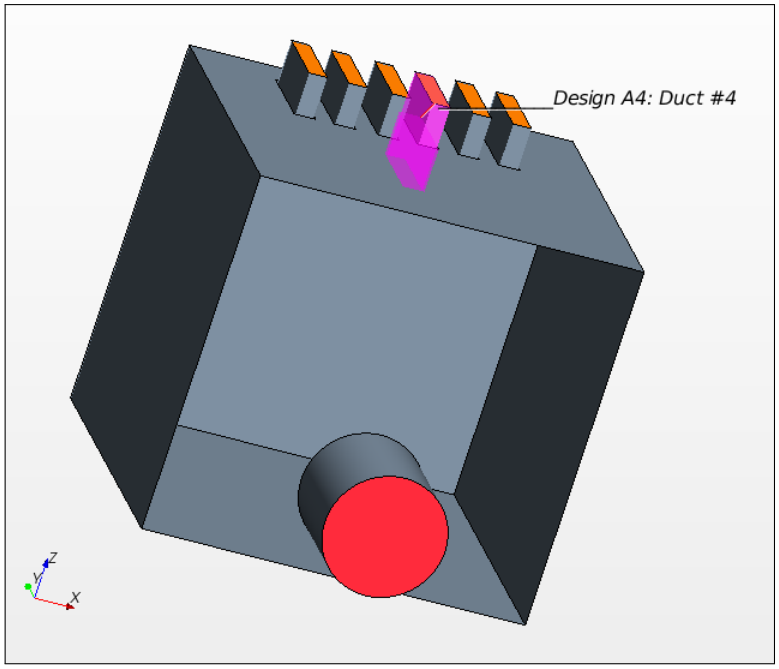

Figure 4.14: Design A4 inlet-plenum

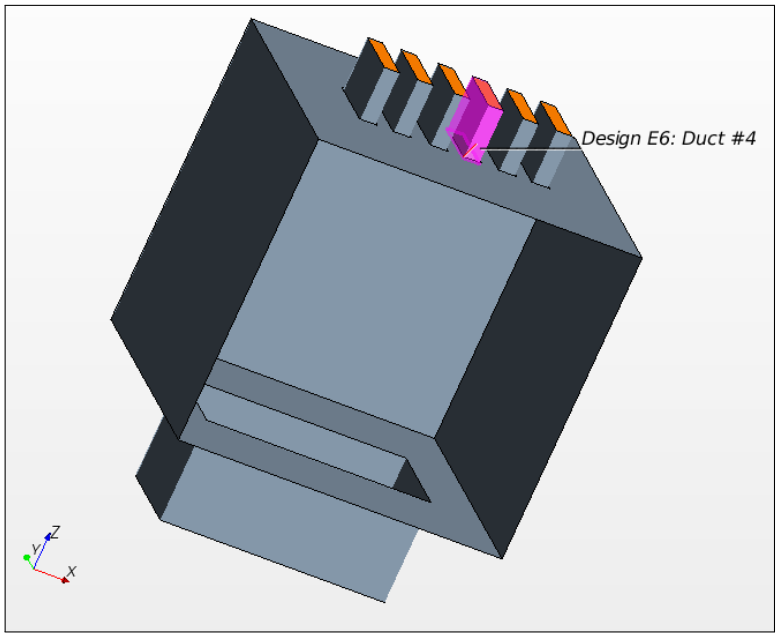

Figure 4.15: Design E6 inlet-plenum

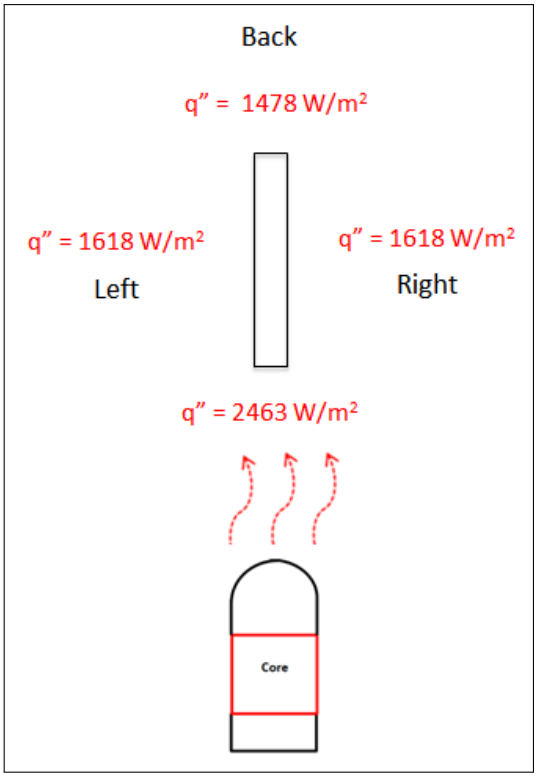

Figure 4.16: Thermal design HTA

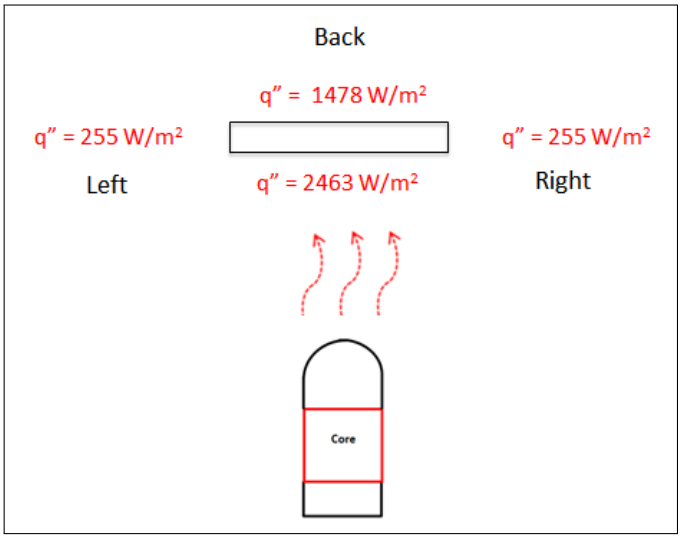

Figure 4.17: Thermal design HTB

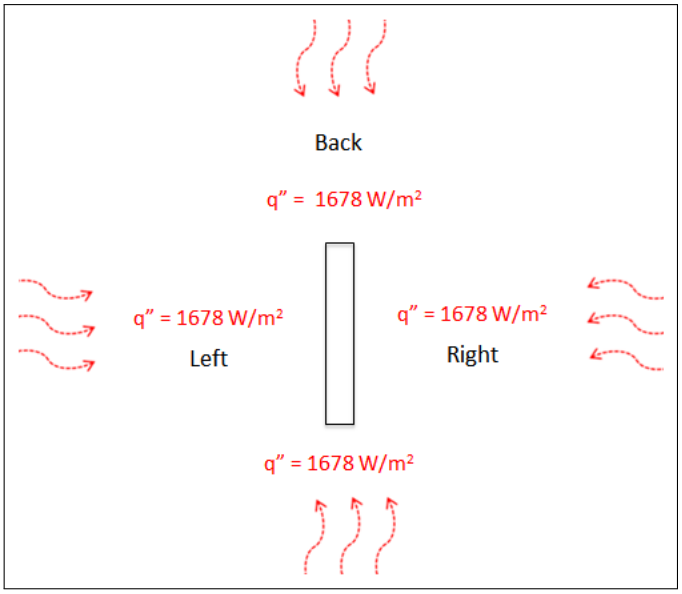

Figure 4.18: Thermal design HTC

4.4.3. Inlet-Plenum

Based on the conclusions of the RCCS Project Report (Appendix B), which identified the need to model the RCCS individual components in order to reduce computational overhead, a CFD analysis of the inlet-plenum was performed. This analysis was necessary in order to obtain inlet boundary conditions for the follow-on Duct 4 CFD and entropy generation rate analysis, since limited experimental data was available to establish boundary conditions at the heated duct inlets (Muci, 2014b).

Using as-built dimensions, a computer aided design (CAD) solid model of the inlet-plenum was created using SOLIDWORKS, imported into STAR-CCM+, where a trimmer mesh was generated and a CFD simulation was conducted. The CFD solid models of the inlet-plenums are shown in Figures 4.14 and 4.15. The trimmer meshing model was chosen for this analysis since the MATLAB boundary analysis code was written for a structured mesh. Simulations were performed, and a mesh refinement study was conducted.

The following simulation settings and models were used for the inlet-plenum simulation: 3-D, ideal gas, temperature dependent air properties, realizable two-layer (Norris-Reynolds) K-Epsilon turbulence model with the two-layer all y^+ wall treatment (CD-adapco, 2015a). Although a coupled solver is available, the steady-state

segregated solver using a second order upwind convection scheme was chosen. The segregated solver was chosen because a slight improvement in residual convergence behavior was observed using the segregated solver.

All inlet-plenum walls were assigned adiabatic boundary conditions, and inlet boundary conditions were specified based on forced circulation experimental data for temperature and velocity (Muci, 2014b). Inlet and outlet experimental turbulence data (e.g., turbulent kinetic energy, turbulence intensity) was not available, so turbulence information was estimated at the inflow and outflow boundaries (Hamman et al., 2015). The following boundary conditions were applied at the inlet: temperature 298 K; velocity 4.54 m/s; turbulence intensity 2.5%; turbulence length scale 0.03048 m. A pressure outlet boundary condition of 0 Pascal was set at the inlet-plenum outlets to the heated ducts. Fifty-six processor on Big-STEM were used to run the simulation.

Typically, spatial (i.e., grid) convergence has been achieved after running the simulation on successively finer grids until a negligible change in the important dependent variables are observed. In this study, three variables, presented in Table 5.1, were monitored during the mesh refinement study. Although adequate spatial convergence was obtained with Mesh 2X, the simulation associated with Mesh 4X was chosen for analysis. The final mesh used for this study consisted of 22 near-wall boundary layers (i.e., prism layers) and mesh size of 9.7 million elements; mesh metrics (e.g., volume change and face validity) met the guidance specified in the user manual. Table 4.1 presents the results of the mesh refinement study. Figures 4.19 and 4.20 show the mesh used for this study.

The CFD results predict a complex flow path within the inlet-plenum, which is best described using Figures 4.21 and 4.22. Air enters the inlet-plenum at 4.54 m/s ($Re_D = 89{,}196$), impacts the back wall (similar to a water jet impacting a stationary flat plate), spreading along the back wall to the side, bottom, and top walls; and the flow exits through the Duct 4 outlet, one of six outlets, at an average velocity of 5.0 m/s ($Re_D = 24{,}695$). The nonuniformity in velocity exiting the inlet-plenum makes it

difficult to experimentally measure velocity at the riser duct inlets (cf. Figure 4.32).

Table 4.1: Inlet-Plenum spatial convergence results (Design A4)

Simulation	Number of Elements	Avg. Velocity (m/s)	Avg. Tke (J/kg)	Avg. Tdr (m^2/s^3)	Run Time (hrs)
Mesh 1X	2,327,564	5.12	0.92	51.5	2.9
Mesh 2X	4,626,241	5.10	0.86	49.6	6.1
Mesh 4X	9,742,233	5.04	0.84	48.8	13.8

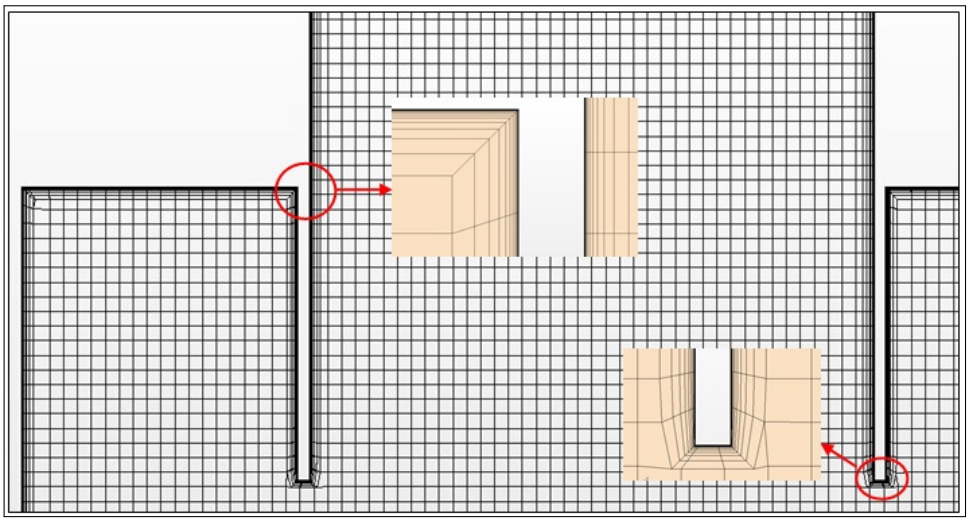

Figure 4.19: Inlet-plenum Duct 4 vertical plane (Mesh 4X)

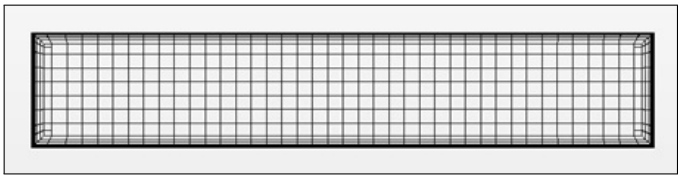

Figure 4.20: Inlet-plenum outlet to Duct 4 (Mesh 4X)

One of the most challenging aspects of the inlet-plenum CFD analysis was obtaining good iterative convergence. For the inlet-plenum simulation, steady-state conditions and convergence criteria were based on the behavior of residuals and riser duct outlet average dependent variables: velocity, turbulent kinetic energy, and turbulent dissipation rate. Although a significant amount of numerical experimentation

was performed prior to and during this study, solution residual convergence continues to be problematic (cf. Appendix B).

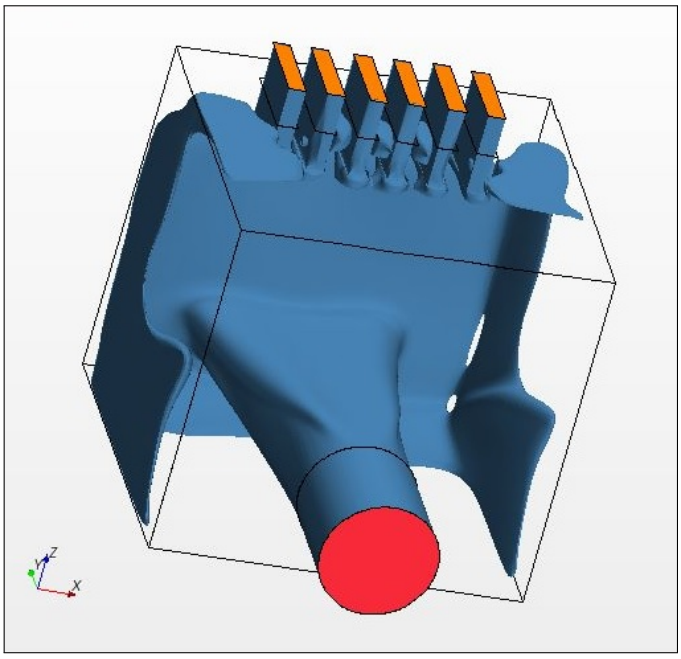

Figure 4.21: Duct 4 isovelocity 2.5 m/s plot (Mesh 4X)

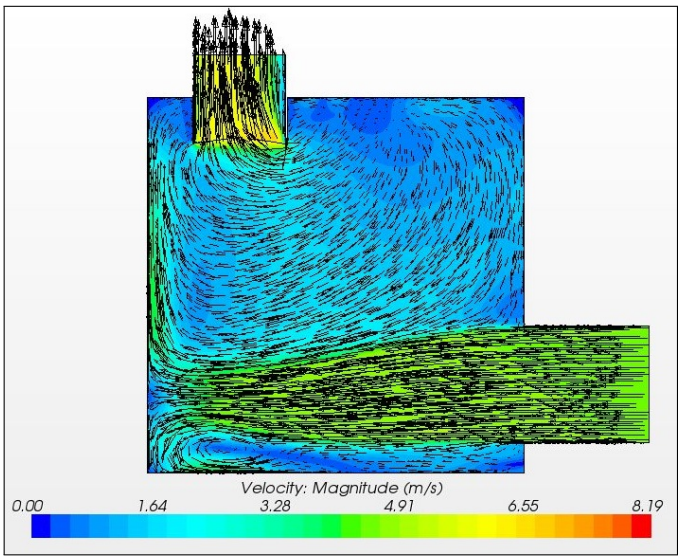

Figure 4.22: Duct 4 vertical plane vector-velocity plot (Mesh 4X)

Figures 4.23 and 4.24 show the behavior of the average turbulent dissipation rate for the outlet boundary to Duct 4. The steady segregated solver was run for 2500 iterations expecting that the outlet velocity, Tdr, and Tke values would reach a

constant value indicating that steady-state conditions were reached. Upon reaching 2500 iterations, both velocity and Tke reached steady-state; yet, Tdr did not reach steady-state. Therefore, the transient segregated solver was ran at a time-step of 0.001 seconds, for 0.033 seconds, and 30 inner iterations until Tdr eventually reached a constant value indicating steady-state conditions. In Figure 4.23, it is not clear why the Tdr residual only drops approximately two decades; but it is most likely due to the complex flow patterns that develop within the inlet-plenum.[28] Given the behavior of the residuals, especially the Tdr residual, the importance of collecting experimental data to compare with CFD results should be emphasized. Unfortunately, experimental data collection faced challenges as well.

There was a limited number of velocity measurements in the scaled experiment available for comparison with CFD results, primarily due to the operating limitations of the velocity transducers. For example, air velocity transducers were placed in the middle of the flow cross section inside the inlet of the six ducts located inside the inlet-plenum. The transducers were placed 4.44 cm (1.75 in.) downstream from the bottom of the riser ducts. The velocity transducer technical manual recommends that the probes be placed 7.5 diameters downstream of anything that can cause flow turbulence, which corresponds to 57.2 cm (22.5 in.) (TSI, 2013). In addition, the maximum operating temperature range of the transducer is 93 °C (199 °F); therefore the transducers must be placed close to the riser duct inlets to prevent exceeding the maximum operating temperature of the transducer.[29] Consequently, the velocity transducer data collected at the six riser ducts was not used for this CFD study. The transducers were used mostly for diagnostics during UW experiments to see if a riser was behaving differently from the other five (Muci, 2014b). Figure 4.25 shows the inlet-plenum and velocity probe at the University of Wisconsin - Madison experimental facility. And, Figure 4.26 shows the Duct 4 vertical plane CFD results,

[28] A study by Bovo and Davidson (2013) related to numerical modeling of impinging jets provides some insight into the problems associated with residual convergence. In fact, the authors state that impinging jets are difficult to model in CFD.

[29] Duct front surface temperatures, collected during the UW experiment, were on the order of 300 °C (572 °F) (Muci, 2014b).

including the area of high turbulent kinetic energy at the inlet to Duct 4.

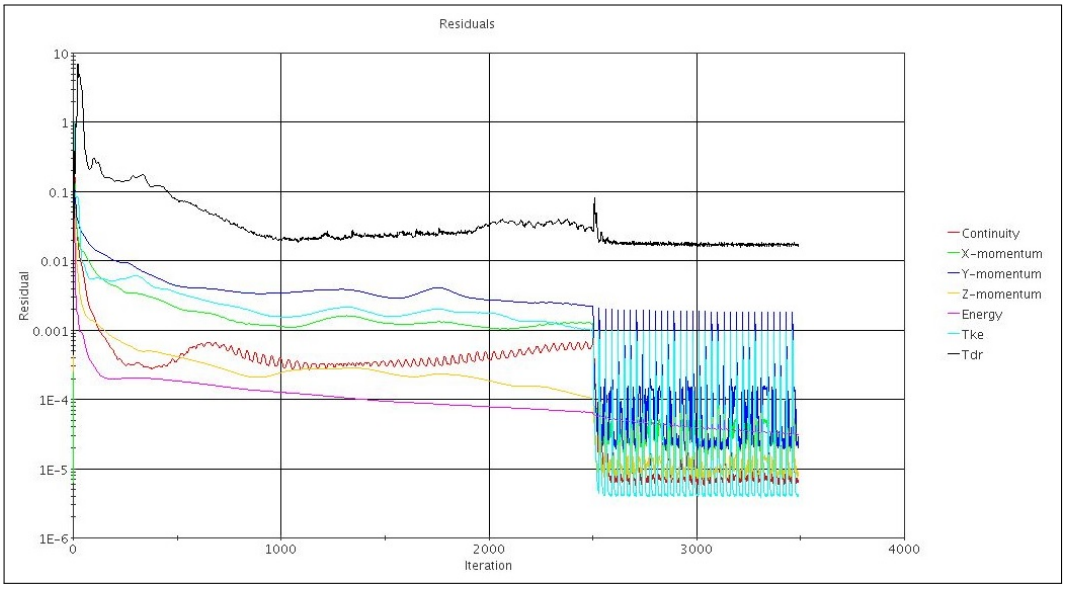

Figure 4.23: Inlet-plenum residuals vs. iterations (Mesh 4X)

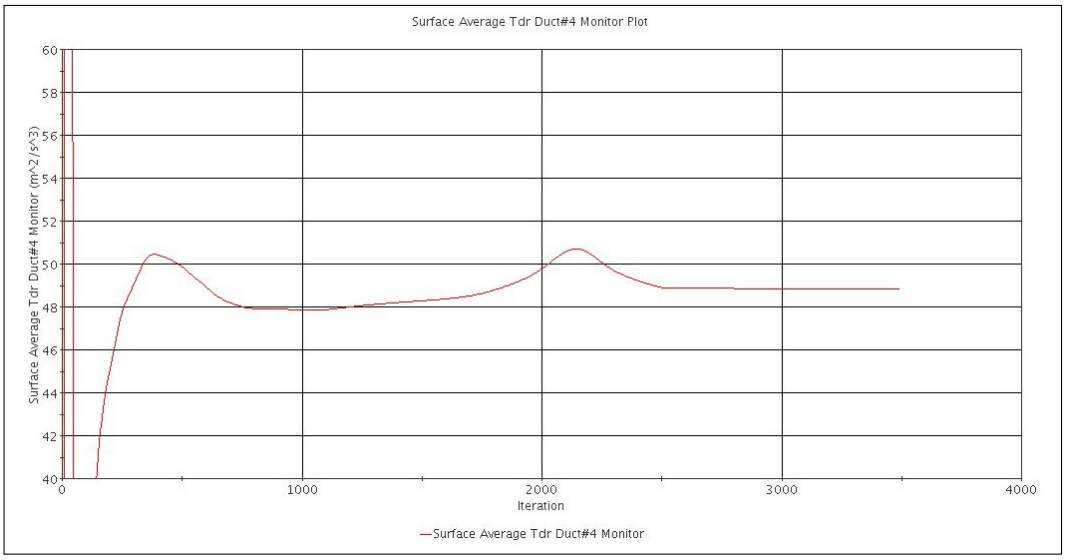

Figure 4.24: Inlet-plenum residuals vs. Tdr (Mesh 4X)

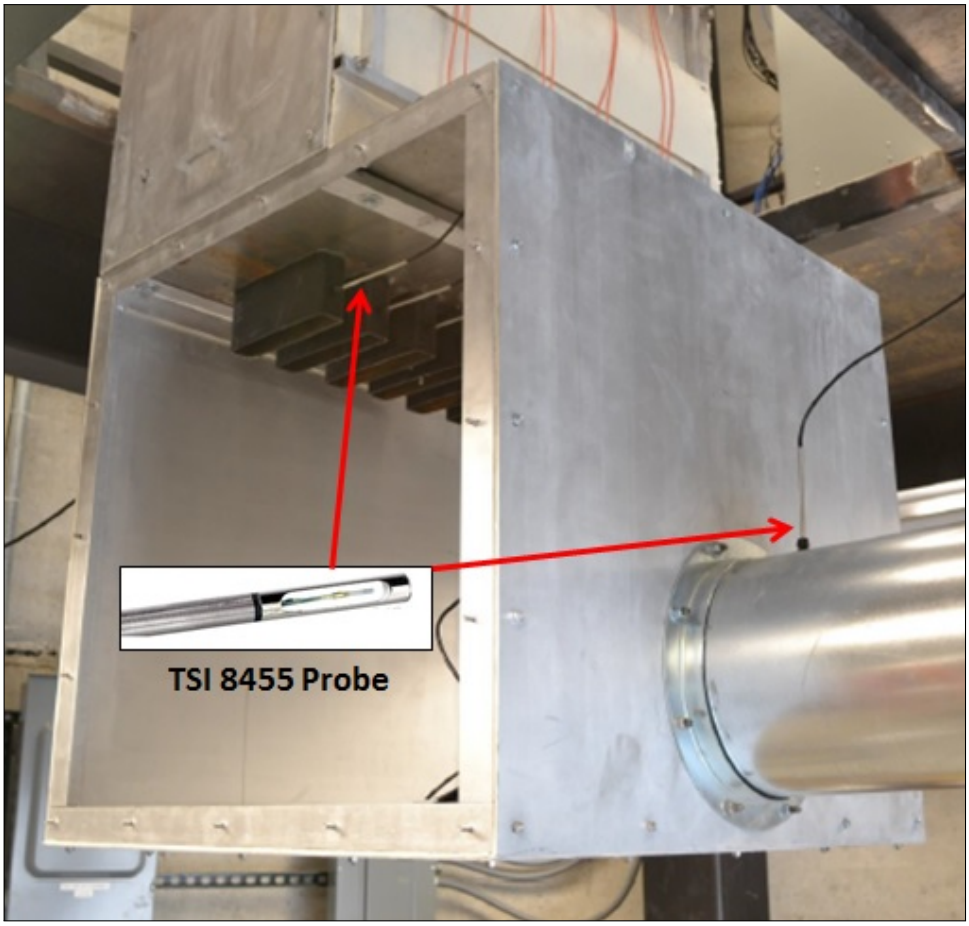

Figure 4.25: Inlet-plenum (University of Wisconsin)

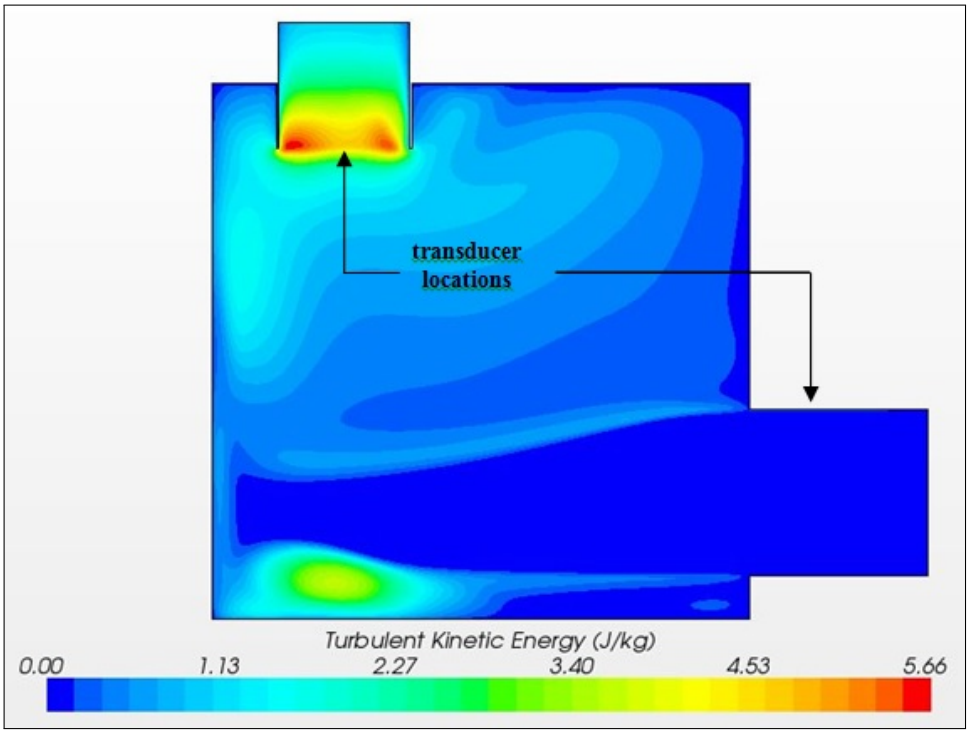

Figure 4.26: Duct 4 vertical plane contour plot (Mesh 4X)

4.4.4. Duct 4

An effort was made to obtain a structured mesh for the Duct 4 simulations using the STAR-CCM+ trimmed cell mesher (cf. Figure 4.29). In this figure, two areas are identified: a structured mesh area and an unstructured mesh area. As can be seen in the figure, difficulties were encountered in obtaining a fully structured mesh. Since the MATLAB code written for this study requires a structured mesh (cf. Figure 4.30), the trimmed cell mesher was abandoned in favor of using the Trelis meshing software.

Using Trelis, a clustered mesh in the wall normal direction was developed using a mesh bias scheme factor (wall normal expansion ratio) of 1.057. This value of the bias scheme factor was chosen in order to obtain wall y^+ values of approximately one. The Duct 4 structured mesh was imported into STAR-CCM+ where simulations were performed in order to develop velocity and temperature fields. The final mesh (i.e., one 40 inch section) used for this study consisted of 1.28 million elements; mesh metrics (e.g., volume change and face validity) met the guidance specified in the STAR-CCM+ user manual.

Due to computational resource constraints, which are discussed in Appendix B, only 80 inches of Duct 4 were modeled; additionally, two models each 40 inches in height were developed. The first 40 inches (1.016 m) of Duct 4 will be referred to as Duct 4 first section (0"–40"), and the remaining 40 inches (1.016 m) will be referred to as Duct 4 second section (40"–80").

A mesh refinement study of Duct 4 study was not performed due to long simulation run times (e.g., five days per simulation) using the available computational resources; although, a very fine mesh was used for the Duct 4 CFD analyses. Nevertheless, based on the mean velocity profiles in Figures 4.27 and 4.28, which show that the viscous sublayer was resolved (cf. Appendix C), and the maximum values of wall y^+, which ranged from 0.4 to 1.5, sufficient mesh elements were used to compute boundary layer parameters for this design comparison study. The mesh used for this study is shown in Figure 4.30.

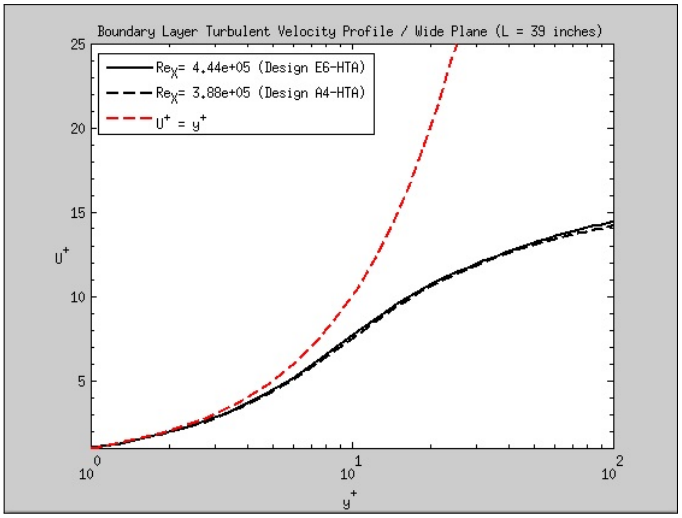

Figure 4.27: Mean velocity profiles (wide plane, 1.9 m)

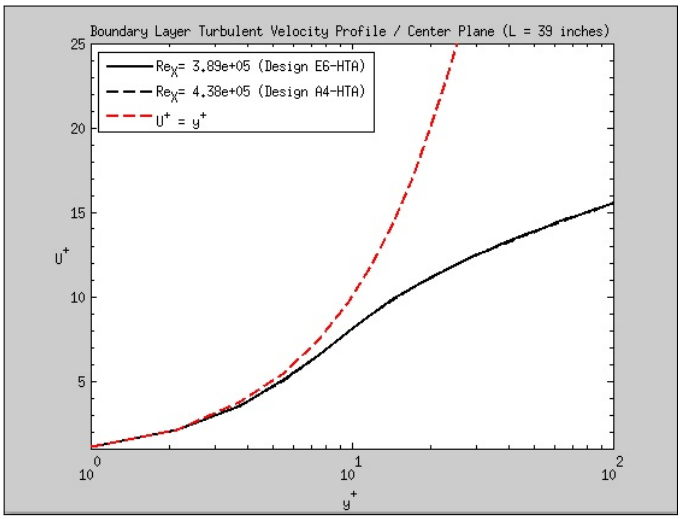

Figure 4.28: Mean velocity profiles (center plane, 1.9 m)

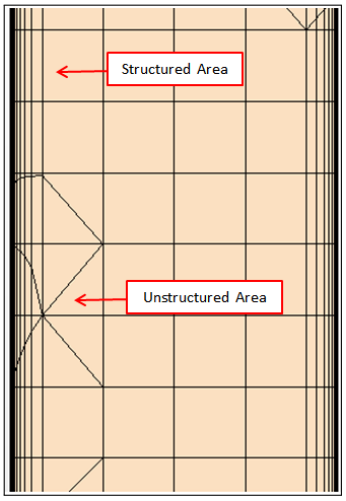

Figure 4.29: Unstructured mesh

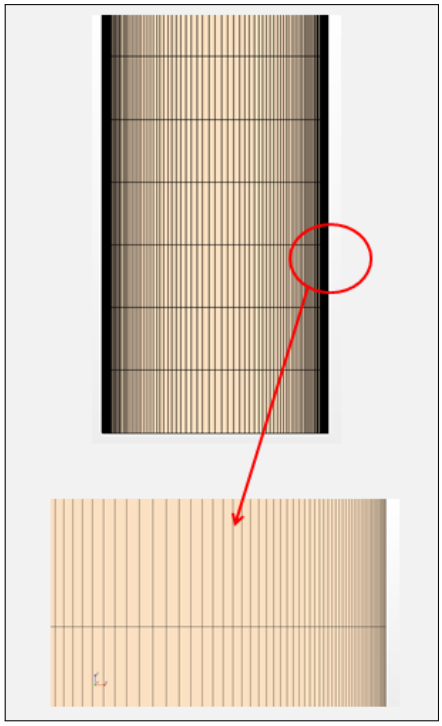

Figure 4.30: Duct 4 structured mesh

The following simulation settings and models were used for the Duct 4 simulation: 3D, second order upwind discretization, steady, coupled solver, ideal gas, temperature dependent air properties, K-Epsilon ($k-\epsilon$) Low-Re turbulence model with the low y^+ wall treatment. According to the STAR-CCM+ User Guide (Version 8.04), The Low-Re turbulence model by Lien et al. (1996) "... is dubbed the 'Standard Low-Reynolds Number K-Epsilon Model' because it has identical coefficients to the Standard K-Epsilon model, but provides more damping functions. These functions let it be applied in the viscous-affected regions near walls." Since turbulence modeling was not the focus of this work, readers are encouraged to consult the literature for additional information (CD-adapco, 2015a; Jones and Launder, 1972; Lien et al., 1996). Noteworthy is that the limitations and usage of RANS turbulence models is acknowledged and known by the author.

The inlet boundary conditions used for the Duct 4 simulation were obtained from an independent analysis of Design A4 inlet–plenum and Design E6 inlet–plenum (cf. Section 4.4.3). The location of the data plane (outlined in pink), where boundary conditions were extracted, is shown in Figure 4.31.

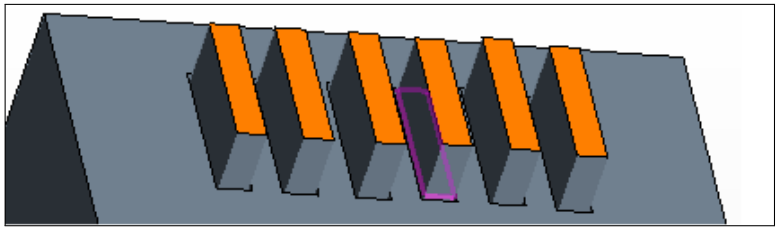

Figure 4.31: Inlet-plenum data plane (pink outline)

One of the unique features of this research was the modeling, simulation, and analysis of a nonuniform 3-D velocity distribution throughout Duct 4. This non-uniformity created challenges associated with analyzing boundary layer information during the post-processing phase of this study, primarily the result of the determining the location of the freestream velocity and temperature. Figure 4.32 depicts the nonuniform velocity contours near the inlet to Duct 4; for comparison purposes, a uniform velocity contour is shown as well.

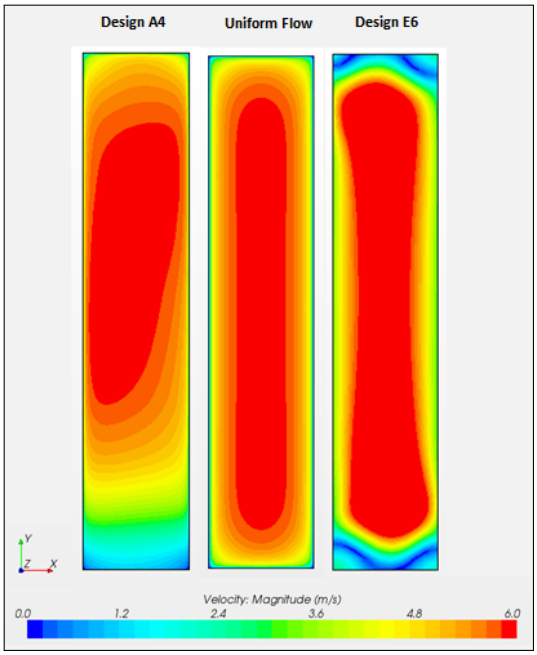

Figure 4.32: Duct 4 velocity contours

In preparation for the analysis phase of this study, Duct 4 was divided into 4 planes: top plane, center plane, bottom plane, and a wide plane. The planes are

abbreviated T, C, B, and W respectively (cf. Figures 4.33, 4.34, 4.35). Typically referred to as a 2.5D ('two-and-a-half-dimensional') analysis, this analysis configuration was used for the following reasons:

1. to reduce computational overhead given the available resources,

2. to approximate a 3D simulation,

3. and to utilize a boundary layer analysis process consistent with that used in Appendix A.

Classic boundary layer equations, such as th 99% velocity boundary layer thickness (Equation 4.1), momentum thickness (Equation 4.2), 99% thermal boundary layer thickness (Equation 4.3), and enthalpy thickness (Equation 4.4) are restricted to 2D (Cebeci, 2002; Langtry, 2006; White, 1979).[30] Therefore, important physics such as end-wall boundary layers, which are present in 3D ducts, cannot be analyzed.

$$u(y) = 0.99U_\infty \tag{4.1}$$

$$\theta = \int_0^\infty \frac{\rho u}{\rho_\infty U_\infty}\Big(1 - \frac{u}{U_\infty}\Big)dy \tag{4.2}$$

$$(T - T_\infty) = 0.99(T_w - T_\infty) \tag{4.3}$$

$$\theta_h = \int_0^\infty \frac{\rho u}{\rho_\infty U_\infty}\Big(\frac{h - h_\infty}{h_w - h_\infty}\Big)dy \tag{4.4}$$

The 3D Star-CCM+ Duct 4 results were exported to a boundary layer analysis code developed using MATLAB, where heat transfer, fluid flow, entropy generation rate parameters were computed using the '2-D Direct Method Model' discussed in

[30] In Equation 4.4, h can be replaced by c_pT assuming that specific heat capacity, c_p, is constant (Cebeci, 2002).

Section 3.2. These results were compared with the 'Lumped Parameter Model' (Section 3.1) results.

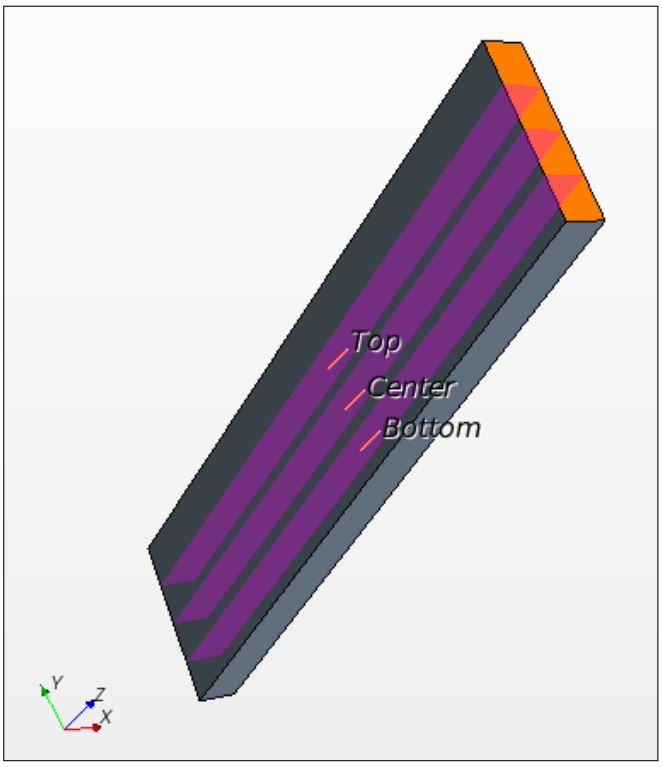

Figure 4.33: Duct 4 analysis planes (T, C, B)

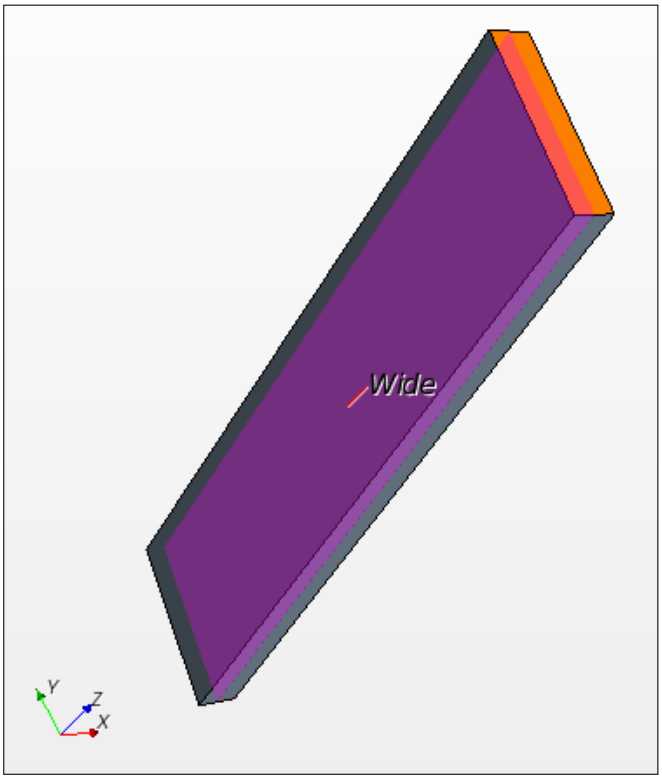

Figure 4.34: Duct 4 analysis plane (W)

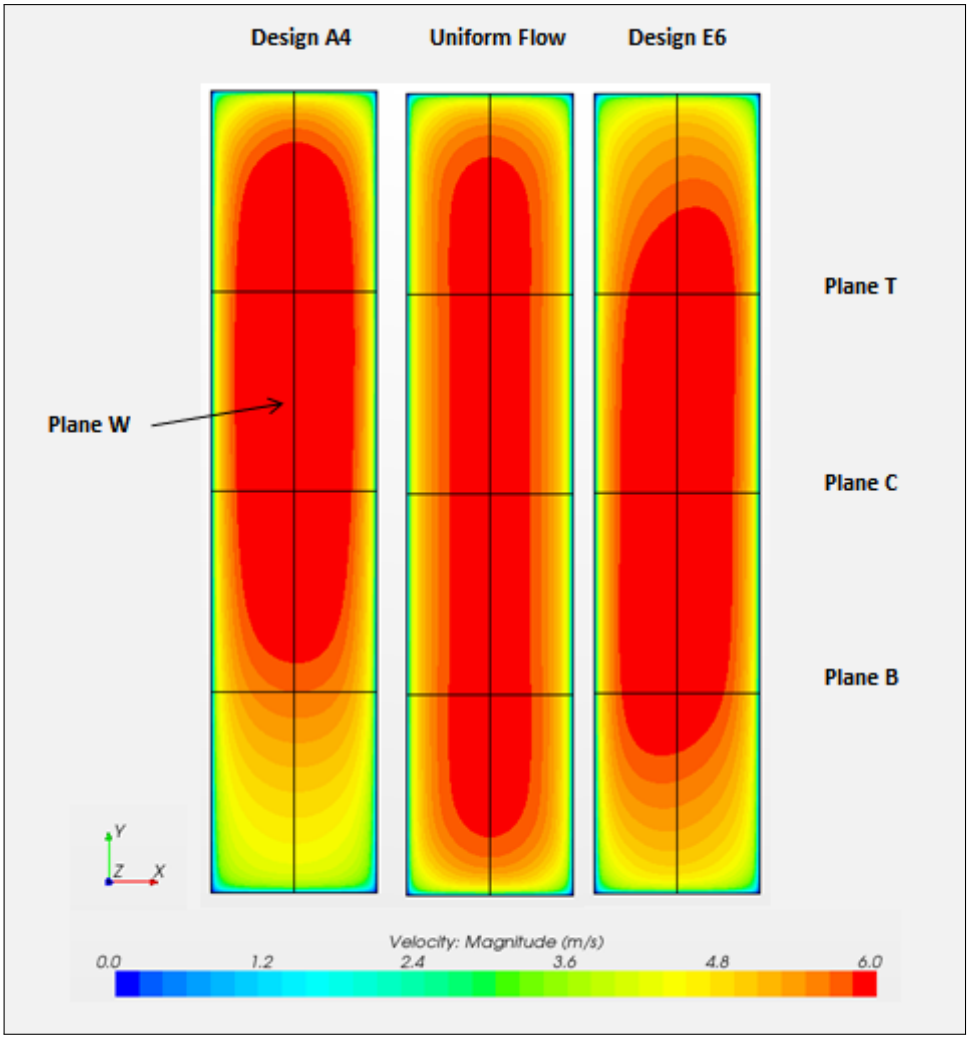

Figure 4.35: Analysis planes

Boundary layer development in duct flow differs from that of a flat plate (cf. Appendix A) for several reasons, including the presence of end-wall boundary layers. On each side of the duct, individual boundary layers develop; and eventually they coalesce. Consider the channel flow (e.g., duct flow) shown in Figure 4.36 where 'uniform' steady viscous flow enters the duct from, for example, the inlet-plenum. Wall friction causes the boundary layers, initially laminar, to develop and transition to turbulence further downstream. Since the flow is constrained by the duct walls, the boundary layers eventually coalesce. The location where the boundary layers coalesce is referred to as the entrance length (L_e). Yet in order to determine the location of the boundary layer, prior to coalescence, freestream parameters such as velocity and temperature must be calculated.

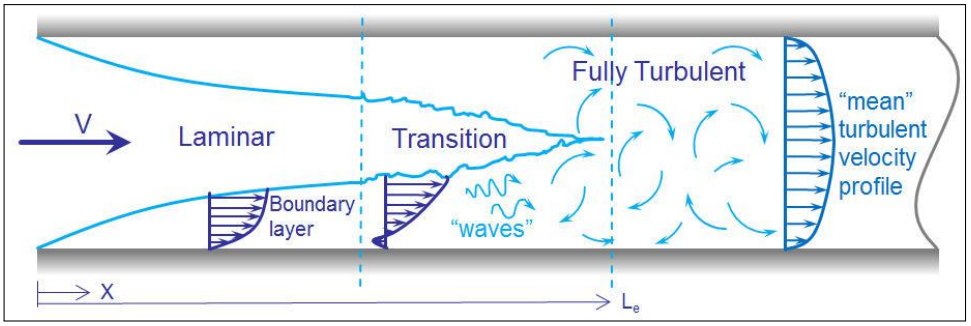

Figure 4.36: Boundary layer development (Simon, 2015)

Using the approach by Nolan (2013) to determine freestream conditions for the boundary layer analyses of Appendix A, three techniques were evaluated for computing freestream parameters (e.g., velocity, temperature).[31] Technique 1 (cf. Figure 4.37) is based on computing freestream velocity and temperature based on a predetermined values of freestream velocity gradient (e.g.,$-2.8\ \frac{1}{s} < dU/dy < +2.8\ \frac{1}{s}$) and freestream temperature gradient (e.g.,$-60\ \frac{K}{m} < dT/dy < +60\ \frac{K}{m}$). Technique 2 (cf. Figure 4.38) is based on establishing freestream velocity where the maximum velocity and minimum temperature exist. Technique 3 (cf. Figure 4.39) is based on establishing freestream velocity at the location where freestream temperature is a minimum. Technique 3 implicitly assumes that the thickness of the thermal and viscous boundary layer are the same.

The technique used to determine freestream parameters and their locations is relatively straightforward. Using Figure 4.39 as an example, the areas in red represent locations on the data plane where freestream temperature meets the temperature gradient requirement of $-60\ \frac{K}{m} < dT/dy < +60\ \frac{K}{m}$. The temperatures at each one of those locations are averaged, resulting in an 'averaged' local freestream temperature. The freestream velocity is assumed to occur at the same wall normal freestream temperature locations; and the velocity is averaged to obtain the corresponding freestream velocity.

[31] The range of values for the gradients of dU/dy and dT/dy, applicable only to this study, are based on numerical experimentation. For example, in order to obtain a realistic freestream velocity and/or temperature profile, gradient values are modified until at least one value of temperature or velocity in the wall normal direction is obtained. The author recognizes the uncertainty associated with this approach; unfortunately, there is a lack of published literature related to modeling and simulation of boundary layer development for nonuniform flows.

It is self-evident that Technique 3 would not be a good choice for this study, since the viscous boundary layer profile, due to its nonuniformity, does not approximate the thermal boundary layer profile. Although Technique 2 could have been used, Technique 1 was chosen as the method to compute freestream flow parameters (e.g., velocity, temperature), primarily to be consistent with the technique suggested by Nolan (2013) and described in the two preceding paragraphs.

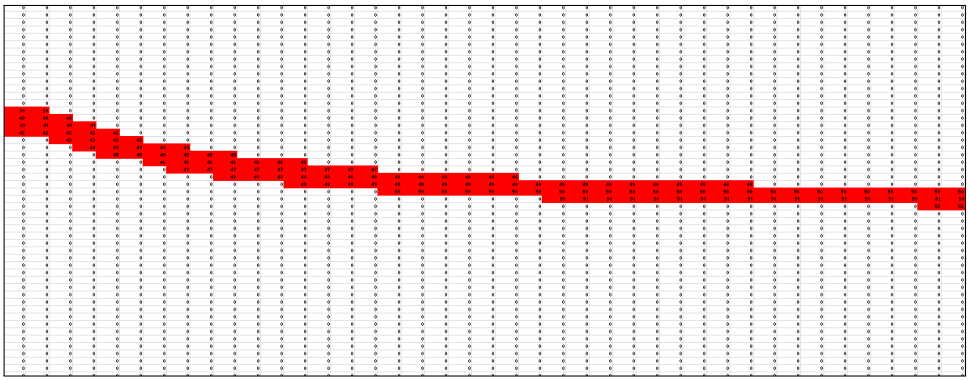

Figure 4.37: Freestream gradient map (Technique 1)

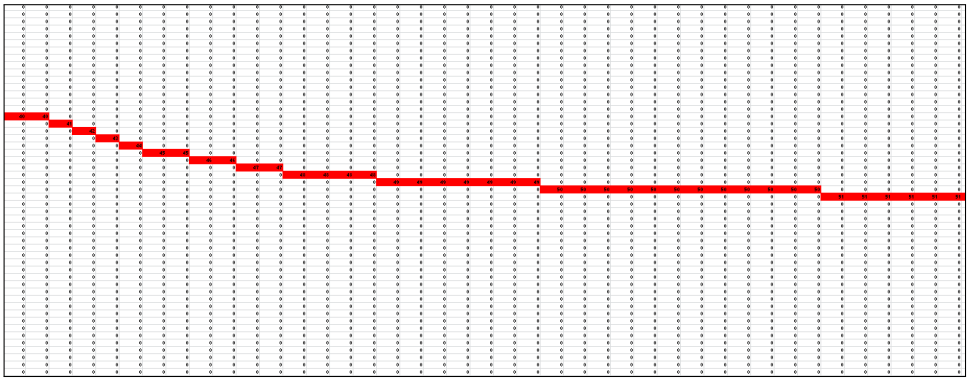

Figure 4.38: Freestream gradient map (Technique 2)

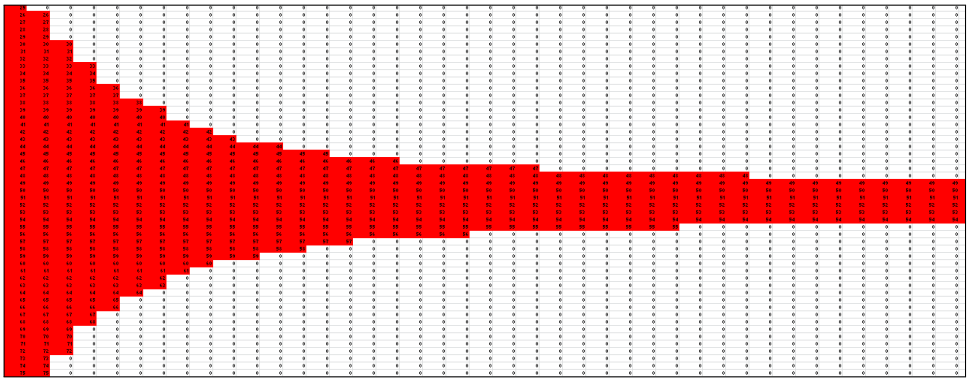

Figure 4.39: Freestream gradient map (Technique 3)

Chapter 5: Results

5.1. Traditional HTFF Analysis

Using traditional HTFF analysis techniques such as comparing experimental flow parameters (e.g, temperature, mass flow) and local flow parameters (e.g, shear stress and heat transfer coefficient), Design A4(HTA) was compared with the designs listed in Table 5.1. All designs were constrained to a constant inlet-plenum mass flow rate of 0.392 kg/s and a constant heat transfer rate of 16.3 kW (Muci, 2014a).

Tables 5.1 and 5.2 present typical CFD average flow parameters for the two sections of Duct 4.[32] Note that the flow parameters do not vary significantly between designs making it difficult to deduce the best design. Therefore, local flow parameters such as wall shear stress and convective heat transfer coefficient were analyzed. Analysis of the local flow parameters revealed that the air flowing in the first section (0"–40") experienced entrance effects (e.g., varying wall shear stress and heat transfer coefficient). Yet, as the air entered the second section (40"–80"), it had transitioned to fully turbulent flow as confirmed by the wall shear stress and heat transfer coefficient reaching constant values. Figures 5.1 through 5.8 illustrate the entrance effects as the fluid transitioned from laminar to turbulent flow.

Table 5.1: Flow parameters (0"–40")

Design	ΔT(K)	ΔP(Pa)	$\dot{m}$(kg/s)	Power(W)
A4(HTA)	19.9	9.2	$6.1x10^{-2}$	919
E6(HTA)	18.2	6.4	$6.2x10^{-2}$	919
E6(HTB)	17.6	6.4	$6.2x10^{-2}$	919
E6(HTC)	18.0	6.4	$6.2x10^{-2}$	919

Table 5.2: Flow parameters (40"–80")

Design	ΔT(K)	ΔP(Pa)	$\dot{m}$(kg/s)	Power(W)
A4(HTA)	17.1	7.7	$6.1x10^{-2}$	919
E6(HTA)	16.9	8.1	$6.2x10^{-2}$	919
E6(HTB)	16.2	8.1	$6.2x10^{-2}$	919
E6(HTC)	16.7	8.1	$6.2x10^{-2}$	919

[32]The results presented in Tables 5.1 and 5.2 are flow parameters calculated using an 'area weighted average' at an applied power of 919 W for a 3D simulation characterized by entrance effects and nonuniform flow and heat transfer; therefore, use of the 1D equation $\dot{Q} = \dot{m}c_p\Delta T$ with 'area weighted average' parameters as input will not produce a value of 919 W (Mann, 2013).

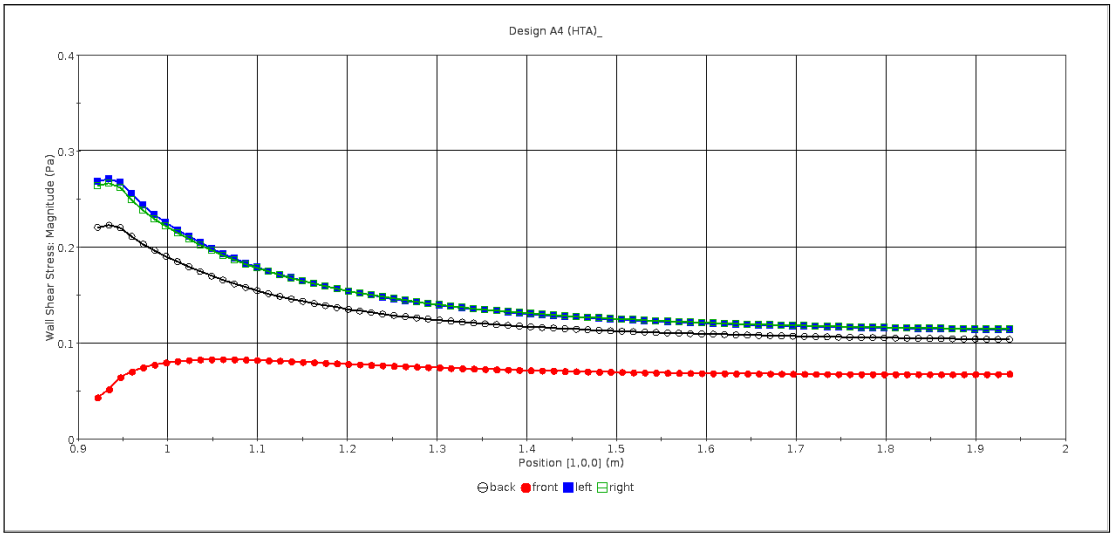

Figure 5.1: Wall shear stress vs. freestream direction - A4(HTA)

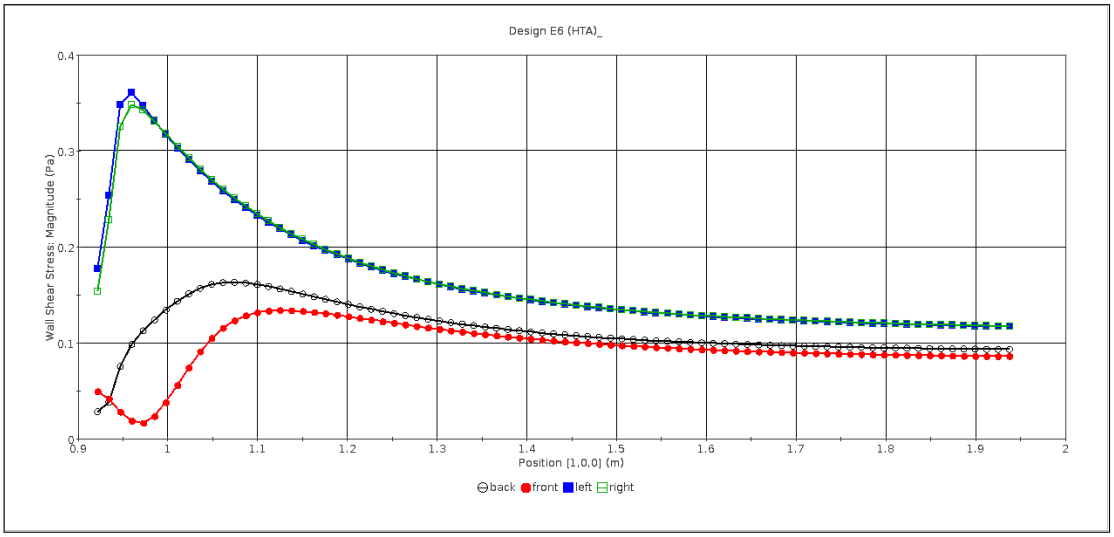

Figure 5.2: Wall shear stress vs. freestream direction - E6(HTA)

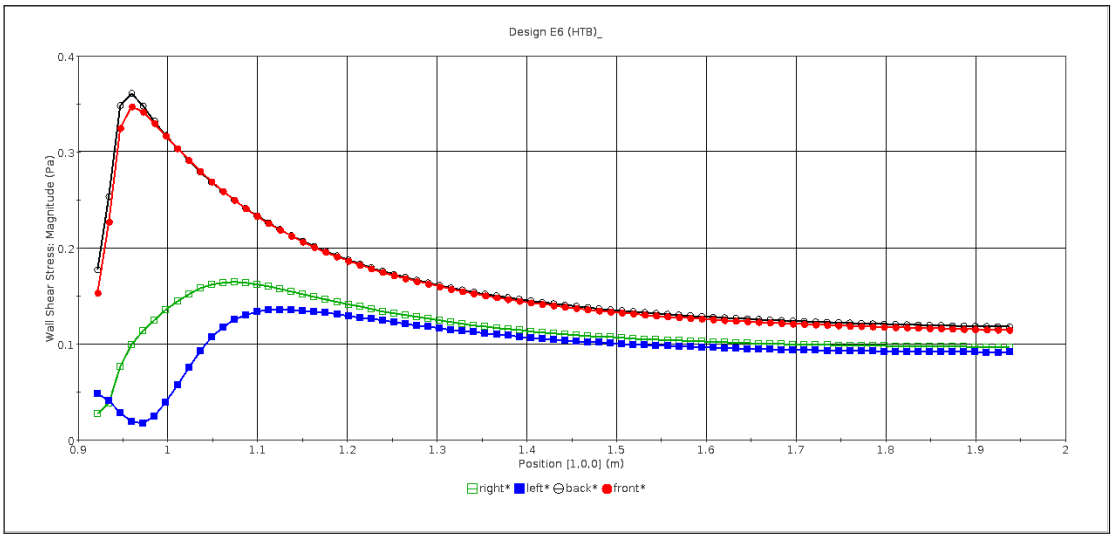

Figure 5.3: Wall shear stress vs. freestream direction - E6(HTB)

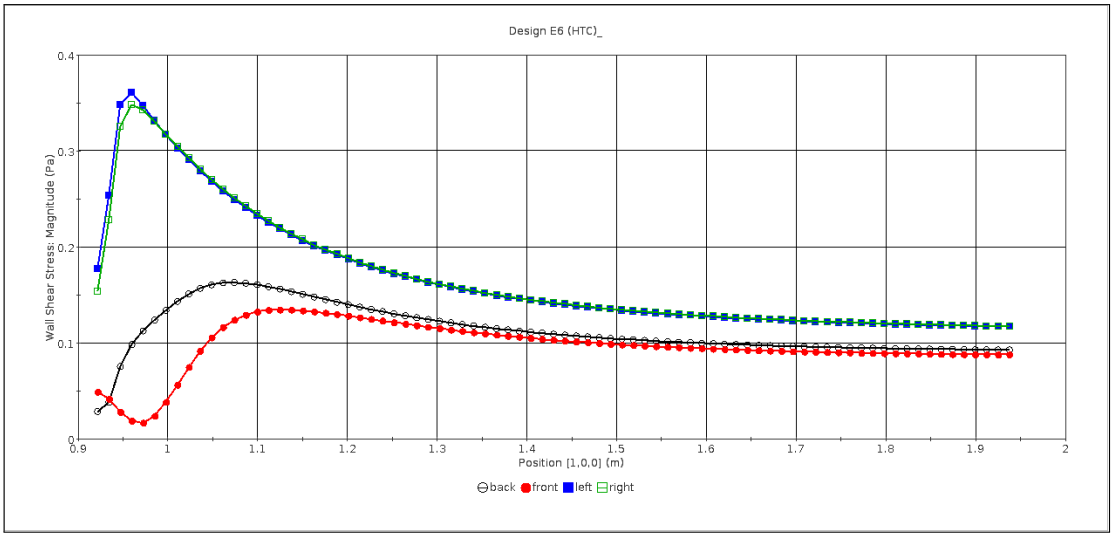

Figure 5.4: Wall shear stress vs. freestream direction - E6(HTC)

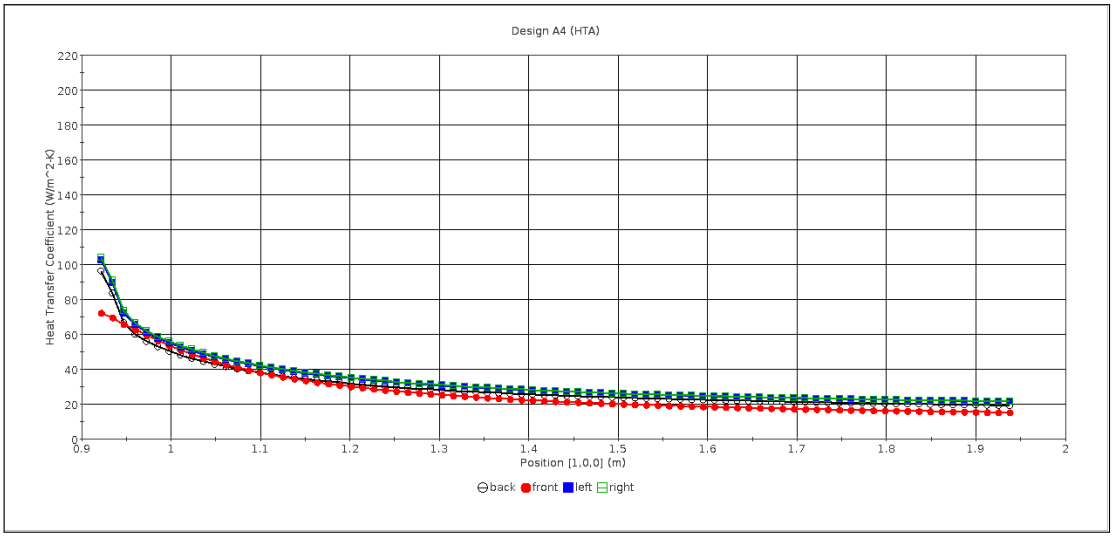

Figure 5.5: Heat transfer coefficient vs. freestream direction - A4(HTA)

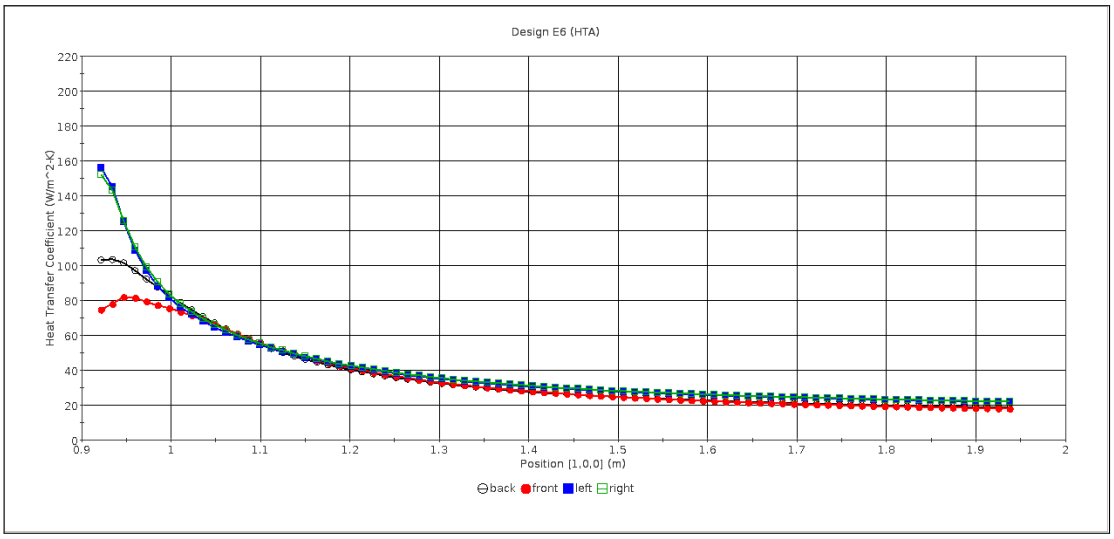

Figure 5.6: Heat transfer coefficient vs. freestream direction - E6(HTA)

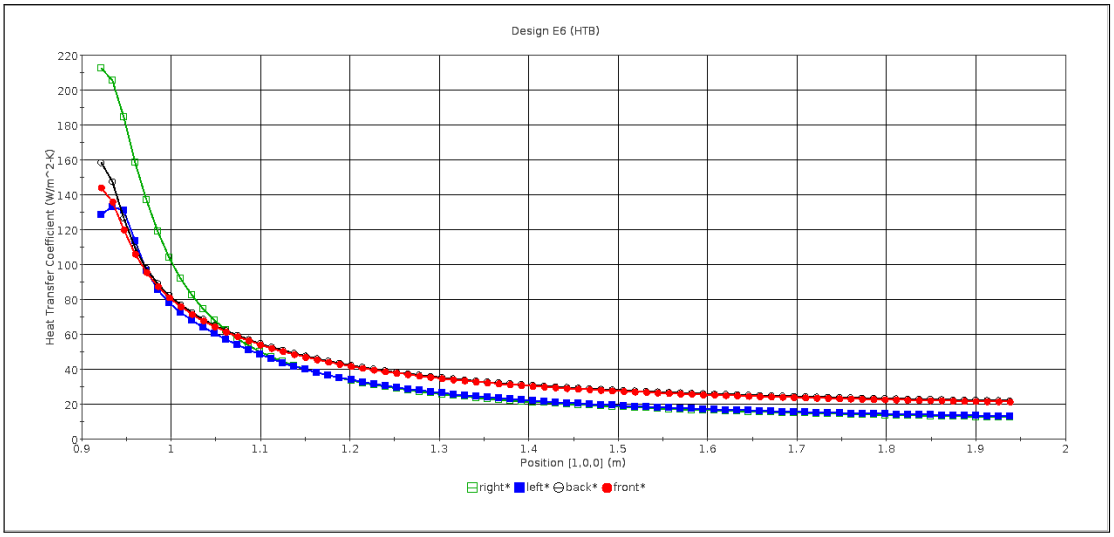

Figure 5.7: Heat transfer coefficient vs. freestream direction - E6(HTB)

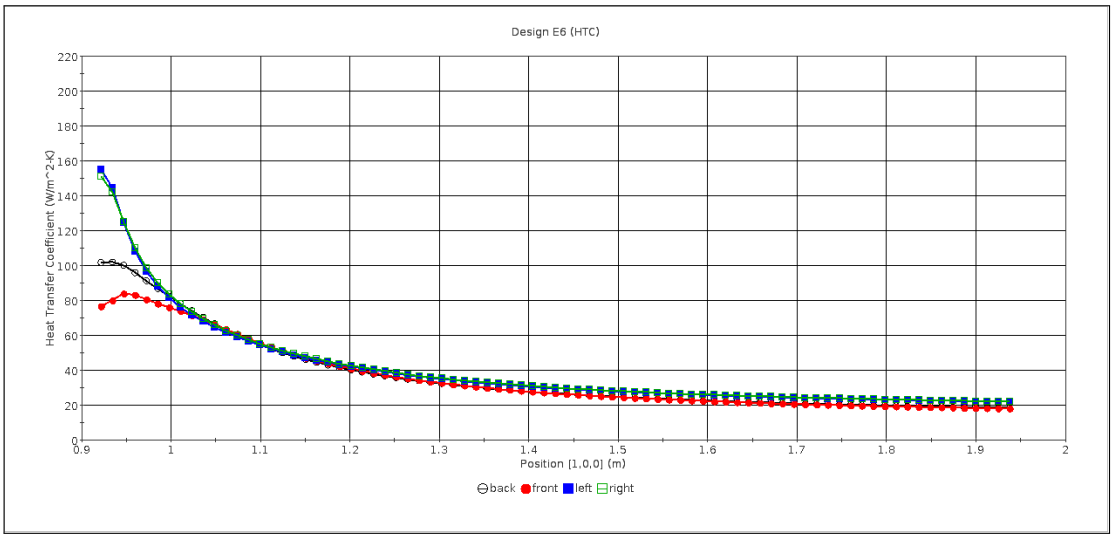

Figure 5.8: Heat transfer coefficient vs. freestream direction - E6(HTC)

The graphs presented in Figures 5.1 through 5.8 require some explanation.[33] The figures represent Duct 4 first section (0"–40") wall shear stress and heat transfer coefficient results. There are four plots on each graph, representing the left (blue), right (green), front (red), and back (black) sides of the duct (cf. Figure 4.16). For example, the plots associated with the right side of the duct, represent the average of the parameter values (e.g., wall shear stress or heat transfer coefficient) obtained from each of the three horizontal data planes T, C, and B (cf. Figure 4.35). Likewise, the plots associated with the left side of the duct, represent the average of the parameter

[33]The figures were produced using STAR-CCM+.

values (e.g., wall shear stress or heat transfer coefficient) obtained from each of the three horizontal data planes T, C, and B.

It should be noted that the boundary layer development in the heated duct is different, yet similar in some ways to the boundary layer development on an isothermal flat plate (cf. Appendix A). In the entrance region of Duct 4, laminar boundary layers (viscous and thermal) develop simultaneously along all four walls; and they eventually coalesce. But on an isothermal flat plate, only one viscous boundary layer develops; and it continues to grow along the freestream length of the plate. A similarity between the duct and the flat plate boundary layer development can be seen by comparing the skin friction coefficient and heat transfer coefficient parameters as the fluid transitions from laminar to turbulent flow. Specifically, the transition process is similar to that depicted in Figure 1.8 where the skin friction coefficient decreases, reaching a minimum value, then increases, where it reaches a local maximum value. Typically referred to as entrance effects, this heat transfer and fluid flow feature is depicted in Figures 5.1 through 5.8.

Referring to Design E6(HTA) (cf. Figure 5.2), the wall shear stress values on the left and right sides of the duct initially increase, reaching a peak value of approximately 0.35 Pa. The shear stress gradually decreases reaching a constant value of approximately than 0.12 Pa. The steady shear stress value is an indication that viscous boundary layer transition from laminar to turbulent is complete. Noteworthy is that the shear stress values along the front and back walls show a similar behavior; but their values differ. Also, transition occurs further downstream. The reason for this unique behavior is due to the nonuniform velocity distribution depicted in Figure 4.32. As expected all three graphs of the wall shear stress for Designs E6 have the same shape and relative magnitude (cf. Figures 5.2 to 5.4); this is expected since all three designs have the same inlet boundary conditions.

The thermal boundary layer development is depicted in Figures 5.5 through 5.8. A transition profile, similar to the wall shear stress transition profile, is observed. For example, the heat transfer coefficient for Design A4(HTA) (cf. Figure 5.5) attains

a peak value of approximately $100\frac{W}{m^2 \cdot K}$. It gradually decreases, reaching a constant value of approximately $20\frac{W}{m^2 \cdot K}$, indicating that the thermal boundary layer transition is complete. Noteworthy is that the entrance effects have a significant impact on the heat transfer. For example, the convective heat transfer coefficient near the inlet of Design A4(HTA), Figure 5.5, is approximately 3.5 to 5 times the value of the heat transfer coefficient 40 inches downstream; and the convective heat transfer coefficient near the inlet of Design E6(HTA), Figure 5.6, is approximately 3.5 to 7.5 times the value of the heat transfer coefficient 40 inches downstream.[34]

In simple geometries with uniform flow, such as flat plates, the typical skin friction coefficient or wall shear stress transition profile is observed. But in complex industrial-type simulations, such as those performed in this study, the entire transition profile may not be observed. For example, note that the beginning of the viscous boundary layer transition for Design A4(HTA), Figure 5.1, is not depicted since the inlet boundary data plane for this design was located approximately four inches downstream of the duct inlet (cf. Figure 4.31); therefore, the viscous boundary layer transition for this design had already begun.[35] Furthermore, this modeling effect is not seen in the thermal boundary layer development since the heat flux boundary condition begins at the vertical height location of the inlet boundary data plane; although a finer mesh in the freestream direction may have provided more insight into the thermal boundary layer entrance effects. Regardless, it should be emphasized that RANS turbulence models neither predict nor should they be used to predict laminar to turbulent transition. In short, the exact location where transition occurs is uncertain; but, what is certain is that a transition from laminar flow to turbulent flow does occur over a given entrance length.

The entrance length is difficult to predict computationally and to measure experimentally; yet, the entrance length can be approximated.[36] Since the hydrodynamic

[34]The impact of heat transfer entrance effects can be significant depending on the system design and application (Boyd and Armstrong, 2010).

[35]Recall from Section 4.4.2, that the A4 riser ducts penetrate four inches into the inlet-plenum.

[36]There is a lack of detailed experimental investigations related to entrance length for fully developed turbulent channel flow and what appears to be a gap in the knowledge of turbulent duct flows (Lien et al., 2004).

(i.e., viscous) and thermal entry lengths are independent of Reynolds number (Re) or the Prandtl number (Pr), they can be approximated as 10 times the hydraulic diameter (cf. Equation 5.1), which for this analysis corresponds to 1.6 meters for Design A4 and 1.7 meters for Designs E3 (cf. Figure 5.6) (Cengel, 1998).[37] Additional details regarding boundary layer transition can be found in Appendix A.

$$L_{thermal} \approx L_{hydrodynamic} \approx 10 D_{hydraulic} \tag{5.1}$$

The heat transfer and fluid flow analysis of the Duct 4 second section (40"–80") was not complicated by entrance effects since wall shear stress and heat transfer coefficient had reached a constant value, indicating that turbulent boundary layer is fully developed. Yet, consistent with traditional heat transfer and fluid flow approaches, additional analyses were performed.

Velocity and temperature contours are presented in Figures 5.9 and 5.10. Note that there are three contour plots associated with each figure. Specifically, contour plots associated with Design A4(HTA) and Design E6(HTA) are presented. Additionally, a third contour plot depicting uniform flow and uniform heat flux are presented between the A4 and E6 contour plots for comparison purposes. An area of low velocity near the wall of Design A4 is clearly shown by the yellow color at the bottom of the A4 contour plot; and a smaller area of reduced velocity is clearly shown by the yellow color at the bottom of the E6 contour plot. Note that the areas of low velocity correspond to areas of higher temperatures shown in Figure 5.10.

In addition to the contour plots, profiles of velocity, temperature, and a turbulent mean velocity profile were extracted from the midpoint of the Duct 4 (40"–80") section.[38] The vertical black dotted lines in Figures 5.9 and 5.10 represent the line probe location where temperature and velocity data was extracted to generate the

[37] Recall that the viscous boundary layer development for Design A4 started 4 inches earlier than the viscous boundary layer development for Design E6; and the thermal boundary layer development began at the same vertical location for Designs A4 and E6.

[38] Figure 5.13 illustrates that the viscous sublayer was resolved, which is consistent with the value of 0.7 for the maximum wall $y+$. For additional details related to resolving the viscous sublayer, refer to Appendix C.

velocity and temperature profiles shown in Figures 5.11 through 5.13. The areas of lower velocity and corresponding higher temperatures are clearly shown by the plots on the left portion of Figures 5.11 and 5.12.

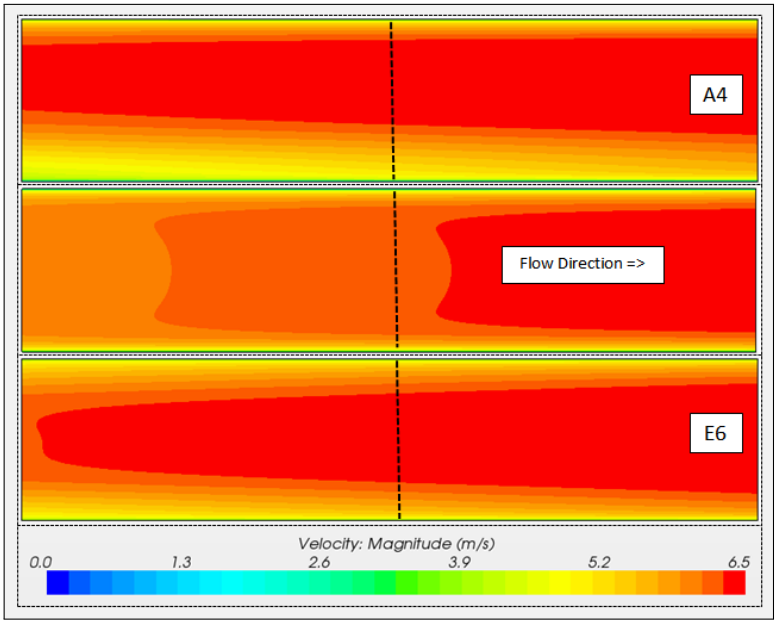

Figure 5.9: Velocity contour plots (40”–80”) - A4/E6 (HTA)

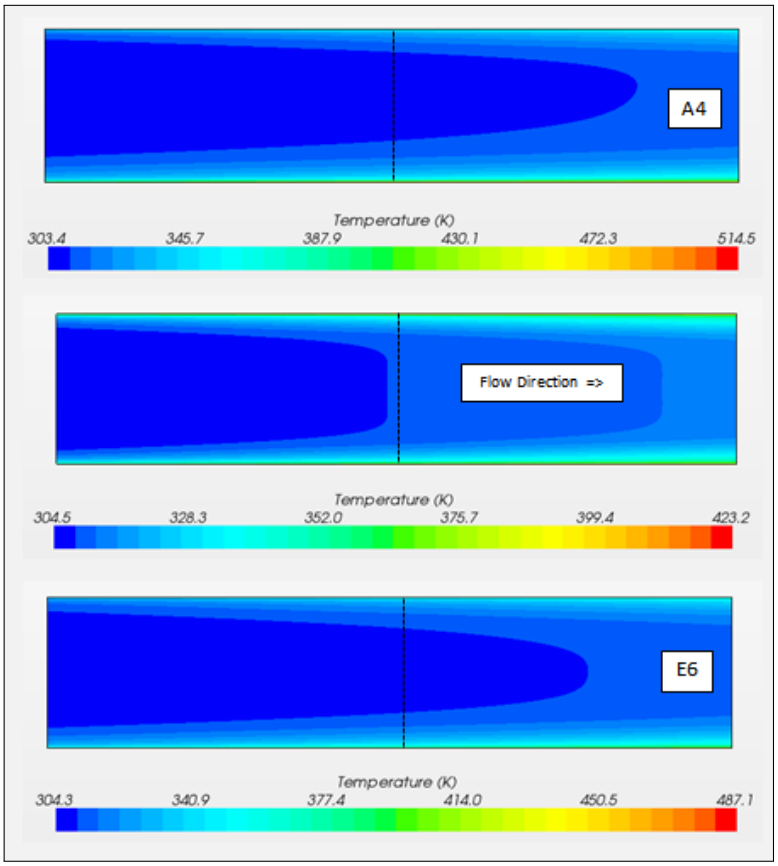

Figure 5.10: Temperature contour plots (40”–80”) - A4/E6 (HTA)

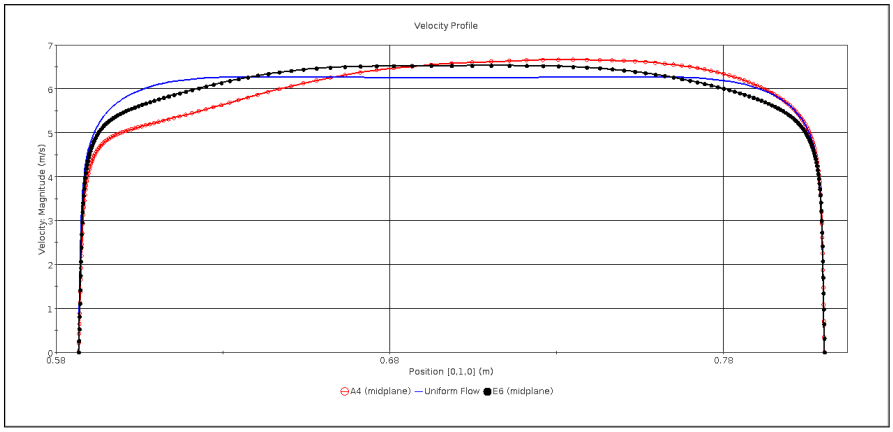

Figure 5.11: Velocity horizontal profile plots - A4/E6 (HTA)

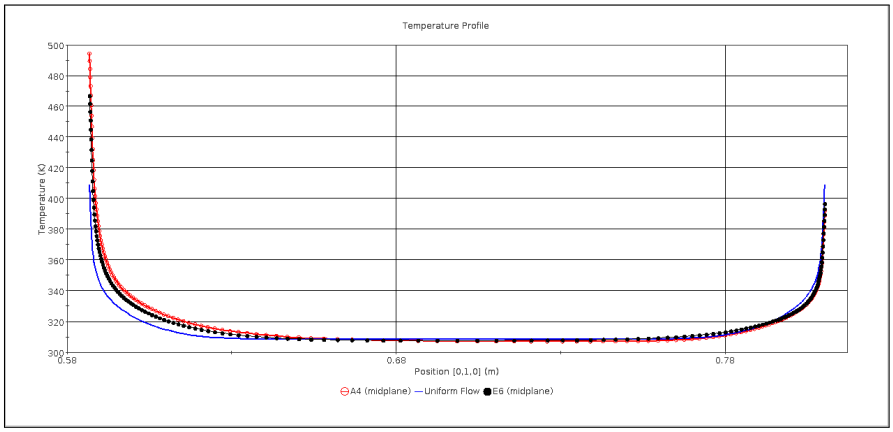

Figure 5.12: Temperature horizontal profile plots - A4/E6 (HTA)

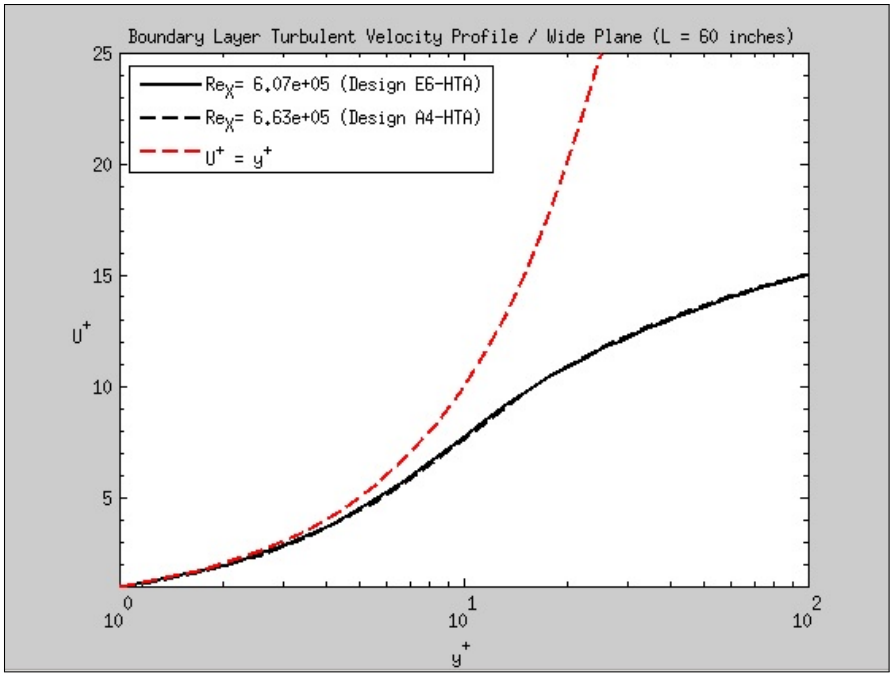

Figure 5.13: Boundary layer velocity profiles (wide plane, L = 2.4 m)

Although boundary layer thickness was not required as input for any of the calculations involving wall shear stress or convective heat transfer coefficient, local boundary layer thickness was computed as part of this study to show the impact of nonuniform fluid flow and heat transfer including entrance effects on boundary layer development. Equations 4.1 through 4.4 were used to compute boundary layer thickness. Note that each method is dependent upon freestream conditions (e.g., velocity and temperature). Furthermore, recall that each equation is restricted to 2D; yet end-wall boundary layers are present in 3D ducts. Figures 5.14 through 5.21 show the development of the hydrodynamic (i.e., viscous) and thermal boundary layers associated with the top, center, and bottom data planes (left/right duct walls) for the first section (0" – 40") of Designs A4 and E6.[39]

Note the development of the typical profile for the thermal boundary layers (cf. Figure 5.18) and the development of the erratic profile for the hydrodynamic (i.e., viscous) boundary layers (cf. Figure 5.14). Contributing to the erratic behavior of the hydrodynamic boundary layers is the nonuniform velocity associated with each design, entrance effects, smaller changes in velocity near the freestream area, and the process used to compute freestream velocity (cf. Figure 4.37). Noteworthy is that the thermal boundary layer profiles of Figures 5.18 and 5.20 have a similar shape as the Technique 3 freestream gradient map (cf. Figure 4.39). The stair-stepping boundary layer profile is consistent with boundary layer profiles illustrated in Figure 6 of Appendix A. Although a finer mesh in the streamwise direction would minimize the stairstepping, this was not practical due to computational resource constraints; nevertheless, sufficient streamwise mesh elements were used to model the general behavior of the entrance effects.

Using Equation 5.2, a hand-calculation was performed in order to estimate the hydrodynamic boundary layer thickness (White, 1991). Although the equation is only applicable to flat plate turbulent boundary layers, the result should approximate the boundary layer thickness values presented in Figures 5.14 and 5.16. The equation

[39]The Duct 4 first section (0" – 40") corresponds to 0.9m to 1.9m, which is the vertical height measured relative to the inlet-plenum.

was applied at a freestream distance of $L = 1.4\ m$. The computed boundary layer thickness (δ) was 14 mm, which approximates the boundary layer thickness depicted in the figures.

$$\frac{\delta}{x} = \frac{0.16}{Re_x^{1/7}} \tag{5.2}$$

Finally, using only traditional HTFF techniques, what is the best design? Well, evaluating the designs strictly from a shear stress perspective, it appears that Design A4(HTA), Figure 5.1, is the better design since overall it has a lower wall shear stress at the inlet; although, it does have a slightly higher wall shear stress within the turbulent region, except for the duct front wall, which is much lower. In general, a lower wall shear stress implies lower resistance to flow; that is, improved natural circulation flow or lower pumping requirements for forced circulation.

Evaluating the designs based on the heat transfer coefficient, it appears that Design E6(HTA), Figure 5.6, or Design E6(HTC), Figure 5.8, would be better choices compared to Design A4(HTA), Figure 5.5, since the heat transfer coefficient for both of those designs is slightly larger in turbulent boundary layer region, even though Design E6(HTB), Figure 5.7, has a larger heat transfer coefficient, during the transition phase, on the right duct wall.

So, in general and based on traditional heat transfer and fluid flow analyses, Design A4(HTA) has an overall lower wall shear stress (good); and Designs E6(HTA) and E6(HTC) have an overall higher heat transfer coefficient (good).

Yet, from a practical perspective the lack of variation between flow parameters (cf. Table 5.1) coupled with the complexities of interpreting four plots on each graph, make it difficult to determine the best design for a reactor safety system such as the RCCS. Therefore, in order to help determine the optimal design, especially given the wall shear stress and heat transfer coefficient entrance effects, an entropy generation analysis (EGA) was performed; this analysis is discussed in Section 5.2.

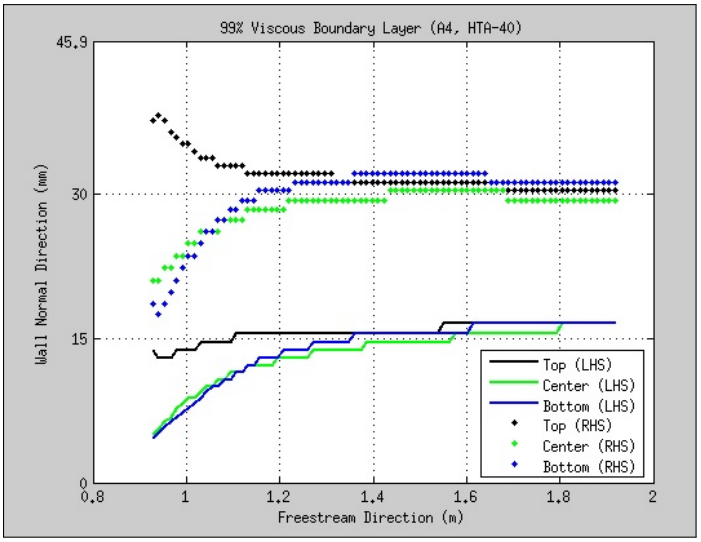

Figure 5.14: 99% boundary layer (A4) - left(LHS)/right(RHS)

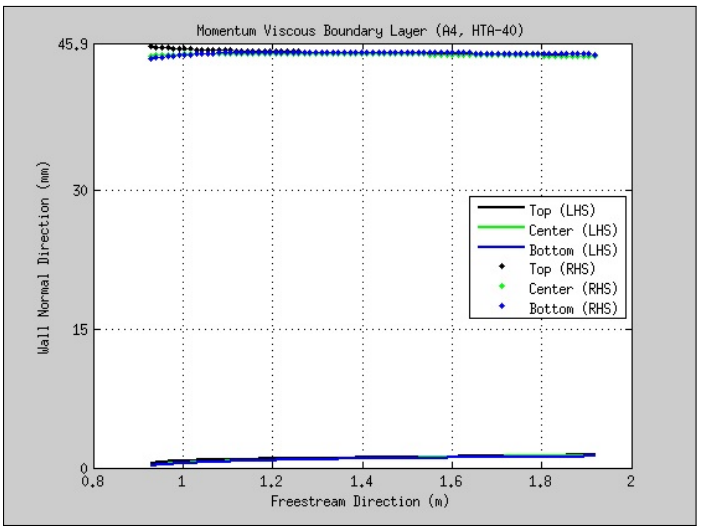

Figure 5.15: Momentum boundary layer (A4) - left(LHS)/right(RHS)

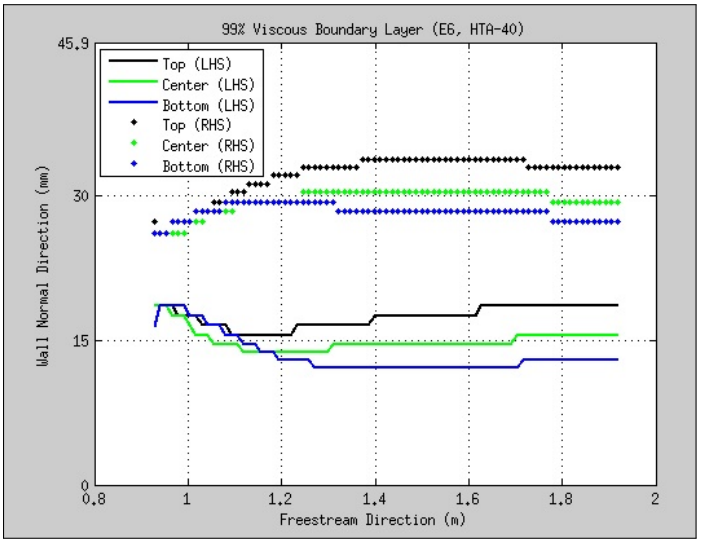

Figure 5.16: 99% Boundary layer (E6) - left(LHS)/right(RHS)

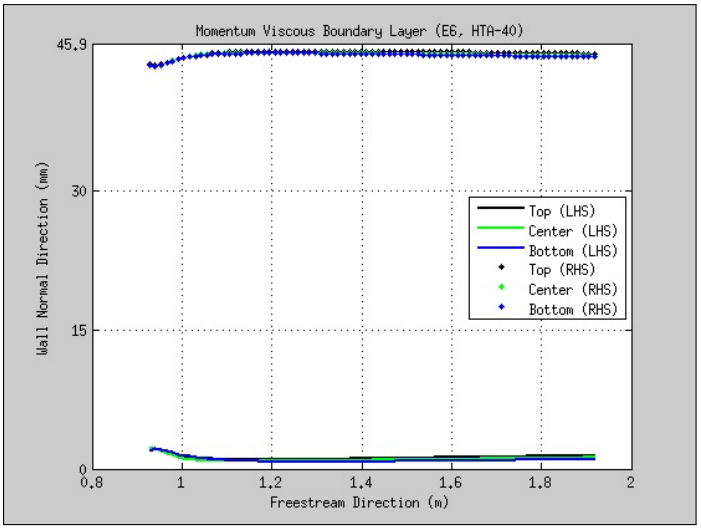

Figure 5.17: Momentum boundary layer (E6) - left(LHS)/right(RHS)

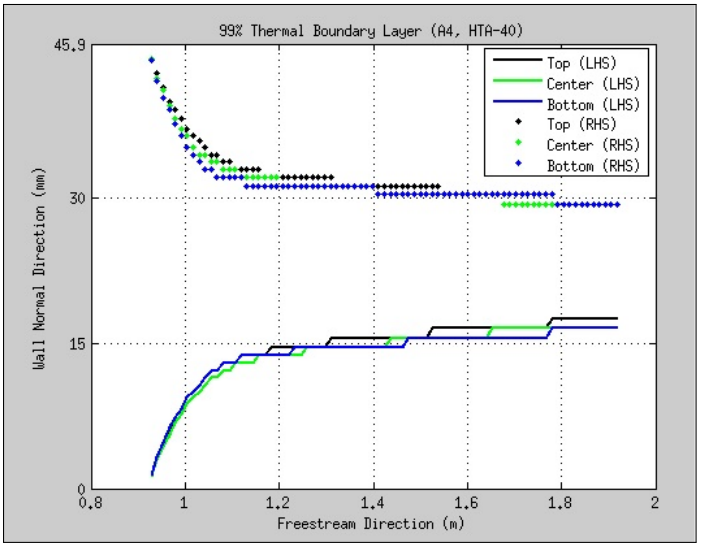

Figure 5.18: Thermal boundary layer (A4) - left(LHS)/right(RHS)

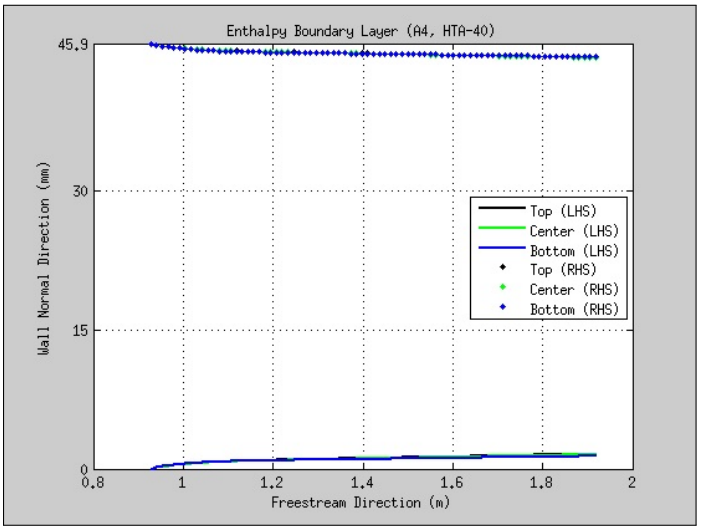

Figure 5.19: Enthalpy boundary layer (A4) - left(LHS)/right(RHS)

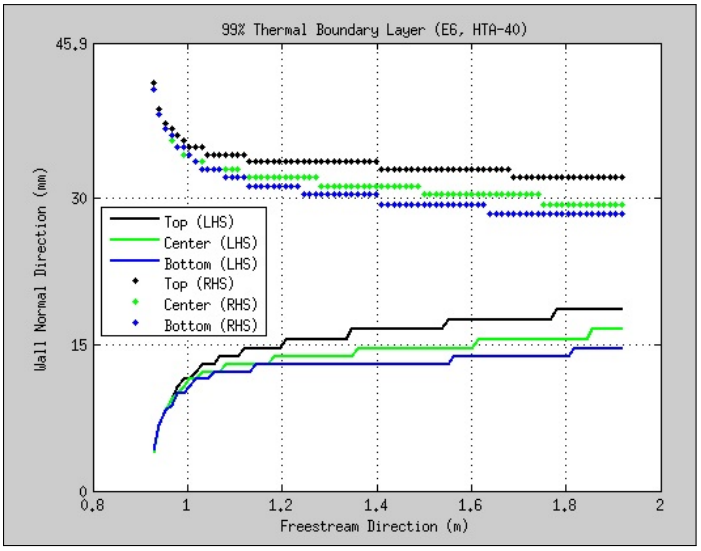

Figure 5.20: Thermal boundary layer (E6) - left(LHS)/right(RHS)

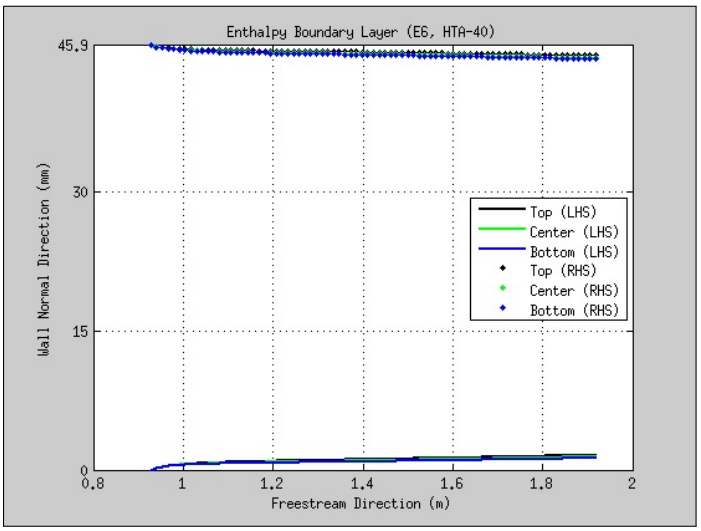

Figure 5.21: Enthalpy boundary layer (E6) - left(LHS)/right(RHS)

5.2. Entropy Generation Analysis

5.2.1. Duct 4

Using entropy generation analysis (EGA) techniques, an optimal RCCS design was determined. Consistent with the entropy generation minimization (EGM), the design with the smallest value of entropy generation rate (EGR), in general, should be considered as the best design since this design has less viscous and thermal dissipation losses. Using the Direct Method Model (cf. Section 3.2), EGR was calculated by first computing the volumetric entropy generation rate for each data plane (cf. Figures 4.33 and 4.34). The entropy generation rate per unit area $\dot{S}''$ was then

calculated by integrating entropy generation rate per unit volume $\dot{S}'''$ in the wall normal direction. Finally, surface area weighted average EGR was calculated.

The EGA results are presented in Figures 5.22 to 5.24. Figure 5.22 compares the entropy generation rate (EGR) of the various designs. Noteworthy is that the viscous contribution to EGR is negligible; this can be seen in Figure 5.23. Reviewing Figure 5.24, it can be concluded that designs E6(HTA) and E6(HTC) have the largest percentage reduction in EGR [i.e., smallest EGR relative to Design A4(HTA)] suggesting that these designs should be evaluated for further improvements. But, since the HTC design (cf. Figure 4.18), which has an equal heat flux load applied at all sides of the duct, is not necessarily applicable to the existing RCCS experimental facility, only the E6(HTA) design was analyzed further using traditional HTFF techniques.

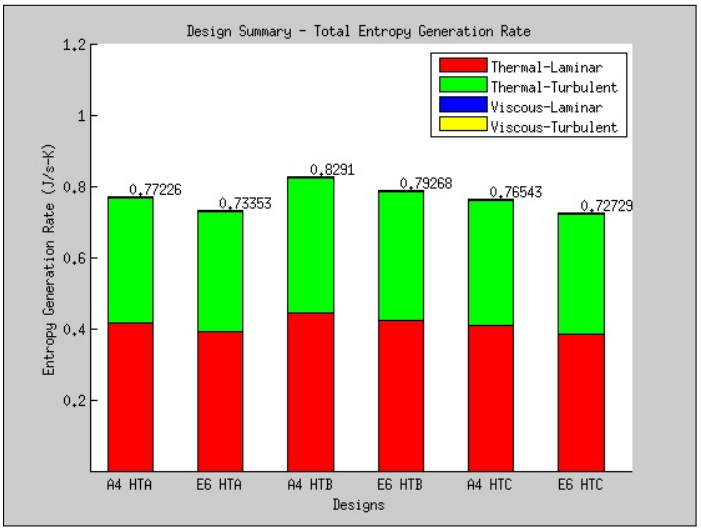

Figure 5.22: Design comparison

Noteworthy is that the author recognizes the importance of quantifying uncertainty, typically exemplified through the use of error bars. Yet, given the computational overhead and resource requirements associated with sensitivity analyses for each of the items described in Section 5.4.4, the complexities associated with uncertainty analyses, and the lack of experimental data, solution uncertainty was not quantified. In fact, quantifying solution uncertainty is beyond the scope of this study (Groves, 2014; Lockwood, 2012). Additional information related to sensitivity analysis and computing numerical uncertainty can be found in Oberkampf and Roy (2010).

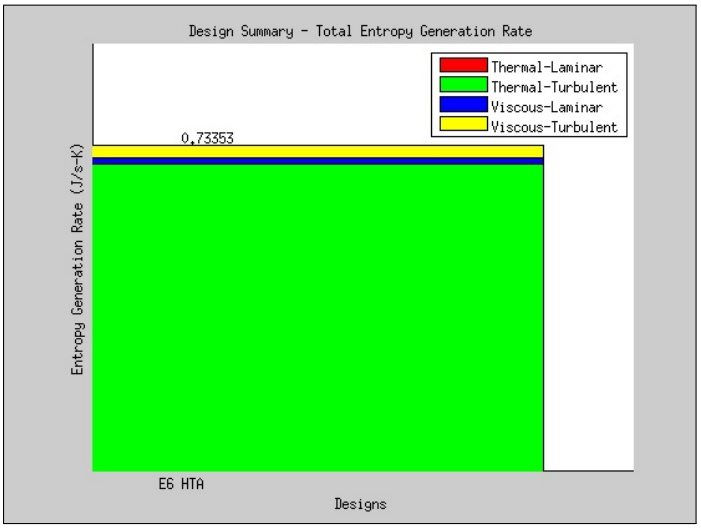

Figure 5.23: Relative viscous entropy contribution (E6-HTA)

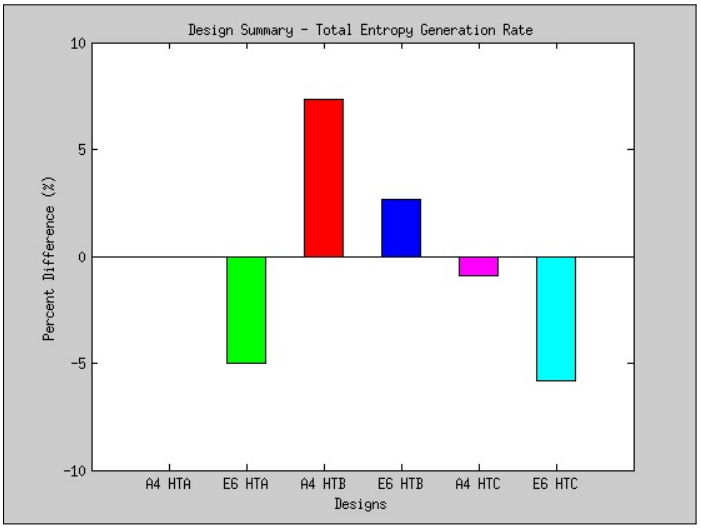

Figure 5.24: Relative design comparison

Based on the results of the entropy generation rate analysis, a more detailed look at Design A4(HTA) and Design E6(HTA) was warranted. Therefore consistent with the process introduced by Denton (1993) and applied by Walsh et al. (2011), an entropy dissipation coefficient, defined in Equation 5.3 was calculated. The results are presented in Figures 5.25 through 5.28.

$$C_d = \frac{T_\infty \dot{S}''}{\rho_\infty U_\infty^3} \tag{5.3}$$

Figures 5.25 through 5.28 depict the individual contributions to dissipation. Specif-

ically, both the thermal and viscous contributions are depicted, including the laminar and turbulent contributions. Consistent with the results presented in Figure 5.23, it is clear that the viscous contribution to total dissipation is negligible. In all of the figures, the entrance effects can be observed; eventually the dissipation plots reach a steady value, indicating that the flow is fully turbulent.

Prior to leaving this section, it is prudent to briefly discuss how entropy changes as the air flows through the duct. It is important to note that for open systems such as the RCCS, it is the 'change in entropy' from the duct inlet to the duct outlet, in addition to mass flowrate, that provide useful information for engineering design evaluations. Table 5.3 presents the area-weighted surfaced averaged entropy values for the A4(HTA) and E6(HTA) designs, (0"-40") section. Consistent with the EGA results, the difference in entropy is smaller for design E6(HTA) compared to Design A4(HTA). Noteworthy is that the global averaged approach to EGA (e.g., Equation 3.1) fails to provide the details necessary to conduct a thorough analysis of local entropy generation within the hydrodynamic and thermal boundary layers, for example capturing entrance effects.

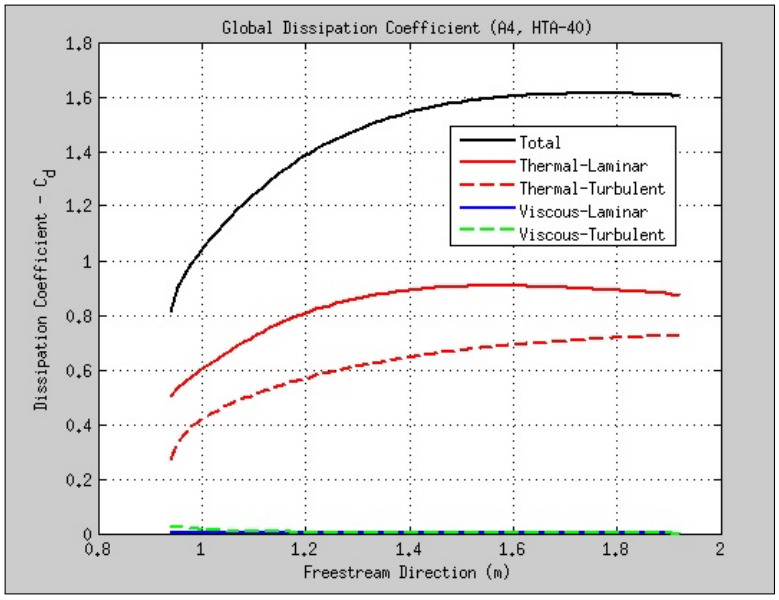

Figure 5.25: Global entropy dissipation coefficient (A4-HTA)

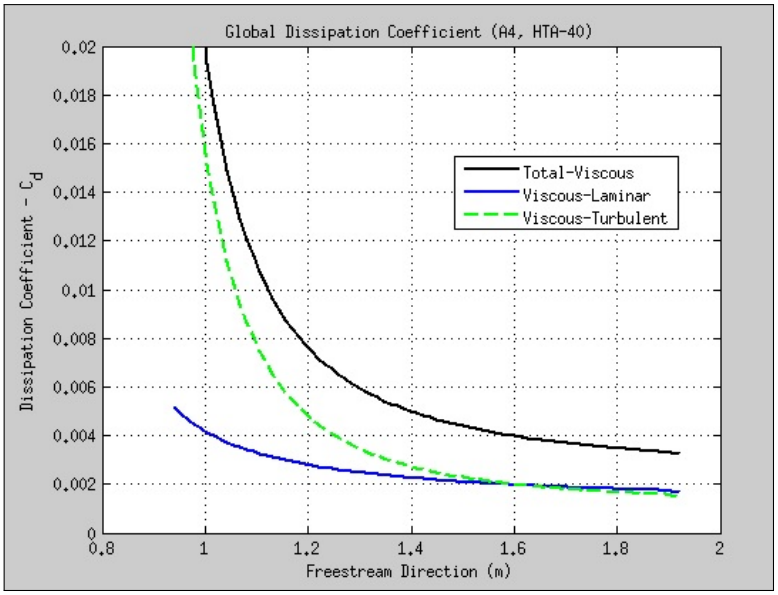

Figure 5.26: Global viscous entropy dissipation coefficient (A4-HTA)

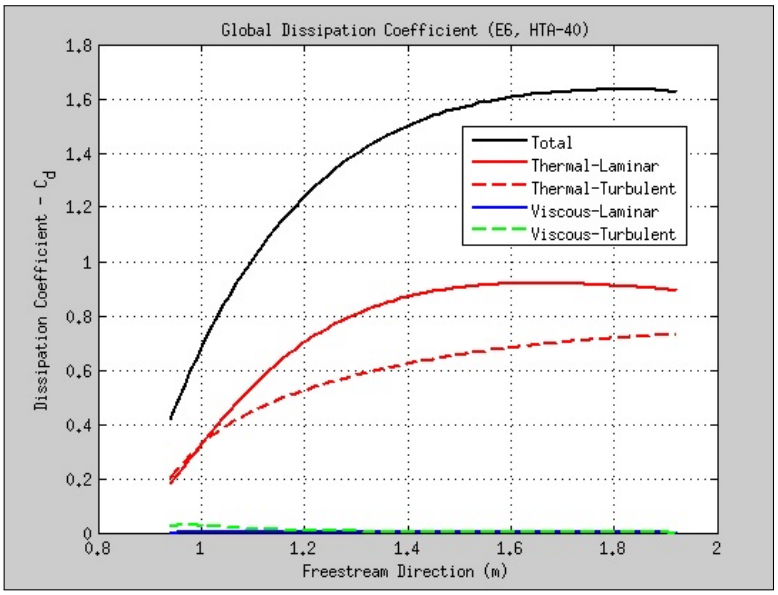

Figure 5.27: Global entropy dissipation coefficient (E6-HTA)

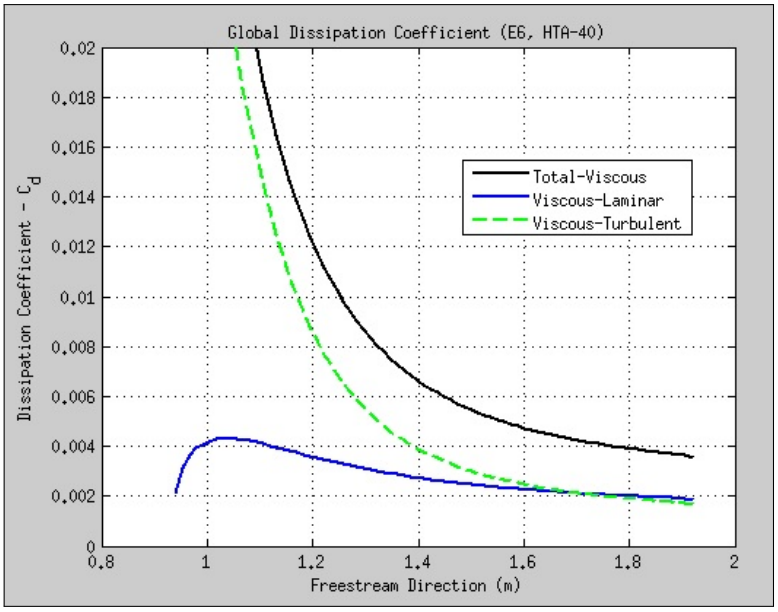

Figure 5.28: Global viscous entropy dissipation coefficient (E6-HTA)

Table 5.3: Duct 4 entropy results (0"–40")

Design	Outlet 'S' (J/kg-K)	Inlet 'S' (J/kg-K)	ΔS (J/kg-K)	EGR (J/s-K)
A4(HTA)	2473.2	2380.2	93.0	0.8
E6(HTA)	2467.9	2382.5	85.5	0.7

5.2.2. Inlet-Plenum

Using the EGA indirect method applied by Herwig and Kock (2007), an entropy generation analysis was performed on the inlet-plenum of both the A4 and E6 designs. The results of the inlet-plenum EGA concluded that an entropy generation rate reduction of approximately 2% can be obtained by modifying the A4 design so that the riser-ducts are flush with the top wall of the inlet-plenum, reducing internal flow restrictions.[40] Although an EGA analysis was not performed on the outlet-plenum, these results suggest that an EGR reduction could be accomplished by redesigning the A4 riser-duct outlets to be flush with the bottom wall of the outlet-plenum (cf. Figure 1.3).

[40] An EGR of 2% is conservative in that the turbulent contribution due to turbulent fluctuations entropy was not considered.

5.3. Analysis Summary

Given the information learned from the thermal analysis of Section 5.1 and the entropy generation analysis results of Section 5.2.1, it is prudent to revisit the traditional HTFF analysis of Designs A4(HTA) and E6(HTA). Referring to Figures 5.29 and 5.30 it can be seen that Design E6(HTA) experiences a larger shear stress coefficient and a higher heat transfer coefficient (cf. green plots). Since the shear stress has negligible impact on Duct 4 EGR and the heat transfer coefficient has a significant impact on Duct 4 EGR, it can be concluded that Design E6(HTA) is the best design. This is consistent with the results presented in Figures 5.22 and 5.24.

5.4. Verification and Validation

Including elements of an agreed upon V&V methodology in the design process is mandatory for safety-related calculations (Hamman et al., 2012), yet it is important that non-safety-related calculations (e.g., basic research) should have some degree of rigor established – on par with the risk associated with the use of incorrect results. Therefore, a certain level of V&V rigor, consistent with that expected for basic and applied research, was followed. Although a formal V&V methodology such as ASME NQA-1 was not followed, several elements of a typical V&V methodology such as iterative convergence, consistency, spatial convergence, and comparison of numerical results with experimental data or results published in the literature were applied throughout portions of this study including the Appendix A and B studies.

What follows is a brief overview of some of the typical V&V elements analyzed as part of this study, including application of boundary conditions and model calibration. It should be noted that this information is an original contribution to this dissertation in that it exemplifies the importance of identification and documentation of factors that impact solution uncertainty in addition to documenting the information contained in the technical reports (e.g., Appendices A & B), a practice which is consistent with the documentation goals of V&V, discussed by Oberkampf and Roy (2010), which include reproducibility, traceability, and transparency - all of which should be followed as a requirement in the application of commercial and research

CFD codes, especially by those involved in nuclear-related design engineering.

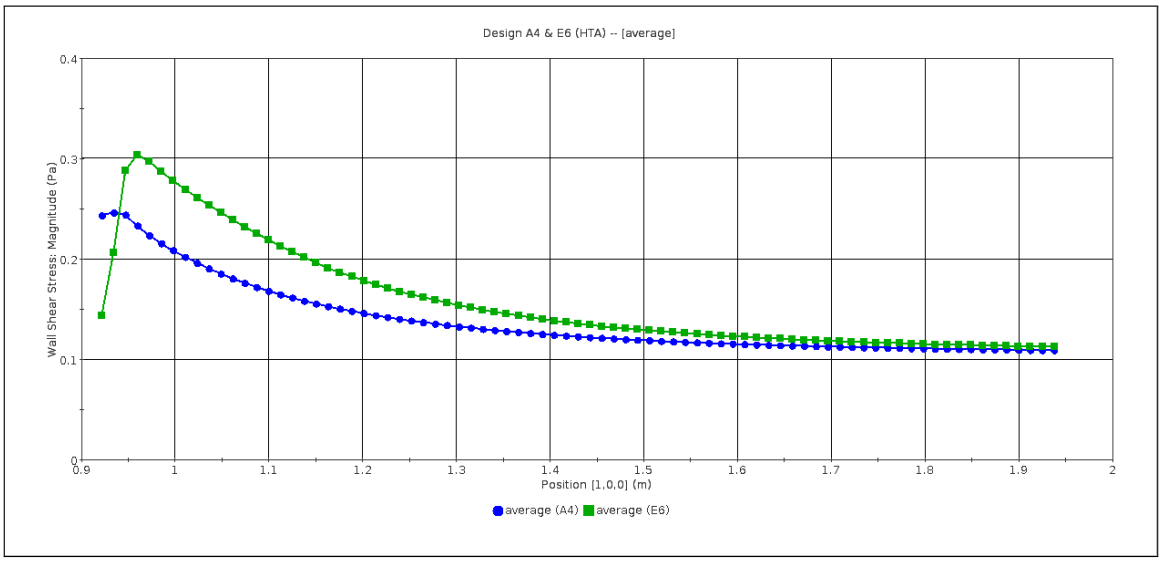

Figure 5.29: Wall shear stress vs. freestream direction (A4/E6 HTA)

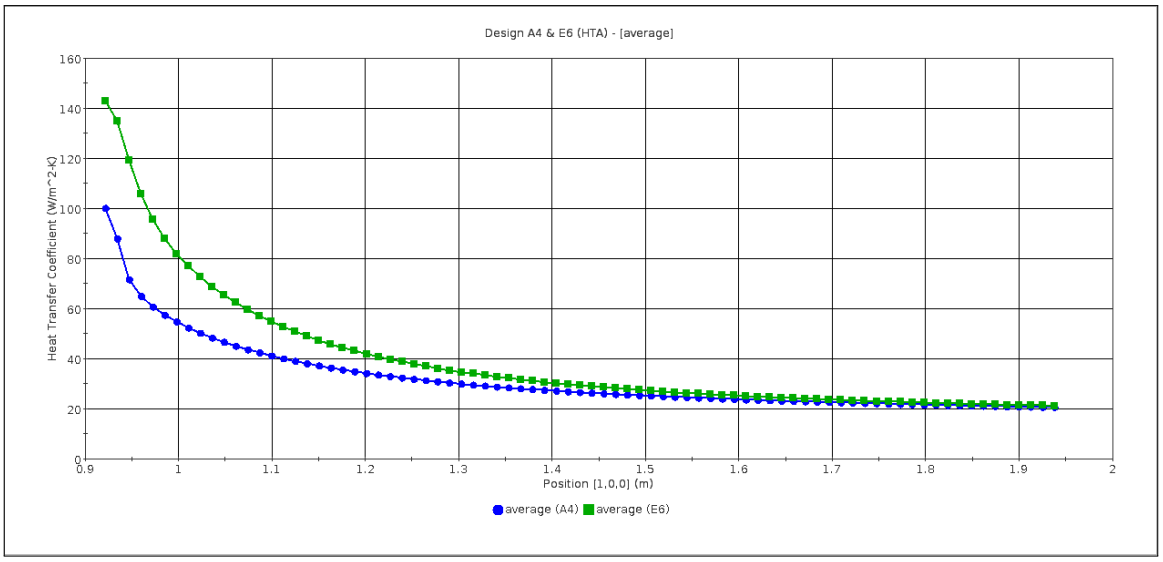

Figure 5.30: Heat transfer coefficient vs. freestream direction (A4/E6 HTA)

5.4.1. Boundary Conditions

As previously mentioned, a MATLAB code was written to post-process velocity and turbulent viscosity results from STAR-CCM+. Boundary layer parameters such as wall shear stress, volumetric entropy generation rate, boundary layer thickness were calculated (cf. Appendix A).

Some of the V&V elements followed during the STAR-CCM+ modeling and simulation process and development of the MATLAB code included, code commenting and peer review, revision control, hand calculations, and comparison of the results with those published in the literature. The following results demonstrate the process used to compare the MATLAB code results with results published in the literature. Specifically, the MATLAB code calculations, which were dependent on the modeling and simulation process (e.g., boundary conditions), were compared with the boundary layer transition results of Ghasemi et al. (2013), Nolan and Zaki (2013), and Walsh et al. (2011).

To establish that the MATLAB DNS results were calculated correctly, a qualitative comparison was made between the results presented by Nolan and Zaki (2013) in Figure 5.31 and the results computed using the MATLAB code presented in Figure 5.32.[41] Upon comparing the DNS solid black plots it can be seen that both plots reach a minimum and subsequent maximum value near the same freestream location; additionally, the minimum and maximum skin friction coefficient values are approximately the same. Therefore, it was concluded that the MATLAB results approximate the Nolan and Zaki (2013) results reasonably well.

To establish that the MATLAB RANS results were calculated correctly, a visual comparison was made between the results presented by Ghasemi et al. (2013) in Figure 5.33 (Graph B) and the results (Graph A) calculated using the MATLAB code (cf. Appendix A, Figure 5.33). Upon comparing the SST $k-\omega$ plots, a noticeable difference, with respect to the beginning and ending of the transition region, can be seen; in fact, the results of Ghasemi et al. (2013) transition to turbulence sooner.

[41] The DNS results were calculated using DNS velocity results of Nolan and Zaki (Nolan and Zaki, 2012).

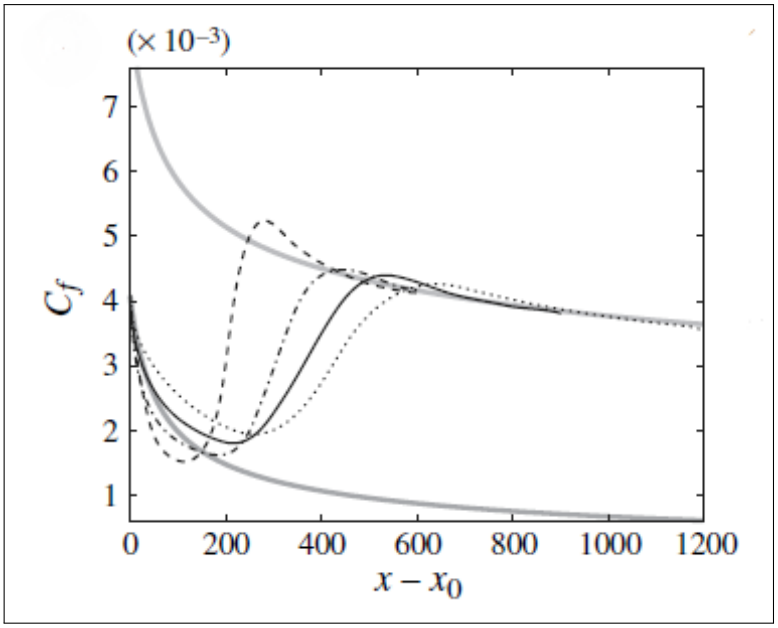

Figure 5.31: Skin friction (C_f), DNS ZPG (solid) (Nolan and Zaki, 2013)

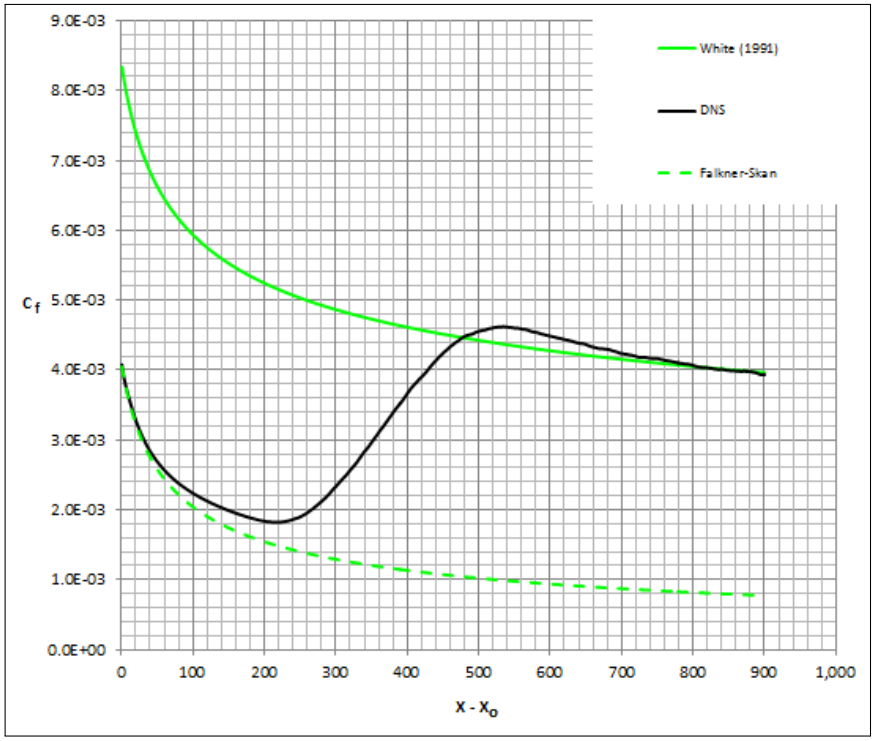

Figure 5.32: Skin friction (C_f), ZPG (MATLAB-Nolan and Zaki DNS data)

A significant amount of time was spent exploring the differences between the two plots. Based on the information provided in project files and the publication by Ghasemi et al. (2013), the most likely cause of the difference is that Ghasemi applied a constant freestream turbulent intensity of 3% at the inlet, including the

boundary layer area, resulting in the boundary layer transitioning to turbulence prematurely. The basis for this conclusion can be better understood by referring to Figure 5.34, which is a plot of skin friction coefficient (C_f) versus the square root of Reynolds number ($\sqrt{Re_x}$). This figure consists of two plots, shown in 'red,' which were developed from $SSTk-\omega$ RANS results. The BC1 plot (red dots) resulted from applying, as an inlet boundary condition, a 3% freestream turbulence intensity throughout the boundary layer and freestream area; while, the BC2 plot (solid red) resulted from applying, as an inlet boundary condition, a 3% turbulence intensity only in the freestream area of the inlet. The BC1 plot approximates the corresponding plot of Ghasemi et al. (2013).

In short, sufficient rigor should be followed when calculating and applying boundary conditions.

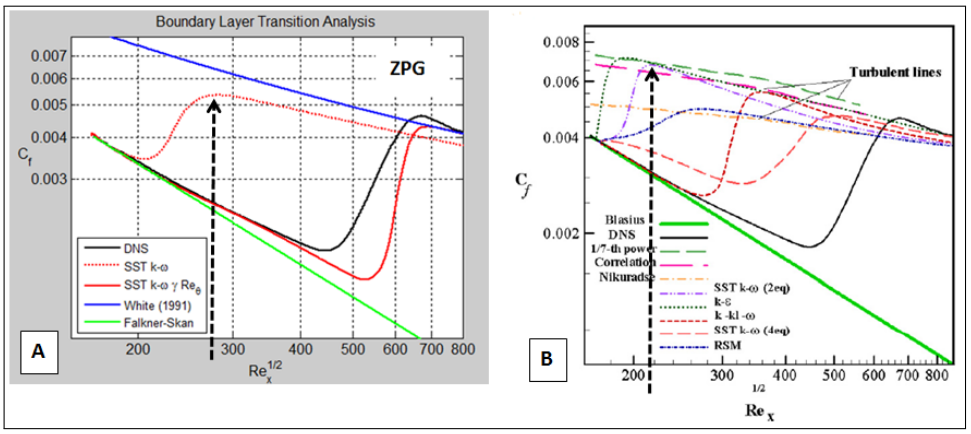

Figure 5.33: Graph "A" (Appendix A) Graph "B" (Ghasemi et al., 2013)

5.4.2. Calibration

In addition to boundary conditions, sufficient rigor should be followed when using RANS transition models, specifically the $\gamma - Re_\theta$ transition model.[42] It was concluded by Ghasemi et al. (2013) that "It has been shown that the RANS transitional models are able to predict the onset of transition and evaluate entropy generation in transitional regions."[43] Yet, the $\gamma - Re_\theta$ transition model is not predictive; in fact, it must

[42]The $\gamma - Re_\theta$ transition model is a four-equation model.

[43]Given the level of rigor required when using the $\gamma - Re_\theta$ transition model, insufficient information (e.g., wall y^+ values) was documented in the journal article to inform readers as to the reason why the transition models did not approximate the DNS results.

be calibrated. Based on the Ghasemi's results shown in Figure 5.33, the transition models were not calibrated. For example, Figure 5.35 shows two $\gamma - Re_\theta$ plots. The red plot shows the 'uncalibrated' RANS results, and the green plot shows the RANS results 'calibrated' to DNS results. Both plots used the $\gamma - Re_\theta$ transition model framework, and the Suluksna-Juntasaro correlation (CD-adapco, 2015a; Malan et al., 2009; Suluksna et al., 2009).

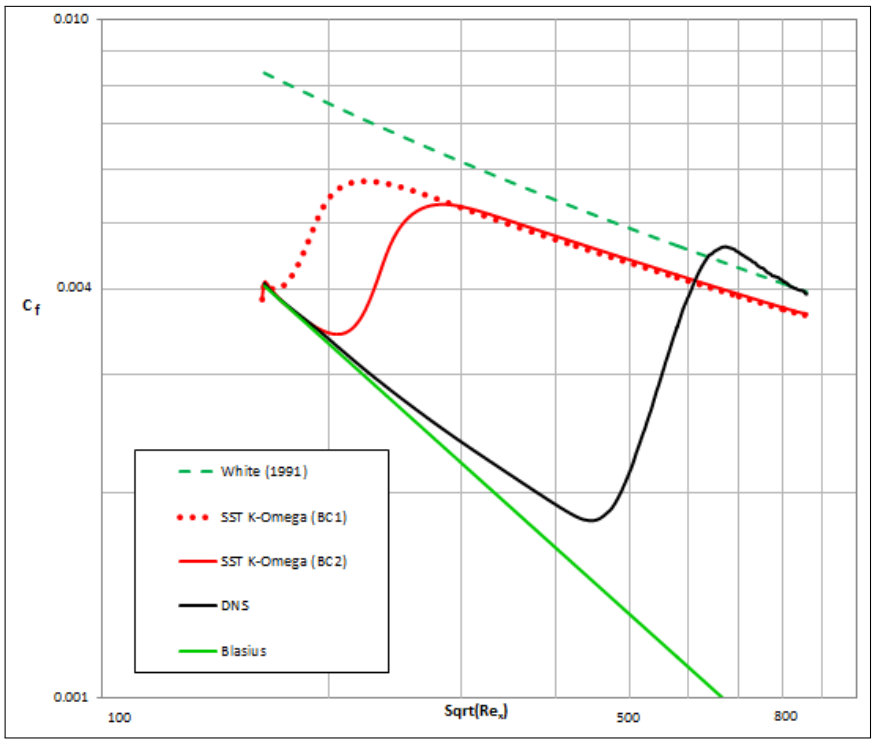

Figure 5.34: BC influence on RANS turbulence models

Unfortunately, the $\gamma - Re_\theta$ model calibration process is complex and time consuming. For example, the $\gamma - Re_\theta$ model is sensitive to mesh density; in fact, numerical testing on flat plates by Langtry (2006) revealed that at y^+ values less than 0.001, the transition location moved downstream. Therefore, the STAR-CCM+ User Guide (Version 8.04.010) requires that wall normal mesh spacing should be fine enough to obtain $0.1 \leq y^+ \leq 1$ and that *all* y^+ or *low* y^+ wall treatments should be used (CD-adapco, 2015a). The 2012 ANSYS Fluent Theory Guide (Release 14.5) has the following mesh and discretization restrictions: "In order to capture the laminar and transitional boundary layers correctly, the mesh must have a y^+ of approximately one. If the y^+ is too large (i.e., > 5), then the transition onset location moves up-

stream with increasing y^+. It is recommended that you use the bounded second order upwind based discretization for the mean flow, turbulence and transition equations." Malan et al. (2009) and Langtry (2006) provide a detailed analysis of the $\gamma - Re_\theta$ model, including model development, testing, and calibration. Again, rigor is required when using the $\gamma - Re_\theta$ transition model. For additional details on the capabilities, limitations and behavior of the $\gamma - Re_\theta$ model developed by Langtry (2006) as part of his dissertation, readers are urged to consult the literature.

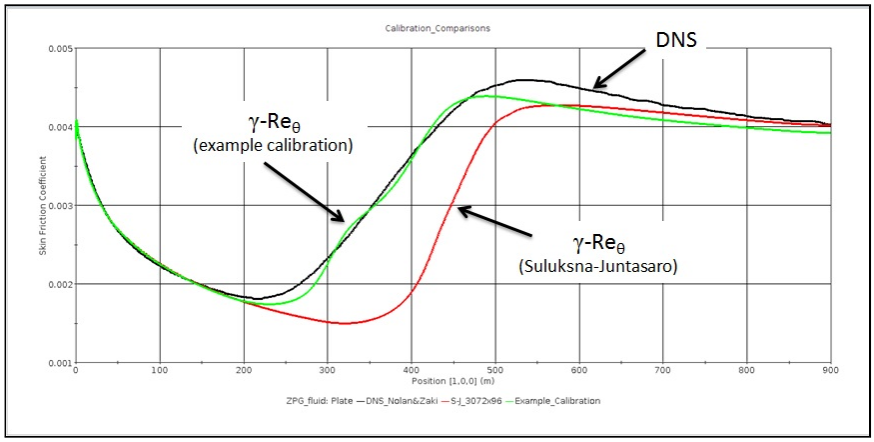

Figure 5.35: RANS transition model (C_f vs. x) - example calibration

A qualitative graphical comparison, similar to that described above, with the literature was performed for the entropy generation rate results. The details of that study can be found on Appendix A, page 149.

5.4.3. Other Elements of V&V

Although it is not common to include plots of solution residual convergence in CFD studies, it is the author's opinion that efforts should be made to include solution residual plots since they provide information on solution uncertainty. Figure 5.36 depicts the residual convergence of the Duct 4 simulation.[44] All residuals decreased to less than $1.0x10^{-10}$. The first 60 thousand iterations represent only the fluid flow simulation (no heat transfer), and the remaining residuals represent the heat transfer and fluid flow simulation. Yet, not all CFD simulation residuals will show such good convergence, especially those associated with complex geometries and flows

[44]The residual is the degree to which the discretized equation is satisfied in each computational element. In general residuals should drop about three orders of magnitude.

(Bovo and Davidson, 2013; Hamman and Berry, 2010; Hamman et al., 2015). For example, Figure 5.37 depicts the residual behavior for the Design E6 inlet-plenum simulation. Similar to the Design A4 inlet-plenum simulation, discussed in Section 4.4.3, the Tdr residual only decreased approximately a few decades, remaining at approximately $1x10^{-2}$.

In addition to residuals, consistency such as mass and energy conservation was evaluated. In this study, simulation consistency was evaluated by monitoring mass and energy quantities. Plots of net mass flowrate and net heat transfer are shown in Figures 5.38 and 5.39. The net mass flowrate curve and the net heat transfer curves suggesting that steady state has been reached. For example, net mass flowrate reaches a value of zero, while net heat transfer reaches a value of 0.074 watts, which is 0.008% of the total power input.

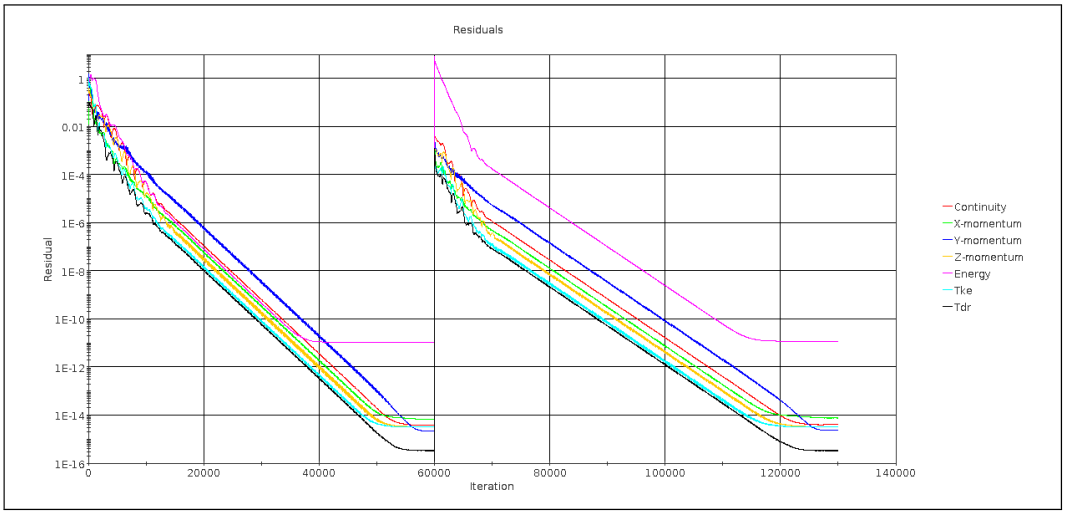

Figure 5.36: Duct 4 residuals vs. iterations (example)

Spacial convergence is an important element of the V&V process. Yet, a mesh refinement study of Duct 4 was not performed due to computational resource constraints. For example, run time for one Duct 4 simulation, with a residual convergence similar to that illustrated in Figure 5.36 using 56 processors on Big-STEM, was approximately five days (120 hours). But, a fine mesh was developed for Duct 4 (Figure 4.30), and results from this study demonstrate that the viscous sublayer was resolved (Figures 4.27 and 4.28).

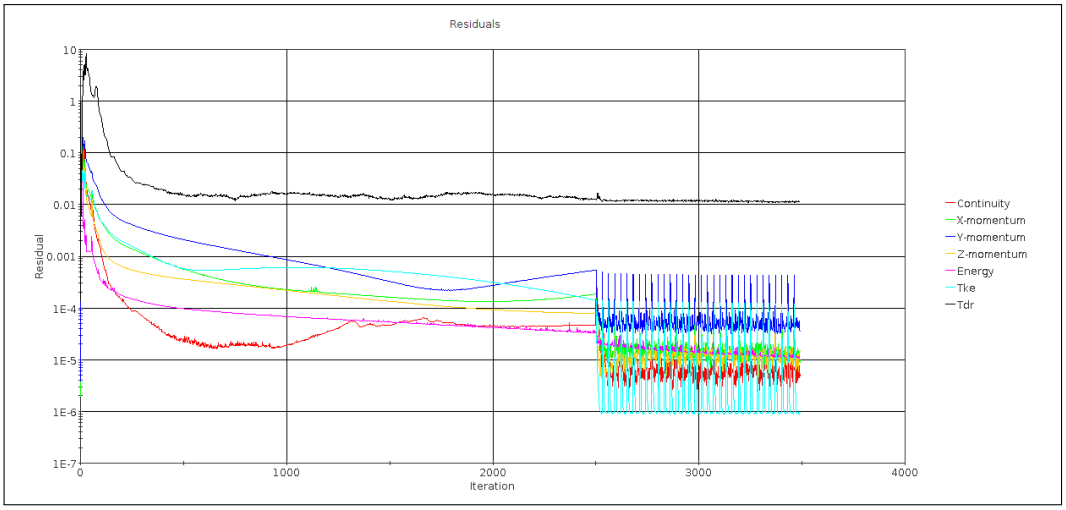

Figure 5.37: Inlet-plenum residuals vs. iterations (Design E6)

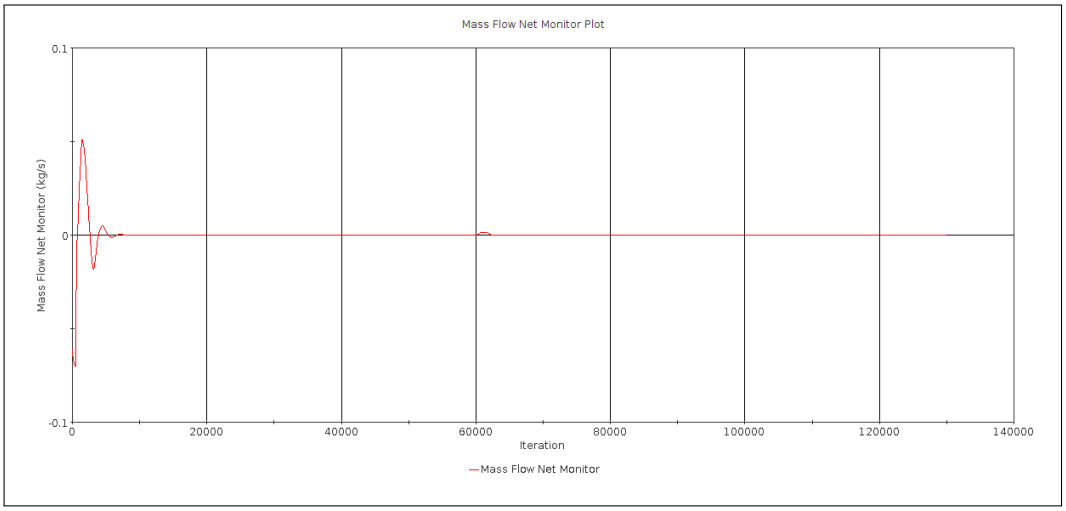

Figure 5.38: Net mas flow vs. iterations (Design A4 HTA)

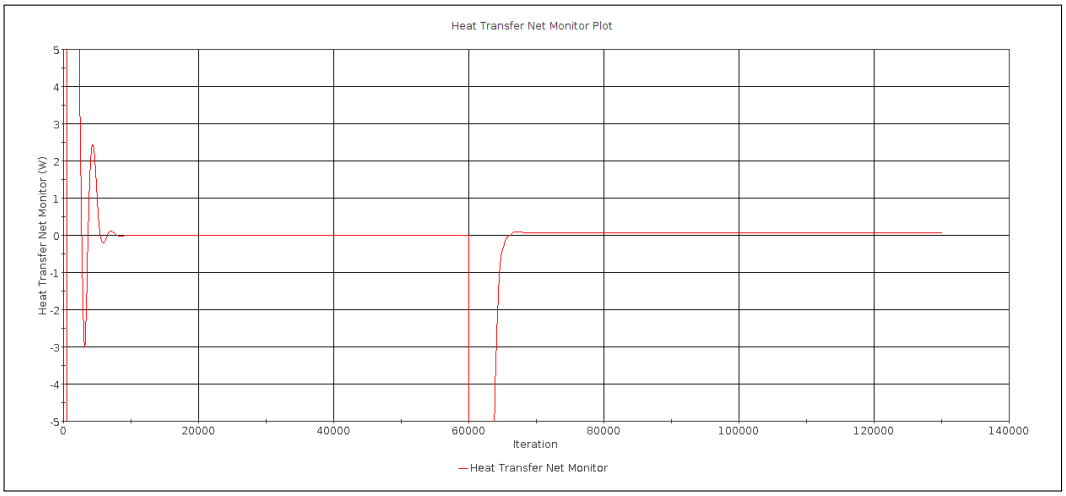

Figure 5.39: Net heat transfer vs. iterations (Design A4 HTA)

As mentioned in the body of this dissertation and described in detail by Hamman et al. (2015), the CFD results were not compared with experimental data. In fact, the intent of this study was not to compare CFD results with experimental data; although additional experimental data would have been used, if available. The main objective of this study was to compare different RCCS designs using traditional heat transfer analysis techniques and entropy generation analysis, acknowledging the existing limitations in modeling, simulations and computing.

5.4.4. Solution Uncertainty

Consistent with good engineering practice, the expected use of the results (e.g., journal article, nuclear experiment design), and available project funds, a verification and validation (V&V) methodology, for example similar to that presented by the NPARC Alliance Alliance (2015) or other quality control processes, should be followed (Hamman and Berry, 2010; Hamman et al., 2012). Throughout this research study an informal V&V process was followed, which included several V&V elements such as mesh refinement, verification of consistency (i.e., mass and energy conservation), residual convergence, and an informal code review. Therefore, several areas of uncertainty should be addressed.

As the uncertainty list is addressed, the reader should keep in mind that this study compared the performance of Duct 4 under two different inflow conditions (A4 and E6) and three heat transfer scenarios (HTA, HTB, HTC) using *the same* analysis tools (e.g., STAR-CCM+, Trelis), *the same* entropy generation analysis code (i.e., MATLAB), and *the same* computational mesh. So in general, it would be expected that any deviation from "true answer," for example due to a 'bug' in the MATLAB code, a coarse computational mesh, or the use of a RANS based turbulence model (e.g., $k - \epsilon$) in CFD simulations with entrance effects, would be reflected equally for both designs. Furthermore, given the computational overhead and resource requirements associated with sensitivity analyses for each of the items in the list, the complexities associated with uncertainty analyses, and the lack of experimental data, solution uncertainty was not quantified. In fact, quantifying

solution uncertainty is beyond the scope of this dissertation. Noteworthy is that it has been the author's experience (cf. vita) that engineering design processes still rely on the application of a 'safety factor' to compensate for design uncertainty (Hamman et al., 2012; Shigley and Mitchell, 1983; Ullman, 2003).

The areas of uncertainty are identified, using italicized text, as follows:

Item #1: The Small Thermal Turbulence Assumption (STTAss) is most likely not valid for the heat flux boundary conditions analyzed. The heat flux values applied to the walls of Duct 4 result in relatively large temperature gradients. According to Kramer-Bevan (1992), "This assumption (STTAss) is valid if convection dominates the flow. From this it can be assumed that flows with large thermal gradients might not be modelled accurately under STTAss. Further research is required to determine the processes for which STTAss is valid."

Item #2: A mesh refinement study was not conducted for Duct 4. Due to computational resource constraints, a mesh refinement study for the Duct 4 simulation was not performed. Therefore, a relatively fine mesh was developed and used in the analysis of all the Duct 4 studies. Noteworthy is that the Duct 4 wall y^+ values ranged from $0.7 < y^+ < 1.5$, values which are within the viscous sublayer. Additionally, it was shown that the viscous sublayer was resolved (Figures 4.27 and 4.28).

Item #3: Duct 4 experienced nonuniform flow conditions and entrance effects; yet empirical correlations, some of which require a uniform velocity field, were used in this study. A thorough literature search, associated with conditions under which the empirical correlations used in this study are valid, was not performed. Nevertheless, from a historical perspective, the conditions under which the experimental data (used to develop the empirical correlations) was collected should be put in perspective. The Colburn correlation will be used as an example.

The Colburn correlation, Equation 5.4, is a common empirical correlation found in the engineering textbooks and the literature (Cengel, 1998; Colburn, 1933, 1964). The equation consists of three non-dimensional parameters, the Nusselt number (Nu), Reynolds number (Re), and Prandtl number (Pr); each non-dimensional parameter

is related to material thermal properties and geometry ($Nu = \frac{hD}{k}$).

$$Nu = 0.023 Re_D^{0.8} Pr^{\frac{1}{3}} \tag{5.4}$$

Noteworthy is the uncertainty associated with Colburn correlation, which was developed in the early 1930s using experimental data from the late 1920s.[45] To put the relative uncertainty in perspective, Morris and Whitman (1928), and Sherwood and Petrie (1932) address the uncertainty related to their experimental data, especially the challenges of what temperatures to use in the evaluation of the thermal properties (e.g., viscosity, density, thermal conductivity). For example, Sherwood and Petrie (1932) state "It is difficult to estimate the probable error in the determination of the coefficient, h, in the tests reported. Extreme accuracy in the various measurements was not attempted, since it was soon found that, in the limited time available for the work (2 years, part time), accuracy must of necessity be sacrificed to a certain degree, in order that series of tests might be completed."

Item #4: Inlet boundary conditions for Duct 4 were obtained from a CFD simulation, characterized by residual convergence problems described in Section 4.4.3. Although the inlet-plenum CFD simulation was characterized by residual convergence problems, the author does not believe the inlet boundary conditions adversely effect the Duct 4 design comparison (Paragraph 2, Section 5.4.4).

Item #5: The use of the EVM closure models contributes to uncertainty. The capabilities and limitations of the EVM closure model is discussed in Section 2.3.2.

Item #6: The EGR results were not compared with experimental data. Although experimental data was collected for the air RCCS (and Duct 4), insufficient experimental data was collected to compare with the EGR results. But, the EGR results were compared with the global Lumped Parameter Model. The EGR results for the A4(HTA) model was 0.77 W/K; while the EGR results using the Lumped Parameter Model was 0.61 W/K. Given the fidelity of the local EGR approach, as compared with the global approach, the results of the comparison are of similar magnitude.

[45] The nuclear engineering discipline did not exist in the 1930s.

Item #7 The underlying assumption in the derivation of the governing equations is constant fluid and thermal properties, but temperature dependent properties were used for the CFD analyses. The average change from inlet to outlet (0" - 80") in density, dynamic viscosity, thermal conductivity is approximately 10%; specific heat capacity changes by only 1%. Although the uncertainty could be computed by re-running all simulations using constant properties at various temperatures, sensitivity analyses of this type are beyond the scope of this research study.

Item #8: Local freestream velocity calculations contributes to uncertainty. Freestream parameters such as velocity, temperature, and density are utilized to compute boundary layer parameters such as boundary layer thickness (99%, momentum, enthalpy), heat transfer coefficient, coefficient of friction, and entropy dissipation coefficient. Noteworthy is that the entropy results presented in Figures 5.22 and 5.24 are not impacted by freestream velocity.

Yet, there is some uncertainty with the techniques used to determine freestream velocity, especially at the entrance effect locations. Figures 5.40 and 5.41 present the results of comparing Technique 2 to Technique 1, and Technique 3 to Technique 1 for both the A4 and E6 designs.

Item #9: Inlet boundary conditions for Duct 4 were interpolated from the Duct 4 inlet-plenum outlet mesh onto the Duct 4 inlet mesh. Figures 5.42 and 5.43 depict contour plots of the interpolation process. Contour plot 'A' represents the inlet-plenum Duct 4 data plane (cf. Figure 4.31) of velocity magnitude, which was interpolated onto the inlet of the Duct 4 model, depicted in contour plot 'C.' Contour plots 'B' and 'D' show the computational mesh overlayed onto the velocity magnitude contour plots. In short, interpolation contributes to solution uncertainty.

In spite of the acknowledged solution uncertainty, this work provides a path forward on design decisions by establishing both traditional HTFF techniques and EGA as design discriminators to advance gas-cooled reactor designs using cross-cutting boundary layer and entropy analysis techniques.

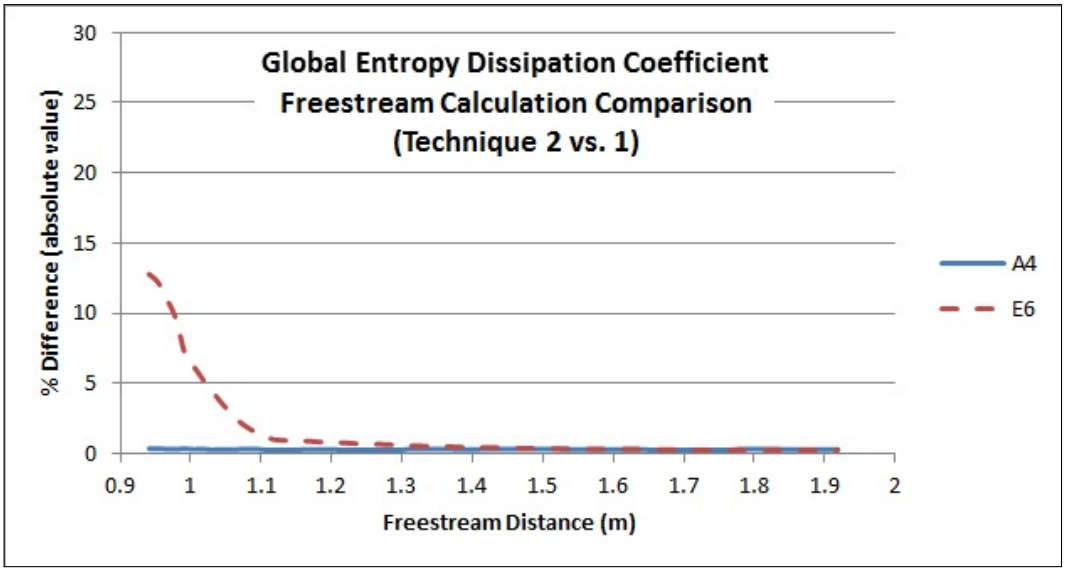

Figure 5.40: Entropy dissipation coefficient uncertainty (2 vs. 1)

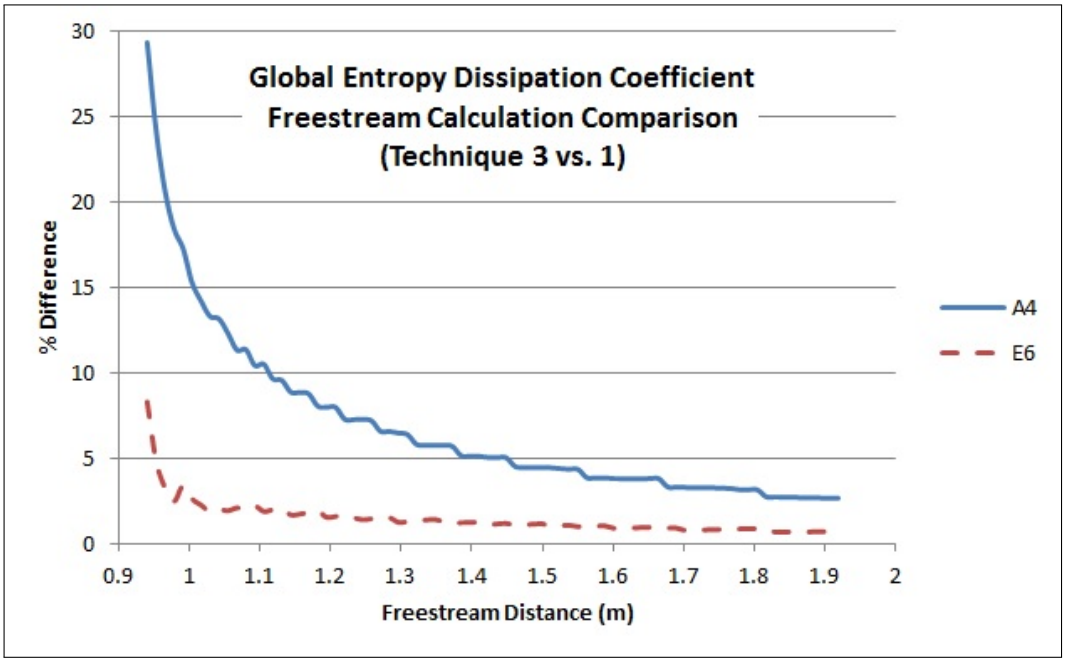

Figure 5.41: Entropy dissipation coefficient uncertainty (3 vs. 1)

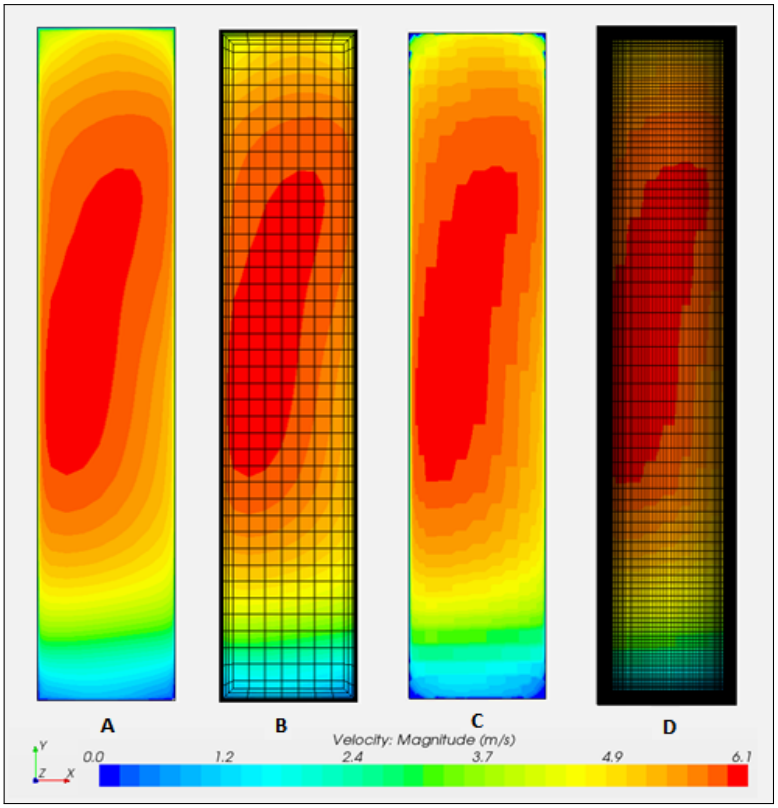

Figure 5.42: Data plane interpolation (A4)

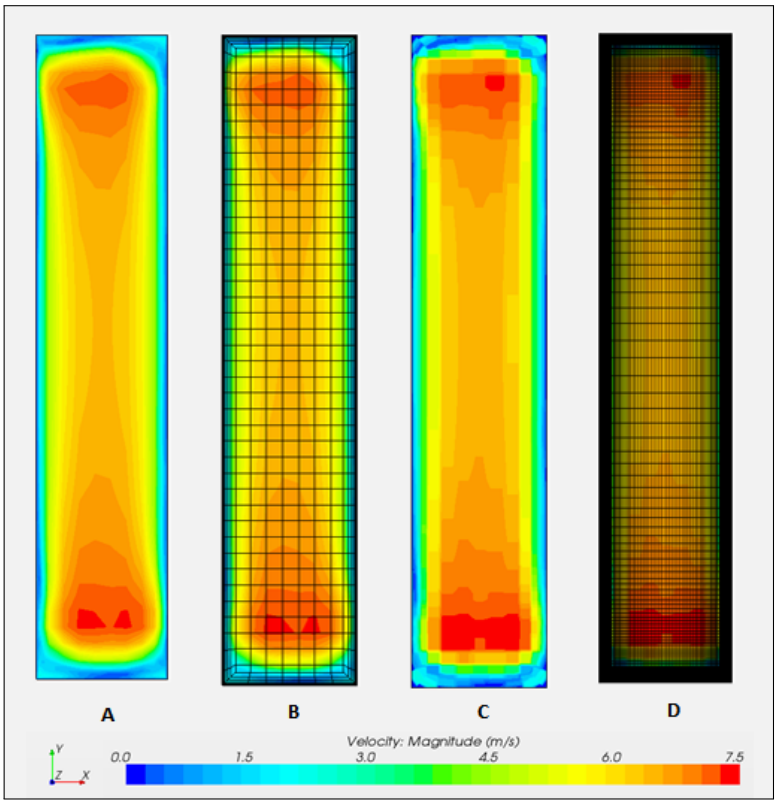

Figure 5.43: Data plane interpolation (E6)

Chapter 6: Conclusions and Contributions

6.1. Summary

This work is the culmination of independent research coupled with committee expectations in both basic and applied research performed with the purpose of demonstrating that traditional heat transfer and fluid flow techniques coupled with entropy generation minimization can be used as a design discriminator. The initial phase of the research was performed as part of two separate research projects, but with entropy generation analysis as the common link. The project reports, associated with the initial phase of research, are included as appendices. This research is unique in that it consists of an integrated approach to simulating heat transfer and fluid flow for a $\frac{1}{4}$ - scale air reactor cavity cooling system, characterized by nonuniform fluid flow and heat transfer, using entropy generation analysis (EGA) and traditional engineering analysis techniques.

The basic research, documented in Appendix A, was focused on the analysis of RANS viscous boundary layer transition characteristics associated with flat plate fluid flow characterized by zero, adverse, and favorable pressure gradients. Flat plate boundary layer characteristics, including entropy generation within the boundary layer, were studied since this is the most basic geometry on which a turbulent boundary layer develops. Direct numerical simulation (DNS) results, obtained under the influence of a zero pressure gradient (ZPG), were used as a reference to assess the RANS simulation results. The classical skin friction coefficient and local entropy generation rates were used as performance metrics. An important conclusion, directly related to the primary focus of this dissertation, was that RANS turbulence models neither predict nor should they be used to 'predict' laminar to turbulent transition.

The air RCCS applied research was focused on modeling and simulation of the UW $\frac{1}{4}$ - scale air RCCS. Several CFD simulations were performed. The computational overhead and resource requirements of the integrated RCCS model (i.e., inlet-plenum, riser-ducts, outlet plenum, and exhaust piping), coupled with simulation convergence problems and insufficient experimental data prompted the abandoning

of the integrated model in favor of modeling major components of the RCCS, specifically the inlet plenum and a heated duct. As part of this final analysis, CFD results were compared to limited experimental data. Since experimental heat flux measurements were not available for the duct walls, a calibration process was followed. The calibration process consisted of changing the duct wall heat flux CFD boundary conditions until the duct core air flow CFD temperature profile approximated the experimental data. The calibration results are presented in Figure 8 of Appendix B. An important conclusion, directly related to the primary focus of this dissertation, was that modeling and simulation of the air RCCS is complex, suggesting that modeling and simulation efforts should focus on individual components (e.g., inlet-plenum) rather than the integrated system.

A CFD simulation of the inlet-plenum was performed to establish inlet boundary conditions for Duct 4 since insufficient experimental data was available. The details of this simulation, including details on why experimental data was not available, are reported by Hamman et al. (2015). This research concluded that "CFD modeling of the RCCS inlet-plenum was challenging, primarily due to the desire to resolve the boundary layer in support of future work, turbulence model uncertainties, the complex flow patterns that develop in the plenum, the residual convergence difficulties, and the significant amount of computational resources required to conduct the simulation. Based on the lack of experimental turbulence data, the results predicted by different turbulence models, and the challenges associated with residual convergence (e.g., Tdr residual), the CFD inlet-plenum results should be considered qualitative."

Using lessons learned from the initial phase of research [i.e., Appendices A and B, Hamman et al. (2015)] and recognizing that the inlet-plenum research concluded that the CFD results should be considered qualitative, a design comparison study, using traditional HTFF techniques and entropy generation analysis, was performed. Specifically, several CFD simulations of two geometric designs (A4 and E6) were performed. But, due to computational overhead and resource requirements, it was not practical to model the entire length of Duct 4. So, approximately 60% (80

inches) of the length of the duct was modeled using the CFD results obtained from the inlet-plenum simulation as inlet boundary conditions; several heat flux boundary conditions (HTA, HTB, and HTC) were applied while keeping the power applied to the duct constant. The A4 design results were compared with the results of an alternate air RCCS designs in an effort to identify improvements to the existing UW $\frac{1}{4}$ - scale air RCCS. Based on EGA results coupled with traditional HTFF results, Design E6(HTA) was determined to be the best design.

6.2. Conclusions and Recommendations

Upon completion of this study, the following conclusions can be made:

1. Traditional HTFF techniques coupled with EGA are useful engineering design and evaluation tools. Entropy generation analysis is beneficial in that it provides the engineer with EGR information at a local level, revealing the location of viscous and thermal irreversibilities and the impact of design changes on these irreversibilities. Additionally, it allows the engineer to evaluate the relative performance, from both a viscous and thermal perspective, of different designs. The design constraint being that the design with the minimum EGR is presumably the most efficient design. Finally, local and global EGR information provides insight, not provided by traditional HTFF techniques, into the behavior of flows characterized by nonuniform flow and heat transfer.

2. Flat plate boundary layer studies are important in providing insight into flow features, such as boundary layer development and entropy generation rate, that should be expected in 3D ducts as the working fluid transitions from laminar to turbulent flow.

3. HTFF analyses of systems and designs characterized by nonuniform flow, heat transfer, and entrance effects are challenging, primarily due to nonuniform flow, boundary layer development, and determining local freestream velocity.

4. Since the inlet-plenum was modeled as having adiabatic walls, the only contributor to dissipation in the $\frac{1}{4}$ - scale air RCCS inlet-plenum is viscous dissipa-

tion. Therefore, any future design improvement efforts should consider design changes that impact viscous dissipation, for example redesigning the riser-ducts so they are flush with the inlet-plenum top wall, similar to Design E6.

5. The primary contributor to dissipation in the $\frac{1}{4}$ - scale air RCCS ducts is heat transfer. Therefore, any future design improvement efforts should consider design changes that impact heat transfer such as duct-to-duct spacing and material placement, including emissivity.

6. One of the motivations for evaluating the RCCS design for improvements was flow instabilities, which were discovered during testing of the UW experimental facility. Therefore, any redesign of the air RCCS should consider the recommendations mentioned in items 4 and 5.

6.3. Discipline Contributions

As a result of this research, several contributions to the nuclear engineering discipline were made:

The first contribution is the development of a design and analysis process, which incorporates traditional boundary layer heat transfer and fluid flow (HTFF) analysis techniques and entropy generation analysis (EGA), for the study of flows characterized by nonuniform flow and heat transfer. This work established both traditional HTFF techniques and EGA as design discriminators to advance gas-cooled reactor designs using cross-cutting boundary layer and entropy analysis techniques that can be applied to other engineering design processes such as the Idaho National Laboratory's Advanced Test Reactor (ATR) irradiation experiment design process (Hamman et al., 2012).

The second contribution is the detailed modeling and simulation efforts, directed at resolving the viscous and thermal boundary layers, of the air RCCS inlet-plenum and heated duct, which is characterized by nonuniform flow and heat transfer. To the best of the authors knowledge, no efforts have been made by other researchers to resolve these boundary layers. Noteworthy is that efforts to resolve the air RCCS viscous and thermal boundary layers have identified additional modeling and simulation

challenges not reported in the literature, including 3D entrance effects, computation of freestream variables, solution residual convergence issues, and the identification of experimental measurement needs in support of the validation of CFD codes.

The third and final contribution to the nuclear engineering discipline is the identification and thorough documentation of the factors that impact solution uncertainty in addition to documenting the information contained in the technical reports (Appendices A & B), a practice which is consistent with the documentation goals of V&V, discussed by Oberkampf and Roy (2010), which include reproducibility, traceability, and transparency. These goals should be followed as a requirement in the application of commercial and research CFD codes, especially by those involved in nuclear-related design engineering.

Supporting contributions include:

1. application of several techniques to determine local freestream velocity and temperature for non-uniform flows,

2. identification of the primary dissipation mechanism for the air RCCS scaled experimental facility,

3. identification of a design change (i.e., E6-HTA), which improves upon the original $\frac{1}{4}$ - scale air RCCS,

4. demonstrating the importance of a rigorous approach to establishing CFD inlet boundary conditions for transitional flows,

5. demonstrating the importance of access to simulation specific DNS or experimental data for use in the calibration and in the understanding of limitations of RANS transitional turbulence models, and

6. identification of experimental measurement needs, such as heat flux sensors and turbulence intensity measurements for the UW and ANL RCCS experimental facilities in support of verification and validation of CFD codes.

References

Abu-Ghannam, B. J., Nigim, H. H., and Kavanagh, P. "Surface curvature and pressure gradient effects on boundary layer transition." *Engineering Turbulence Modelling and Experiements–4*. eds. W. Rodi and D. Laurence. New York: Elsevier, 1999. 533–541.

Adeyinka, O. B. and Naterer, G. F. "Modeling of Entropy Production in Turbulent Flows." *Journal of Fluids Engineering* 126, 2004: 893–899.

AGARD. "A Selection of Test Cases for the Validation of Large-Eddy Simulations of Turbulent Flows." Tech. Rep. AGARD-AR-345, Advisory Group for Aerospace Research & Development, Neuilly-sur-Seine, France, 1998.

AIAA. "Guide for the Verification and Validation of Computational Fluid Dynamics Simulations." Tech. Rep. AIAA G-077-1998, AIAA, Reston, Virginia, 1998.

Alabi, K., Ladeinde, F., vonSpakovsky, M., Moorhouse, D., and Camberos, J. "Assessing CFD Modeling of Entropy Generation for the Air Frame Subsystem in an Integrated Aircraft Design/Synthesis Procedure." 44th AIAA Aerospace Sciences Meeting and Exhibit, Reno, Nevada: AIAA, 2006.

Alliance, NPARC. "Overview of CFD Verification and Validation." `http://www.grc.nasa.gov/WWW/wind/valid/tutorial/overview.html`, 2015. Web. 1 March 2015.

ANSYS. "ANSYS FLUENT Theory Guide." Tech. Rep. Release 14.5, ANSYS, Canonsburg, Pennsylvania, 2012.

ANSYS. "FLUENT." `http://www.ansys.com/`, 2015. Web. 1 March 2015.

ASME. "Quality Assurance Requirements for Nuclear Facility Applications." Tech. Rep. ASME-NQA-1-2008, ASME, New York, 2008.

ASME. "Standard for Verification and Validation in Computational Fluid Dynamics and Heat Transfer." Tech. Rep. ASME V&V 20-2009, ASME, New York, 2009.

Ball, J. M. and James, R. D. "The Scientific Life and Influence of Clifford Ambrose Truesdell III." *Archive for Rational Mechanics and Analysis* 161, 2002: 1–26.

Bechtel National, et al. "Preliminary Safety Information Document for the Standard MHTGR, Volume 1." Tech. Rep. HTGR-86-024 Amendment 13, Department of Energy, 1992. Published by Stone & Webster Engineering Corp.

Bejan, A. *Entropy Generation Through Heat and Fluid Flow*. New York: John Wiley & Sons, 1982.

Bejan, A. *Entropy Generation Minimization: The Method of Thermodynamic Optimization of Finite-Size Systems and Finite-Time Processes*. New York: CRC Press, 1996.

Bejan, A. *Convection Heat Transfer*. Hoboken, New Jersey: John Wiley & Sons, 2013, fourth ed.

Bejan, A., Tsatsaronis, G., and Moran, M. *Thermal Design & Optimization*. New York: John Wiley & Sons, 1996.

Ben-Naim, A. *Entropy Demystified: The Second Law Reduced to Plain Common Sense*. Hackensack, New Jersey: World Scientific, 2012, revised ed.

Bovo, M. and Davidson, L. "On the Numerical Modeling of Impinging Jets Heat Transfer–A Practical Approach." *Numerical Heat Transfer, Part A* 64, 2013: 290–316.

Boyd, C. F. and Armstrong, K. W. "Computational Fluid Dynamics Analysis of Natural Circulation Flows in a Pressurized-Water Reactor Loop under Severe Accident Conditions." Tech. Rep. NUREG-1922, U.S. Nuclear Regulatory Commission, Washington, DC, 2010.

Bradshaw, P. and Perot, J. B. "A Note on Turbulent Energy Dissipation in the Viscous Wall Region." *Physics of Fluids A* 5, 1993: 3305–3306.

Bredberg, J. "On the Wall Boundary Condition for Turbulence Models." Tech. Rep. 00/4, Chalmers University of Technology, Göteborg, Sweden, 2000.

CD-adapco. "STAR-CCM+." `http://www.cd-adapco.com/`, 2015a. Web. 1 March 2015.

CD-adapco. "STAR-CD." `http://www.cd-adapco.com/`, 2015b. Web. 1 March 2015.

Cebeci, T. *Convective Heat Transfer*. New York: Springer, 2002, second revised ed.

Cengel, Y. A. *Heat Transfer: A Practical Approach*. New York: McGraw-Hill, 1998.

Chhabra, A. and Singh, G. "Analysis & Integrated Modeling of the Performance Evaluation Techniques for Evaluating Parallel Systems." *International Journal of Computer Science and Security* 1, 2007: 1–10.

Colburn, A. P. "A Method of Correlating Forced Convection Heat-Transfer Data and a Comparison with Fluid Friction." *Transactions of the American Institute of Chemical Engineers* 29, 1933: 174–210.

Colburn, A. P. "A Method of Correlating Forced Convection Heat-Transfer Data and a Comparison with Fluid Friction (1933)." *International Journal of Heat and Mass Transfer* 7, 1964: 1359–1384.

Corradini, M. "Experimental Studies of NGNP Reactor Cavity Cooling System with Water." Tech. Rep. NEUP 09-202, University of Wisconsin - Madison, 2012. Project No. 09-781.

csimsoft. "Trelis 14 Advanced Meshing Software." `http://www.csimsoft.com/trelis.jsp`, 2015. Web. 1 March 2015.

Dave, A., Hu, R., Manera, A., Merzari, E., and Pointer, W. D. "CFD Simulations of NSTF." *Transactions of the American Nuclear Society*. vol. 107. 2012 ANS Winter Meeting and Nuclear Technology Expo, San Diego, California: ANS, 2012, 1323–1326.

Denton, J. D. "The 1993 IGTI Scholar Lecture: Loss Mechanisms in Turbomachines." *Journal of Turbomachinery* 115, 1993: 621–656.

Drost, M. K. and White, M. D. "Numerical Predictions of Local Entropy Generation in an Impinging Jet." *Journal of Heat Transfer* 113, 1991: 823–829.

El-Nashar, A. I. "To Parallelize or not to Parallelize, Speed Up Issue." *International Journal of Distributed and Parallel Systems* 2, 2011: 14–28.

Favre, A. "Formulation of the Statistical Equations of Turbulent Flows with Variable Density." *Studies in Turbulence*. eds. T.B. Gatski, C.G. Speziale, and S. Sarkar. New York: Springer-Verlag, 1992. 324–341.

Ferziger, J. H. and Perić, M. *Springer-Verlag Berlin Heidelberg*. New York: McGraw-Hill, 2002, third ed.

Frisani, A. *Analysis of the Reactor Cavity Cooling System for Very High Temperature Gas-Cooled Reactors Using Computational Fluid Dynamics Tools*. Master's thesis, Texas A&M University, College Station, Texas, 2010.

Ghasemi, E., McEligot, D. M., Nolan, K. P., Crepeau, J., Tokuhiro, A., and Budwig, R. S. "Entropy generation in a transitional boundary layer region under the influence of freestream turbulence using transitional RANS models and DNS." *International Communications in Heat and Mass Transfer* 41, 2013: 10–16.

Groves, C. E. *Computational Fluid Dynamics Uncertainty Analysis for Payload Fairing Spacecraft Environmental Control Systems*. Ph.D. thesis, University of Central Florida, Orlando, Florida, 2014.

Hamman, K. D. and Berry, R. A. "A CFD simulation process for fast reactor fuel assemblies." *Nuclear Engineering and Design* 240, 2010: 2304–2312.

Hamman, K. D., Guillen, D. P., and Murray, P. E. "Bounding Thermal Analysis in the ATR Small B-Positions (0.875 inch diameter)." Tech. Rep. ECAR-1687, Idaho National Laboratory, Idaho Falls, Idaho, 2012. Internal Report.

Hamman, K. D. and Skerjanc, W. F. "AGR–2 Pre–Test Prediction Analyses using the PARFUME Code for U.S. Fuel Particles." Tech. Rep. ECAR-1020 Rev. 2, Idaho National Laboratory, Idaho Falls, Idaho, 2012. Internal Report.

Hamman, K. D., Tokuhiro, A. T., Muci, M. A., and Corradini, M. L. "CFD Analysis of the $\frac{1}{4}$-Scale Air Reactor Cavity Cooling System Inlet Plenum." 23rd International Conference on Nuclear Engineering (ICONE23), Chiba, Japan: JSME, 2015. Accepted.

Hanjalić, K. and Jakirlić, S. "Second-Moment Turbulent Closure Modelling." *Closure Strategies for Turbulent and Transitional Flows*. eds. B.E. Launder and N.D. Sandham, Part A, chap. 2. Cambridge, England: Cambridge University Press, 2002. 47–101.

Herwig, H. and Kock, F. "Direct and indirect methods of calculating entropy generation rates in turbulent convective heat transfer problems." *Heat and Mass Transfer* 43, 2007: 207–215.

Hu, R. and Pointer, W. D. "CFD Analyses of Natural Circulation in the Air-Cooled Reactor Cavity Cooling System." Sun Valley, Idaho: M&C 2013, 2013.

Iandoli, C. L., Sciubba, E., and Zeoli, N. "The Computation of the Entropy Generation Rate for Turbomachinery Design Applications: Some Theoretical Remarks and Practical Examples." *International Journal of Energy Technology and Policy* 6, 2008: 64–95.

Jansen, K. E. *The Role of Entropy in Turbulence and Stabilized Finite Element Methods*. Ph.D. thesis, Stanford University, Stanford, California, 1993.

Jonas, P., Hladik, O., Mazur, O., and Uruba, V. "By–pass Transition of Flat Plate Boundary Layers on the Surfaces Near the Limit of Admissible Roughness." *Journal of Physics: Conference Series 318*. 13th European Turbulence Conference (ETC13), Warsaw, Poland: IOP Publishing, 2011.

Jones, W. P. and Launder, B. E. "The Prediction of Laminarization with a Two-Equation Model of Turbulence." *International Journal of Heat and Mass Transfer* 15, 1972: 301–314.

Kachanov, Y. S. "Physical Mechanisms of Laminar-Boundary-Layer Transition." *Annual Review of Fluid Mechanics* 26, 1994: 411–482.

Kähler, C. J., Scharnowski, S., and Cierpka, C. "On the uncertainty of digital PIV and PTV near walls." *Experiments in Fluids* 52, 2012: 1641–1656.

Kays, W. M. "The 1992 Max Jakob Memorial Award Lecture: Turbulent Prandtl Number - Where Are We?" *Journal of Heat Transfer* 116, 1994: 284–295.

Kepner, J. "HPC Productivity: An Overarching View." *International Journal of High Performance Computing Applications* 18, 2004: 393–397.

Knupp, P. and Salari, K. *Verification of Computer Codes in Computational Science and Engineering*. New York: Chapman & Hall/CRC, 2003.

Kock, F. *Bestimmung der lokalen Entropieproduktion in turbulenten Strömungen und deren Nutzung zur Bewertung konvektiver Transportprozesse*. Ph.D. thesis, Hamburg University of Technology, Hamburg, Germany, 2003.

Kock, F. and Herwig, H. "Local entropy production in turbulent shear flows: a high-Reynolds number model with wall functions." *International Journal of Heat and Mass Transfer* 47, 2004: 2205–2215.

Kramer-Bevan, J. S. *A Tool for Analysing Fluid Flow Losses*. Master's thesis, University of Waterloo, Waterloo, Ontario, 1992.

Langtry, R.B. *A Correlation–Based Transition Model using Local Variables for Unstructured Parallelized CFD Codes*. Ph.D. thesis, University of Stuttgart, Stuttgart, Germany, 2006.

Launder, B. E. "On the Computation of Convective Heat Transfer in Complex Turbulent Flows." *Journal of Heat Transfer* 110, 1988: 1112–1128.

Lien, F. S., Chen, W. L., and Leschziner, M. A. "Low-Reynolds-Number Eddy-Viscosity Modelling Based on Non-Linear Stress-Strain/Vorticity relations." *Engineering Turbulence Modelling and Experiments 3: Proceedings of the Third International Symposium on Engineering Turbulence Modelling and Measurements*. eds. W. Rodi and G. Bergeles. Crete, Greece: Elsevier, 1996, 91–100.

Lien, K., Monty, J. P., Chong, M. S., and Ool, A. "The Entrance Length for Fully Developed Turbulent Channel Flow." *Proceedings of the Fifteenth Australasian Fluid Mechanics Conference*. Fifteenth Australasian Fluid Mechanics Conference, Sydney, Australia: The University of Sydney, 2004.

Lisowski, D. D., Muci, M.A., Anderson, M. H., and Corradini, M. L. "Design Considerations for a Scaled Reactor Cavity Cooling System with Air for the VHTR." The 15th International Topical Meeting on Nuclear Reactor Thermal-Hydraulic (NURETH-15), Pisa, Italy: ANS, 2013.

Lockwood, B. A. *Gradient-Based Approaches for Sensitivity Analysis and Uncertainty Quantification within Hypersonic Flows*. Ph.D. thesis, University of Wyoming, Laramie, Wyoming, 2012.

Lommers, L. "Reactor Cavity Cooling System (Module 10d) (Technology Course for the Nuclear Regulatory Commission)." `https://inlportal.inl.gov/portal/server.pt/document/95764/module_10d_-_rccs_pdf`, 2010. Web. 8 March 2015.

Lomperski, S., Pointer, W. D., Tzanos, C. P., Wei, T. Y. C., Crooks, C. M., and Rodriguez, O. A. "Generation IV Nuclear Energy System Initiative, RCCS Studies and NSTF Preparation Air-Cooled Option." Tech. Rep. ANL-GenIV-142, Argonne National Laboratory, Lemont, Illinois, 2010.

Lomperski, S., Pointer, W. D., Tzanos, C. P., Wei, T. Y. C., and Krauss, A. R. "Generation IV Nuclear Energy System Initiative. Air-Cooled Option RCCS Studies and NSTF Preparation." Tech. Rep. ANL-GenIV-179, Argonne National Laboratory, Lemont, Illinois, 2011.

Malan, P., Suluksna, K., and Juntasaro, E. "Calibrating the γRe_θ Transition Model for Commercial CFD." 47th AIAA Aerospace Sciences Meeting Including The New Horizons Forum and Aerospace Exposition, Orlando, Florida: AIAA, 2009.

Malvern, L. E. *Introduction to the Mechanics of a Continuous Medium*. Upper Saddle River, New Jersey: Prentice-Hall, 1969.

Mann, D. "CD-adapco Energy Imbalance Technical Article Number 11487." `https://steve.cd-adapco.com/Site_Login`, 2013.

MathWorks. "MATLAB." `http://www.mathworks.com/`, 2015. Web. 30 April 2015.

Mayle, R. E. "The 1991 IGTI Scholar Lecture: The Role of Laminar-Turbulent Transition in Gas Turbine Engines." *Journal of Turbomachinery* 113, 1991: 509–537.

Mayle, R. E. and Schulz, A. "The Path to Predicting Bypass Transition." *Journal of Turbomachinery* 119, 1997: 405–411.

McEligot, D. M., Nolan, K. P., Walsh, E. J., and E., Laurien. "Effects of Pressure Gradients on Entropy Generation in the Viscous Layers of Turbulent Wall Flows." *International Journal of Heat and Mass Transfer* 51, 2008a: 1104–1114.

McEligot, D. M., Walsh, E. J, Laurien, E., and Spalart, P. R. "Entropy Generation in the Viscous Parts of Turbulent Boundary Layers." *Journal of Fluids Engineering* 130, 2008b: 061205–1–061205–12.

Menter, F.R., Esch, T., and Kubacki, S. "Transition Modelling Based on Local Variables." *Engineering Turbulence Modelling and Experiments 5*. eds. W. Rodi and N. Fueyo, chap. 6. Kidlington, England: Elsevier, 2002. 555–564.

Meyer, J. P. and Olivier, J. A. "Heat Transfer in the Transitional Flow Regime." *Evaporation, Condensation and Heat Transfer*. ed. Amimul Ahsan, chap. 12. Cambridge, England: InTech, 2011. 245–260.

Moin, P. and Mahesh, K. "DIRECT NUMERICAL SIMULATION: A Tool in Turbulence Research." *Annual Review of Fluid Mechanics* 30, 1998: 539–578.

Moore, J. and Moore, J. G. "Entropy Production Rates from Viscous Flow Calculations Part I – A Turbulent Boundary Layer FLow." *ASME Paper 83-GT-70*. ASME 1983 International Gas Turbine Conference and Exhibit, Phoenix, Arizona: ASME, 1983, 1–8.

Morris, F. H. and Whitman, W. G. "Heat Transfer for Oils and Waters in Pipes." *Industrial and Engineering Chemistry* 20, 1928: 234–240.

Muci, M. A. "RCCS Tests 14 and 16, Experimental Data." 2014a. 15 September 2014 email correspondence: Moses Muci and Kurt Hamman.

Muci, M. A. *Thermal Hydraulic Analysis of an Experimental Reactor Cavity Cooling System with Air*. Master's thesis, University of Wisconsin - Madison, Madison, Wisconsin, 2014b.

Müller, I. *A History of Thermodynamics: The Doctrine of Energy and Entropy*. New York: Springer-Verlag Berlin Heidelberg, 2007.

Naterer, G. F. and Camberos, J. A. *Entropy-Based Design and Analysis of Fluids Engineering Systems*. New York: CRC Press, 2008.

Nguyen, T., Petrov, V., and Manera, A. "Design of a Scaled Experimental Facility for the NGNP Reactor Cavity Cooling System." *Transactions of the American Nuclear Society*. vol. III. 2014 ANS Winter Meeting and Nuclear Technology Expo, Anaheim, California: ANS, 2014, 1629–1632.

Nolan, K. P. "Re: Int par (Matlab syntax text to compute integral parameters)." 2013. 28 January 2013 email correspondence: Kevin Nolan and Donald McEligot.

Nolan, K. P. and Zaki, T. A. "DNS data of Kevin Nolan and Tamer Zaki." 2012. 13 June 2012 email correspondence: Kevin Nolan and Donald McEligot.

Nolan, K.P. and Zaki, T.A. "Conditional Sampling of Transitional Boundary Layers in Pressure Gradients." *Journal of Fluid Mechanics* 728, 2013: 306–339.

Oberkampf, W. L . and Roy, C. J. *Verification and Validation in Scientific Computing*. New York: Cambridge University Press, 2010.

Oberkampf, W. L. and Trucano, T. G. "Verification and Validation Benchmarks." *Nuclear Engineering and Design* 238, 2008: 716–743.

Omotowa, O. A. *Scaling Approach and Thermal-Hydraulic Analysis in the Reactor Cavity Cooling System of a High Temperature Gas-Cooled Reactor and Thermal-Jet Mixing in a Sodium Fast Reactor*. Ph.D. thesis, University of Idaho, Idaho Falls, Idaho, 2014.

Orhan, Ö. E. *Investigation of the Effect of Turbulence on Entropy Generation in Turbomachinery*. Ph.D. thesis, Middle East Technical University, Ankara, Turkey, 2014.

Orhan, Ö. E. and Uzol, O. "Comparison of entropy generation figures using entropy maps and entropy transport equation for an air cooled gas turbine blade." *Proceedings of ECOS 2012*. The 25th International Conference on Efficiency, Cost, Optimization, Simulation and Environmental Impact of Energy Systems (ECOS 2012), Perugia, Italy: Firenze University Press, 2012, 107–114.

Pope, S. B. *Turbulent Flows*. New York: Cambridge University Press, 2001.

Reed, H. L. and Saric, W. S. "Linear Stability Theory Applied to Boundary Layers." *Annual Review of Fluid Mechanics* 28, 1996: 389–428.

Reynolds, W. C. and Perkins, H. C. *Engineering Thermodynamics*. New York: McGraw-Hill, 1977, second ed.

Roache, P. *Verification and Validation in Computational Science and Engineering*. Albuquerque, New Mexico: Hermosa Publishers, 1998.

Saric, W. S., Reed, H. L., and Kerschen, E. J. "Boundary-layer Receptivity to Freestream Disturbances." *Annual Review of Fluid Mechanics* 34, 2002: 291–319.

Sayadi, T., Hamman, C. W., and Moin, P. "Fundamental and subharmonic transition to turbulence in zero-pressure-gradient flat-plate boundary layers." Baltimore, Maryland: 64th Annual APS DFD Gallery of Fluid Motion, 2011. Video: `http://arxiv.org/abs/1110.3986`.

Sayadi, T., Hamman, C. W., and Moin, P. "Direct Numerical Simulation of Complete H-type and K-type Transitions with Implications for the Dynamics of Turbulent Boundary Layers." *Journal of Fluid Mechanics* 724, 2013: 480–509.

Schäfer, M. *Computational Engineering: Introduction to Numerical Methods*. New York: Springer-Verlag Berlin Heidelberg, 2006.

Schlichting, H. *Boundary-Layer Theory*. New York: McGraw-Hill, 1968, sixth ed.

Sciacovelli, A., Verda, V., and Sciubba, E. "Entropy generation analysis as a design tool - A review." *Renewable and Sustainable Energy Reviews* 43, 2015: 1167–1181.

Sciubba, E. "Some Remarks About the Computation of the Entropy Generation Rate in Turbomachinery." *International Journal of Transport Phenomena* 11, 2009: 79–96.

Sherwood, T. K. and Petrie, J. M. "Heat Transmission to Liquids Flowing in Pipes." *Industrial and Engineering Chemistry* 24, 1932: 736–745.

Shigley, J. E. and Mitchell, L. D. *Mechanical Engineering Design*. New York: McGraw-Hill, 1983, fourth ed.

Shuttleworth, M. "Peer Review Process." `http://tinyurl.com/pes8oet`, 2015. Web. 1 March 2015.

Simon. "Home in the Earth (tech notes)." `http://www.homeintheearth.com/`, 2015. Web. 16 March 2015.

Suluksna, K., Dechaumphai, P., and Juntasaro, E. "Correlations for Modeling Transitional Boundary Layers Under Influences of Freestream Turbulence and Pressure Gradient." *International Journal of Heat and Fluid Flow* 30, 2009: 66–75.

Systemes, Dassault. "SOLIDWORKS." `http://www.solidworks.com/`, 2015. Web. 1 March 2015.

Tannehill, J. C., Anderson, D. A., and Pletcher, R. H. *Computational Fluid Mechanics and Heat Transfer*. Philadelphia: Taylor & Francis, 1997, second ed.

TSI, Inc. "Air Velocity Transducer, Model 8455/8465/8475, Operation and Service Manual." Tech. Rep. 1980329 Rev. G, TSI, Shoreview, Minnesota, 2013. Web. 22 November 2014.

Tzanos, C. P. "CFD Analysis for the Applicability of the Natural Convection Shutdown Heat Removal Test Facility (NSTF) for the Simulation of the VHTR RCCS." Tech. Rep. ANL-GenIV-55, Argonne National Laboratory, Lemont, Illinois, 2005.

Ullman, D. G. *The Mechanical Design Process*. New York: McGraw-Hill, 2003, third ed.

Versteeg, H. K. and Malalasekera, W. *An Introduction to Computational Fluid Dynamics–The Finite Volume Method*. Harlow, England: Pearson Education Limited, 1995.

Walsh, E. J., McEligot, D. M., Brandt, L., and Schlatter, P. "Entropy Generation in a Boundary Layer Transitioning Under the Influence of Freestream Turbulence." *Journal of Fluids Engineering* 133, 2011: 061203–1–061203–10.

Wang, C., Gao, P., Tan, S., and Wang, Z. "Forced convection heat transfer and flow characteristics in laminar to turbulent transition region in rectangular channel." *Experimental Thermal and Fluid Science* 44, 2013: 490–497.

Whitaker, S. *Introduction to Fluid Mechanics*. Malabar, Florida: Krieger Publishing Company, 1992.

White, F. M. *Fluid Mechanics*. New York: McGraw-Hill, 1979.

White, F. M. *Viscous Fluid Flow*. New York: McGraw-Hill, 1991, second ed.

Wilcox, D. C. *Turbulence Modeling for CFD*. La Cañada, California: DCW Industries, 2000, second ed.

Winterton, R.H.S. "Where did the Dittus and Boelter Equation come from?" *International Journal of Heat and Mass Transfer* 41, 1998: 809–810.

Wu, X. and Moin, P. "Transitional and turbulent boundary layer with heat transfer." *Physics of Fluids* 22, 2010: 85–105.

Yang, X., Du, J., and Wang, Z. "An effective speedup metric for measuring productivity in large-scale parallel computer systems." *The Journal of Supercomputing* 56, 2011: 164–181.

Zaki, T. A. and Durbin, P. A. "Continuous Mode Transition and the Effects of Pressure Gradient." *Journal of Fluid Mechanics* 563, 2006: 357–388.

Appendix A: EPSCoR Project Report

The EPSCoR project report, which begins on the next page, is a summary of the initial boundary layer research that was conducted in preparation for the follow-on research described in the main body of this dissertation.

The purpose of EPSCoR study was to compare and contrast the transition characteristics of Reynolds-averaged Navier-Stokes turbulence and transition models, under the influence of pressure gradients, using the classical skin friction coefficient and local entropy generation rate as metrics. The following is a synopsis of the conclusions from that report. Readers are urged to refer to the main body of the report in order to better understand the context of the conclusions.

1. RANS turbulence models neither predict nor should they be used to predict laminar to turbulent transition.

2. Additional studies (e.g., uncertainty quantification) to characterize the RANS turbulence models ability to accurately predict entropy-related boundary layer parameters should be performed.

3. A fundamental understanding of the capabilities and limitations of RANS transition models should be established prior to their use.

4. Although the RANS transition model calibration process is complex and time consuming, when experimental data and/or DNS results are used to assess the performance of transition models, an effort should be made to calibrate the transition models in order to minimize error.

5. Unlike the well-documented Navier-Stokes equations, whose theoretical basis has been established for well over 100 years in the form of textbooks and journal articles, a sound theoretical basis for both the fluid friction and heat transfer entropy generation contributions is lacking.

TRANSITION BOUNDARY LAYER ENTROPY GENERATION ANALYSIS
(A Comparison between DNS and RANS Turbulence Modeling)

Fundamental Fluid Physics Studies for Energy Efficiency and Sustainability Project
(U. S. DOE Experimental Program to Stimulate Competitive Research/DE-SC0004751)

EPSCoR Project Report (CH-1A)

by

Kurt D. Hamman
(Graduate Student)

and

Akira Tokuhiro, Ph.D.
(Major Professor)

Department of Mechanical Engineering
University of Idaho

July 28, 2014

Abstract

The ability of cooling systems to remove heat while operating as efficiently as possible is a function of near-wall boundary layer characteristics. Research has shown that environmental effects, such as pressure gradients, affect boundary layers and consequently the performance of energy systems. In an effort to better understand the impact that environmental effects have upon boundary layers and ultimately to improve the efficiency of energy systems, the enigmatic concept of entropy has been used in various engineering and fundamental research studies, including recent efforts to characterize boundary layers during the transition from laminar to turbulent flow. The purpose of this study was to compare and contrast the transition characteristics of Reynolds-averaged Navier-Stokes turbulence and transition models, under the influence of pressure gradients, using the classical skin friction coefficient and local entropy generation rate as metrics. Numerical tools including STAR-CCM+ and Matlab were used to produce and analyze boundary layer numerical information related to local entropy generation rate. Verification, validation, and code quality assurance principles were followed in an effort to establish the accuracy and reliability of the numerical results. The following conclusions were drawn from this study: (1) RANS turbulence models should not be used to "predict" transition; (2) additional studies to characterize RANS turbulence models ability to accurately predict entropy-related boundary layer parameters should be performed; (3) transition models are not "predictive" models in that they require calibration; (4) a fundamental understanding of the capabilities and limitations of transition models is required prior to their use; (5) more educational literature, focused on the theoretical basis and history of the entropy generation mathematical expressions, is warranted.

Table of Contents

A. INTRODUCTION 126
B. LITERATURE REVIEW 128
Entropy Generation 128
Boundary layer transition 130
Turbulence Modeling 131
Verification and Validation 134
C. GOVERNING EQUATIONS 136
D. COMPUTATIONAL PROCESS AND TOOLS 139
Meshing Software 140
CFD Software 142
Boundary Conditions 143
MATLAB Code 144
Verification and Validation 145
E. RESULTS 146
F. CONCLUSIONS 150
G. REFERENCES 152
H. APPENDICES 157
Appendix A: Falkner-Skan Solution Process 157
Appendix B: Graphical Results 159

Note:

Change one (CH-1) to this report was issued on July 30, 2014. It was issued to correct a typographical error related to the independent variables (x, y, x) in the second term on the right-hand side of Equation (1). All of the remaining equations were verified to be consistent with the referenced literature. Change one 'A' (CH-1A) reflects a formatting change to accommodate binding margins.

A. INTRODUCTION

The ability of a cooling system to remove heat is a function of the working fluid near-wall boundary layer characteristics, including thickness, viscous dissipation (conversion of mechanical energy into heat), velocity gradients, and temperature gradients. Noteworthy is that an increase in mass flow rate increases viscous dissipation and decreases system efficiency. While a decrease in heat transfer corresponds to a decrease in temperature gradients resulting in an increase in system efficiency. Consequently, optimizing energy systems is a trade-off between heat transfer and mass flow rate; therefore, understanding boundary layer effects on system designs is an important step in improving the efficiency of energy systems.

Optimizing energy systems, from an efficiency perspective (as opposed to a reliability, cost, or size perspective), must include a critical analysis of the second law of thermodynamics. The second law is used extensively in the analysis of thermodynamic cycles, for example the Rankine cycle. But, the second law also can be used to evaluate systems and components that are not necessarily associated with cycles, for example heat exchangers and boundary layers (Bejan et al. 1996a). The primary parameter used in the analysis of heat exchangers and boundary layers is the local entropy generation rate, which consists of a fluid friction and a heat transfer contribution.

It is well known that the design and performance of a cooling system depends on whether or not the boundary layer is laminar, transitional, or turbulent. Laminar flows commonly are described as small fluid particles flowing in parallel layers, with no mixing between layers; hence, they are characterized as having poor heat transfer characteristics. Turbulent flows have good heat transfer properties including reliable friction and heat transfer correlations; yet modeling their behavior can be complex. Unfortunately, the unpredictability and complexities associated with transitional flows make it difficult to develop robust empirical friction and heat transfer correlations. In fact, Meyer and Olivier (2011) state “It is normally advised when designing heat exchangers to remain outside the transitional flow regime due to the uncertainty and flow instability in this region.”

Therefore utilization of computational fluid dynamics (CFD) in the design and evaluation of thermal systems and components requires that CFD codes have good numerical models, and most importantly accurate and robust turbulence and transition models.

Recognizing the importance of accurately modeling transition, including the shortcomings of using Reynolds-averaged Navier-Stokes (RANS) turbulence models to predict transition, efforts have been made to develop and improve transition models. In 2004, Menter et al. (2006a) introduced a framework (i.e., two transport equations without correlations), that they coupled with the SST K-Omega (k-ω) turbulence model; they named the framework the "γ-Re_θ model."[1] This framework was developed for implementation in CFD codes, primarily commercial CFD codes which are based on unstructured meshes with the capability of running in parallel on large high performance computers. Other commercial CFD code vendors have implemented this framework as well.

One of the most difficult and time consuming steps of the modeling and simulation process is verifying that the mathematical equations are solved right (e.g., correct syntax, mesh refinement analyses), comparing the numerical results with experimental data and/or DNS results, establishing the relative error of the results, and finally demonstrating that an appropriate level of software quality (e.g., version control, code documentation) was maintained. Typically referred to as 'Verification, Validation, and Uncertainty Quantification' (VV&UQ) and Code Quality Assurance (QA), these step are mandatory for safety-related calculations (i.e., nuclear reactor safety); yet, it is important that non-safety-related calculations (e.g., fundamental research) should have some degree of rigor established - on par with the risk associated with the use of incorrect results. Noteworthy is that different organizations establish different methodologies, which incorporate VV&UQ and QA principles. For example, the nuclear industry follows the ASME-NQA-1 quality assurance requirements for software associated with nuclear safety systems; while academia relies on the peer review process to evaluate the quality of computational research [Roache 1998, ASME 2008, Shuttleworth 2014]. Additionally, several professional

[1] Commonly referred to as the 'Gamma-ReTheta model'

societies and investigators have published V&V literature, but to date only V&V guidelines have been agreed upon [AIAA 1998, ASME 2009].

The purpose of this 11 month study was to compare and contrast the transition characteristics of Reynolds-averaged Navier-Stokes (RANS) turbulence and transition models, under the influence of pressure gradients, using the classical skin friction coefficient and local entropy generation rate as metrics [Walsh et al. 2011, McEligot et al. 2008a, McEligot et al. 2008b].[2] The transition characteristics associated with several pressure gradients, including adverse and favorable pressure gradients, were analyzed. Flat plate boundary layer characteristics were studied, since this is the simplest geometry on which a turbulent boundary layer develops. Direct numerical simulation (DNS) results, obtained under the influence of a zero pressure gradient (ZPG), were used as an initial baseline to assess the RANS simulation results[3]. The commercial computational fluid dynamics (CFD) code STAR-CCM+ was used to generate the RANS velocity fields. Two turbulence models were evaluated: the RANS Menter SST K-Omega (k-ω) turbulence model, and the Gamma ReTheta (γ-Re_θ) transition model [Cd-adapco 2013]. The entropy-related parameters were calculated using a MATLAB code developed for this study [MathWorks 2013]. The DNS velocity fields were generated, using a research code, developed independently from this study [Nolan and Zaki 2013, 2012].

B. LITERATURE REVIEW

Entropy Generation

Over the last three decades, there has been some interest in studying entropy from both a fundamental and applied research perspective. Yet, the popularity of this engineering discipline should not be considered bourgeoning. In a 2010 seminar, Camberos, an engineer at the U.S. Air Force Research Laboratory, shared his perspective on this concept: *"Given the universal applicability of the concept of entropy, the almost*

[2] This study was conducted over an 11 month period, beginning on August 19, 2013 and ending on July 28, 2014.

[3] Although experimental data was not available for comparison purposes, it should be noted that, in general, DNS results are considered equivalent to experimental data. [AGARD 1998, Ferziger 1998, Moin et al. 1998]

reverent recognition that the second law of thermodynamics holds a central place in modern science, it is surprising that the mention of entropy often elicits confusion, blank stares, and sometimes even bland indifference when presented to most audiences, even those technically inclined." In spite of its enigma, progress continues to be made in entropy-related research, including incorporating entropy into the engineering design process.

In 1982, Bejan, in an effort to provide a means of modeling and optimizing thermodynamic designs of real systems, introduced an optimization concept that integrated fluid mechanics, heat transfer, and thermodynamics. Referred to as "Entropy Generation Minimization (EGM)," this concept included the inherent thermodynamic reversibility of a system in the engineering analysis and optimization process; the theoretical foundation, including examples, was limited to analytical expressions. As a result of the growth of the EGM field (1980s and 1990s), Bejan wrote a new book related to optimization of engineering systems and components. The book expanded on topics similar to those found in his 1982 book, but presented the subject matter in more of a chronological format. For example, entropy-related thermodynamic, fluid mechanics, and heat transfer concepts were presented first followed by component then system applications [Bejan 1996b]. In 2008, Naterer and Camberos introduced a design methodology, based on the concept of entropy, referred to as "Entropy-based Design (EBD)." In addition to including analytical expressions in the design and analysis process, the theoretical foundation of their EBD book extended to experimental and numerical techniques such as particle image velocimetry (PIV) and CFD.

From more of a fundamental research perspective, Walsh and McEligot have published several research articles related to the entropy generation in boundary layers [Walsh, McEligot et al. 2011; McEligot et al. 2008a; McEligot, Walsh et al. 2008b]. Their efforts were directed at developing new knowledge of the entropy generation process. As a start, their primary focus was the study of entropy generation due to friction in viscous boundary layers for isothermal flows experiencing varying streamwise pressure gradients on flat-plate geometry. Their research utilized DNS results to quantify the entropy

generation rate during the transition from laminar to turbulent flow for several pressure gradients, including zero pressure gradient (ZPG), favorable pressure gradient (FPG), and adverse pressure gradients (APG). In their 2011 publication, they suggested evaluating boundary layer entropy-related phenomena using RANS codes: *"Provided Reynolds-averaged Navier-Stokes codes can predict the transition process adequately including sensitivity to inflow turbulence length scale - which is problematical - some may be useful in predicting entropy generation rates S''' or S''*.

Boundary layer transition

Although the majority of engineering flows can be categorized as turbulent, a significant amount of research related to transitional flow has been conducted. A motivation for this research is the fact that laminar and turbulent flow properties differ significantly; for example, significant increases in friction and heat transfer properties are observed during the transition process [Meyer and Olivier 2011; Wang et al. 2013]. Additionally, the onset of boundary layer transition can change depending on the system design. For example, studies have shown that adverse and favorable pressure gradients, surface roughness, and system inlet conditions such as freestream turbulence intensity and oscillatory velocity behavior influence boundary layer transition.

Environmental effects on transition, such as the pressure gradient influence on boundary layer streak intensity, were studied by Zaki and Durbin (2006), using direct numerical simulation (DNS) predictions. Their effort was directed at understanding the behavior of boundary layer streaks and characterizing the relationship between streak intensity and transition location. One of the conclusions from this study was that *". . . the boundary-layer streaks are highly unstable, and adverse pressure gradient has little contribution; transition takes place swiftly independent of the mean gradient in pressure."* Moreover, a recent numerical study by Nolan and Zaki (2013) provides insight into the relationship between boundary layer streaks and transition onset, including the relationship between turbulent spot growth rates and pressure gradient. From an experimental perspective, Abu-Ghannam et al. (1999) studied, using a wind tunnel, the

effects of curvature on boundary layers under ZPG and FPG conditions at turbulence intensity levels ranging from 0.8% to 6.4%. They concluded that transition was delayed on a surface with convex curvature at low levels of turbulence intensity; yet, at high turbulence levels and ZPG, transition along convex surfaces behaved similarly to flat surfaces. More recently, Jonas et al. (2011) performed wind tunnel studies, which investigated boundary layer development on an aerodynamically smooth surface and on surfaces covered with sandpaper. One of several conclusions reached by Jonas et al. was that *"Turbulent spot production starts sooner and with higher intensity in the rough wall boundary layer than in the smooth one at otherwise equal conditions and the increase of the free stream turbulence intensity amplifies this process."* The general conclusion that can be drawn from these research studies is that predicting the thermal and viscous characteristics of transition flow is important, yet difficult, since the underlying physical phenomena that occur when laminar flow transitions to turbulent flow, under the influence of pressure gradients and different geometries, is complex.

Turbulence Modeling

Motivated by the desire to understand the physical phenomena associated with the onset and transition to turbulence, and to improve existing turbulence and transition models, researchers continue to study fluid flows using numerical modeling techniques including DNS and RANS [Nolan and Zaki 2013, Sayadi et al. 2013, Menter et al. 2006a, Menter et al. 2006b][4]. This motivation partly stems from the need to improve CFD software used for industrial applications such as nuclear reactors and turbomachinary, especially given that significant changes in heat transfer and friction occur during the transition process. Some generalities about DNS and RANS are presented in this report, but a detailed discussion of RANS and DNS is beyond the scope of this study. Additional

[4] DNS and RANS are numerical techniques to approximate turbulence behavior. DNS solves the Navier-Stokes equations without the need for any turbulence modeling. RANS computes the mean velocity; the turbulent velocity fluctuations are modeled and based on mean flow variables. [AGARD 1998, Pope 2001]

details about these turbulence modeling approximations can be found in textbooks, for example Pope (2001) and Wilcox (1994).

The DNS approach to simulating turbulent flow has demonstrated that this numerical technique is capable of predicting the onset and transition to turbulence. For example, Menter et al. (2006) state that DNS is a suitable tool for transition prediction, but not without some shortcomings: *". . . the proper specification of the external disturbance level and structure poses substantial challenges. These methods are far too costly for engineering applications, and are currently used mainly as research tools and substitutes for controlled experiments."* Although DNS codes are capable of predicting boundary layer transition, they are used primarily as research tools due to the fact that they require more computational overhead (e.g., mesh resolution, data averaging requirements, and computing power) compared to RANS, and presently they are not well-suited for most engineering designs with complex geometries.

Unlike DNS, research has shown that RANS turbulence modeling is not capable of adequately predicting transition [Menter et al. 2006a, Menter et al. 2006b, Sayadi and Moin 2012, Ghasemi et al. 2013, Owen et al. 2013, Ghasemi et al. 2014]. For example, Menter (2006b) states that *"RANS averaging eliminates the effects of linear disturbance growth and is therefore difficult to apply to the transition process."* And, Sayadi and Moin (2012) state that *"The Reynolds-averaged Navier-Stokes (RANS) approach is not suitable for application to transitional flows."* Moreover, from a quantitative perspective, the ZPG RANS SST k-ω (2 eq) results presented in by Ghasemi et al. (2014) in their Figure 4 predict a much earlier transition onset and shorter transition length compared with the DNS results. Specifically, the error associated with the transition onset and transition length is approximately 80% and 90% respectively; errors of this magnitude are unacceptable in engineering designs, especially designs associated with nuclear technology. A similar conclusion, related to the inability of RANS turbulence models to predict transition adequately can be drawn upon examination of Figure 10 of Owen et al. (2013). Yet, RANS based codes continue to be the computational tool of choice for industrial CFD

applications. The primary reason for their popularity is their lower computational overhead, and their robustness and reliability (coupled with experimental data).

Recognizing the shortcoming in the ability of RANS models to predict transition, a 'calibrated predictive' modeling framework called the γ-Re_θ (Gamma ReTheta) model was introduced by Menter in 2004 [Menter et al. 2006a, Langtry 2006a, Langtry 2006b]. The framework consists of two transport equations, one equation for intermittency (γ) and the other equation for transition momentum thickness Reynolds number ($\overline{Re_{\theta t}}$); the transport equations are coupled with the SST K-Omega (k-ω) turbulence model. Noteworthy is that unlike turbulence models, the γ-Re_θ framework does not model the physics; it provides a means to transport the physics. But, the framework is designed to allow CFD analysts to input or modify existing transition models, such as transition length (F_{length}) and/or critical momentum thickness Reynolds number ($Re_{\theta c}$), which describe the physics. This framework has been implemented in commercial CFD codes. For example, the commercial CFD software Fluent has implemented the RANS based 'calibrated predictive' transition model framework; but, the specific empirical correlations are proprietary [Cd-adapco 2013, ANSYS 2012, Malan et al. 2009, Menter et al. 2006a]. Cd-adapco has implemented the γ-Re_θ framework including the Suluksna-Juntasaro empirical correlation in their STAR-CCM+ CFD software [Suluksna et al. 2009, Cd-adapco 2013].

Unfortunately, the γ-Re_θ model calibration process is complex and time consuming. Furthermore, the γ-Re_θ model is sensitive to mesh density; for example, numerical testing on flat plates by Langtry (2006a) revealed that at y^+ values less than 0.001, the transition location moved downstream. Therefore, the STAR-CCM+ User Guide requires that wall normal mesh spacing should be fine enough to obtain $0.1 \leq y^+ \leq 1$ and that all y^+ or low y^+ wall treatments should be used. [Cd-adapco 2013] The ANSYS Fluent Theory Guide (2012) has the following mesh and discretization restrictions: *"In order to capture the laminar and transitional boundary layers correctly, the mesh must have a y+ of approximately one. If the y^+ is too large (that is, > 5), then the transition onset location moves upstream with increasing y^+. It is recommended that you use the bounded second order upwind based discretization for the mean flow, turbulence and transition equations."*

Malan et al. (2009) and Langtry (2006a) provide a good analysis of the γ-Re_θ model, including model development, testing, and calibration.

Several project publications evaluated Fluent's 'Transition SST Model,' which essentially is the γ-Re_θ model [Ghasemi et al. 2013, Owen et al. 2013, Ghasemi et al. 2014]. Based on a review of their research, it is not clear why the Fluent Transition SST Model, referred to as the "SST k-ω (4 eq)" model by Ghasemi et al. (2013) and as the "transitional k-ω four equation" model by Owen et al. (2013), behaved as shown in these publications. For example, referring to Figure 10 of Owen et al., which presents plots of C_f vs. $Re_x^{1/2}$, it is noted that the transition model results of Owen et al. compare very well with the DNS results; but Ghasemi et al. transition model results, presented on the same figure, compare poorly with the DNS results. Owen concludes his paper with the following: *"*Overall the present study shows improvements over the CFD results by Ghasemi et al. likely due to the much finer grid used and the more accurate inlet boundary conditions for turbulent structures." Noteworthy is that Owen et al. used a fine mesh (i.e., grid) of 1,000,000 computational elements, and Ghasemi et al. used a coarser mesh of approximately 150,000 elements. Given that the transition model most likely would require calibration and recalling that it has mesh density requirements (i.e., wall y^+ restrictions), a discussion by Owen et al. (2013) and Ghasemi et al. (2013, 2014) related to the maximum/minimum wall y^+ values including a discussion related to the calibration of the transition model would have been beneficial. Therefore, it is difficult to conclude with any certainty as to the reason for the differences between the transition model results of Ghasemi et al. (2013, 2014) and Owen et al. (2013).

Verification and Validation

Advances in computer technology over the last 30 years has resulted in a great deal of emphasis on the use of computers to simulate physical processes; consequently, a new computational engineering field, loosely referred to as Verification and Validation (V&V),

has emerged.[5] In 1998, Patrick Roache authored the popular book 'Verification and Validation in Computational Science and Engineering,' which provides a good discussion on V&V concepts, applications, and lessons learned; furthermore, he provides a practical discussion on code quality assurance and certification, an often overlooked aspect of the modeling and simulation process. In 2003, Knupp and Salari published their book 'Verification of Computer Codes in Computational Science and Engineering,' which addresses the concept of verification from more of a mathematical perspective, specifically verifying the code order of accuracy. William Oberkampf and Christopher Roy (2010) coauthored a recent book titled 'Verification and Validation in Scientific Computing,' which encompasses a lot of information from a mathematical, computer science, engineering, risk, and management and planning perspective. Collectively these books provide a solid foundation for managers, technical leads, and computational engineers and analysts to understand and apply V&V techniques in the engineering design process.

A basic explanation of V&V is warranted in this report. The V&V process is used to establish that the mathematical equations, used to describe the physical phenomena of interest, were solved correctly and that the correct mathematical equations were used to describe the physical phenomena. For example and with respect to "correct mathematical equations," it would be inappropriate to use the Bernoulli Equation to describe viscous dissipation in a boundary layer; with respect to solving the "mathematical equations correctly," it is paramount that the code syntax is free of errors (i.e., bugs).

Code verification, establishing that the code is mathematically correct (e.g., free of coding errors), is the first step in the V&V process. Some code verification activities include: simple tests such as verifying the code conserves mass, order of accuracy and mesh refinement studies, and evaluation of discretization error (assuming an exact solution is available) [Oberkampf and Roy 2010]. The responsibility for software verification 'primarily' resides with the commercial code vendors and independent code developer.

[5] Loosely speaking, the use of the term V&V implicitly assumes, but not necessarily, that uncertainty quantification (UQ) and code quality assurance (QA) principles are included as well.

But, 'ultimately' the responsibility for ensuring the responsibility for code verification rests with the user.

Validation, determining that the results of the simulation are an accurate representation of the real world, primarily resides with the CFD practitioner [AIAA 1998, ASME 2009]. As part of the validation process, CFD practitioners rely on experimental data and/or DNS results to assess their numerical results. Noteworthy, the underlying assumption is that the experimental data and/or DNS results are accurate. In fact, Roache's statement (1998) *"Experimental data is not as sacrosanct as many computational practitioners believe,"* highlights the importance of CFD practitioners understanding the capabilities and limitations of not only experimental data, but DNS results as well. Likewise, it is important that experimentalists understand the capabilities and limitations of computational mechanics.

C. GOVERNING EQUATIONS

Entropy transport in turbulent incompressible flows can be described using the time-averaged entropy transport equation presented below, where the third and fourth terms on the right-hand side of Equation (1) represent the entropy generation rate contributions from dissipation and temperature, respectively [Herwig and Kock 2007].

$$\rho\left(\frac{\partial \bar{s}}{\partial t}+\bar{u}\frac{\partial \bar{s}}{\partial x}+\bar{v}\frac{\partial \bar{s}}{\partial y}+\bar{w}\frac{\partial \bar{s}}{\partial z}\right)=\overline{div(\frac{\vec{q}}{T})}-\rho\left(\overline{\frac{\partial u's'}{\partial x}}+\overline{\frac{\partial v's'}{\partial y}}+\overline{\frac{\partial w's'}{\partial z}}\right)+\overline{(\frac{\Phi}{T})}+\overline{(\frac{\Phi_\Theta}{T^2})} \quad \text{Equation(1)}$$

x, y, z represent Cartesian coordinates

u, v, w represent velocity components

s represents entropy

T represents temperature

Φ represents dissipation of mechanical energy (fluid friction contribution)

Φ_Θ represents loss of mechanical energy (heat transfer contribution)

Since entropy is a function of temperature and pressure, and CFD codes use mass, momentum, and the energy equation (i.e., first law of thermodynamics) to compute temperature and pressure fields, it is not necessary for CFD codes to solve Equation (1). Therefore, entropy can be computed during the post-processing process. But, determining the mathematical formulation for the entropy generation terms (heat transfer and fluid friction) is not simple. Contributing to this complexity is the challenges associated with modeling turbulent flow.

The analyses performed as part of this report focus on the entropy generation fluid friction term $\overline{(\frac{\Phi}{T})}$; specifically, this study is limited to isothermal flows [Schlichting 1968, Walsh et al. 2011, Ghasemi et al. 2013, Owen et al. 2013, Ghasemi et al. 2014]. The terminology and symbols used in this report are consistent with that presented by Walsh et al. (2011). The equations used to develop the velocity fields (e.g., Navier-Stokes equations), boundary layer equations, and theoretical formulation of metrics (e.g., for example wall shear stress, momentum thickness) are beyond the scope of this report; therefore, they will not be presented here. Their formulations can be found in fluid dynamics textbooks [Wilcox 1994, White 1991, Potter 1997].

In total, four entropy-related equations are presented and discussed; these equations were used to generate the results presented in the Appendix B. The secondary purpose of presenting these equations is to resolve any questions as to the correct form of the equations.[6] Specifically, Equations (2) through Equation (4) are the primary entropy-related equations used to compute DNS and RANS entropy results presented in the appendix. Additionally, Equation (4), the 'integral equation for entropy generation,' was verified to be consistent with Rotta's (1962) Equation (20.22) and Ghasemi et al. (2013) Equation (7). Equation (5) was extracted from Schlichting Equation (23.8d) [1968] to resolve any questions related to the appropriate form of the dissipation function, specifically the presence of a negative sign associated with the Reynolds shear stress term.

[6] Several references have conflicting formulations of entropy-related equations, most likely the result of typographical errors and/or confusing nomenclature. [Walsh et al. 2011, Equation (5) and Equation (8); Ghasemi et al. 2013, Equation (5); and Ghasemi et al. 2014, Equation (2)]

The approximate volumetric entropy generation rate:

$$(S'''_{ap})^+ \approx [\frac{\partial U^+}{\partial y^+} - (\overline{uv})^+](\frac{\partial U^+}{\partial y^+})] \quad \text{Equation (2)}$$

The entropy generation integral equation:

$$(S'')^+ = \frac{TS''}{\rho u_\tau^3} = \int_0^{y^+} (S'''\{y^+\})^+ dy^+ \quad \text{Equation (3)}$$

$$(S''\{\delta\})^+ \approx \int_0^\delta \left(\frac{\partial U^+}{\partial y^+}\right)^2 dy^+ - \int_0^\delta (\overline{uv})^+ \left(\frac{\partial U^+}{\partial y^+}\right) dy^+ \quad \text{Equation (4)}$$

$$- \int_0^\delta [\overline{(u^2)^+} - \overline{(v^2)^+}] \left(\frac{\partial U^+}{\partial x^+}\right) dy^+$$

$$-(d/dx^+) \int_0^\delta U^+ (1/2)(\overline{q^2})^+ dy^+$$

$$-(1/2) \overline{v_\delta^+ [\left(u_\delta^2\right)^+ + \left(v_\delta^2\right)^+ + \left(w_\delta^2\right)^+]} - \overline{v_\delta^+ p_\delta^+}$$

$$\overline{\mu \Phi} = (\mu \frac{\partial \bar{u}}{\partial y} + \tau'_{xy}) \frac{\partial \bar{u}}{\partial y} \quad \text{Equation (5)}$$

where $\tau'_{xy} = -\rho \overline{u'v'}$

The dissipation coefficient equation is included for completeness [Walsh et al. 2011]:

$$C_d = \frac{TS''}{\rho U_\infty^3} = (S''\{\delta\})^+ \left(C_f/_2\right)^{\frac{3}{2}} \quad \text{Equation (6)}$$

A review of the literature related to Equation (4) reveals that the foundation for this equation is an energy equation, specifically the total energy dissipation equation [Rotta, 1962]. As noted by Walsh et al. (2011), the first four terms on the right-hand-side of Equation (4) were derived by Rotta, and referred to as "Rotta's approach." The last two terms represent turbulent diffusion and pressure diffusion in the freestream. A more detailed discussion on the foundation of Equation (4) is presented by Walsh et al. (2011).

More recently, two additional freestream terms, presented at a 2014 project review meeting, are believed to contribute to the 'integral for entropy generation equation' [McEligot, 2014a]. Equation (7) includes the two additional terms (presented in wall coordinates) referred to as terms seven and eight; their relative contribution to the entropy generation integral equation was not examined as part of this study.

$$(S''\{\delta\})^+ \approx \int_0^\delta \left(\frac{\partial U^+}{\partial y^+}\right)^2 dy^+ - \int_0^\delta (\overline{uv})^+ \left(\frac{\partial U^+}{\partial y^+}\right) dy^+ \qquad \text{Equation (7)}$$

$$- \int_0^\delta [\overline{(u^2)^+} - \overline{(v^2)^+}] \left(\frac{\partial U^+}{\partial x^+}\right) dy^+$$

$$-(d/dx^+) \int_0^\delta U^+ (1/2)(\overline{q^2})^+ dy^+$$

$$-(1/2)\, \overline{v_\delta^+ \left[\left(u_\delta^2\right)^+ + \left(v_\delta^2\right)^+ + \left(w_\delta^2\right)^+ \right]} - \overline{v_\delta^+ p_\delta^+}$$

$$- V_\delta^+ \left(\frac{1}{2}\right) \left(\overline{q^2}\right)_\delta^+ + \left(\frac{\partial}{\partial y^+} \left[\left(\frac{1}{2}\right) \left(\overline{q^2}\right)^+ + (v^+)^2 \right] \right)_\delta$$

D. COMPUTATIONAL PROCESS AND TOOLS

The CFD modeling and boundary layer analysis process used for this study is presented in Figure 1. A computational mesh, similar to – but coarser than – the DNS meshes used by Nolan and Zaki (2013) was generated for each of the four RANS simulation design cases. Trelis, the commercial version of Sandia National Laboratories (SNL) CUBIT meshing software, was used to generate the RANS meshes [Cimsoft 2013, SNL 2014]. This software was chosen due to its robustness and user options in generating a structured mesh with elements clustered in the plate wall normal direction. The meshes were imported into STAR-CCM+ commercial CFD software where simulations were performed in order to develop velocity, turbulence intensity, and turbulent viscosity predictions. A mesh refinement study was performed; the final RANS mesh parameters presented in Table 1. The results were exported to a boundary layer analysis code developed using MATLAB, where the CFD predictions were used to compute skin friction and entropy fields.

Meshing Software

Trelis Pro 14.0.4, was used to generate the meshes for the RANS studies. A clustered mesh in the wall normal direction was developed using a mesh bias scheme factor (wall normal expansion ratio) of 1.057. This value of the bias scheme factor was chosen in order to obtain wall y^+ values less than one. Consistent with STAR-CCM+ User Guide (2013) mesh wall y^+ restrictions that $0.1 < y+ < 1$, wall y^+ values for all pressure gradient cases evaluated using the γ-Re_θ model were within the range $0.11 < y+ < 0.22$. Note that for V&V purposes and given that the γ-Re_θ model behavior (for example predicted transition location) is sensitive to mesh parameters, including y+ values, good engineering practice is to report mesh bias scheme factors and y+ values [Langtry, 2006a]. The final mesh sizes were based on the ZPG mesh refinement study, which was performed in both the wall normal direction and freestream directions. The performance of the commercial CFD software residuals were evaluated as part of the mesh refinement study as well; the residuals for the ZPG are presented in Figure 2. Note that although the converged value of the residual for the intermittency transport equation is adequate ($\sim 1x10^{-5}$), it is not clear why this residual did not reach a value on the order of $1x10^{-14}$, a value reached by the other residuals. The intermittency residual showed some sensitivity to mesh refinement, but an analysis of its behavior was not performed because an in-depth examination of the intermittency residual was beyond the scope of this study.

Table 1 is a summary of mesh and mesh design parameters, specifically: analysis type, mesh design, Thwaites pressure gradient parameter (λ_θ), Falkner-Skan parameter (β), domain geometry, grid size, and number of computational elements, respectively (Nolan and Zaki 2013).[7] The Table 1 DNS mesh values were reported by Nolan and Zaki (2013), and the DNS_{mean} values were obtained from the averaged raw DNS results of Nolan and Zaki (2012) via McEligot. The DNS_{mean} Falkner-Skan parameters and DNS_{mean} Thwaites pressure gradient parameter presented in Table 1 were computed using the MATLAB boundary analysis code to verify the DNS data was consistent with the Nolan and Zaki

[7] The DNS_{mean} Falkner-Skan parameter (β) was derived from the slope 'm' of a log-log plot of freestream velocity versus Reynolds number, similar to Nolan and Zaki (2013) Figure 1(a), created with the Matlab code.

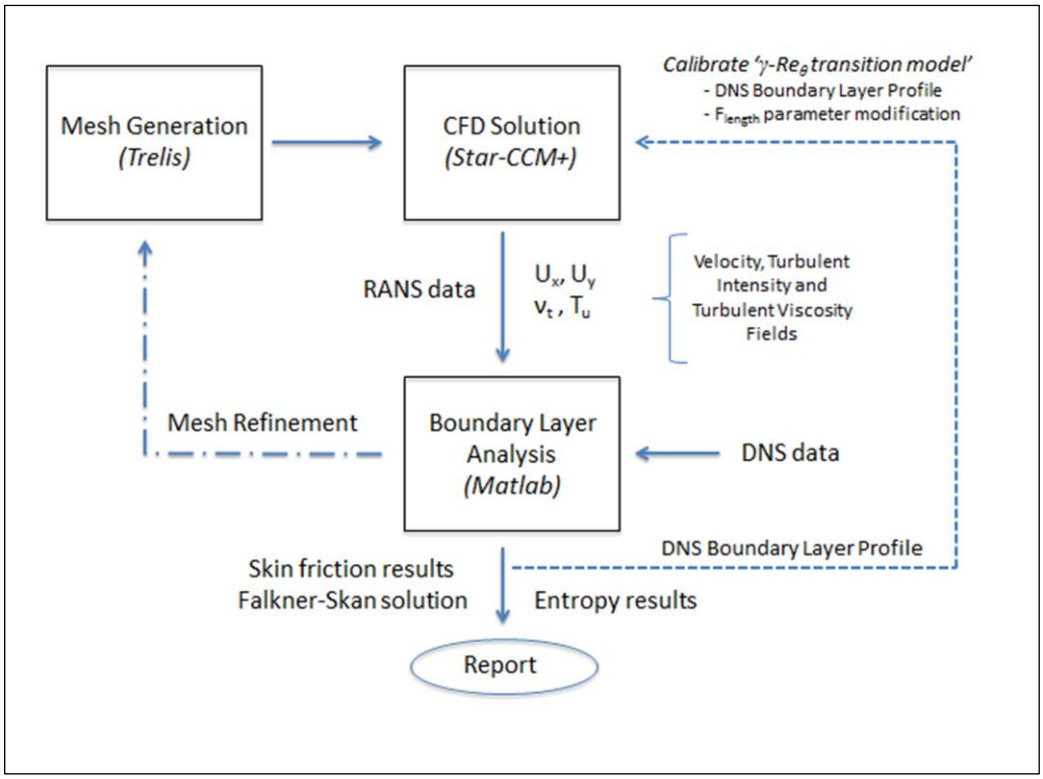

Figure 1 CFD Modeling and Boundary Layer Analysis Process

Table 1 Mesh Parameters: analysis type, mesh design, Thwaites pressure gradient parameter, Falkner-Skan parameter, domain geometry, grid size, and number of computational

Analysis	Design	λ_θ	β	Lx	Ly	Lz	nx	ny	nz	# Elements
DNS	**ZPG**	0	0	900	40	30	3072	192	192	113,246,208
DNS	**FPG**	0.02	0.11	1200	40	30	4096	192	192	150,994,944
DNS	**APG**	-0.02	-0.08	600	40	30	2048	192	192	75,497,472
DNS	**APG_{strong}**	-0.04	-0.14	600	40	30	2048	192	192	75,497,472
DNS_{mean}	**ZPG**	0.000	0.007	900	40	N/A	1536	96	N/A	147,456
DNS_{mean}	**FPG**	0.025	0.118	1200	40	N/A	1024	96	N/A	98,304
DNS_{mean}	**APG**	-0.020	-0.089	600	40	N/A	1024	96	N/A	98,304
DNS_{mean}	**APG_{strong}**	-0.036	-0.150	600	40	N/A	1024	96	N/A	98,304
RANS	**ZPG**	-	-	900	40	N/A	3072	96	N/A	294,912
RANS	**FPG**	-	-	1200	40	N/A	4096	96	N/A	393,216
RANS	**APG**	-	-	600	40	N/A	2048	96	N/A	196,608
RANS	**APG_{strong}**	-	-	600	40	N/A	2048	96	N/A	196,608

desired Falkner-Skan parameter. Figure 3 presents the DNS streamwise Thwaites pressure gradient parameters, computed from the Matlab code, for each design case. The Figure 3 values were smoothed and filtered to eliminate numerical noise caused by differentiation in the streamwise direction [Matlab 2013]. Note that the Thwaites pressure gradient parameters reported in Table 1 are approximated values extracted from Figure 3, located in Appendix B, just prior to the beginning of boundary layer transition; additionally, the Thwaites pressure gradient parameter was not computed for the RANS design cases. Figure 4 compares the ZPG Thwaites pressure gradient parameter filtered/smoothed and unfiltered/unsmoothed results.[8] The equation for Thwaites' pressure gradient parameter is shown in Equation (8),

$$\lambda_\theta = \frac{\theta^2}{\nu}\frac{dU_\infty}{dx} \qquad \text{Equation (8)}$$

where, θ represents boundary layer momentum thickness and ν represents kinematic viscosity [Abu-Ghannam et al. 1999].

CFD Software

The commercial CFD code STAR-CCM+ was used to generate the two-dimensional steady-state RANS velocity fields for this study [Cd-adapco 2013]. The CFD software was computed on a ZaReason 'Fortis Extreme 2' workstation with an AMD FX-8350 8-core processor and Linux Ubuntu 12.04 LTS operating system (Linux). STAR-CCM+ uses a cell-centered finite volume discretization technique and an unstructured mesh generator. Two generalized solvers are available, coupled and segregated. Several turbulence models are provided including variants of the K-Epsilon (k-ε) and K-Omega (k-ω) models. Additionally, a turbulence transition modeling framework, referred to as the γ-Re_θ (gamma ReTheta)

[8] Parameters dependent on freestream gradients and computed using the MATLAB code were smoothed and filtered to eliminate numerical noise. The numerical noise was believed to be the result of differentiating terms, which are a function of integral parameters, along the freestream direction. Figure 6 shows the stair-stepping pattern that develops along the freestream direction for boundary layer thickness (e.g., integral parameter).

model is provided allowing users to implement transition models or use the default Suluksna-Juntasaro model [Cd-adapco 2013]. The following simulation settings were used to generate the RANS velocity fields: constant density, second order upwind discretization, SST-Mentor k-ω turbulence model, and the segregated solver. In an effort to evaluate the STAR-CCM+ transition model, one ZPG simulation using the γ-Re_θ model was performed.

Boundary Conditions

Boundary conditions for the CFD simulation were chosen in order to approximate those used by Nolan and Zaki (2013). Specifically, the inlet velocity profile was extracted from the DNS data of Nolan and Zaki, which had a freestream inlet velocity of approximately 1.0; the turbulence intensity profile was derived from the DNS Reynolds stress values [Nolan & Zaki 2012]. Consistent with the Nolan and Zaki (2013) inlet boundary condition constraint that Reynolds Number, with a characteristic length based on the boundary layer thickness, equals 800, the following material and turbulence properties were derived: dynamic viscosity = 1.262078×10^{-3}; density = 1.0; and boundary layer thickness = 1.009662846 at a freestream distance ($X-X_0$) of 33.398 downstream of the leading edge of the plate. And, the shape of the top boundary of the computational domain was based on the averaged raw DNS X and Y coordinates provided by Nolan and Zaki (2012). Although the STAR-CCM+ units for these parameters are in standard MKS units, the material properties are not associated with any specific working fluid since the RANS simulation was based on the DNS simulation, which consisted of non-dimensionalized parameters, by Nolan and Zaki (2013). A flow-split boundary condition was applied at the outlet; and a wall-slip boundary condition was applied at the top boundary.[9] A wall no-slip boundary condition was applied at the bottom boundary (plate), and a low y+ wall treatment was used [Cd-adapco, 2013].

It should be noted that the DNS simulation of Nolan and Zaki was a transient simulation in that their free stream turbulence was synthesized from Fourier modes in

[9] The flow-split and wall-slip boundary conditions extrapolate velocity from the adjacent cell value. Additional details on boundary conditions can be found in Cd-adapco (2013).

time, and Orr-Sommerfeld and Squire modes in the wall-normal direction [Nolan and Zaki 2013]. Unfortunately, the mathematical implementation of their free stream turbulence synthesization was not made available; therefore, only steady-state RANS simulations, using a time-independent inlet velocity profile, were conducted.[10] Therefore the validity, from both a theoretical and practical perspective, of using a steady-state RANS approach to approximate a transient DNS simulation is not clear [Wilcox 1994, Pope 2001, Cd-adapco 2013].

Finally, and with respect to boundary conditions, the importance of applying the correct boundary conditions should not be overlooked. The results presented in Figure 5 are presented to demonstrate the effect of inlet boundary conditions on boundary layer transition location. The plots in Figure 5 associated with BC1 represent the results of applying a turbulence intensity profile, which was derived from the Nolan and Zaki (2012) velocity results, at the inlet boundary. This is the correct boundary condition, which is used to represent a freestream turbulence intensity of 3%. The plots associated with BC2 represent the results of applying an incorrect turbulence intensity profile at the inlet boundary. Specifically, BC2 represents the results of applying turbulence intensity value of 3% not only in the freestream, but within the boundary layer as well. As expected, application of a 3% turbulence intensity value, throughout the freestream and boundary layer, results in both the SST K-Omega (k-ω) RANS model and the Gamma ReTheta (γ-Re_θ) transition model beginning the transition to turbulence further upstream as compared to the BC1 plots. Noteworthy is the sensitivity of the γ-Re_θ model to the location of transition onset (i.e., a relatively large change in location of transition onset is observed as compared to the k-ω model).

MATLAB Code

A MATLAB code was written to compute entropy generation and boundary layer parameters that are not typically computed by commercial CFD software. The results

[10] Unsteady RANS simulations are referred to as URANS. Depending on the application, turbulence type, and type of averaging (e.g., time, spatial, ensemble), the validity of using a URANS solution approach may be called into question.

produced by the MATLAB code were computed on a HP Pavilion g6 Notebook PC with a Windows 7 operating system; the MATLAB code was run on the ZaReason Linux box as well. The MATLAB code takes, as inputs, DNS and RANS velocity profiles and computes entropy related parameters such as point-wise (local) entropy generation rate and dissipation coefficient. For example, Equation (2) and the first four terms of Equation (4) are computed. Noteworthy is freestream velocity was computed using a portion of a Matlab function provided by Kevin Nolan via Don McEligot (Nolan, 2013). The function determines freestream velocity by computing the wall normal velocity gradients, and flagging those gradients that have values between 0.002 and -0.002.[11] The values of velocity that correspond to the flagged velocity gradients are averaged to produce a local freestream velocity as a function of freesteam distance $\{U(x)_\infty\}$. In general, the Matlab code is capable of computing the majority of parameters and results computed and presented in other research work [Nolan and Zaki 2013, Walsh et al. 2011, Ghasemi et al. 2013]. The Matlab code results are presented in Appendix B.

Verification and Validation

Consistent with good engineering practice, the expected use of the entropy data, and available project funds, an informal verification and validation methodology (V&V) similar to that performed by Hamman and Berry (2009) was followed for this study. The V&V process included a mesh refinement study, which was conducted in the freestream and wall normal directions, an iterative convergence study, and verification of consistency study (i.e., mass conservation) [NPARC Alliance 2007]. Additionally, independent spreadsheet calculations performed by McEligot (2014b) were used to check MATLAB code results, a code-to-code comparison with an independent MATLAB code developed by Skifton (2014) was performed, a peer review of the data produced by the MATLAB code was performed (McEligot 2014b, Skifton 2014), and a qualitative comparison with results

[11] The basis for establishing a velocity gradient constraint between 0.002 and -0.002 is not clear, other than the values are small and centered about zero. Some numerical experimentation was performed by the author of this report by altering these values. Stability issues for the FPG and APG cases were observed.

published in the literature (Nolan and Zaki 2013, Walsh et al. 2011) was performed.[12] Any errors (e.g., software syntax errors) identified during the peer review were corrected. Finally, revision control was established and detailed documentation of the Matlab syntax was performed.

E. RESULTS

The results of this study are presented in Figures 6 through 16 located in the appendix to this report.[13] The results primarily include a comparison of RANS results to DNS results. For example, boundary layer development and coefficient of friction analyses for establishing boundary layer transition location are presented. Additionally, entropy-related parameters including entropy generation rate and dissipation coefficient are presented. Finally, the results of a study using a 'calibrated' SST k-ω γ-Re_θ transition model are presented in Figure 13 through Figure 16; these results are compared with uncalibrated results for the ZPG design.[14]

Figure 6 presents four graphs of DNS boundary layer thickness metrics versus freestream distance; each graph has three plots. The four graphs represent the ZPG case (top left), the FPG case (top right), the APG-2 case (bottom left), and the APG-4 case (bottom right). The plots associated with each graph include boundary layer thickness θ_{99}, displacement thickness δ^*, momentum thickness θ, and a polynomial fit of the boundary layer thickness. The function associated with the polynomial fit was used as input to the STAR-CCM+ transition model boundary layer profile depicted in Figure 1. The largest turbulent boundary layer thickness is associated with the FPG case, which, when compared

[12] In the context of a formal V&V methodology, the author recognizes that code-to-code comparisons are not validation activities, and they are not "strictly speaking" verification activities [Trucano et al. 2003].

[13] Some figures in this appendix have text within the graph to identify the transition location (beginning and ending). For example, the top-left graph in Figure 3 has the following text: "C_{fmin} @ $X\text{-}X_0$ = 219 ($Re_x^{1/2}$ = 447)" indicates that the minimum value of the coefficient of friction (transition onset) occurs at a freestream distance of 219, which corresponds to a $Re_x^{1/2}$ value of 447.

[14] Calibrated is defined as the process of adjusting physical modeling parameters in the computational model to improve agreement with experimental data. For example, the physical modeling parameters of the γ-Re_θ transition model were adjusted so that the coefficient of friction predicted by the transition model agreed with the DNS coefficient of friction results [Oberkampf and Roy 2010].

with the ZPG case, would be expected due to the longer computational domain. The APG-4 design boundary layer thickness exceeds that of the APG-2 design.

Figure 7 presents the local skin friction development as a function of the square-root of the freestream Reynolds number metric. Each graph has three plots representing the Menter SST k-ω RANS turbulence model, the k-ω γ-Re_θ transition model, and the Nolan and Zaki DNS results.[15] Again, the DNS results were used to assess the turbulence models. As defined here, the beginning of the transition region is where the respective turbulence model coefficient of friction reaches a minimum and the transition region end is where the coefficient of friction reaches a maximum.

The Falkner-Skan plot represents the theoretical lower bound of the coefficient of friction behavior; while the White plot (Equation 6-78, 1991) presented as Equation (9) below, represents the upper bound of the coefficient of friction behavior[16].

$$C_f = \frac{0.455}{ln^2(0.06Re_x)} \qquad \text{Equation (9)}$$

The Falkner-Skan equation was solved using a fixed-step fourth order Runge-Kutta solver available in Matlab. An overview of the numerical process to obtain the Falkner-Skan solution is presented in Appendix A. The local skin friction coefficient, based on Falkner-Skan parameters, was verified to be correct by comparing the skin friction coefficient profile (for each pressure gradient) to the local values obtained from the correlation presented by White (Equation 4-81, 1991). This correlation is presented below as Equation (10).

$$C_f(x) = \frac{2\mu\,(\frac{\partial u}{\partial y})_{wall}}{\rho U^2(x)} = f_0'' \sqrt{\frac{2(1+m)\nu}{Ux}} \qquad \text{Equation (10)}$$

[15] Recall that the Menter SST k-ω turbulence model is coupled with the γ-Re_θ model.

[16] Equation (9) is the same correlation used by Nolan and Zaki (2013).

The ZPG DNS results compare well with the Falkner-Skan profile for β=0. But as the pressure gradient changes, the DNS results deviate from Falkner-Skan profile. Nolan and Zaki (2013) did not compare their coefficient of friction pressure gradient results to the Falkner-Skan solution; furthermore, additional research studies with similar coefficient of friction and Falkner-Skan comparisons could not be located. Studies such as these would have been beneficial for comparison purposes. Note that the coefficient of friction obtained from White (1991) is not plotted for the FPG, APG-2, and APG-4 designs since this correlation is only applicable to the ZPG design. Additionally, the FPG freestream square-root of Reynolds number upper bounds is approximately 1100, but the maximum value shown in the figure is limited to 800 for comparison purposes.

Figure 8 presents the approximate local entropy generation rate as a function of boundary layer y^+ values. The local entropy generation rate for each plot corresponds to the location, for each model, where the transition from laminar to turbulent ($C_{f,min}$) flow begins. Neither the Menter SST k-ω RANS turbulence model nor the γ-Re_θ transition model accurately predicts local entropy generation rate (or coefficient of friction) at this location. Quantitatively, this can be seen in Figure 9, where the percent error (using DNS as the comparison value) reaches values on the order of 50%. It should be noted that percent error is not a good measure when DNS comparison values approach a value of zero. For example, the extremely large error values at y^+ locations beginning at y^+ of 50 are the result of the denominator in the percent error equation approaching a value of zero faster than the numerator. Therefore the root mean square error (RMSE) was computed as a global indicator of error. The RMSE mathematical expression is presented in Equation (11); and the results are presented in Table 2.

$$RMSE = \sqrt{\frac{\sum_{i=1}^{n}\{(\gamma Re\theta\ value)_i - (DNS\ value)_i\}^2}{n}} \qquad \text{Equation (11)}$$

Table 2 Root Mean Square Error (γ-Re_θ vs. DNS)

Pressure Gradient	S''' RMSE	C_d RMSE
ZPG Calibrated	5.759E-02	4.756E-05
ZPG	1.312E-01	2.860E-04
FPG	1.124E-01	3.253E-04
APG-2	1.663E-01	3.424E-04
APG-4	2.004E-01	6.114E-04

Figure 10 presents the DNS local dissipation coefficient for each design as a function of freestream distance; and Figure 11 presents the RANS local dissipation coefficient as a function of freestream Reynolds number. Only the first four terms of Equation (4), presented below as Equation (12), were analyzed for this study since DNS results did not include appropriate values to compute term five and term six of Equation (4).

$$(S''\{\delta\})^+ \approx \int_0^\delta \left(\frac{\partial U^+}{\partial y^+}\right)^2 dy^+ - \int_0^\delta (\overline{uv})^+ \left(\frac{\partial U^+}{\partial y^+}\right) dy^+ \qquad \text{Equation (12)}$$

$$- \int_0^\delta [\overline{(u^2)^+} - \overline{(v^2)^+}] \left(\frac{\partial U^+}{\partial x^+}\right) dy^+$$

$$-(d/dx^+) \int_0^\delta U^+ (1/2)(\overline{q^2})^+ dy^+$$

As part of the V&V process, results from this study were compared, from a qualitative perspective, with the literature. The ZPG Figure 10 results, which are based on a freestream inlet turbulence of 3%, were compared with the Figure 6 results of Walsh et al. (2011), which are based on a freestream inlet turbulence of 4.7%. Qualitatively, the results compared well except for term 4, the turbulent energy flux contribution. Specifically, the term 4 results of Walsh et al. (2011) are positive towards the end of the computational domain ($450 < Re_x^{½} < 550$); while, the term 4 results from this study are negative towards the end of the computational domain ($700 < Re_x^{½} < 800$). Extensive

Matlab code debugging was performed; and syntax errors identified were corrected. Additionally, the work of Rotta (1962) was reviewed to confirm the leading sign (i.e., +/-) for each term. Finally, a code-to-code comparison was performed between two independent Matlab codes with similar models with the same ZPG DNS input [Skifton 2014]. To date, the reason for the difference between the term 4, Figure 10 (ZPG) results presented in this study and the term 4 Figure 6 results of Walsh et al. (2011) is not known.

Figure 12 presents the percent difference between the γ-Re_θ transition model and the DNS results at the same freestream location. As expected, a large error occurs near the DNS transition region since the transition model was not calibrated to approximate the DNS results.

In an effort to demonstrate the possible improvement in error, the ZPG γ-Re_θ transition model was calibrated, by systematically changing the function governing transition length (i.e., F_{length}) until the γ-Re_θ approximated the DNS results [Cd-adapco 2013, Suluksna et al. 2009]. The calibration process proved to be time consuming; nevertheless, the results demonstrate the use of the calibrated transition model. Figures 13 through 16 present the results of the ZPG case using the calibrated γ-Re_θ transition model.

F. CONCLUSIONS

Given that commercial CFD codes do not solve the entropy transport equation, including entropy generation terms, as part of their software product, a significant amount of code development work and testing was required to write a MATLAB code to produce the entropy-related results for the five independent studies (ZPG, FPG, APG-2, APG-4, ZPG calibrated).

Based on the results of these independent studies, the following is concluded:

1. RANS turbulence models neither “predict” nor should they be used to “predict” transition.

2. Additional studies (e.g., uncertainty quantification) to characterize RANS turbulence models ability to accurately predict entropy-related boundary layer parameters should be performed.

3. A fundamental understanding of the capabilities and limitations of transition models should be established prior to their use. For example, the γ-Re_θ transition model is sensitive to mesh density and inlet boundary conditions. Furthermore, users should be aware that the transition models are not "predictive models." They are "calibrated" models in that they require users to input parameters such as the boundary layer profile; additionally, they require users to alter physical modeling parameters, such as transition length, to improve agreement with experimental data and/or DNS results.

4. Although the calibration process is complex and time consuming, when experimental data and/or DNS results are used to assess the performance of transition models, an effort should be made to calibrate the transition models in order to minimize error.

5. Unlike the well-documented Navier-Stokes equations, whose theoretical basis has been established for well over 100 years in the form of textbooks and journal articles, a sound theoretical basis for both the fluid friction and heat transfer entropy generation contributions is lacking. For example, the mathematical description of the entropy generation integral equation, Equation (7), has eight terms whose theoretical basis is not entirely clear. And, only 4 of the 8 terms were analyzed in this study; so the relative contribution of each term to the dissipation coefficient is not known. Furthermore, even after reviewing Schlichting (1968) and Denton (1993), the theoretical basis of the dissipation coefficient is not clear. Therefore more educational literature, focused on the theoretical and historical aspects of entropy generation including the basis for the associated mathematical expressions, is warranted.

G. REFERENCES

Abu-Ghannam, B.J., Nigim, H.H., and Kavanagh, P., (1999). Surface curvature and pressure gradient effects on boundary layer transition. Engineering Turbulence Modelling and Experiements-4, Rodi, W. and Laurence, D. (editors), Elsevier, New York.

Advisory Group for Aerospace Research & Development (AGARD) Fluid Dynamics Panel Working Group 21, 1998. A Selection of Test Cases for the Validation of Large-Eddy Simulations of Turbulent Flows (AGARD-AR-345). Neuilly-sur-Seine, France. AGARD Advisory Report No. 345.

American Institute of Aeronautics and Astronautics (AIAA), 1998. Guide for the Verification and Validation of Computational Fluid Dynamics Simulations (AIAA G-077-1998). Reston, Virginia.

American Society of Mechanical Engineers (ASME), 2008. Quality Assurance Requirement for Nuclear Facility Applications (ASME NQA-1-2008). New York.

American Society of Mechanical Engineers (ASME), 2009. Standard for Verification and Validation in Computational Fluid Dynamics and Heat Transfer (ASME V&V 20-2009). New York.

ANSYS Inc., 2012. ANSYS-FLUENT Theory Guide, Release 14.5. Canonsburg, Pennsylvania.

Bejan, A., 1982. Entropy Generation through Heat and Fluid Flow. John Wiley & Sons, New York.

Bejan, A., Tsatsaronis, G., and Moran, M., 1996a. Thermal Design & Optimization. John Wiley & Sons, New York.

Bejan, A., 1996b. Entropy Generation Minimization – The Method of Thermodynamic Optimization of Finite-Size Systems and Finite-Time Processes. CRC Press, New York.

Cambaros, J.A., 2010. Entropy Mystique: The Second Law of Thermodynamics in Aerospace Systems Analysis & Design. Purdue University School of Aeronautics and Astronautics Seminar.
https://engineering.purdue.edu/AAE/AboutUs/News/Events/20101207SpecialSeminarJose Camberos (accessed 7.9.2014)

CD-adapco, 2013. STAR-CCM+ User Guide, Version 8.04. New York.

Cimsoft, 2013. Trelis 14 Advanced Meshing Software. American Fork, UT.

Crepeau, J. (Project Director), circa 2011. Fundamental Fluid Physics Studies for Energy Efficiency and Sustainability. Department of Energy Experimental Program to Stimulate Competitive Research (DOE EPSCoR) Project Narrative, Award DE-SC0004751. University of Idaho, Moscow, Idaho.

Denton, J.D., 1993. Loss Mechanisms in Turbomachines. ASME J. Turbomach., 115(4), pp. 621-656.

Ferziger, J.H., 1998. Direct and Large Eddy Simulation of Turbulence. Numerical Methods in Fluid Mechanics, Alain Vincent (Editor), in CRM Proceedings and Lecture Notes (Volume 16), American Mathematical Society.

Ghasemi, E., McEligot, D.M., Nolan, K.P., Crepeau, J., Tokuhiro, A., and Budwig, R.S., 2013. Entropy generation in a transitional boundary layer region under the influence of freestream turbulence using transitional RANS models and DNS. International Communications in Heat and Mass Transfer, 41, 10-16.

Ghasemi, E., McEligot, D.M., Nolan, K.P., Crepeau, J., Siahpush, A., Budwig, R.S., and Tokuhiro, A., 2014. Effects of adverse and favorable pressure gradients on entropy generation in a transitional boundary layer region under the influence of freestream turbulence. International Journal of Heat and Mass Transfer, 77, 475-488.

Herwig, H. and Kock, F., 2007. Direct and indirect methods of calculating entropy generation rates in turbulent convective heat transfer problems. Heat Mass Transfer, 43, 207-215.

Hamman, K.D. and Berry, R.A., 2010. A CFD simulation process for fast reactor fuel assemblies. Nuclear Engineering and Design, 240, 2304-2312.

Jonas, P., Hladik, O., Mazur, O., and Uruba, V., 2011. By-pass transition of flat plate boundary layers on the surfaces near the limit of admissible roughness. 13th European Turbulence Conference (ETC13), 12-15 September 2011, Warsaw Poland. Published in Journal of Physics: Conference Series 318, IOP Publishing, Philadelphia, Pennsylvania.

Knupp, P. and Salari, K., 2003. Verification of Computer Codes in Computational Science and Engineering. Chapman & Hall/CRC, New York.

Langtry, R.B., 2006a. A Correlation-Based Transition Model using Local Variables for Unstructured Parallelized CFD Codes. Doctoral Thesis, University of Stuttgart, Germany.

Langtry, R., Menter, F.R., Likki, S.R., Suzen, Y.B., Huang, P.G., and Volker, S. , 2006b. A Correlation-Based Transition Model Using Local Variables – Part II: Test Cases and Industrial Applications. Journal of Turbomachinery, 77, 423-434.

Malan, P., Suluksna, K., and Juntasaro, E., 2009. Calibrating the γ-Re_θ Transition Model for Commercial CFD. 47th AIAA Aerospace Sciences Meeting Including The New Horizons Forum and Aerospace Exposition, 5-8 January 2009, Orlando, Florida.

McEligot, D.M., Nolan, K.P., Walsh, E.J., and Laurien E., 2008a. Effects of pressure gradients on entropy generation in the viscous layers of turbulent wall flows. International Journal of Heat and Mass Transfer, 51, 1104-1114.

McEligot, D.M., Walsh, E.J, Laurien, E., and Spalart, P.R., 2008b. Entropy Generation in the Viscous Parts of Turbulent Boundary Layers. Journal of Fluids Engineering, 130, 061205-1 to 061205-12.

McEligot, D.M., 2014a. Anatomy of Entropy Generation in Boundary Layers (Presentation - Slide 13, Alternate Approach). January 15, 2014 EPSCoR Project Review Meeting, Boise, Idaho.

McEligot, D.M., 2014b. Various e-mail communications with K.D. Hamman related to debugging MATLAB code.

MathWorks, 2013. MATLAB R2013a (Student Version) Natick, Massachusetts.

Menter, F.R., Langtry, R.B., Likki, S.R., Suzen, Y.B., Huang, P.G., and Volker, S., 2006a. A Correlation-Based Transition Model Using Local Variables Part 1 - Model Formulation. Journal of Turbomachinery, 128, 413-422.

Menter, F.R., Langtry, R., and Volker, S., 2006b. Transition Modelling for General Purpose CFD Codes. Flow Turbulence Combust, 77, 277-303.

Meyer, J.P. and Olivier, J.A., 2011. Heat Transfer in the Transitional Flow Regime (Chapter 12), in Evaporation, Condensation, and Heat Transfer (Amimul Ahsan, editor). InTech, Rijeka, Croatia.

Moin, P. and Mahesh, K., 1998. DIRECT NUMERICAL SIMULATION: A Tool in Turbulence Research. Annu. Rev. Fluid Mech., 30, 539-578.

Naterer, G.F and Camberos, J.A., 2008. Entropy – Based Design and Analysis of Fluids Engineering Systems. CRC Press, New York.

Nolan, K.P. and Zaki, T.A., 2012. DNS data of Kevin Nolan and Tamer Zaki. (June 13, 2012 email correspondence: Kevin Nolan and Donald McEligot.)

Nolan, K.P., 2013. Re: Int par (Matlab syntax text to compute integral parameters). (January 28, 2013 email correspondence: Kevin Nolan and Donald McEligot.)

Nolan, K.P. and Zaki, T.A., 2013. Conditional sampling of transitional boundary layers in pressure gradients. Journal of Fluid Mechanics, 728, 306-339.

National Program for Applications-Oriented Research in CFD (NPARC Alliance,) 2007. Overview of CFD Verification and Validation. ww.grc.nasa.gov/WWW/wind/valid/tutorial/overview.html (accessed 7.11.2014).

Oberkampf, W.L . and Roy, C.J., 2010. Verification and Validation in Scientific Computing. Cambridge University Press, New York.

Owen, L.D., Xing, T., McEligot, D.M., Crepeau, J.C., and Budwig, R.S., 2013. Laminar and Transitional Boundary Layer Entropy Generation over a Flat Plate under Favorable and Adverse Pressure Gradients. Proc. ASME 2013 Fluids Engineering Summer Meeting, July 7-11, Incline Village, NV.

Pope, S.B., 2001. Turbulent Flows. Cambridge University Press, Cambridge.

Potter, M.C., and Wiggert, D.C., 1997. Mechanics of Fluids, Second Edition. Prentice-Hall, Upper Saddle River, New Jersey.

Roache, P., 1998. Verification and Validation in Computational Science and Engineering. Hermosa Publishers, Albuquerque, New Mexico.

Rotta, J. C., 1962. Turbulent Boundary Layers in Incompressible Flow. Prog. Aeronaut. Sci., 2. Pergamon, Oxford.

Sandia National Laboratories (SNL), 2014. CUBIT Version 14.1, Albuquerque, New Mexico. https://cubit.sandia.gov/ (accessed 7.10.2013).

Sayadi, T. and Moin, P., 2012. Large eddy simulation of controlled transition to turbulence. Physics of Fluids, 24, 114103-1 to 114103-17.

Sayadi, T., Hamman, C.W., and Moin, P., 2013. Direct numerical simulation of complete H-type and K-type transitions with implications for the dynamics of turbulent boundary layers. Journal of Fluid Mechanics, 724, 480-509.

Schlichting, H., 1968. Boundary-Layer Theory, 6th edition. McGraw-Hill, New York.

Schlichting, H. and Gersten K., 2003. Boundary-Layer Theory, 8th edition. Springer, New York.

Shuttleworth, M. 2014. Peer Review Process. https://explorable.com/peer-review-process (accessed 7.19.2014)

Skifton, R., 2014. Various e-mail communications related to debugging MATLAB codes.

Suluksna, K., Dechaumphai, P., and Juntasaro, E. 2009. Correlations for modeling transitional boundary layers under influences of freestream turbulence and pressure gradient. International Journal of Heat and Fluid Flow, 30, 66-75.

Trucano, T. G., Pilch, M., and Oberkampf, W.L., 2003. On the Role of Code Comparisons in Verification and Validation. Sandia National Laboratory report, SAND2003-2752.

Walsh, E.J., McEligot, D.M., Brandt, L., and Schlatter, P., 2011. Entropy Generation in a Boundary Layer Transitioning Under the Influence of Freestream Turbulence. Journal of Fluids Engineering, 133, 061203-1 to 061203-10.

Wang, C., Gao, P., Tan, S., and Wang, Z., 2013. Forced convection heat transfer and flow characteristics in laminar to turbulent transition region in rectangular channel. Experimental Thermal and Fluid Science, 44, 490 – 497.

Wilcox, David C., 2000. Turbulence Modeling for CFD. DCW Industries, Inc., La Cañada California. pp. 30 – 34.

White, F.M., 1991. Viscous Fluid Flow, 2nd Edition. McGraw-Hill, New York.

Zaki, T.A. and Durbin, P.A., 2006. Continuous mode transition and the effects of pressure gradient. Journal of Fluid Mechanics, 563, 357-388.

H. APPENDICES

Appendix A: Falkner-Skan Solution Process

The following is a general description of the process used to compute the Falkner-Skan (FS) solution for this study, using Matlab. Additional mathematical details related to the Falkner-Skan equation can be found in textbooks written by, for example, Schlichting (2003) and White (1991).

The FS equation, including associated parameters and derived quantities are presented as Equations (A1) through (A5). The underlying assumption in the solution to the FS equation is that the outer velocity field $u(x)$ obeys the power law $u(x) = ax^m$, where x is the freestream coordinate.

Falkner-Skan equation:

$$f''' + ff'' + \beta(1 - f'^2) = 0 \qquad \text{Equation (A1)}$$

where $f = f(\eta)$ is the dimensionless stream function, η is the similarity variable, and β is the Falkner-Skan parameter, which is related to the velocity field power law constant m by Equation (A3). The solution to the wall normal velocity field v is presented by Equation (A5), where ν represents kinematic viscosity.

$$\eta = y\sqrt{\frac{m+1}{2}\frac{a}{\nu}x^{m-1}} \qquad \text{Equation (A2)}$$

$$\beta = \frac{2m}{m+1} \qquad \text{Equation (A3)}$$

$$u(x) = ax^m \qquad \text{Equation (A4)}$$

$$v = -\sqrt{\frac{m+1}{2}\nu a x^{m-1}}\left(f + \frac{m-1}{m+1}\eta f'\right) \qquad \text{Equation (A5)}$$

The process began by solving the Falkner-Skan equation using a fixed-step fourth order Runge-Kutta solver available in Matlab; for example, the similarity variable η and the associated stream function $f = f(\eta)$ (including derivatives f' and f'') were computed. Then η was calculated for each X-Y coordinate position on the DNS mesh, followed by interpolation of the stream function values (f) and the derivatives (f' and f'') onto the DNS mesh so that a Falkner-Skan solution was associated with each DNS mesh point (i.e., X-Y coordinate). Finally, the local velocity field was computed using Equation (A4) and Equation (A5). Once the FS velocity field was computed, additional parameters (e.g., C_f) associated with this study were computed.

Note that the value for the power law constant 'a' where $U(x-x_0) = a(x-x_0)^m$ was computed from the inlet condition U(33.398) = 1 (see boundary condition section of this report); and 'm' was derived, using Equation (A3), from the Falkner-Skan parameter β reported by Nolan and Zaki (2013).

.

Appendix B: Graphical Results

Note: *Some figures in this appendix have text within the graph to identify the transition location (beginning and ending). For example, the top-left graph in Figure 3 has the following text: "C_{fmin} @ X-X_0 = 219 ($Re_x^{1/2}$ = 447)" indicates that the minimum value of the coefficient of friction (transition onset) occurs at a freestream distance of 219, which corresponds to a $Re_x^{1/2}$ value of 447.*

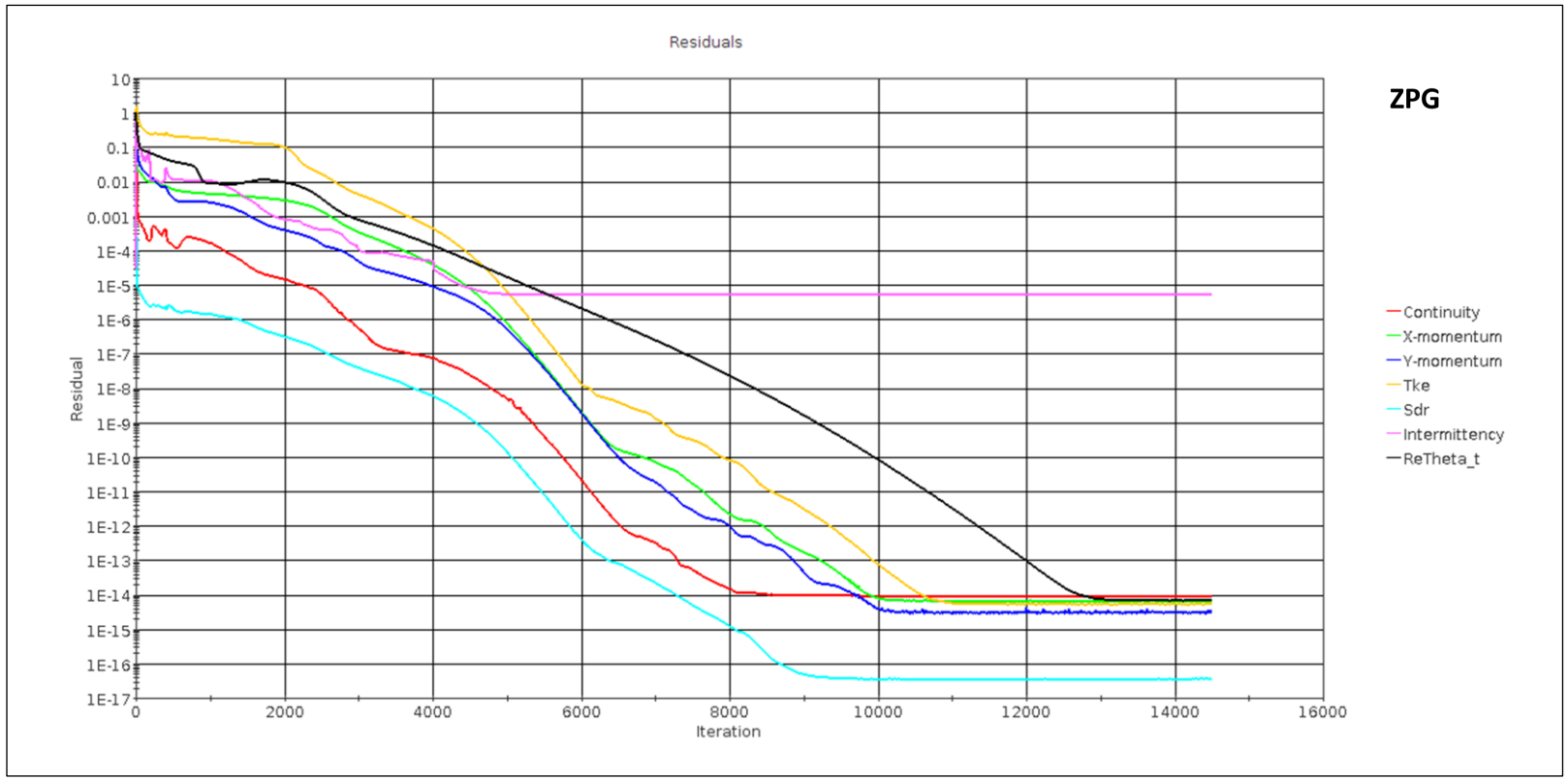

Figure 2 Zero Pressure Gradient (ZPG) Residuals

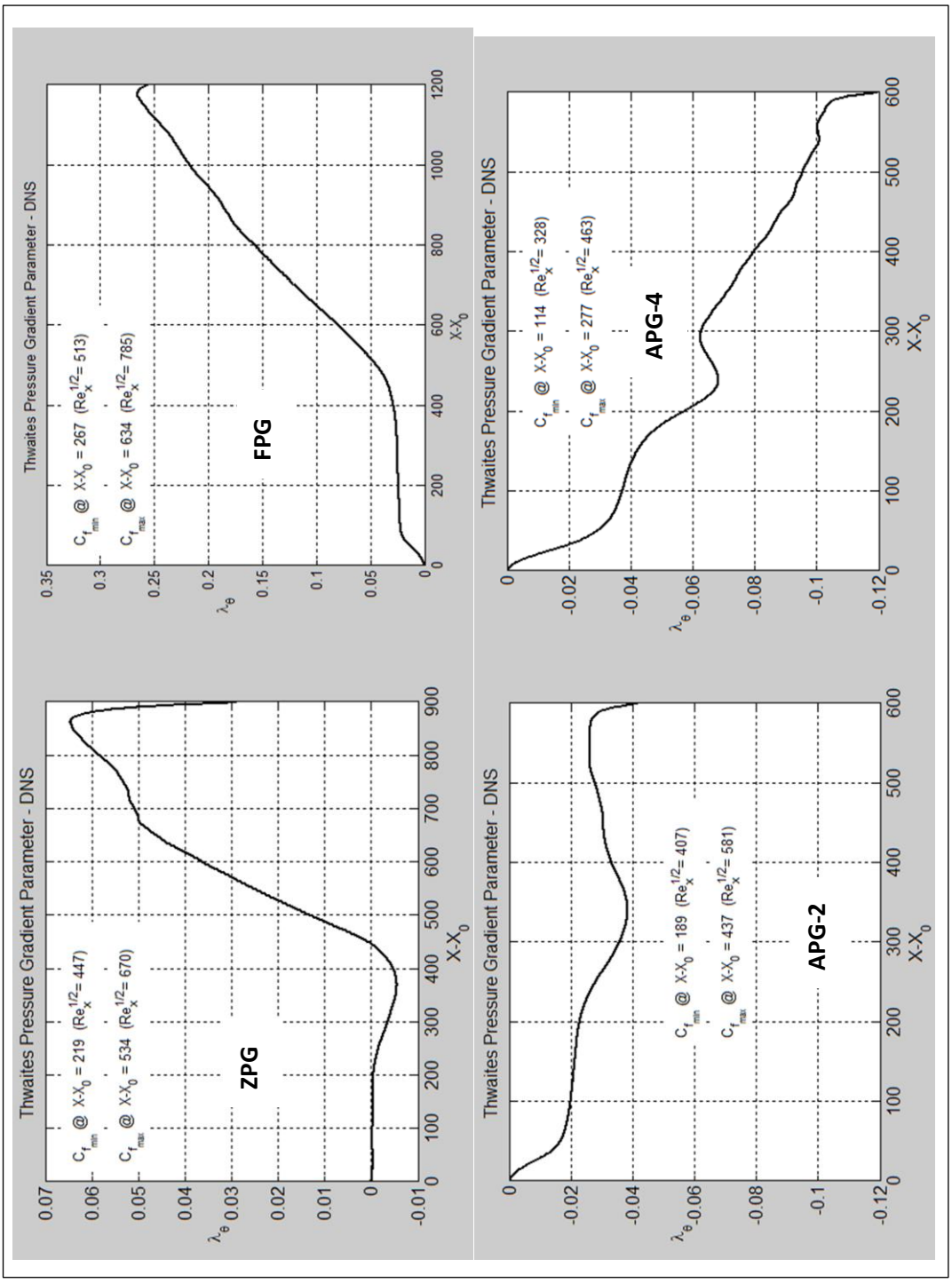

Figure 3 Thwaites Pressure Gradient Parameter (Left to Right, Top to Bottom: ZPG, FPG, APG-2, APG-4)

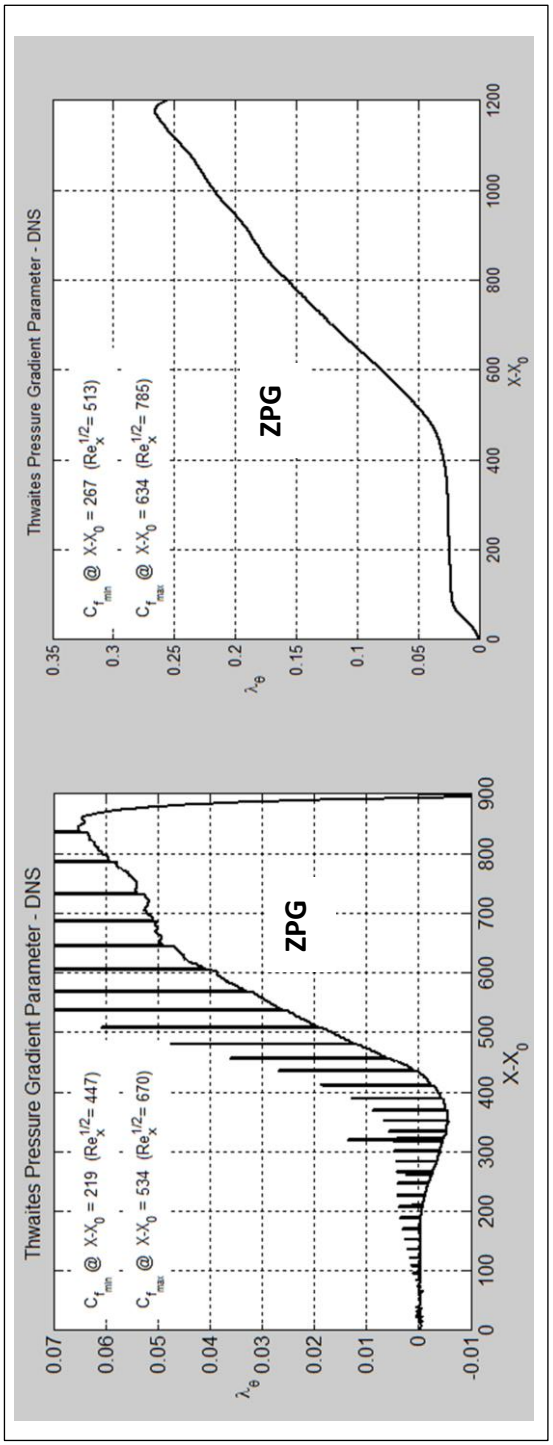

Figure 4 Thwaites Pressure Gradient Parameter (ZPG) { unfiltered/unsmoothed (left), filtered/smoothed (right) }

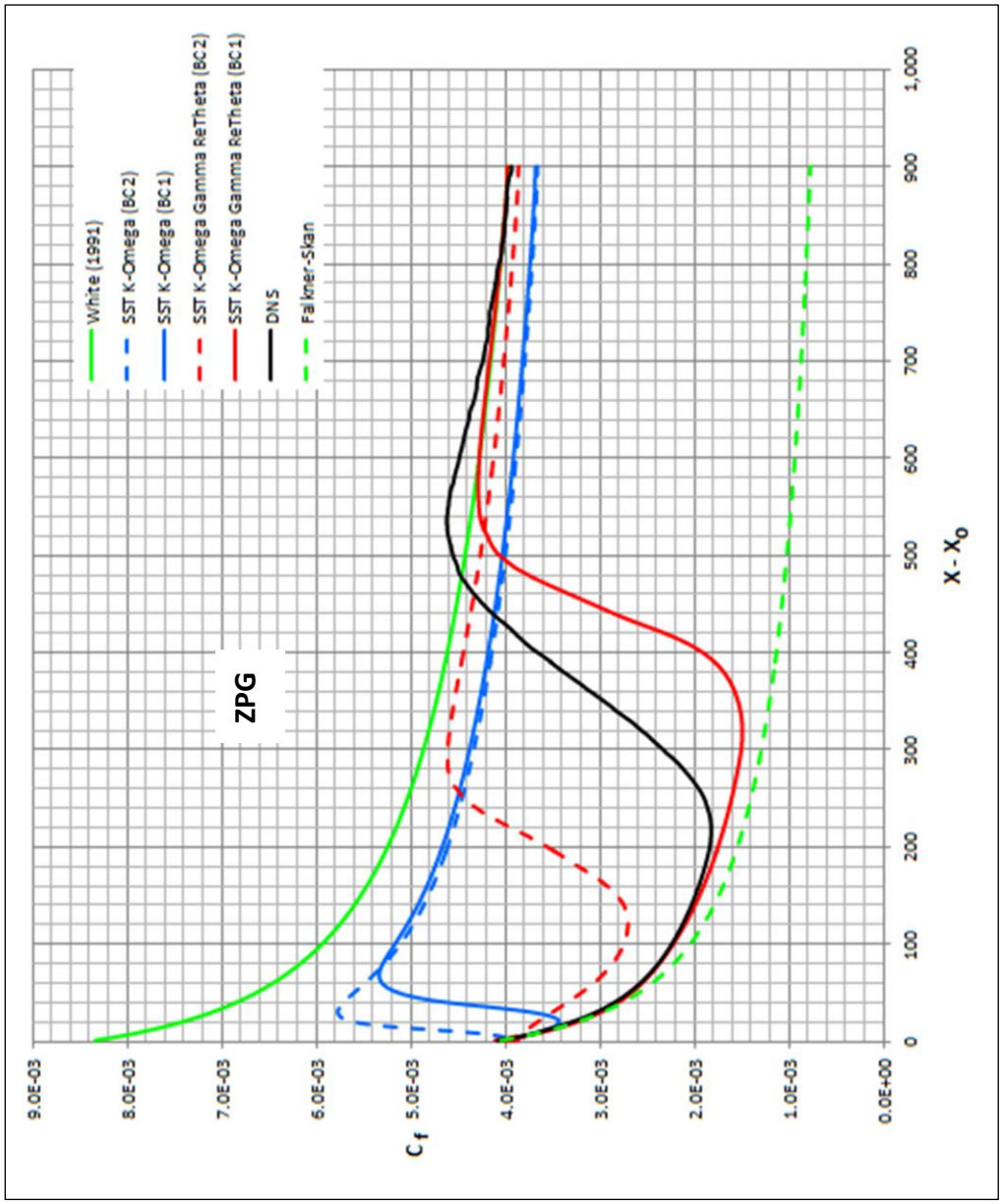

Figure 5 Effects of inlet boundary condition (BC) changes for the ZPG case

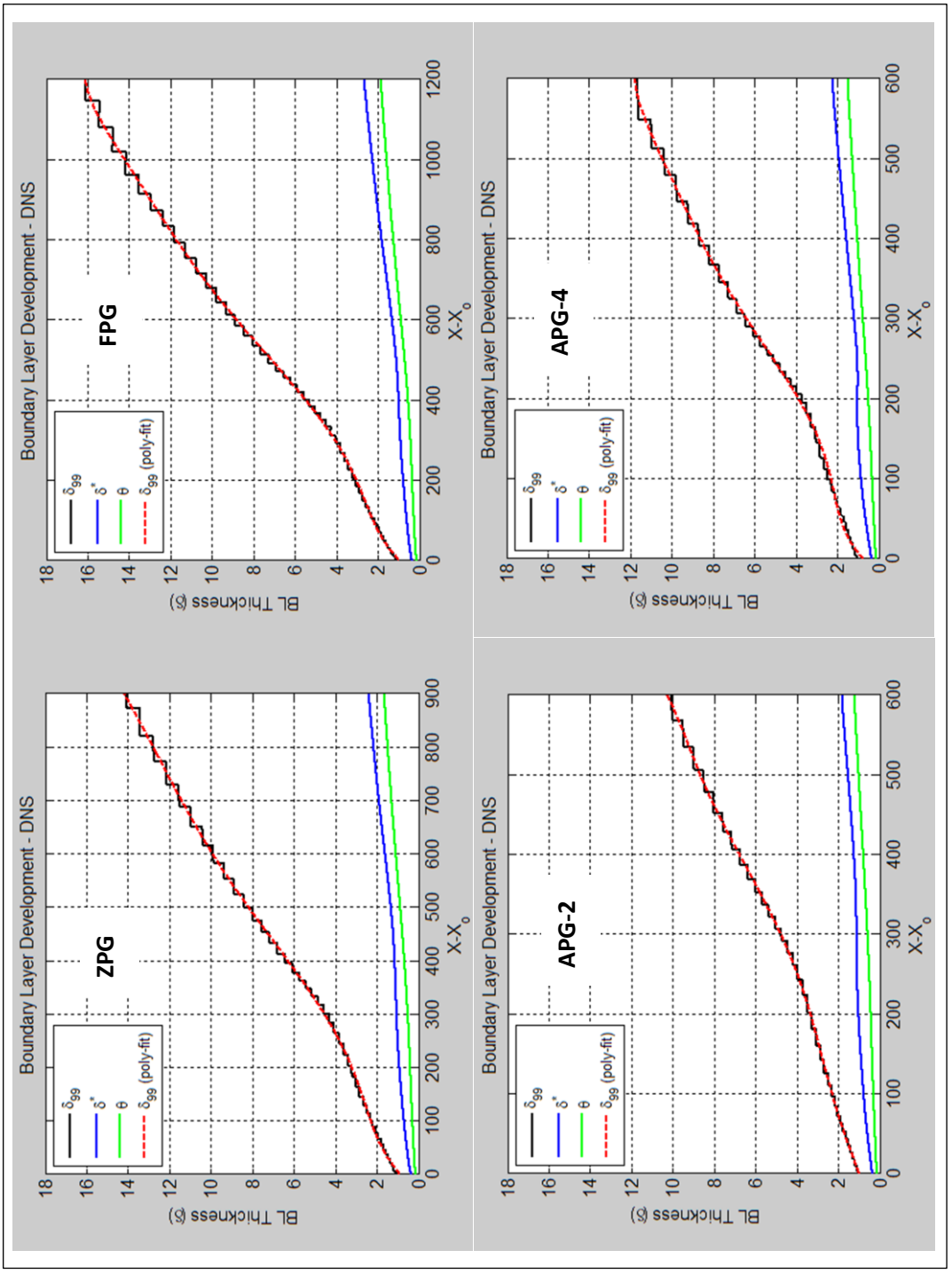

Figure 6 Boundary Layer/Thickness Development (Left to Right, Top to Bottom: ZPG, FPG, APG-2, APG-4)

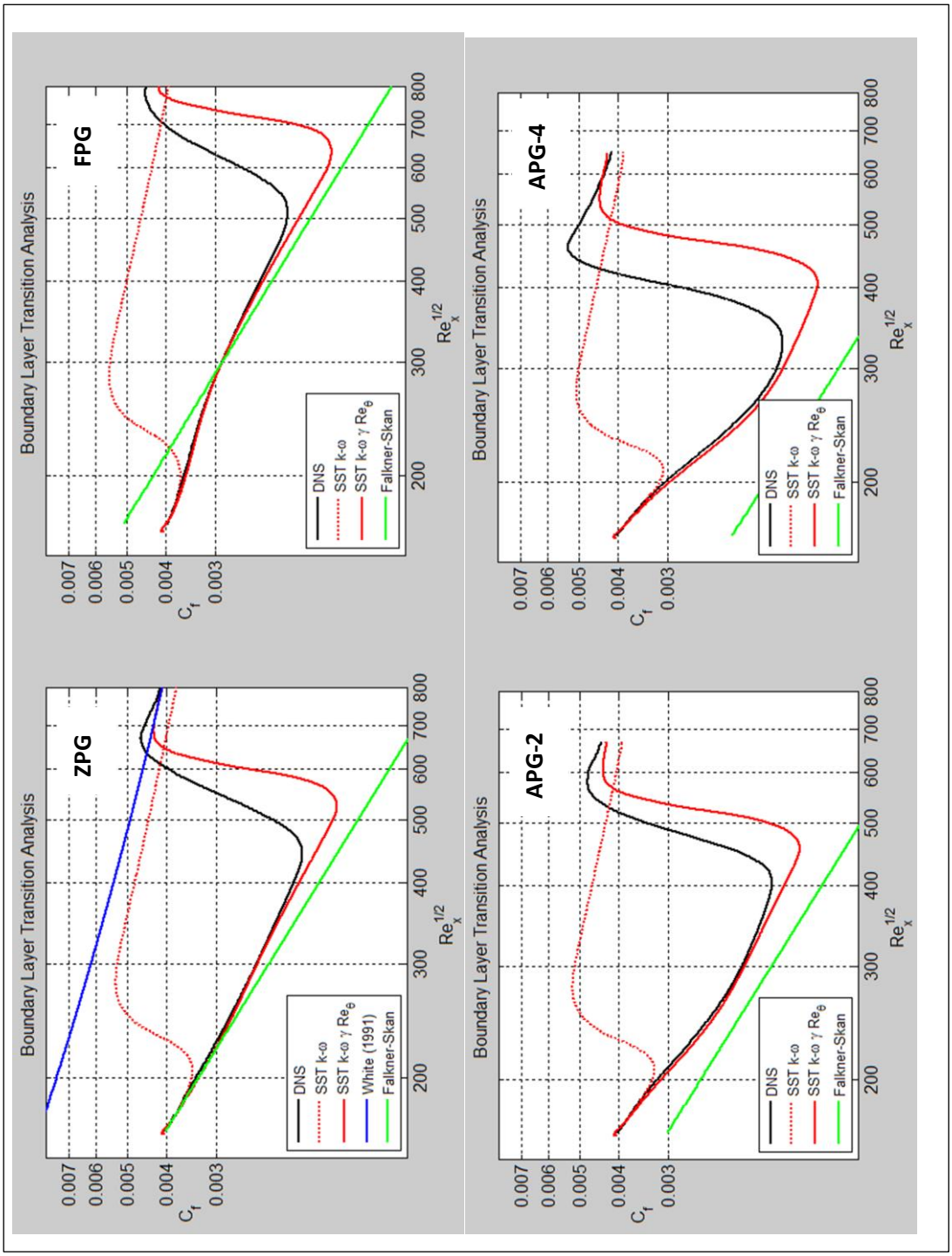

Figure 7 Skin Friction Coefficient Development (Left to Right, Top to Bottom: ZPG, FPG, APG-2, APG-4)

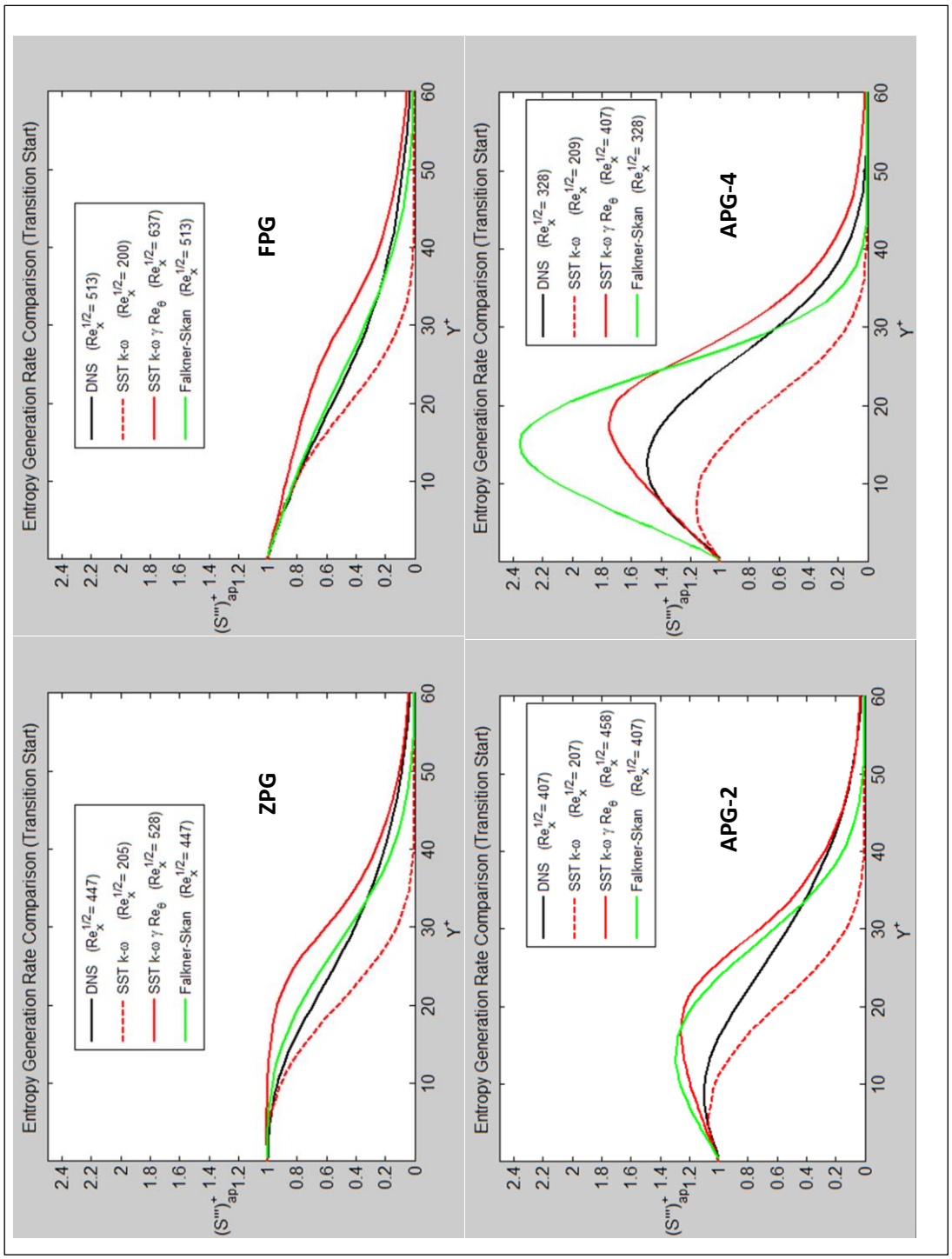

Figure 8 Approximate Entropy Generation Rate (Left to Right, Top to Bottom: ZPG, FPG, APG-2, APG-4)

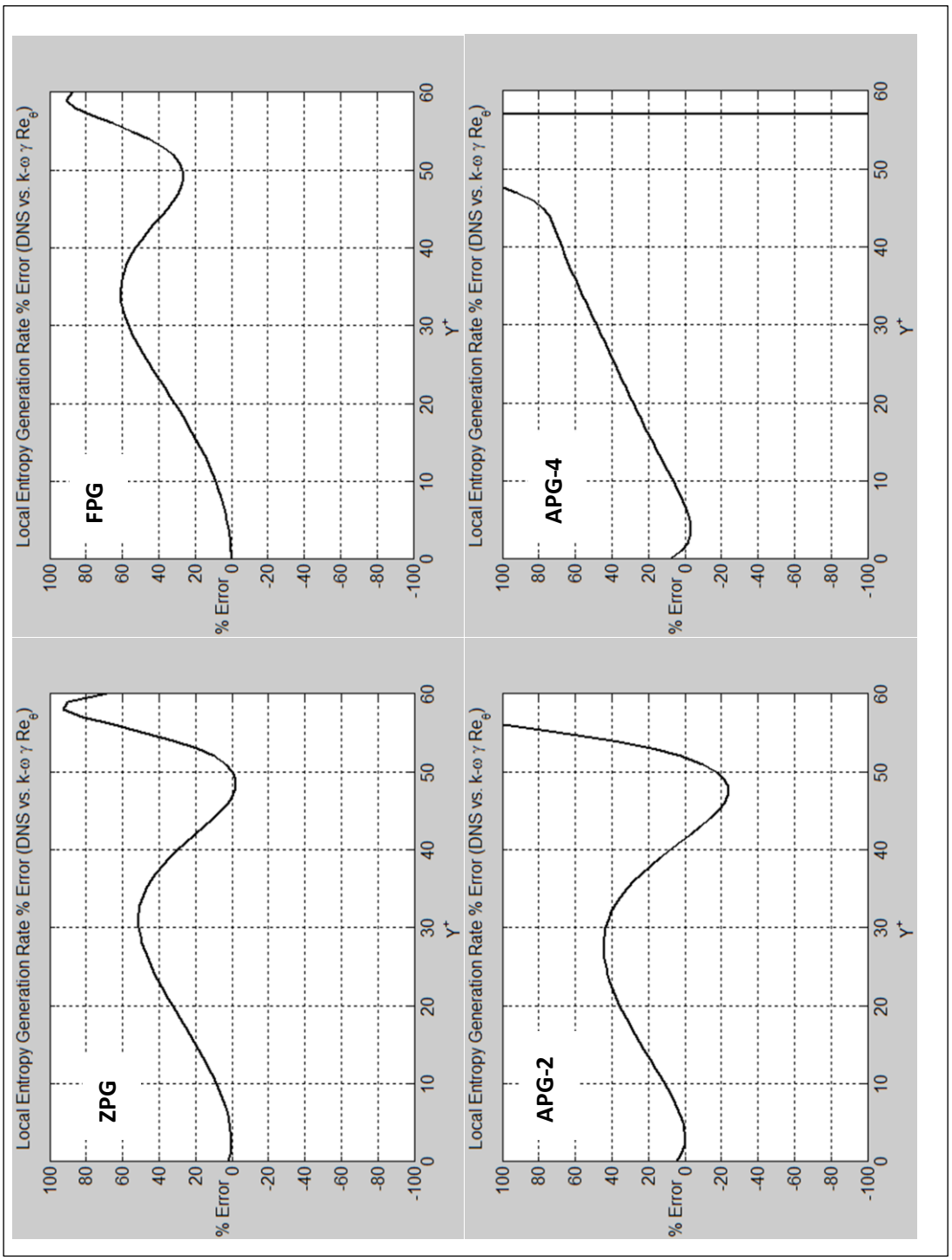

Figure 9 Percent Error Entropy Generation Rate (Left to Right, Top to Bottom: ZPG, FPG, APG-2, APG-4)

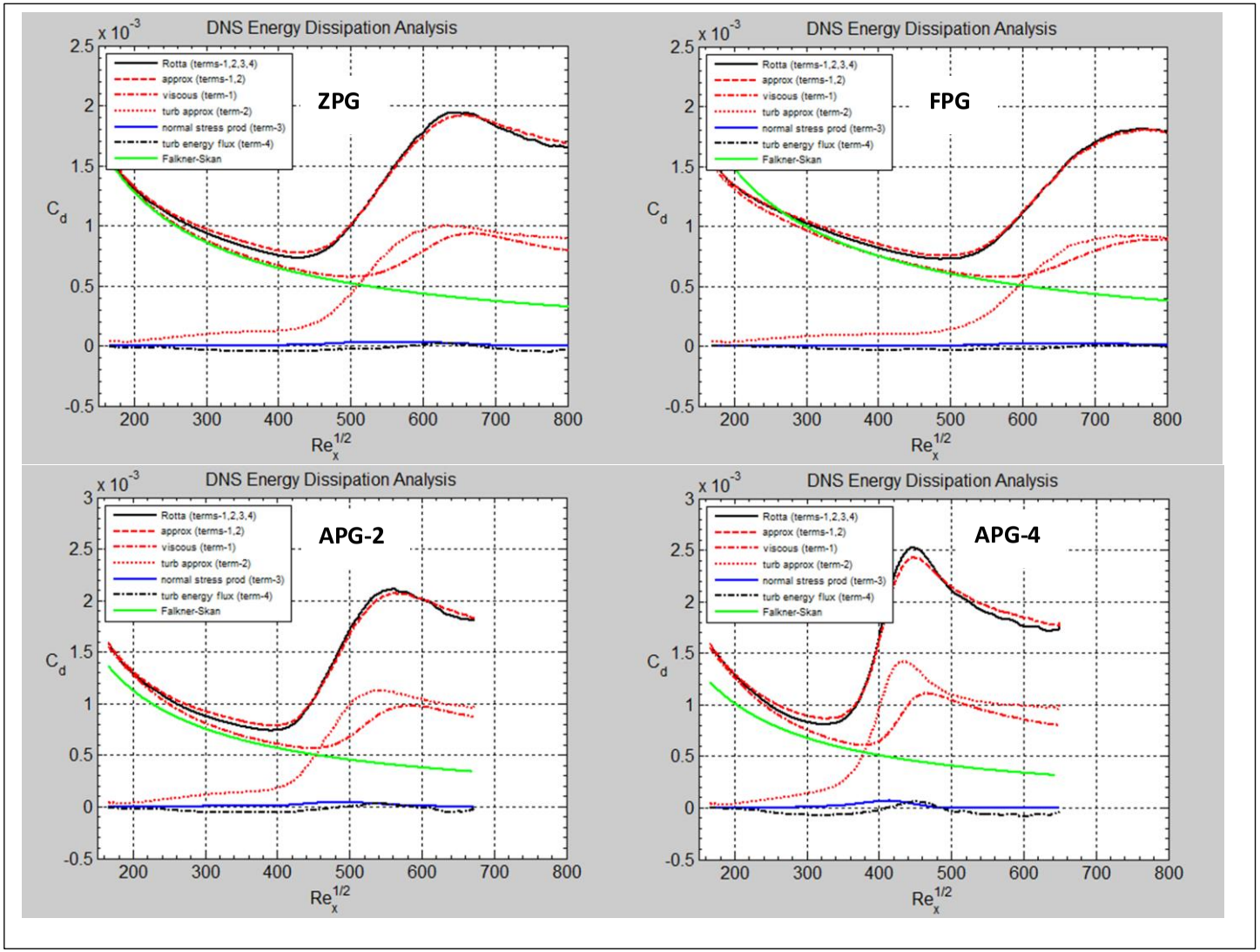

Figure 10 DNS Entropy Dissipation Coefficient (Left to Right, Top to Bottom: ZPG, FPG, APG-2, APG-4)
Note: Different scales were used to support readability of legend.

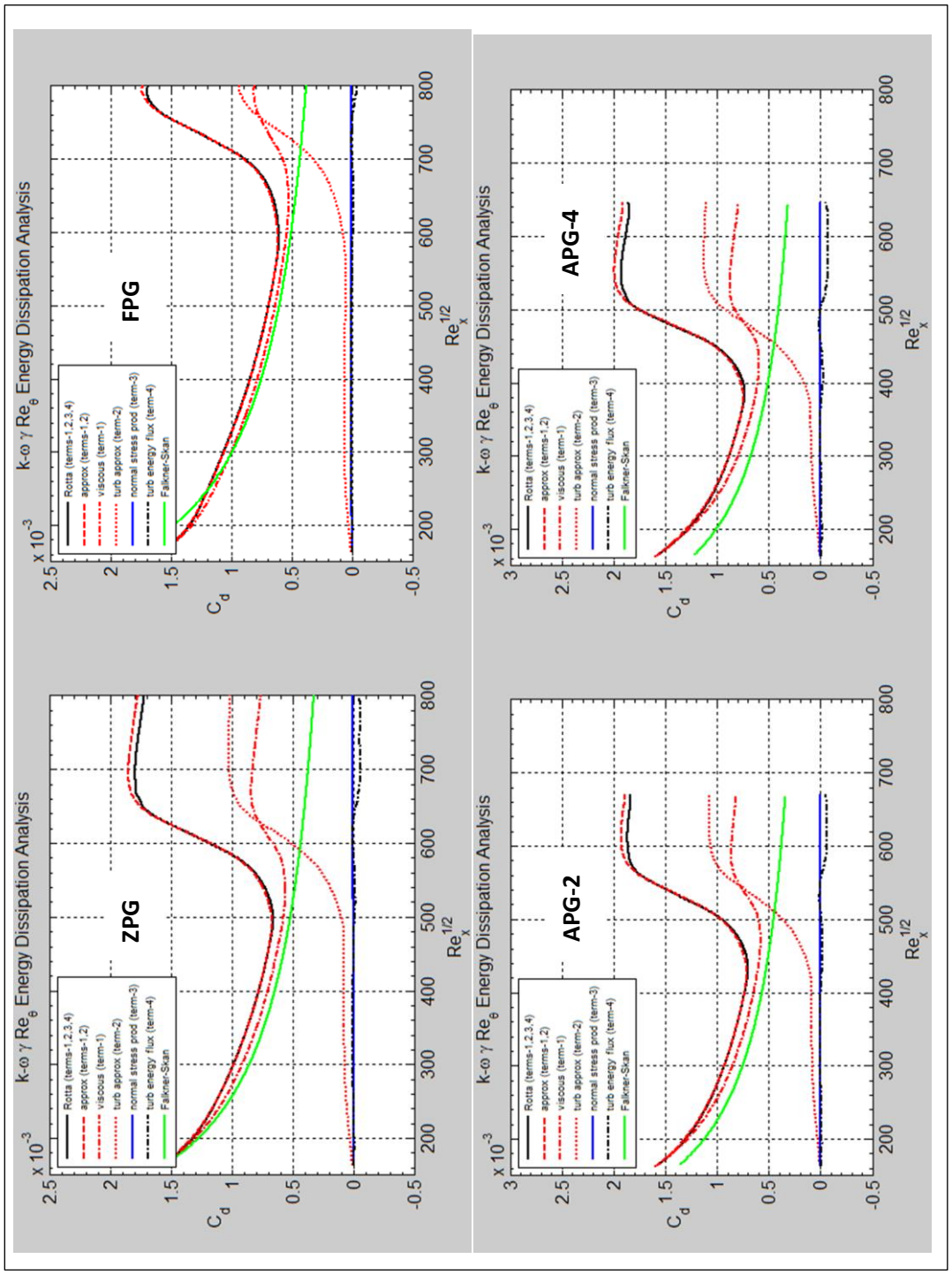

Figure 11 RANS Entropy Dissipation Coefficient (Left to Right, Top to Bottom: ZPG, FPG, APG-2, APG-4)
Note: Different scales were used to support readability of legend.

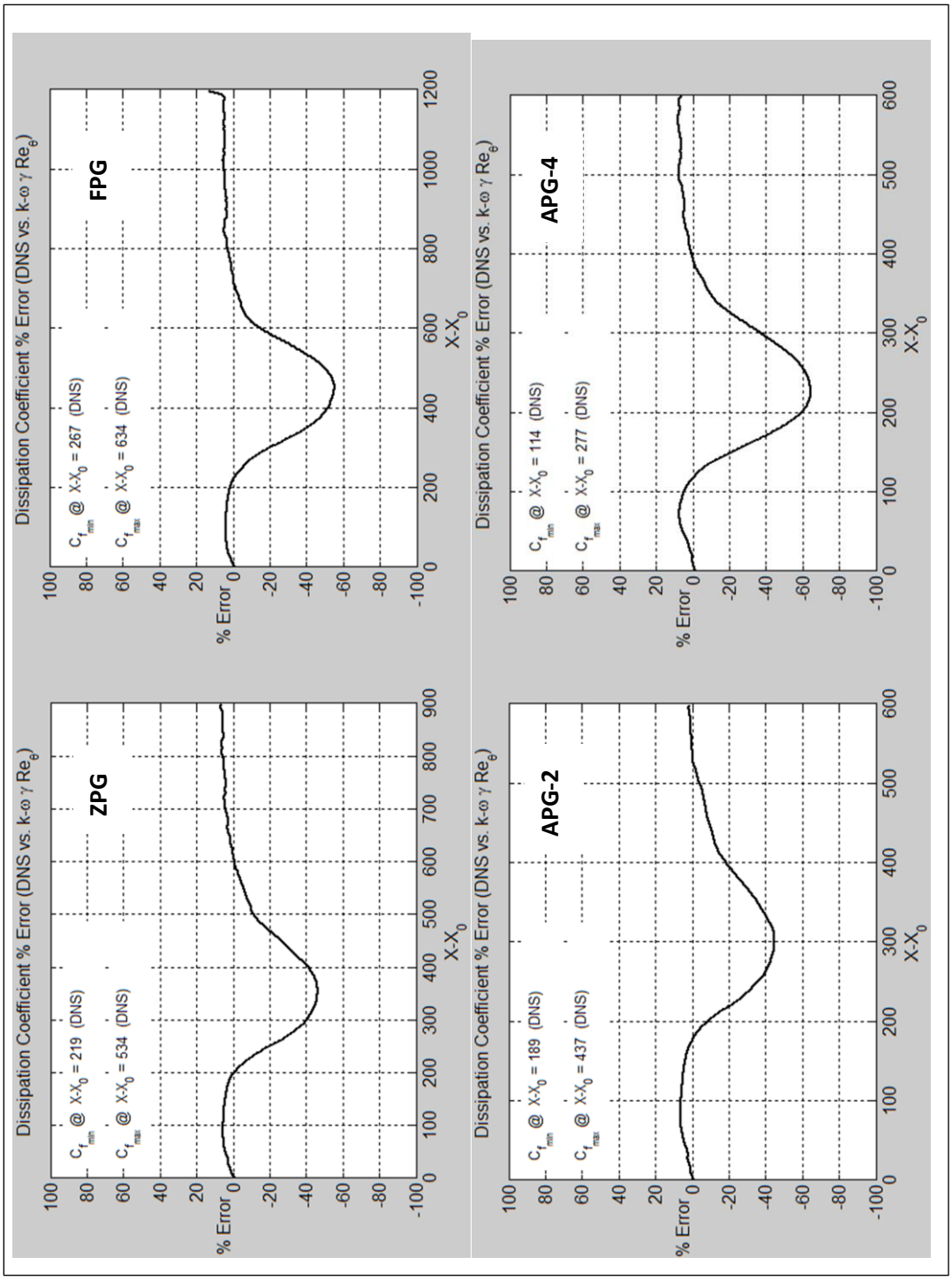

Figure 12 Percent Error Dissipation Coefficient (Left to Right, Top to Bottom: ZPG, FPG, APG-2, APG-4)

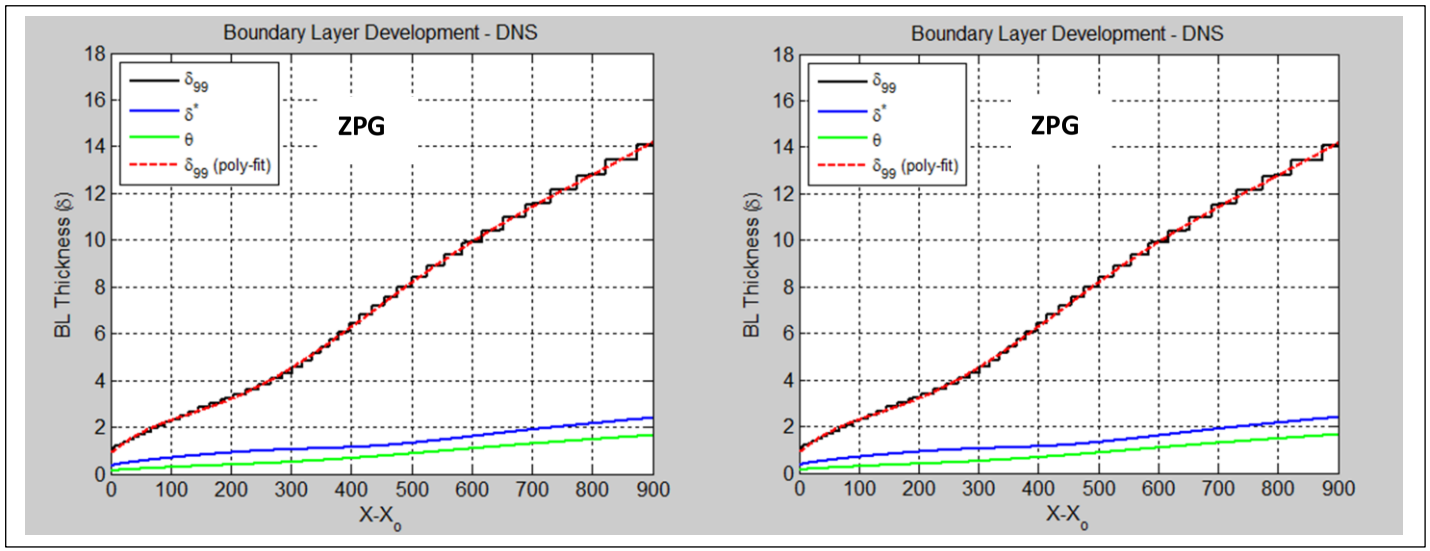

Figure 13 ZPG DNS Boundary Layer/Thickness Development (Left to Right: Non-calibrated, Calibrated)

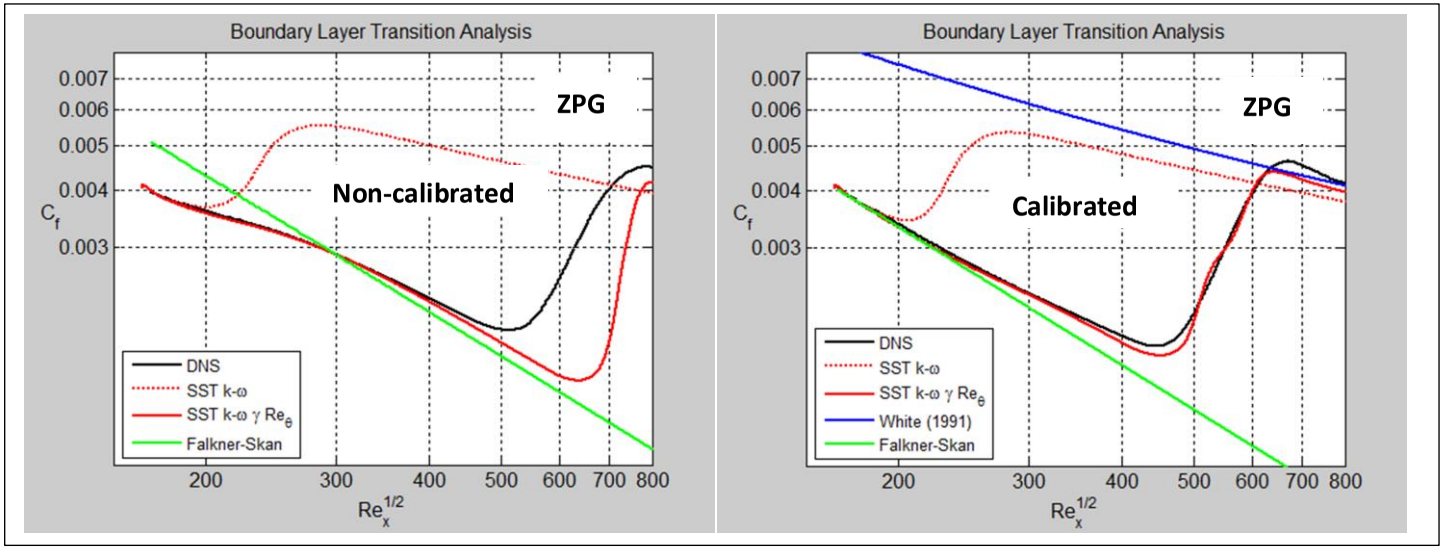

Figure 14 ZPG Skin Friction Coefficient Development (Left to Right: Non-calibrated, Calibrated)

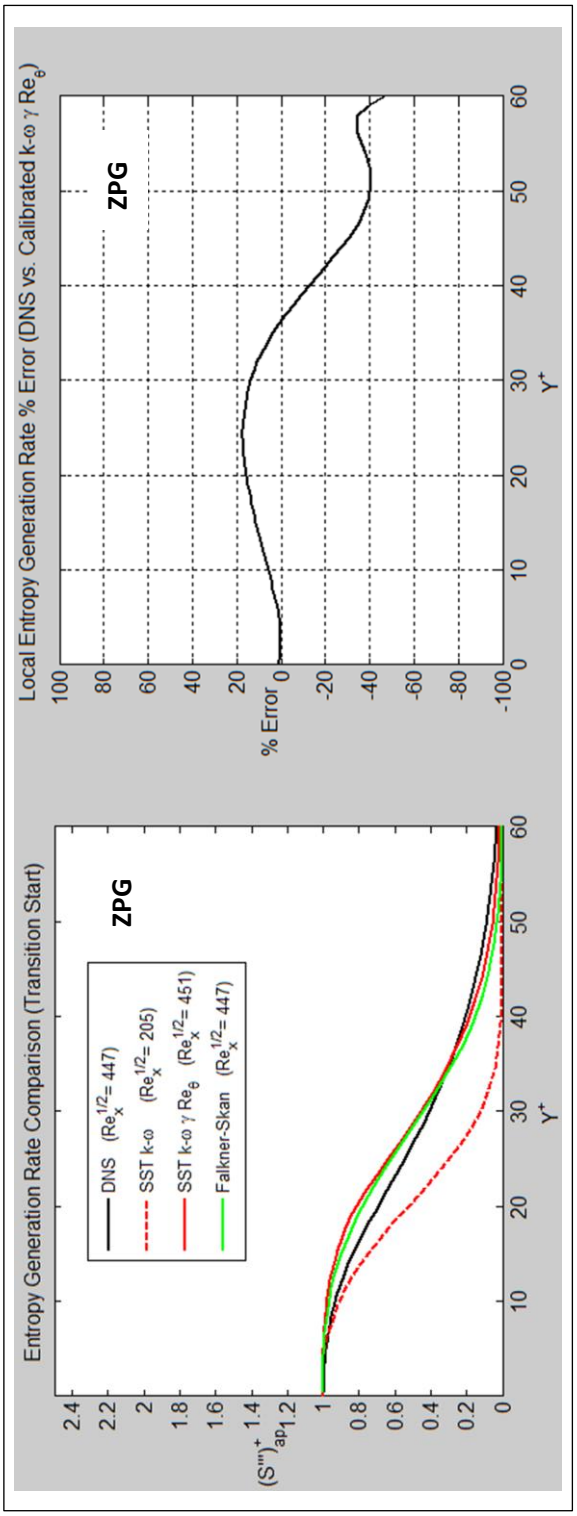

Figure 15 ZPG Approximate Entropy Generation Rate (Left) Percent Error DNS vs. Calibrated k-w γ-Re_θ (Right)

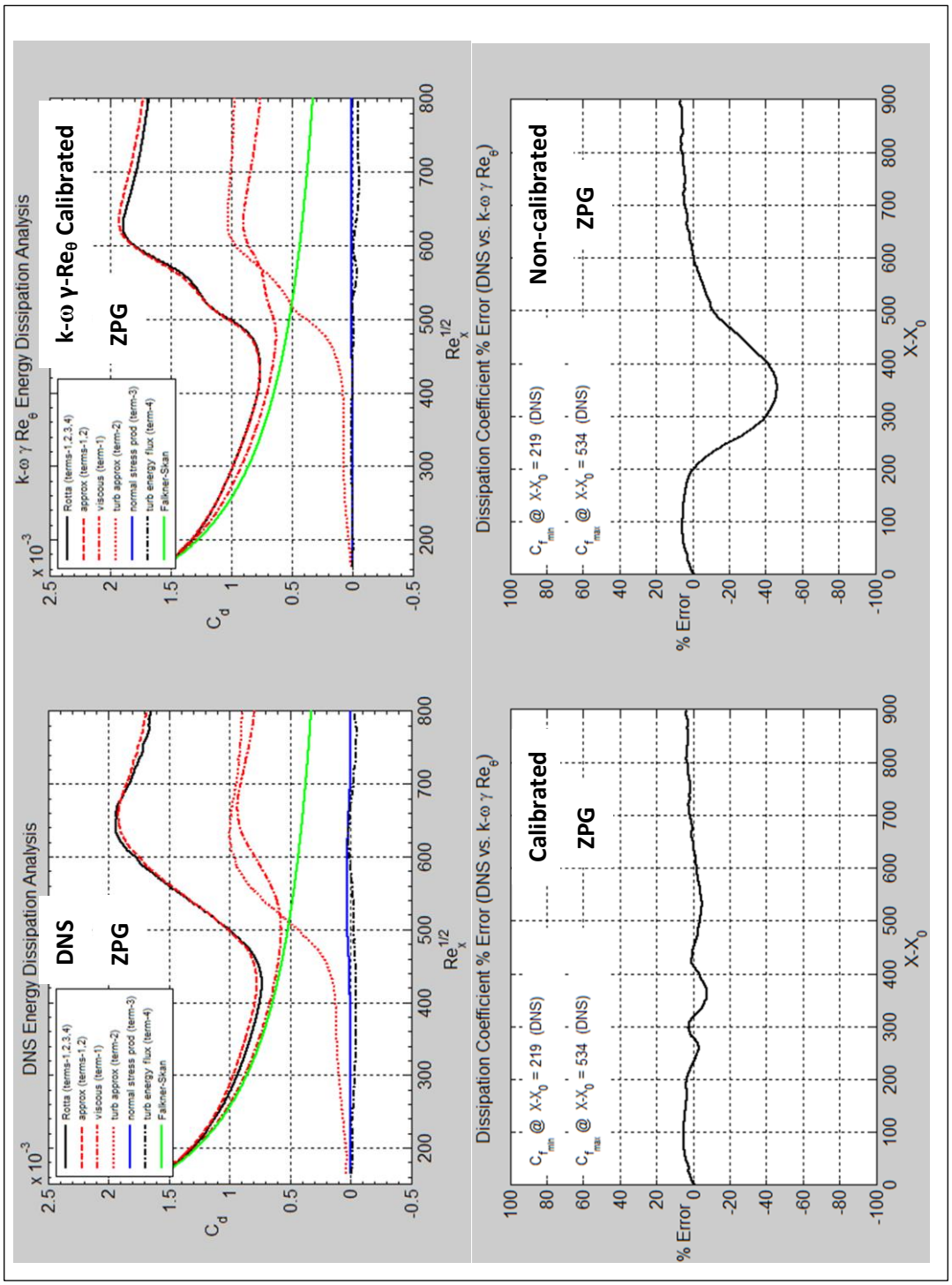

Figure 16 ZPG Dissipation Coefficient Non-calibrated vs. Calibrated k-w γ-Re$_\theta$ (Top Left to Top Right)
Percent Error "Calibrated" (Bottom Left) Percent Error "Non-Calibrated" (Bottom Right)

Appendix B: RCCS Project Report

The RCCS project report, which begins on the next page, is a summary of the initial CFD air Reactor Cavity Cooling System research that was conducted in preparation for the follow-on research described in the main body of this dissertation. The following is a synopsis of the conclusions from that report. Readers are urged to refer to the main body of the report in order to better understand the context of the conclusions.

1. CFD Modeling of the RCCS is complex.

2. The RCCS models require a significant amount of computational resources, requiring the use of high performance computing.

3. To improve solution accuracy, especially in environments of high heat flux, sufficient prism layers should be used to resolve the viscous/thermal boundary layers.

4. The STAR-CCM+ transient coupled solver should be used in simulations with a large number of prism layers and heat transfer present.

5. Computational overhead can be reduced by modeling the major components of the RCCS individually.

Based on the CFD scoping studies presented in this report, the following recommendations are provided in order to support CFD code validation.

1. The UW air RCCS experimental facility should be equipped with the appropriate instrumentation to collect turbulence data.

2. The UW RCCS experimental facility should be equipped with the appropriate instrumentation in the heated duct to measure heat flux, over the length of each duct, on each of the RCCS duct sides.

3. Consideration should be given to conducting a validation experiment, including storing the experimental data in a repository, so that experimental data could be available to other researchers for CFD modeling purposes.

A SUMMARY OF AIR REACTOR CAVITY COOLING SYSTEM SCOPING STUDIES USING COMPUTATIONAL FLUID DYNAMICS TECHNIQUES

Modeling and Test Validation of a Reactor Cavity Cooling System with Air
(U. S. DOE Nuclear Energy University Programs/NEUP 21-3079)

Air RCCS Project Report (CH-1)

by

Kurt D. Hamman
(Graduate Student)

and

Akira Tokuhiro, Ph.D.
(Major Professor)

Department of Mechanical Engineering
University of Idaho

October 15, 2014

Abstract

Computational fluid dynamics (CFD) scoping studies of the University of Wisconsin ¼-scale air reactor cavity cooling system were performed using STAR-CCM+ commercial CFD software. An initial CFD model of the outlet plenum was developed to explore the fluid behavior in the upper plenum, followed by an 'integrated model' of the three major components: inlet plenum, heated ducts, and outlet plenum. The computational overhead requirements of the integrated model, coupled with simulation convergence problems and availability of experimental data prompted the abandoning of the integrated model in favor of modeling one major component and sub-component, specifically the inlet plenum and heated duct #4. As part of this final analysis, CFD results were compared to experimental data using a calibration process, in which the duct wall heat flux boundary conditions were changed until the duct core flow CFD temperature profile approximated the experimental data. The results of this study identified optimal CFD simulation settings and the need for additional experimental data in order to evaluate the capabilities and limitations of a predictive simulation of the air reactor cavity cooling system.

Table of Contents

A. INTRODUCTION 177
B. LITERATURE REVIEW 180
C. COMPUTATIONAL TOOLS 181
CFD Software 181
Hardware 182
D. CFD SCOPING STUDIES 182
Outlet Plenum Analysis (Scoping Study #1) 185
Symmetric Integrated Model (Scoping Study #2) 189
Full Integrated Model (Scoping Study #3) 190
Inlet Plenum Analysis (Scoping Study #4) 190
Symmetric Heated Duct #4 Analysis (Scoping Study #5) 191
E. VERIFICATION AND VALIDATION 194
F. CONCLUSIONS AND RECOMMENDATIONS 194
G. REFERENCES 196
H. APPENDICES 198
Appendix A: Mesh Settings and Metrics 198
Appendix B: Simulation Settings and Boundary Conditions 199

Note:

Change one (CH-1) to this report reflects a formatting change to accommodate binding margins.

A. INTRODUCTION

The air reactor cavity cooling system (RCCS) is a safety related decay heat removal passive cooling system undergoing research and development in support of the new generation nuclear power plants, specifically the very high temperature gas reactor. The RCCS acts as a heat removal medium during normal operating conditions to maintain appropriate temperatures for the reactor cavity concrete, therefore; it is always available to remove decay heat during accident conditions [DOE 1992].

University of Wisconsin (UW) designed, built, and conducted initial testing of a ¼-scale air RCCS. The UW design was based on the ½-scale Argonne National Laboratory Natural Convection Shutdown Heat Removal Test Facility (NSTF), which was based on the General Atomics (GA) RCCS conceptual design [Lomperski et al. 2010, Lomperski et al. 2011]. The UW experimental facility represents a 9.5 degree sector of the GA conceptual design. It includes three major components: inlet plenum, six riser ducts, and an outlet plenum [Muci 2014b].

The UW facility is capable of operating in either forced circulation or natural circulation. In forced circulation, a variable speed fan provides the motive force to move air into the inlet plenum where mixing of the air occurs prior to entering the riser ducts. Upon entering the risers, the air is heated by a bank of 32 heaters capable of generating a power of 40 kW. The heaters, located within the heated cavity, cover approximately 80% of the height of the ducts. The purpose of the heaters is to simulate the radiative and convective heat transfer from the reactor to the ducts. The air flow enters the outlet plenum where mixing occurs before the hot air exits the outlet plenum through two exhaust pipes; the hot air is discharged to the atmosphere via two chimneys [Muci 2014b]. The CFD geometry of the air RCCS is shown in Figure 1.

One of the most popular turbulence models used for the analysis of a wide variety of industrial problems is the K-Epsilon (k-ε) turbulence model [Pope 2001, Wilcox 2000, CD-adapco 2013]. The turbulence model consists of two transport equations: turbulent kinetic energy (k) and turbulent dissipation rate (ε). Therefore, a 3-D simulation requires that a

total of seven transport equations (mass, momentum, energy, and turbulence) are solved by the commercial CFD software. Noteworthy is that a turbulent kinetic energy and turbulent dissipation rate can be related to turbulent intensity (I) using Equation (1) through Equation (3), where L represents length scale, D_h represents hydraulic diameter, v represents local velocity, and C_μ equals 0.09 [Cd-adapco 2009]. Turbulence intensity can be derived from experimentally measured data, so turbulent intensity along with an estimated turbulence length scale, are used as boundary conditions for the two transport equations. If turbulence intensity (I) experimental data is not available, typically thumb rules are used. For example one thumb rule states: "[For] Flow in not-so-complex devices like large pipes, ventilation flows etc. or low speed flows (low Reynolds number). Typically the turbulence intensity is between 1% and 5%." [CD-adapco 2014]

$$k \approx \frac{3}{2}(Iv)^2 \qquad \text{Equation (1)}$$

$$\varepsilon \approx \frac{C_\mu^{3/4} k^{3/2}}{L} \qquad \text{Equation (2)}$$

$$L \approx \frac{D_h}{10} \qquad \text{Equation (3)}$$

STAR-CCM+ provides users with two options for a numerical solver: segregated and coupled. The segregated solver solves the transport equations in an 'uncoupled' fashion. For example, using a SIMPLE-type algorithm, each transport equation is solved independently; although, the linking of the momentum and mass continuity transport equations is accomplished using a predictor-corrector approach. The coupled solver solves the mass and momentum transport equations in a 'coupled' fashion. Each solver has advantages and disadvantages. For example, the coupled solver requires more memory; but it produces more accurate results for compressible flows and high Rayleigh number natural convection flows [STAR-CCM+ 2013].

One of the most difficult and time consuming steps of the modeling and simulation process is verifying that the mathematical equations are solved right (e.g., correct syntax, mesh refinement analyses), comparing the numerical results with experimental data and/or DNS results, establishing the relative error of the results, and finally demonstrating that an appropriate level of software quality (e.g., version control, code documentation) was maintained. Typically referred to as 'Verification, Validation, and Uncertainty Quantification' (VV&UQ) and Code Quality Assurance (QA), these step are mandatory for safety-related calculations (i.e., nuclear reactor safety); yet, it is important that non-safety-related calculations (e.g., fundamental research) should have some degree of rigor established - on par with the risk associated with the use of incorrect results [Oberkampf and Roy 2010]. This short-duration study was focused on CFD scoping studies. Consequently, a formal V&V methodology was not followed, although several components of a typical V&V methodology such as residual convergence, energy conservation, and comparison of numerical results with experimental data were employed.

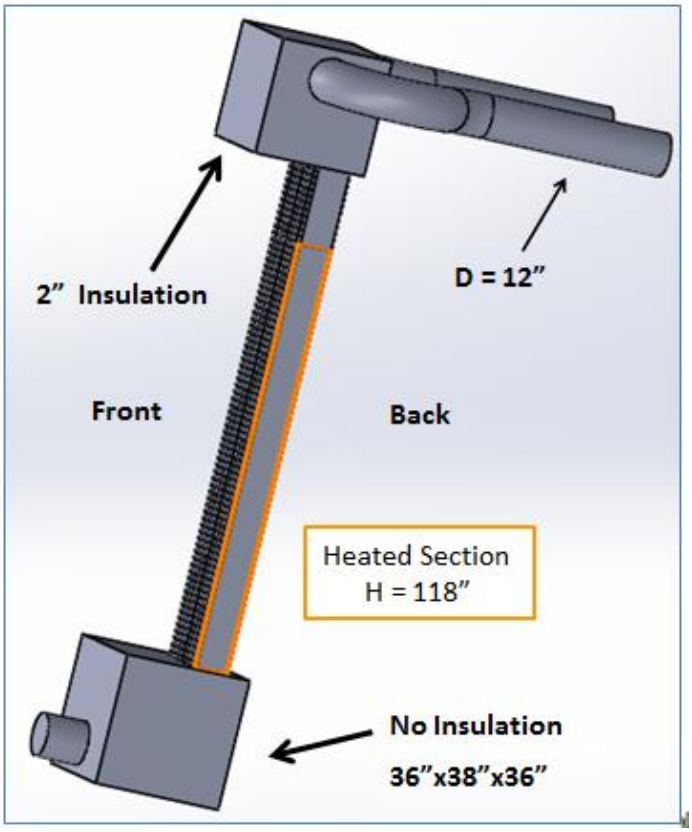

Figure 1 Air RCCS CFD Geometry (Analyses #4 and #5)

B. LITERATURE REVIEW

Several CFD simulations of the RCCS and scaled models of the RCCS have been performed, primarily by Argonne National Laboratory (ANL) where the Natural Convection Shutdown Heat Removal Test Facility (NSTF) is located. One of the purposes of this facility is to generate experimental data for code validation.

In 2005, ANL published a CFD analysis report characterizing the applicability of the NSTF for the simulation of the VHTR RCCS. Two CFD simulations were performed to prove that the NSTF, originally built to provide experimental support for the design and analysis of the PRISM reactor vessel auxiliary cooling system, can be used to produce thermal-hydraulic flows that would replicate those of the full-scale RCCS. Few details were provided about the CFD simulation parameters (e.g., mesh generation information, boundary layer resolution, and numerical solver type), other than noting that the commercial CFD software STAR-CD and the standard high-Re K-Epsilon model were used [Tzanos 2005].

In 2010, ANL published a second report which focused on the analysis of the GA air RCCS design in support of scaling studies and instrumentation support [Lomperski et al. 2010]. The report includes CFD studies of the full-scale GA RCCS and the NSTF 'experiment-scale' simplified RCCS model. This study concluded that the NSTF design reproduces the major flow features of the anticipated RCCS design. STAR-CCM+ commercial CFD software was used for the studies.

In 2011, a follow-on to the second ANL report was published [Lomperski et al. 2011]. The primary objective of this study (and supporting CFD analyses) was the evaluation of experimental scaling relationships, which were to be used in modifying the existing NSTF into a scaled 'experiment model' of the GA RCCS. "In summary, the scaling evaluation updated the basis that the air-cooled RCCS can be simulated at the ANL NSTF facility at a prototypic scale in the lateral direction and about half scale in the vertical direction." Additional CFD studies, including sensitivity analyses and analyses to support instrument placement, were performed. Several CFD design simulations were performed as part of this study; four promising designs were presented. CFD simulation settings were

similar to those reported in the 2010 study; additionally, insight into the mesh settings was provided. For example, information on mesh refinement studies suggest that 3 prism layers were used with the two-layer all y+ K-Epsilon turbulence model; more than 15 million computational elements with local refinement in the riser ducts were used.

In 2012 a conference paper was published summarizing the results of simulating NSTF natural circulation operation, using the commercial CFD code STAR-CCM+ [Dave et al. 2012]. In 2013, a follow-up conference paper to the 2012 paper was published identifying difficulties in obtaining good convergence [Hu and Pointer 2013]. Improved convergence was obtained by shifting from the segregated solver, which is a SIMPLE-type algorithm, to the coupled solver. Additionally, the mesh was refined resulting in greater than 20 million elements. Furthermore, based on a review of the figures presented in the paper, it appears that the number of prism layers was increased from three to five layers.

In 2013, a third conference paper was published summarizing the results of simulating the 'experiment-1/4 scale' RCCS using the commercial CFD code FLUENT [Lisowski et al. 2013]. The CFD simulation was used to assist in determining the placement of six riser ducts within the heated cavity in addition to providing confidence that adequate mixing will take place in the outlet plenum. Due to space limitations, a 6 riser duct heated assembly was constructed instead of a twelve riser duct assembly, which would have been consistent with the ANL 'experiment-1/2 scale' RCCS. The symmetry model consisted of 2.2 million tetrahedral computational elements. The following simulation settings were used: SIMPLE pressure-velocity coupling scheme, SST k-ε turbulence model[1], body force weighted pressure method, and 2nd order spatial discretization.

C. COMPUTATIONAL TOOLS

CFD Software

The commercial CFD software STAR-CCM+ was used to generate the three-dimensional RANS velocity and temperature fields for this study [CD-adapco 2013]. STAR-CCM+ uses a cell-centered finite volume discretization technique and an unstructured

[1] Due to a type-o in the paper, the most likely turbulence model used is SST k-ω.

mesh generator. Two generalized solvers are available, coupled and segregated. SolidWorks was used to generate the solid model geometry, which was imported into STAR-CCM+ [Dassault Systemes 2013].

Hardware

A ZaReason 'Fortis Extreme 2' workstation with an AMD FX-8350 8-core processor and Linux Ubuntu 12.04 LTS operating system (Linux) was used to develop the CFD models. Small models were developed and run on this Linux box, but larger CFD models were run on the University of Idaho Big-STEM (HP DL 980G7) high performance computer. Big-STEM is comprised of 80 cores of the Intel Zeon EZ-4870 2.40 Ghz processors and 4 Tb of RAM with a Red-Hat 6.5 operating system (Linux); 64 processors were allocated for this work.

D. CFD SCOPING STUDIES

The preliminary design phase of the University of Wisconsin (UW) RCCS experimental facility used the commercial CFD code FLUENT to guide the design. During the final year of the project, several RCCS CFD scoping studies using the commercial code STAR-CCM+ were performed by University of Idaho in an effort to evaluate optimal mesh and simulation settings; comparison of the experimental data with the CFD results was performed as well. The realizable two-layer K-epsilon (k-ε) turbulence model in conjunction with the all y+ wall treatment was used for all simulations. A summary of the key mesh settings and simulation parameters are presented in Table 1 and Table 2. Hamman and Tokuhiro provide additional details related to the scoping studies in project summary presentation [Hamman and Tokuhiro 2014].

The information presented in this report briefly describes the scoping studies, which included five CFD analyses. One of the goals of the study was to focus on resolving the boundary layer in order to obtain as accurate a solution as possible, especially in the heated duct region. Initially the scoping studies, primarily Analysis #2, were guided by the FLUENT study performed by Lisowski et al. (2013), SolidWorks geometry provided by Muci

Table 1 – Key Mesh Parameters

	Component	Mesh Type	Boundary Layer Thickness	No. Prism Layers	No. Elements	Wall Y+ (heated)	Wall Y+ (other)	Wall Y+ (duct walls)
Analysis #1 (high velocity)	Outlet Plenum	Prism/Polyhedral	2.5 mm	10	690,920	N/A	0.31	5.00
	Outlet Plenum (Sym)	Prism/Polyhedral	2.5 mm	10	366,428	N/A	0.29	4.95
Analysis #1 (low velocity)	Outlet Plenum	Prism/Polyhedral	2.5 mm	10	690,920	N/A	0.06	1.00
	Outlet Plenum (Sym)	Prism/Polyhedral	2.5 mm	10	366,428	N/A	0.06	0.92
Analysis #2	Full RCCS (Sym)	Prism/Polyhedral	2.5 mm/0.35 mm	10	3,853,442	0.03	0.21	0.67
Analysis #3	Full RCCS	Prism/Polyhedral	3.0 mm	20	9,004,257	0.06	0.09	19.80
Analysis #4	Inlet Plenum	Prism/Polyhedral	3.5 mm	21	2,740,704	N/A	0.06	9.75
Analysis #5	Inlet Plenum	Prism/Polyhedral	3.5 mm	21	2,740,704	N/A	0.03	46.70
	Duct #4 (Sym)	Prism/Trimmer	3.0 mm	20	986,624	0.07	N/A	N/A

Table 2 – Key Simulation Parameters

				Inlet Boundary Conditions					
	Component	Temporal Analysis Type	Numerical Solver	Velocity (m/s)	Tke (J/kg)	Tdr (m^2/s^3)	Turb Intensity	Turb Length Scale	Temperature (C)
Analysis #1 (High)	Outlet Plenum	Steady	Segregated	See Table	See Table	See Table	N/A	N/A	See Table
	Outlet Plenum (Sym)	Steady	Segregated	See Table	See Table	See Table	N/A	N/A	See Table
Analysis #1 (Low)	Outlet Plenum	Steady	Segregated	See Table	See Table	See Table	N/A	N/A	See Table
	Outlet Plenum (Sym)	Steady	Segregated	See Table	See Table	See Table	N/A	N/A	See Table
Analysis #2	Full RCCS (Sym)	Steady	Segregated	(pressure = 0)	6.00E-04	7.92E-05	N/A	N/A	25.0
Analysis #3	Full RCCS	Transient	Segregated	5	3.75E-03	1.24E-03	N/A	N/A	15.9
Analysis #4	Inlet Plenum	Steady	Segregated	5	3.80E-03	1.00E-03	N/A	N/A	16.0
Analysis #5	Inlet Plenum	Transient	Coupled	4.788	N/A	N/A	2%	0.03048	17.2
	Duct #4 (Sym)	Steady	Coupled	0.52, -0.6974, 5.41	5.4964	1.08E+02	N/A	N/A	18.4

(2013), and monthly project progress reports; as much as practical, simulation settings similar to those used in the FLUENT study were selected for the STAR-CCM+ simulations. For example, the Lisowski study used the FLUENT's SIMPLE solver, while the STAR-CCM+ segregated solver was employed.[2]

Based on the importance of resolving the boundary layer, 10 prism layers were used for some of the initial analyses. The number of prism layers was increased in later analyses; the number of prism layers ranged from 20 to 21. Noteworthy is that STAR-CCM+ user documentation suggests that at least 15 cells should be used to resolve the boundary layer for heat transfer simulations, and the y+ values should remain less than 3 [CD-adapco 2013]. The general requirement in the FLUENT user guide is to ensure that at least 10 cells are used to resolve the shear layer (viscous boundary layer) [ANSYS 2012].[3]

Due to the limited computational resources initially available (i.e., 8-core Linux box), early simulations used only 10 prism layers; Table 3 presents computational information. As more computational resources became available (i.e., Big-STEM), the number of prism layers was increased. Consequently (and unexpectedly), residual convergence problems arose. Noteworthy is that accuracy problems, associated with energy conservation in the heat transfer simulations, were present; but they went unidentified for a period of time.

An additional literature search, conducted late in the project, revealed that analysts at Argonne National Laboratory identified a problem associated with energy conservation in previous simulations that utilized the segregated solver; but, they did not experience residual convergence problems [Hu and Pointer 2013]. The energy conservation problems were resolved by utilizing the coupled solver.

Based on the information learned from the Hu and Pointer study, Analysis #5 of this study utilized the coupled solver, which resolved accuracy related to energy conservation; but the residual convergence problems remained (e.g., plenums and Duct #4). Eventually,

---

[2] The STAR-CCM+ segregated solver is based on the SIMPLE algorithm [CD-adapco 2013].

[3] "Generally speaking, it is more important to ensure that the boundary layer is covered with sufficient cells, then to achieve a certain y+ criterion. However, for simulations with high accuracy demands on the wall boundary layer (especially for heat transfer predictions) near wall meshes with y+ ~1 are recommended." [ANSYS 2012]

Table 3 – Computational Overhead Data

	Component	Computational Time (sec)	Computational Time (hrs)	Processors	Simulation Time (sec)
Analysis #1 (High)	Outlet Plenum	12,302	3.4	8 / Aries	N/A
	Outlet Plenum (Sym)	6,510	1.8	8 / Aries	N/A
Analysis #1 (Low)	Outlet Plenum	12,442	3.5	8 / Aries	N/A
	Outlet Plenum (Sym)	6,748	1.9	8 / Aries	N/A
Analysis #2	Full RCCS (Sym)	181,043	50.3	8 / Aries	N/A
Analysis #3	Full RCCS	1,076,906	299.1	64 / Big-STEM	1.86
Analysis #4	Inlet Plenum	7,294	2.0	24 / Big-STEM	N/A
Analysis #5	Inlet Plenum	273,095	75.9	48 / Big-STEM	1.00
	Duct #4 (Sym)	297,448	82.6	48 / Big-STEM	N/A

it was determined, through additional numerical experimentation that running the transient (instead of the steady-state) solver improved residual convergence for the inlet and outlet plenum simulations. Residual convergence issues associated with heated Duct #4 were resolved by using a ramping function to gradually increase boundary conditions (velocity, heat flux, and turbulence parameters) to their desired values; ramping in conjunction with the steady-state coupled solver resulted in satisfactory convergence and energy conservation performance.

Outlet Plenum Analysis (Scoping Study #1)

Two models, a full model and a symmetric model, were developed as part of Scoping Study #1 (outlet plenum study). Figures 2 through 5 present the full model geometry and results; the left exhaust pipe purposely is hidden in Figure 2. Due to the brevity of this report, the symmetric model results are not presented; detailed results can be found in the project summary presentation by Hamman and Tokuhiro (2014).

The initial scoping studies focused on CFD simulations of the outlet plenum, at inlet plenum velocities of approximately 0.5 m/s and 5.0 m/s; Table 4 presents the boundary conditions used for this analysis. As the construction of the UW RCCS progressed, it was realized that the RCCS experiment would not be instrumented to collect experimental data

to establish CFD boundary conditions at the inlets of the 'outlet plenum.' Therefore, efforts were directed to modeling the majority of the RCCS components (e.g., lower plenum, heated ducts, and outlet plenum) since sufficient experimental data at the inlet of the 'inlet plenum' was expected to be available.

Similar to the studies by Argonne National Laboratory, the results of this analysis indicate that large vortex structures develop in the outlet plenum. Also, complex flow structures develop near the bottom wall of the outlet plenum. These complex flow structures are presented in Figures 4 and 5. Noteworthy is that the penetration of the heated ducts into the outlet plenum contribute to the complex flow patterns near the bottom of the outlet plenum. (Similar complexities were predicted in the lower plenum by follow-on CFD simulations.) Figure 3 presents the residuals for the full model; although not presented in this report, the residuals for the symmetric model decreased to less than $1x10^{-2}$. In short, depending on whether the geometry is full or symmetric, residual convergence problems may be present. Although it is not conclusive, the convergence problem in Figure 3 may be the result of imposing two outlet pressure boundary conditions (one for each exhaust) on the full model; the symmetric model only requires one outlet pressure boundary condition.

Table - 4 Outlet Plenum Boundary Conditions

Duct #	Low Velocity Simulation			High Velocity Simulation			Temperature	
	v (m/s)	k (J/kg)	ε (J/kg-s)	v (m/s)	k (J/kg)	ε (J/kg-s)	T (F)	T ('C)
1	0.40	2.40E-05	2.56E-06	4.0	2.40E-03	2.56E-03	150.0	65.6
2	0.45	3.04E-05	3.65E-06	4.5	3.04E-03	3.65E-03	160.0	71.1
3	0.50	3.75E-05	5.01E-06	5.0	3.75E-03	5.01E-03	170.0	76.7
4	0.50	3.75E-05	5.01E-06	5.0	3.75E-03	5.01E-03	170.0	76.7
5	0.45	3.04E-05	3.65E-06	4.5	3.04E-03	3.65E-03	160.0	71.1
6	0.40	2.40E-05	2.56E-06	4.0	2.40E-03	2.56E-03	150.0	65.6

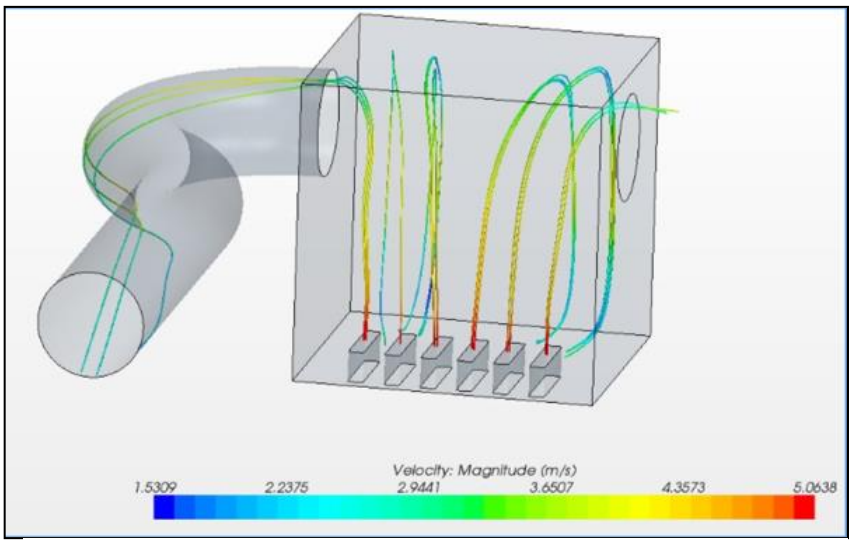

Figure 2 CFD Analysis #1 – Streamlines

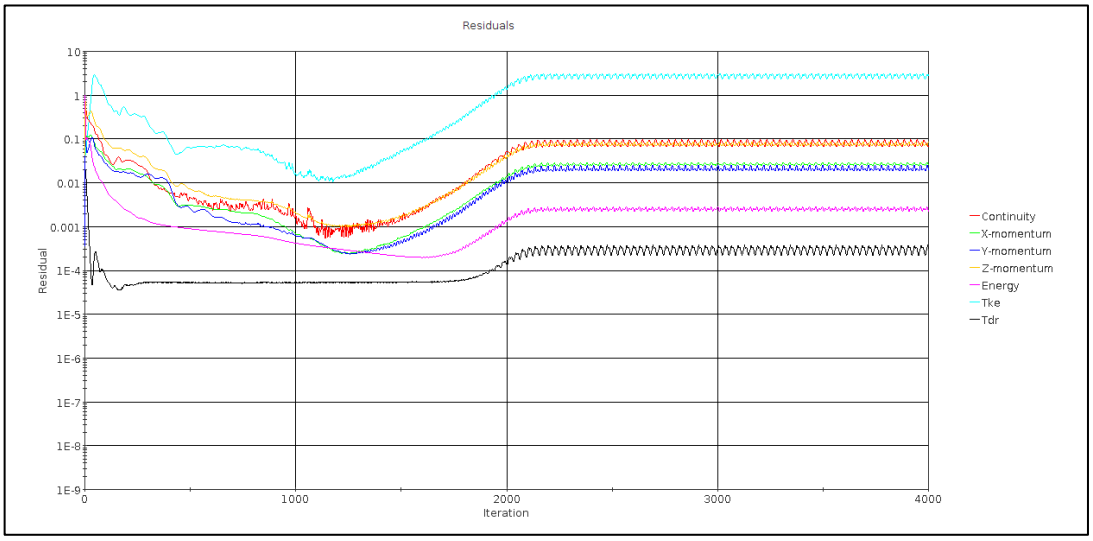

Figure 3 CFD Analysis #1 – Residuals (Full Model)

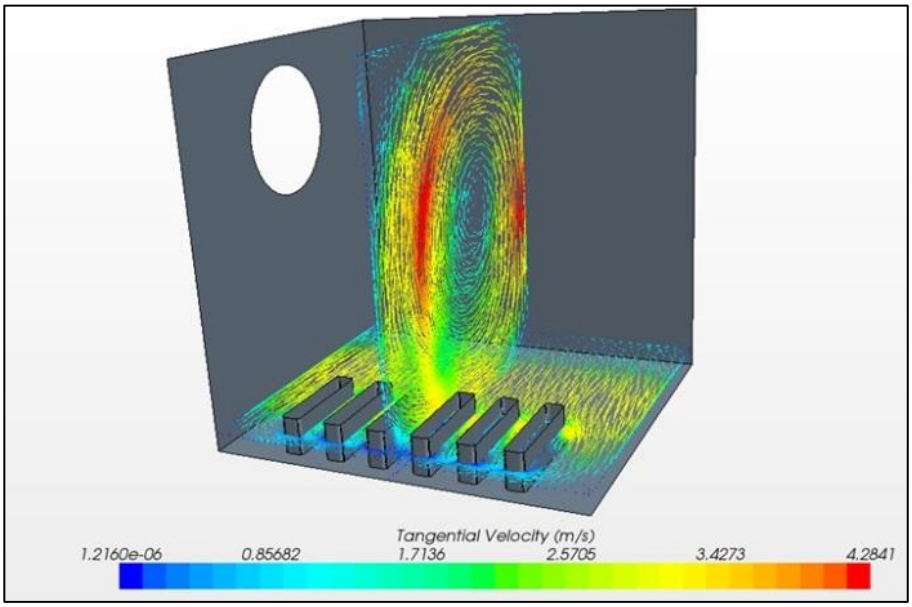

Figure 4 CFD Analysis #1 – Vector Velocity Plot

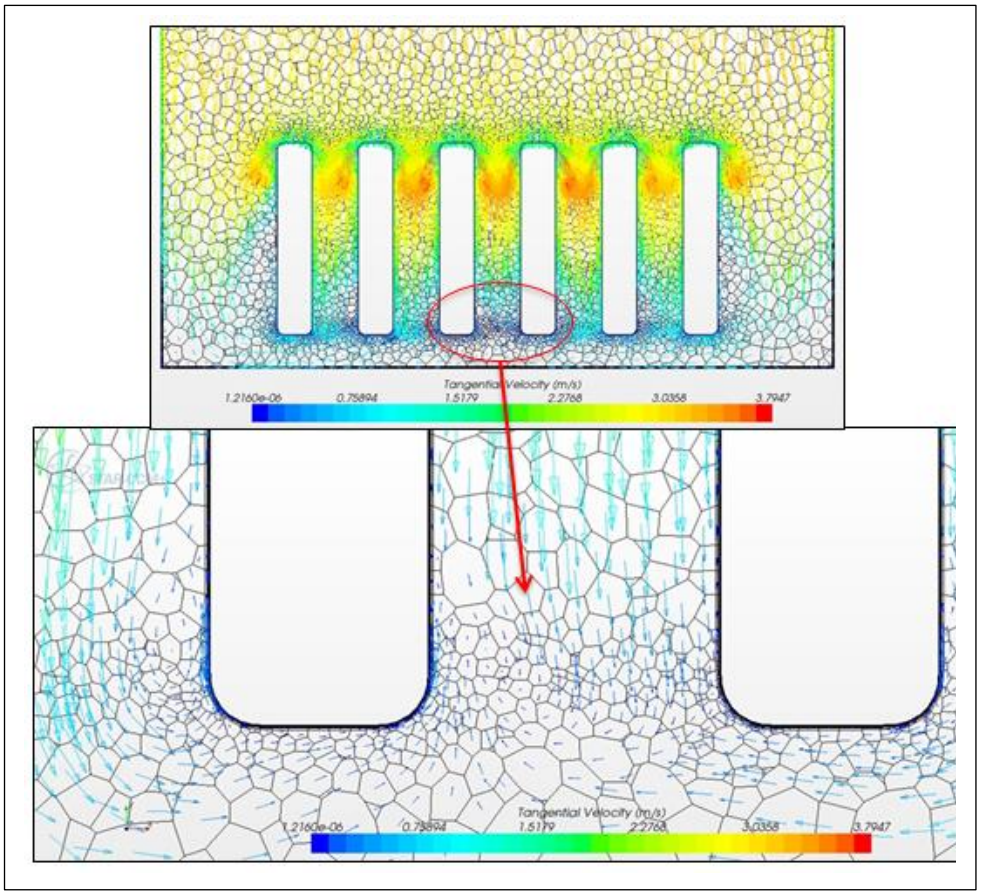

Figure 5 CFD Analysis #1 – 1.7” above bottom wall

Symmetric Integrated Model (Scoping Study #2)

A 3-D simulation, using a symmetric geometry model of the air RCCS was performed in an effort to reproduce the results of Lisowski et al. (2013); the commercial CFD code FLUENT was used for that study. The CFD results are presented in Figure 6. The simulation was performed in three steps. First, adiabatic flow conditions were established using an inlet velocity of 1 m/s, followed by the application of a cosine shaped heat flux with a peak flux of 1.68 kW/m^2; a total power of 9.91 kW was applied. Finally, natural circulation boundary conditions were established, and the simulation was run for 7000 iterations, where the energy residual flattened and all other residuals were reduce to less than 1x10-4. Consistent with the results presented by Lisowski et al. (2013), a 2.36 m/s outlet velocity at the duct was predicted by STAR-CCM+. A boundary layer thickness of 0.35 mm was used for the heated duct walls; the remaining walls were 2.5 mm. The simulation time was 33 hours on the 8 core workstation.

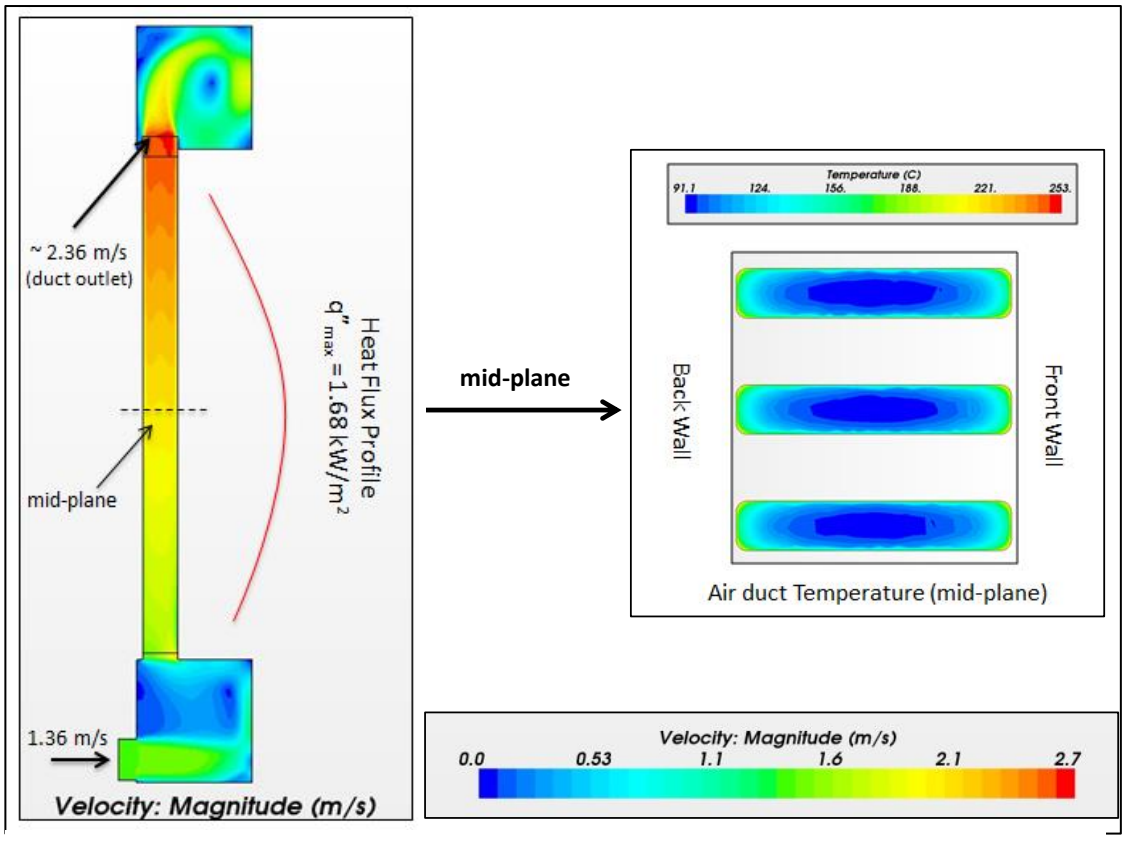

Figure 6 CFD Analysis #2 - Contour Plots

Full Integrated Model (Scoping Study #3)

A third scoping study was performed as part of this study. The purpose of this study was to evaluate the challenges associated with simulating a full 3-D model. Additionally, the intent was to compare forced circulation simulation results with experimental data prior to moving on to a more advanced natural circulation simulation.

Although, a symmetric model reduces the computational overhead; a full model simulation is important in the understanding of abnormal operating conditions (e.g., plugged duct, corrosion buildup in ducts). Unfortunately, the computational overhead coupled with problems associated with residual convergence and energy conservation resulted in abandoning this simulation. Noteworthy is that shifting from the steady-state segregated solver to the transient segregated solver improved residual convergence; but inaccuracies in energy conservation remained. Unfortunately, a transient simulation is computationally expensive. For example, the simulation run time was 299 hours on 64 processors.

Inlet Plenum Analysis (Scoping Study #4)

A fourth scoping study was performed as part of this study. The purpose of this analysis was to provide "qualitative" vector-velocity data of the inlet plenum to assist experimentalists with evaluating the uncertainty of heated duct velocity transducers [Muci 2014b]. While preparing for this study, an error was found in the CFD geometry; therefore, the dimensions of the CFD model were checked. A comparison of the CFD geometry with the "nominal" as-built experimental geometry revealed three errors in the CFD geometry. Specifically, the location of the inlet pipe to the inlet plenum was incorrect; the penetration depth into the inlet plenum was incorrect, and inlet plenum dimensions were increased since unlike the outlet plenum, the inlet plenum did not have any insulation. The CFD geometry was updated (Figure 1), and additional solver testing was performed. Figure 7 presents a vector-velocity plot showing the complex flow structures. Residual convergence

problems were observed. Additional results from this analysis are presented in a project summary by Hamman and Tokuhiro [2014].

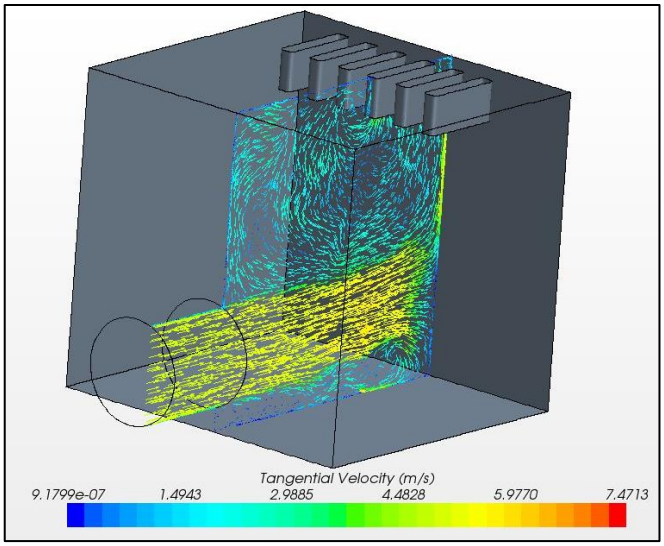

Figure 7 CFD Analysis #4 - Vector Velocity Plot (Duct #4 Plane)

Symmetric Heated Duct #4 Analysis (Scoping Study #5)

A fifth scoping study was performed as part of this study. The purpose of this analysis was to compare the CFD results with experimental data [Muci 2014a]. Based on the information learned in previous analyses, it was decided to abandon the full 3-D integrated modeling approach and independently model the inlet plenum and heated duct #4. In preparation for this final scoping study, an additional literature survey was performed. Two conference papers and several ANL technical papers were located, which provided insight into the problem size (i.e. mesh size), CFD solver settings, and convergence problems experienced by other analysts [Tzanos 2005, Lomperski et al. 2010, Lomperski et al. 2011, Dave et al. 2012, Hu and Pointer 2013]. A review of the additional literature suggests that three to five prism layers were used, yet it is not clear from the reports why the number prism layers were limited to five.

The boundary conditions used at the inlet to the heated duct were obtained from the results of a simulation performed of the inlet plenum. This was necessary since insufficient experimental data was collected at the duct inlets in order to establish CFD inlet boundary conditions. For example, turbulence intensity and temperature were not measured. Additionally, the accuracy of the velocity measurements at the duct inlets was called into question. For example, the 'qualitative' CFD analysis (i.e., Analysis #4) showed that the velocity vectors were not normal to the velocity transducers [Muci 2014b].

The CFD settings for the lower plenum were similar to the settings used in previous simulations except that the transient coupled solver was used; these solver settings resulted in improved residual convergence for the lower plenum. An inlet velocity of 4.8 m/s and a temperature of 17.2 C were imposed on the inlet along with an assumed turbulence intensity of 2% and a turbulence length scale of one-tenth the inlet pipe diameter (0.03048 m); outflow boundary conditions were imposed on all ducts [CD-adapco 2009].

Duct #4 was modeled using simulation settings similar to those used for the inlet plenum except that the steady state coupled solver was used and the mesh type was changed from a polyhedral to a hexahedral to improve mesh metric results. The steady state solver, as opposed to the transient solver, was selected because to reduce computational time. Reduced computational time was critical, especially considering that numerous calibration simulations had to be performed. The surface average outlet values of the inlet plenum simulation were imposed as inlet conditions to duct #4. The boundary conditions applied at the inlet are specified in Table 9 located in the appendix. The boundary conditions at the duct sides were determined through a calibration process where heat flux values were guessed and successive simulations were ran until the core flow temperature CFD profile approximated the experimental values. The duct temperature profile for the final simulation is presented in Figure 8 and the residuals are presented in Figure 9. Additional results are presented by Hamman and Tokuhiro (2014).

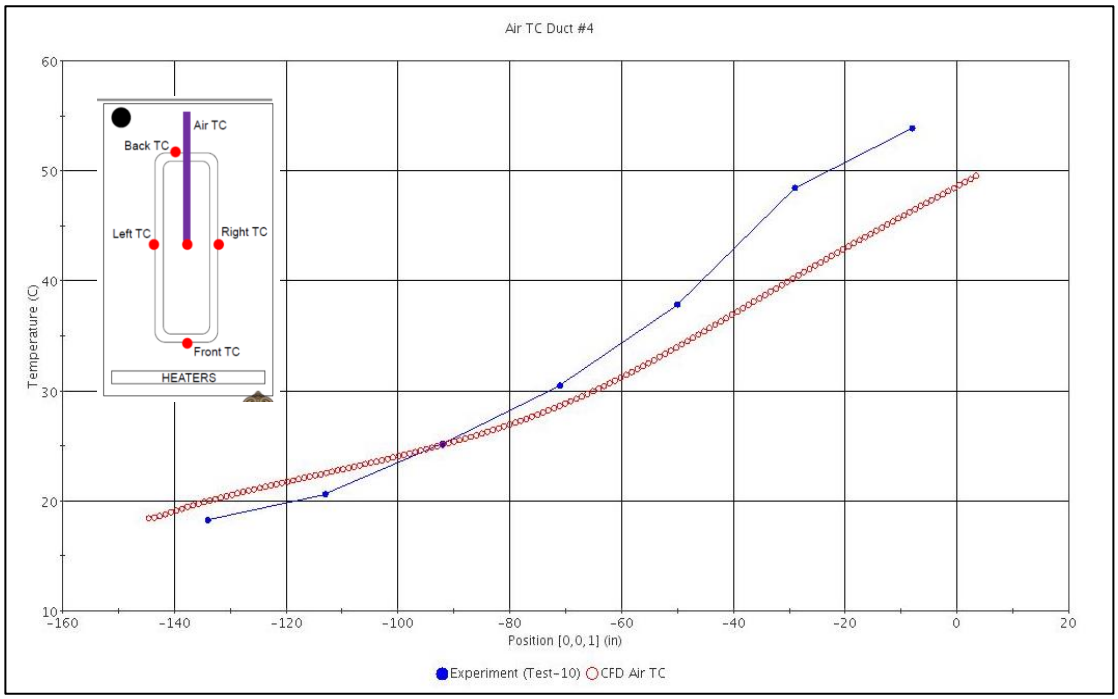

Figure 8 CFD Analysis #5 - Calibration Results (Air TC Location)

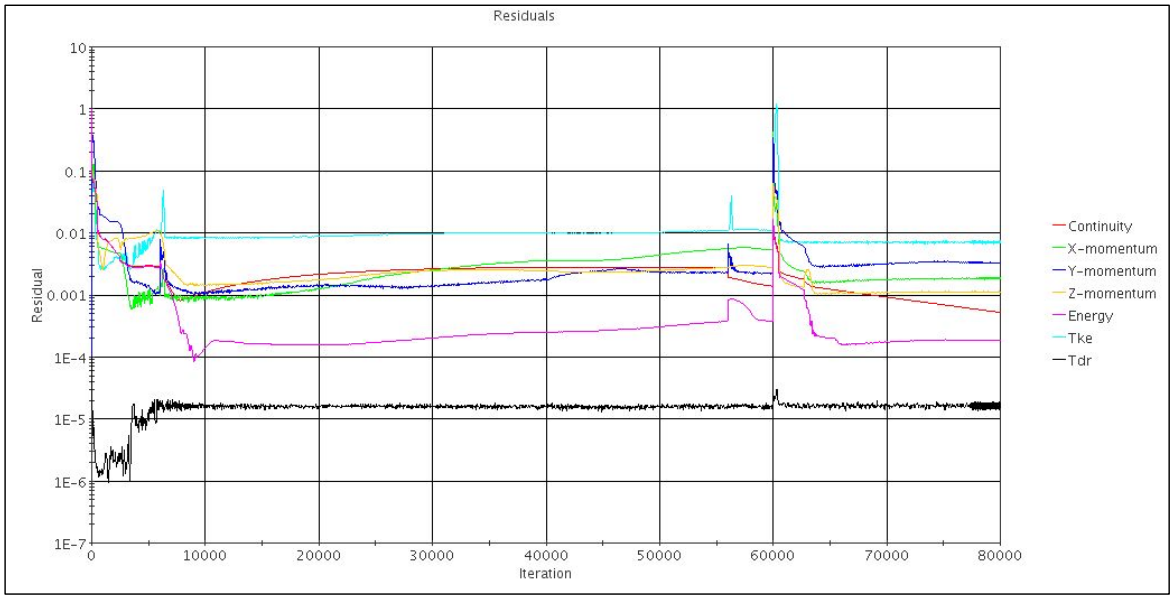

Figure 9 CFD Analysis #5 - Residuals

E. VERIFICATION AND VALIDATION

Consistent with good engineering practice, the expected use of the results, and available project funds, a verification and validation methodology (V&V), for example a methodology similar to that presented by the NPARC Alliance, should be followed when comparing CFD results to experimental data. An informal V&V process was followed. This process included limited mesh refinement studies, primarily due to the complications that arose during this study (e.g., convergence problems and code calibration requirements), an iterative convergence study, and verification of consistency study (i.e., mass and energy conservation) [NPARC Alliance 2008, Oberkampf and Roy 2010].

F. CONCLUSIONS AND RECOMMENDATIONS

Upon completion of this scoping study, the following is concluded:

1. CFD Modeling of the RCCS is complex.
2. The RCCS models require a significant amount of computational overhead, requiring the use of high performance computing.
3. To improve solution accuracy, especially in environments of high heat flux, sufficient prism layers should be used to resolve the velocity and thermal boundary layer.
4. The CFD model is sensitive to boundary layer resolution (i.e., number of prism layers)
5. The STAR-CCM+ ‘transient coupled’ solver should be used in models with a large number of prism layers and heat transfer present.
6. Computational overhead can be reduced by modeling the major components of the RCCS individually.

Based on the CFD scoping studies presented in this report, the following recommendations are provided in order to collect sufficient experimental information to support CFD code boundary conditions and validation:

1. The UW air RCCS experimental facility should be equipped with the appropriate instrumentation to collect turbulent data in order to compute turbulence intensity at key locations, for example upstream of the inlet plenum and at the inlets to the heated ducts.

2. The UW RCCS experimental facility should be equipped with the appropriate instrumentation in the heated duct to measure heat flux, over the length of each duct on each of the RCCS duct sides.

3. Consideration should be given to conducting a validation experiment, including storing the experimental data in a repository, so that experimental data could be available to other researchers for CFD modeling purposes.

G. REFERENCES

ANSYS Inc., 2012. ANSYS-FLUENT Theory Guide, Release 14.5. Canonsburg, Pennsylvania.

CD-adapco, 2009. STAR-CCM+ Version 4.0x Foundation Training. New York.

CD-adapco, 2013. STAR-CCM+ User Guide, Version 8.04. New York.

CD-adapco, 2014. The Steve Portal Technical Article 3716. https://cd-adapco.secure.force.com/index/Site_Login (accessed 10.11.2014).

Dassault Systemes SolidWorks Corporation, 2013. SolidWorks 2013. Waltham, Massachusetts.

Dave, A., Hu, R., Manera, A., Merzari, E., and Pointer, W. D., 2012. CFD Simulation of NSTF. Transaction of American Nuclear Society, Vol. 106 pp. 1323-1326.

Department of Energy (DOE), 1992. Preliminary Safety Information Document for the Standard MHTGR, Volume 1. DOE Report HTGR-86-024 (Document # HTGR-86024 Rev. 13), September 9, 1992.

Hamman, K. D. and Tokuhiro, A., 2014. Air RCCS CFD Models Project Summary, University of Idaho presentation. October 15, 2014.

Hu, R. and Pointer W. D., 2013. CFD Analyses of Natural Circulation in the Air-Cooled Reactor Cavity Cooling System. M&C 2013, 5-9 May 2013, Sun Valley, Idaho.

Lisowski, D. D., Muci, M. A., Anderson, M. H. and Corradini, M. L., 2013. Design Considerations for a Scaled Reactor Cavity Cooling System with Air for the VHTR. 15th International Topical Meeting on Nuclear Reactor Thermal-Hydraulic NURETH-15, 12-17 May 2013, Pisa, Italy.

Lomperski, S., Pointer, W. D., Tzanos, C. P., Wei, T. Y. C., Crooks, C. M., and Rodriguez, O. A., 2010. RCCS Studies and NSTF Preparation Air-Cooled Option. Argonne National Laboratory report, ANL-GenIV-142.

Lomperski, S., Pointer, W. D., Tzanos, C. P., Wei, T. Y. C., and Krauss, A. R., 2011. Generation IV Nuclear Energy System Initiative. Air-Cooled Option RCCS Studies and NSTF Preparation. Argonne National Laboratory report, ANL-GenIV-179.

Muci , M. A., 2013. "RCCS PROJECT – CAD SOLID MODELS." E-mail communications with K.D. Hamman providing SolidWorks models for air RCCS (nominal geometry) on August 28, 2013.

Muci , M. A., 2014a. "Forced Circulation Experimental Data." E-mail communications with K.D. Hamman related to Test-10 experimental data on May 27, 2014.

Muci, M. A., 2014b. Thermal Hydraulic Analysis of an Experimental Reactor Cavity Cooling System with Air. Master Thesis, University of Wisconsin.

National Program for Applications-Oriented Research in CFD (NPARC Alliance,) 2008. Overview of CFD Verification and Validation. www.grc.nasa.gov/WWW/wind/valid/tutorial/overview.html (accessed 7.11.2014).

Oberkampf, W.L . and Roy, C.J., 2010. Verification and Validation in Scientific Computing. Cambridge University Press, New York.

Pope, S.B., 2001. Turbulent Flows. Cambridge University Press, Cambridge.

Tzanos, C. P., 2005. CFD Analysis for the Applicability of the Natural Convection Shutdown Heat Removal Test Facility (NSTF) for the Simulation of the VHTR RCCS. Argonne National Laboratory report, ANL-GenIV-55.

Wilcox, David C., 2000. Turbulence Modeling for CFD. DCW Industries, Inc., La Cañada California.

H. APPENDICES

Appendix A: Mesh Settings and Metrics

Table 5 – Mesh Parameters

	Component	Mesh Type	Boundary Layer Thickness	No. Prism Layers	No. Elements	Wall Y+ (heated)	Wall Y+ (other)	Wall Y+ (duct walls)
Analysis #1 (high velocity)	Outlet Plenum	Prism/Polyhedral	2.5 mm	10	690,920	N/A	0.31	5.00
	Outlet Plenum (Sym)	Prism/Polyhedral	2.5 mm	10	366,428	N/A	0.29	4.95
Analysis #1 (low velocity)	Outlet Plenum	Prism/Polyhedral	2.5 mm	10	690,920	N/A	0.06	1.00
	Outlet Plenum (Sym)	Prism/Polyhedral	2.5 mm	10	366,428	N/A	0.06	0.92
Analysis #2	Full RCCS (Sym)	Prism/Polyhedral	2.5 mm/0.35 mm	10	3,853,442	0.03	0.21	0.67
Analysis #3	Full RCCS	Prism/Polyhedral	3.0 mm	20	9,004,257	0.06	0.09	19.80
Analysis #4	Inlet Plenum	Prism/Polyhedral	3.5 mm	21	2,740,704	N/A	0.06	9.75
Analysis #5	Inlet Plenum	Prism/Polyhedral	3.5 mm	21	2,740,704	N/A	0.03	46.70
	Duct #4 (Sym)	Prism/Trimmer	3.0 mm	20	986,624	0.07	N/A	N/A

Table 6 – Mesh Metrics

	Face Validity 1.00	Face Validity 0.95 to 1.00	Volume Change 1 to 10^{-1}	Volume Change 10^{-2} to 10^{-1}	Volume Change 10^{-3} to 10^{-2}	Volume Change 10^{-4} to 10^{-3}	Volume Change 10^{-5} to 10^{-4}
Analysis #1 (High)	100%	0%	96.126%	3.557%	0.317%	0.00%	0.00%
	100%	0%	96.099%	3.575%	0.326%	0.00%	0.00%
Analysis #1 (Low)	100%	0%	96.126%	3.557%	0.317%	0.00%	0.00%
	100%	0%	96.099%	3.575%	0.326%	0.00%	0.00%
Analysis #2	~ 100%	(7 elements)	93.207%	6.763%	0.030%	0.00%	0.00%
Analysis #3	~ 100%	(9 elements)	99.451%	0.457%	0.075%	0.017%	0.00%
Analysis #4	100%	0%	99.549%	0.253%	0.140%	0.057%	0.00%
Analysis #5 (LP)	100%	0%	99.549%	0.253%	0.140%	0.057%	0.00%
Analysis #5 (Duct)	100%	0%	100%	0%	0%	0%	0%

Appendix B: Simulation Settings and Boundary Conditions

Table 7 – Simulation Settings (1)

				Under-Relaxation Factor					
		Temporal	Numerical						Courant
	Component	Analysis Type	Solver	Velocity	Pressure	Energy	k-ε Turb.	k-ε Viscosity	Number
Analysis #1 (High)	Outlet Plenum	Steady	Segregated	0.7	0.3	0.9	0.8	1.0	N/A
	Outlet Plenum (Sym)	Steady	Segregated	0.7	0.3	0.9	0.8	1.0	N/A
Analysis #1 (Low)	Outlet Plenum	Steady	Segregated	0.7	0.3	0.9	0.8	1.0	N/A
	Outlet Plenum (Sym)	Steady	Segregated	0.7	0.3	0.9	0.8	1.0	N/A
Analysis #2	Full RCCS (Sym)	Steady	Segregated	0.7	0.3	0.9	0.8	1.0	N/A
Analysis #3	Full RCCS	Transient	Segregated	0.8	0.2	0.9	0.8	1.0	N/A
Analysis #4	Inlet Plenum	Steady	Segregated	0.3	0.7	0.9	0.01	0.1	N/A
Analysis #5	Inlet Plenum	Transient	Coupled	N/A	N/A	N/A	0.8	1.0	5.0
	Duct #4 (Sym)	Steady	Coupled	N/A	N/A	N/A	N/A	N/A	5.0

Table 8 – Simulation Settings (2)

		Flow Type	Ideal	Turbulence	Wall
	Component	(Circulation)	Gas (Air)	Model	Treatment
Analysis #1 (High)	Outlet Plenum	Forced	X	Realizable K-Epsilon (two layer)	All Y^+ (two layer)
	Outlet Plenum (Sym)	Forced	X	Realizable K-Epsilon (two layer)	All Y^+ (two layer)
Analysis #1 (Low)	Outlet Plenum	Forced	X	Realizable K-Epsilon (two layer)	All Y^+ (two layer)
	Outlet Plenum (Sym)	Forced	X	Realizable K-Epsilon (two layer)	All Y^+ (two layer)
Analysis #2	Full RCCS (Sym)	Natural	X	Realizable K-Epsilon (two layer)	All Y^+ (two layer)
Analysis #3	Full RCCS	Forced	X	Realizable K-Epsilon (two layer)	All Y^+ (two layer)
Analysis #4	Inlet Plenum	Forced	X	Realizable K-Epsilon (two layer)	All Y^+ (two layer)
Analysis #5	Inlet Plenum	Forced	X	Realizable K-Epsilon (two layer)	All Y^+ (two layer)
	Duct #4 (Sym)	Forced	X	Realizable K-Epsilon (two layer)	All Y^+ (two layer)

Table 9 – Inlet Boundary Conditions

		Inlet Boundary Conditions					
		Velocity	Tke	Tdr	Turb	Turb	Temperature
	Component	(m/s)	(J/kg)	(m^2/s^3)	Intensity	Length Scale	(C)
Analysis #1 (High)	Outlet Plenum	See Table	See Table	See Table	N/A	N/A	See Table
	Outlet Plenum (Sym)	See Table	See Table	See Table	N/A	N/A	See Table
Analysis #1 (Low)	Outlet Plenum	See Table	See Table	See Table	N/A	N/A	See Table
	Outlet Plenum (Sym)	See Table	See Table	See Table	N/A	N/A	See Table
Analysis #2	Full RCCS (Sym)	(pressure = 0)	6.00E-04	7.92E-05	N/A	N/A	25.0
Analysis #3	Full RCCS	5	3.75E-03	1.24E-03	N/A	N/A	15.9
Analysis #4	Inlet Plenum	5	3.80E-03	1.00E-03	N/A	N/A	16.0
Analysis #5	Inlet Plenum	4.788	N/A	N/A	2%	0.03048	17.2
	Duct #4 (Sym)	0.52, -0.6974, 5.41	5.4964	1.08E+02	N/A	N/A	18.4

Table 10 – Heat Transfer Boundary Conditions

		Heat Transfer	Total		
		F/B/L/R	Heat Transfer	Oulet	Ramp
	Component	(W/m^2)	(kW)	Boundary Cond.	Parameters
Analysis #1 (High)	Outlet Plenum	No	N/A	pressure = 0	No
	Outlet Plenum (Sym)	No	N/A	pressure = 0	No
Analysis #1 (Low)	Outlet Plenum	No	N/A	pressure = 0	No
	Outlet Plenum (Sym)	No	N/A	pressure = 0	No
Analysis #2	Full RCCS (Sym)	1678*cosine[f(z)] {all faces}	9.785	pressure = 0	No
Analysis #3	Full RCCS	145.7/0/441.8/441.8	4.365	pressure = 0	No
Analysis #4	Inlet Plenum	No	N/A	flow-split	No
Analysis #5	Inlet Plenum	No	N/A	pressure = 0	No
	Duct #4 (Sym)	2239.9/1318.7/1686.8/NA	1.435	pressure = 0	Yes

Appendix C: Wall-bounded Flows

A common engineering problem is computing temperature and velocity fields for turbulent flows influenced by an adjacent wall. These types of flow problems are typically referred to as 'wall-bounded flows.' For wall-bounded flows, the variation in velocity and temperature gradients near the wall may be large; therefore, it is important to capture the near-wall variation in temperature and velocity in order to accurately compute near-wall velocity and thermal gradients, which are needed to compute wall shear stress and heat transfer.

It has been shown, using dimensional analysis arguments and supported with experimental data, that the velocity and temperature distribution, within the turbulent boundary layer, can be characterized by logarithmic profiles [Cebeci (2002); White (1991)]. The logarithmic laws for velocity and temperature as a function of distance from the wall are shown below in Equations 1 through 5.[1,2]

$$\frac{u}{u_\tau} = \frac{1}{\kappa} ln(\frac{u_\tau y}{\nu}) + c \tag{1}$$

$$u^+ = \frac{1}{\kappa} ln(y^+) + c \tag{2}$$

$$\frac{T_w - T}{T_\tau} = \frac{1}{\kappa_h} ln(\frac{u_\tau y}{\nu}) + c_h \tag{3}$$

$$T_\tau = \frac{\dot{q}_w}{\rho c_p u_\tau} \tag{4}$$

$$T^+ = \frac{1}{\kappa_h} ln(y^+) + c_h \tag{5}$$

[1] The constants c and c_h are determined experimentally.

[2] "While there are, indeed, many flows where these equations achieve a close fit to the actual profiles, it is equally certain that there are many where they do not." (Launder, 1988)

Figure 1 shows a typical turbulent boundary layer velocity profile for incompressible flow over a smooth flat plate. The different regions of the turbulent boundary layer are defined based on the value of y^+ or the wall normal distance (y) to boundary layer thickness (δ) ratio. For example, the inner region begins at ratio of approximately $\frac{y}{\delta} < 0.1$. For $y^+ < 50$, the molecular viscosity has a direct effect on shear stress, but the logarithmic law shows poor agreement with the 'typical velocity profile.' Yet in the 'viscous sublayer' region (i.e., $y^+ < 5$), approximating the velocity profile as $u^+ = y^+$, shows good agreement with the 'typical velocity profile.' Noteworthy is that within the buffer zone neither the logarithmic law nor the viscous sublayer approximation ($u^+ = y^+$) holds.

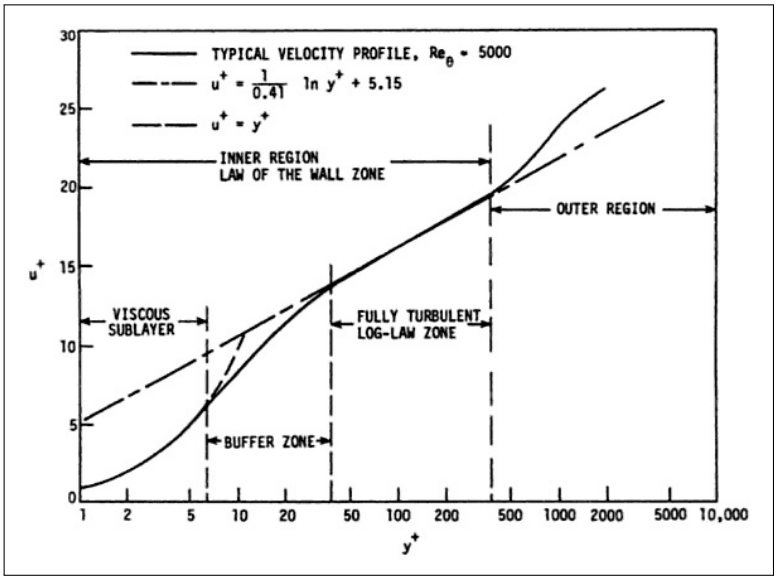

Figure 1: Mean velocity profiles (Tannehill et al., 1997)

It should be pointed out that resolving the viscous sublayer using experimental techniques is difficult since measurements need to be taken near the wall, typically on the order of 1 mm. For example, Kähler et al. (2012) discusses problems associated with measuring the boundary layer thickness in the viscous sublayer. In fact, Figure 2 shows that the experimental PTV data does not adequately resolve the viscous sublayer.

Again, it is necessary to resolve the viscous and thermal boundary layers in order

to determine temperature and velocity gradients near the wall. Given that CFD codes are model-based, requiring boundary conditions for wall-bounded flows, two wall boundary layer modeling approaches exist: wall functions and near-wall models.

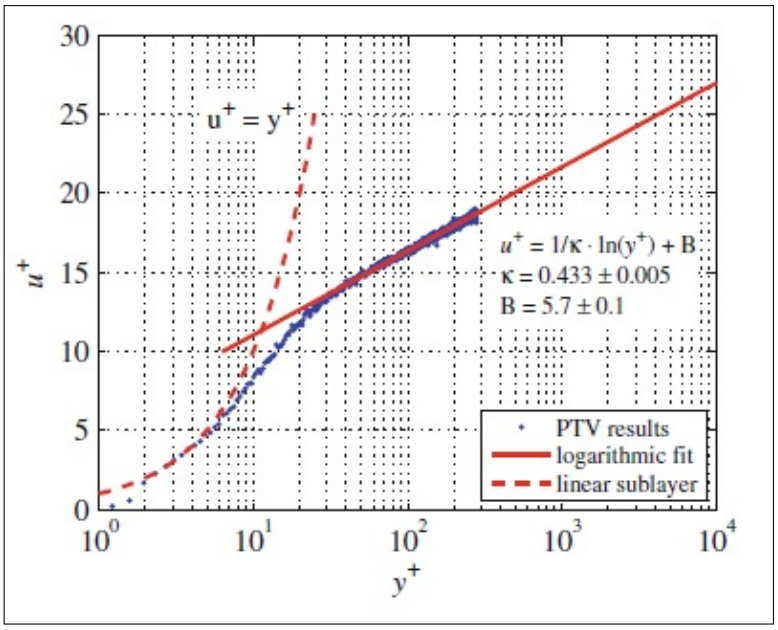

Figure 2: Mean velocity profiles (Kähler et al., 2012)

Wall functions are algebraic relationships that provide 'near wall' boundary conditions for the mean flow and turbulence transport equation, while circumventing the need for an excessive number of grids by placing the first computational node outside the viscous sublayer and estimating velocity and temperature at that node using Equations 1 through 5. Figure 3 is a graph of two non-dimensionalized parameters, velocity (u^+) versus wall distance (y^+). The point identified on the graph represents a wall boundary condition computed using a wall function (e.g., Equation 1).

The near-wall modeling approach actually resolves the viscous sublayer by placing the first computational node within the viscous sublayer. Near-wall boundary conditions are relatively straightforward. For example, applying $u^+ = y^+ = 0$ at the wall represents one boundary condition; and for heat transfer, applying Fourier's law at the wall, represents a second boundary condition. But, modeling turbulence effects near the wall is more rigorous, requiring the use of damping functions to reproduce

the correct asymptotic behavior.[3] Figure 4 is a graph of two non-dimensionalized parameters, velocity (u^+) versus wall distance (y^+), with two turbulent velocity profile plots: DNS and RANS. It should be noted, that unlike the experimental data presented in Figure 2, DNS is capable of 'predicting' the viscous sublayer velocity profile; and RANS is capable of 'modeling' the viscous sublayer.[4]

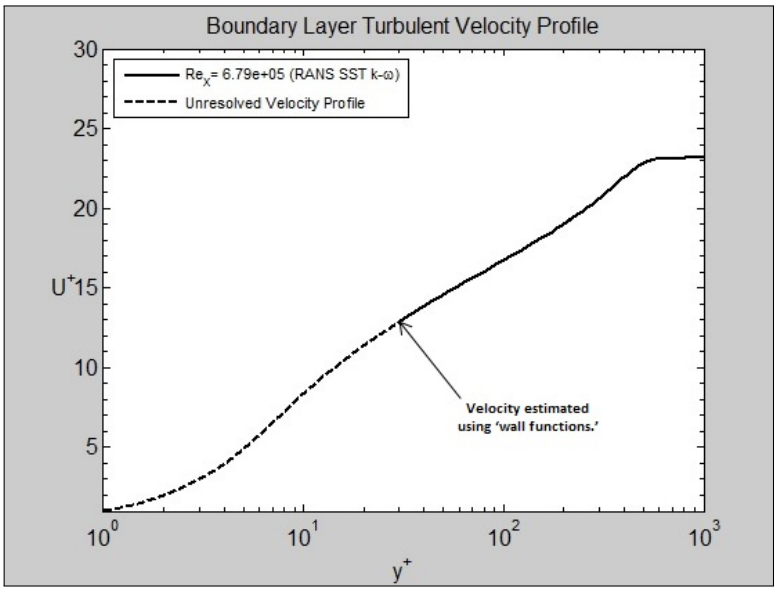

Figure 3: Mean velocity profile, wall function example

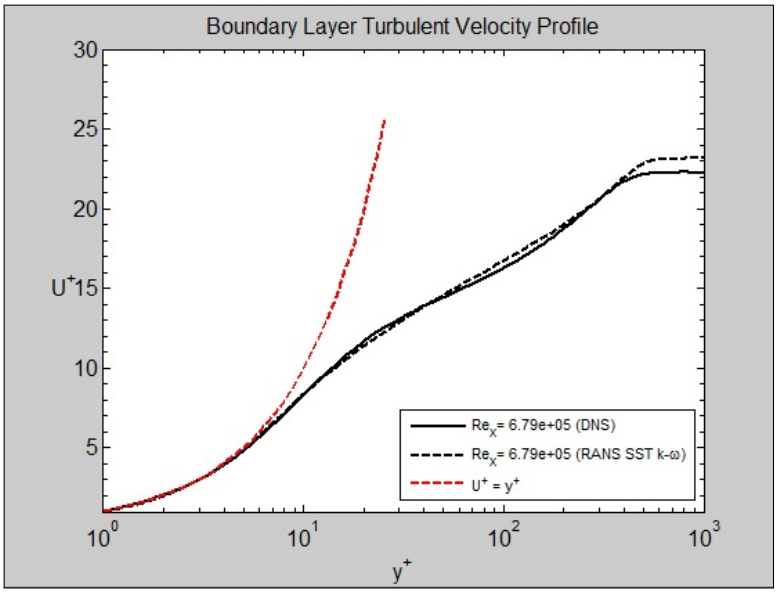

Figure 4: Mean velocity profiles (Appendix A–ZPG)

[3]Bredberg (2000) provides a good overview of wall functions and near-wall boundary conditions.

[4]Additional details related to the CFD DNS/RANS simulation results can be found in Appendix A.

For accurate CFD solutions, especially in situations where high velocity or temperature gradients exist, the near-wall modeling approach should be used. In fact in his well-known paper "On the Computation of Convective Heat Transfer in Complex Turbulent Flows," Launder argues that "... for accuracy and width of applicability, a fine-grid low-Reynolds-number treatment should be employed near the wall in place of wall functions, despite the attractive simplicity of the latter approach." (Launder, 1988).

Unfortunately, resolving the boundary layer requires a significant number of mesh elements near the wall resulting in additional computational overhead. In fact, the first node of a boundary layer resolved using the near-wall modeling approach should be placed at approximately $y^+ = 1$, while the first node of a boundary layer resolved using the wall function approach should be placed at $y^+ \geq 30$ (i.e., in the region where the logarithmic law applies). Figure 5 compares the two wall treatment approaches.

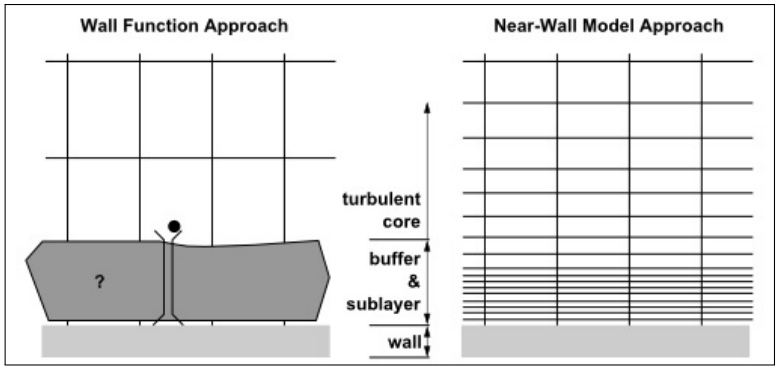

Figure 5: Wall treatment approaches (ANSYS, 2012)

Given the theoretical and practical reasons for using the near-wall modeling approach, it would be prudent to compare a computational mesh that uses wall functions to one that resolves the viscous sublayer. Figure 6 shows a wall function mesh where three prism layers are used to model the boundary layer, and the polyhedral elements are used to model the 3D duct interior. Figures 7 and 8 show a near-wall mesh where 22 prism layers are used to model the boundary layer, and trimmer elements are used to model the 3D duct interior. The maximum wall y^+ value for the near-wall mesh was 0.11 indicating that the viscous sublayer was resolved.

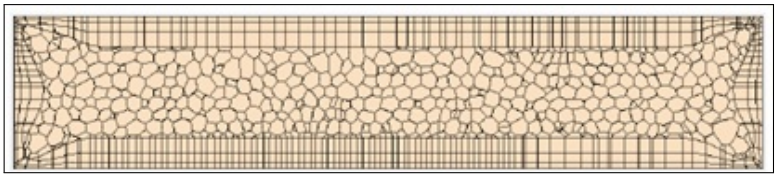

Figure 6: Wall function mesh with 3 prism layers (Lomperski et al., 2011)

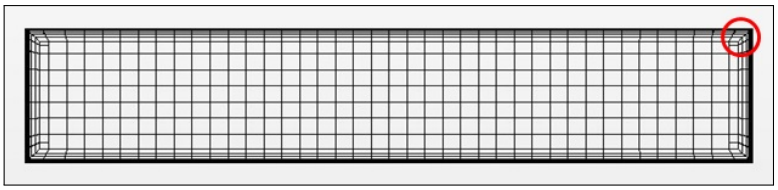

Figure 7: Near-wall mesh (Hamman et al., 2015)

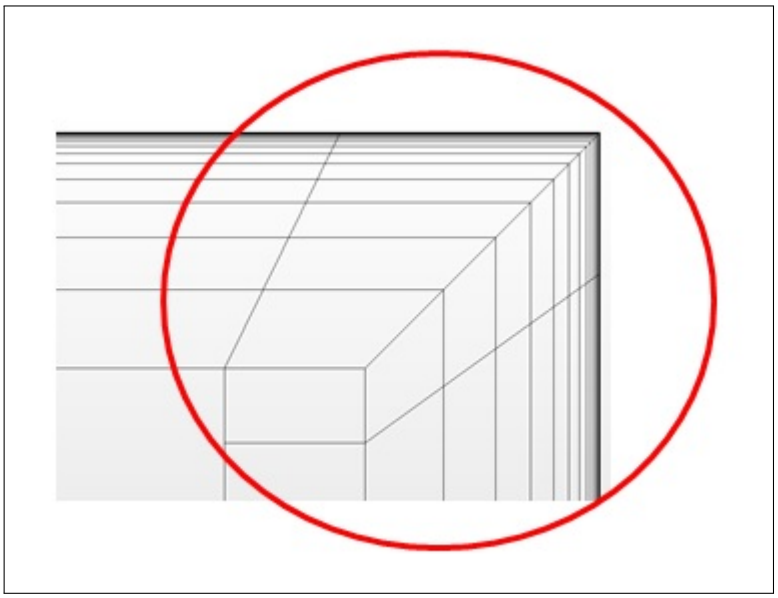

Figure 8: Near-wall mesh with 22 prism layers (Hamman et al., 2015)